The Influence of Pressure Ratio on Film Cooling Performance of a Turbine Blade

by

James V. Bubb, BS

submitted to the Faculty of the
Virginia Polytechnic Institute and State University
in partial fulfillment of the requirements for the degree of

Master's of Science

in

Mechanical Engineering

Approved:

Dr. Thomas E. Diller, Co-Chair

Dr. Wing F. Ng, Co-Chair

Dr. Joseph A. Schetz

July 1999

Blacksburg, Virginia

Keywords: Heat Transfer, Turbine, Film Cooling, Transonic Cascade

The Influence of Pressure Ratio on Film Cooling Performance of a Turbine Blade

James V. Bubb
Virginia Polytechnic Institute and State University, 1999
Advisor: Dr. Thomas E. Diller, Dr. Wing F. Ng

Abstract

The relationship between the plenum to freestream total pressure ratio on film cooling performance is experimentally investigated. Measurements of both the heat transfer coefficient and the adiabatic effectiveness were made on the suction side of the center blade in a linear transonic cascade. Entrance and exit Mach numbers were 0.3 and 1.2 respectively. Reynolds number based on chord and exit conditions is 3×10^6. The blade contour is representative of a typical General Electric first stage, high turning, turbine blade. Tunnel freestream conditions were 10 psig total pressure and approximately 80 ° C. A chilled air coolant film was supplied to a generic General Electric leading edge showerhead coolant scheme. Pressure ratios were varied from run to run over the ranges of 1.02 to 1.20. The density ratio was near a value of 2. A method to determine both the heat transfer coefficient and film cooling effectiveness from experimental data is outlined.

Results show that the heat transfer coefficient is independent of the pressure ratio over these ranges of blowing parameters. Also, there is shown to be a weak reduction of film cooling effectiveness with higher pressure ratios. Results are shown for effectiveness and heat transfer coefficient profiles along the blade.

Acknowledgements

First, I would like to thank the faculty on my committee, Dr. Thomas Diller, Dr. Wing Ng, and Dr. Joseph Schetz. Your help and guidance throughout this research program has been much appreciated. Also, the financial support of the Air Force Office of Scientific Research is gratefully acknowledged.

None of this research could have been accomplished without the help of the rest of the graduate research team: Oliver Popp, Dwight Smith, and Hank Grabowski. Your insights, helping hands, and sense of humor during the long days and nights of tunnel runs were invaluable.

Obviously, I owe a great debt to my parents who saw fit to bring me into this wonderful world and taught me, among other things, the importance of an education, and to my brothers Ryan, Mac, and Bradley who have always been my best friends.

Finally, and most importantly, I want to thank the Lord for giving me the gifts to do all that I do.

Contents

List of Tables

List of Figures

Nomenclature

Symbols

A	Orifice area
C_d	Discharge coefficient
C_p	Specific heat
DR	Density ratio
h	Heat transfer coefficient
I	Momentum ratio
k	Thermal conductivity
$\dot{m}$	Mass flow rate
M	Blowing ratio
Ma	Mach Number
PR	Pressure ratio
q''	Heat flux
r	Recovery factor
S	Coolant hole spacing

T	Temperature
U	Velocity
Tu	Turbulence
x	Downstream distance

Greek Symbols

δ	Uncertainty
γ	Specific heat ratio
η	Adiabatic film cooling effectiveness
ρ	Density
ε	Error value (from Sec. 2.3.2.3)

Subscripts

act	Actual
aw	Adiabatic wall
c	Coolant
d	Drop from freestream
e	Boundary layer edge
∞	Freestream
obj	Objective
r	Recovery
t	Total
w	Wall

Chapter 1

Introduction

1.1 Background

1.1.1 Turbine Blade Heat Transfer

The gas turbine industry continues to push aircraft engine performance to higher levels. New engine designs are yielding higher efficiencies and thrust-to-weight ratios for modern aircraft. Fig. 1.1 is an illustration of a typical aircraft gas turbine. Critical to the increased performance is the increase of turbine inlet temperatures. It is well known that higher turbine inlet temperatures yield higher thermodynamic efficiencies, and present engine designs utilize turbine inlet temperatures well in excess of the operating conditions temperatures of blade materials. A historical perspective of progress of turbine inlet temperature is given in Fig. 1.2. This figure shows the widening difference between the blade temperatures and the turbine inlet temperature. This difference between the turbine inlet temperature and the blade operating temperature is realized through the use of blade cooling. There are many different

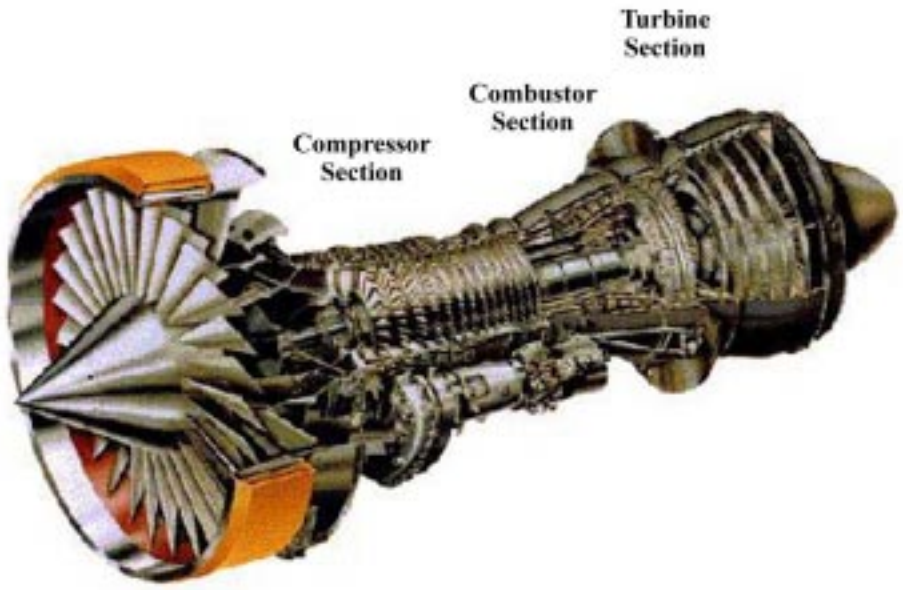

Figure 1.1: Modern Aircraft Engine (Courtesy *General Electric*)

cooling techniques that have been devised and implemented to keep the blade surfaces at lower temperatures. The future trend in engine design is to both increase turbine inlet temperatures further and to increase the temperature difference between the blade and the freestream flow. In order to push the envelope of engine performance further, a better understanding of coolant schemes is essential.

1.1.2 Film Cooling

One widely used blade cooling technique is film cooling. Film cooling is accomplished by injecting, from within the blade, a thin film of cold air along the blade surface separating the blade from the hot freestream gases. This film provides an insulating layer and has the effect of protecting the blade from high temperatures of the hot freestream flow. Fig. 1.3 illustrates three different film cooling schemes.

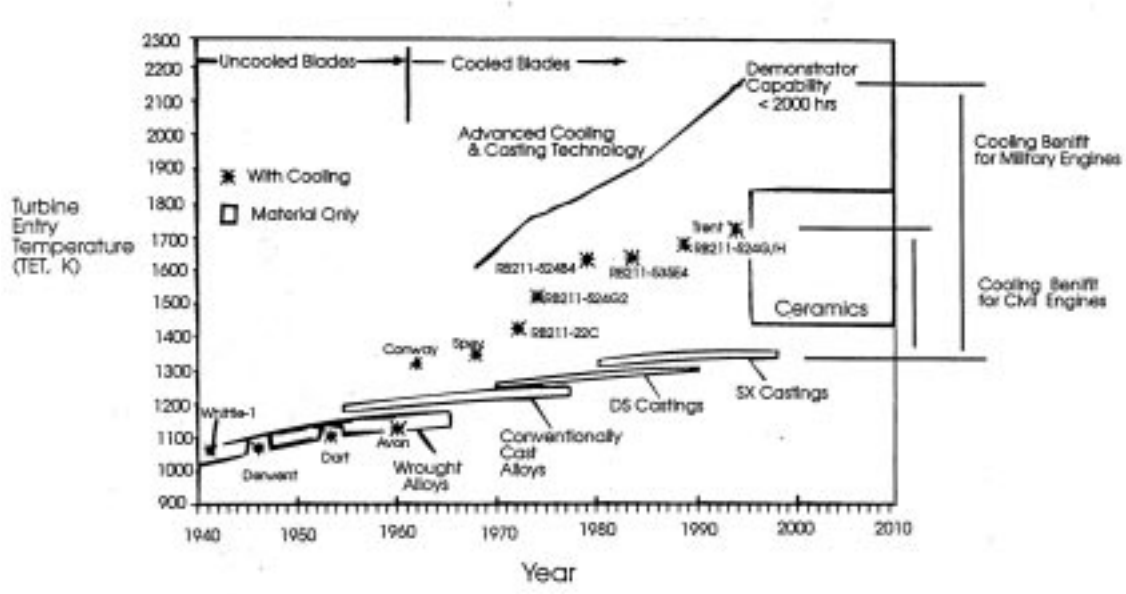

Figure 1.2: Advance of Materails and Cooling Technology, (Courtesy Royal Aeronautical Society/ Aerospace - 1994)

Unfortunately, this cold film protection from heat flux comes at a price. The source of the cold coolant air is bleed-off air from the last stage of the compressor section. This high pressure air bypasses the combustor section of the engine, and in so doing, is maintained at much lower temperatures than the core turbine flow. This bleed-off air, however, is removed from the core mass flow and subtracts from the overall thrust of the engine. Obviously, the engine designer wants to minimize the amount of bleed-off air required to cool the blade. From this, it is apparent that a good understanding of not only how film cooling schemes affect heat transfer is needed, but also an understanding of what parameters control the level of effectiveness provided is needed.

In the past, a great deal of research has been devoted to turbine heat transfer phenomenon, and specifically, film cooling schemes. A good summary of different film cooling research is given by Goldstein [7]. This study continues the understanding of film cooling heat transfer.

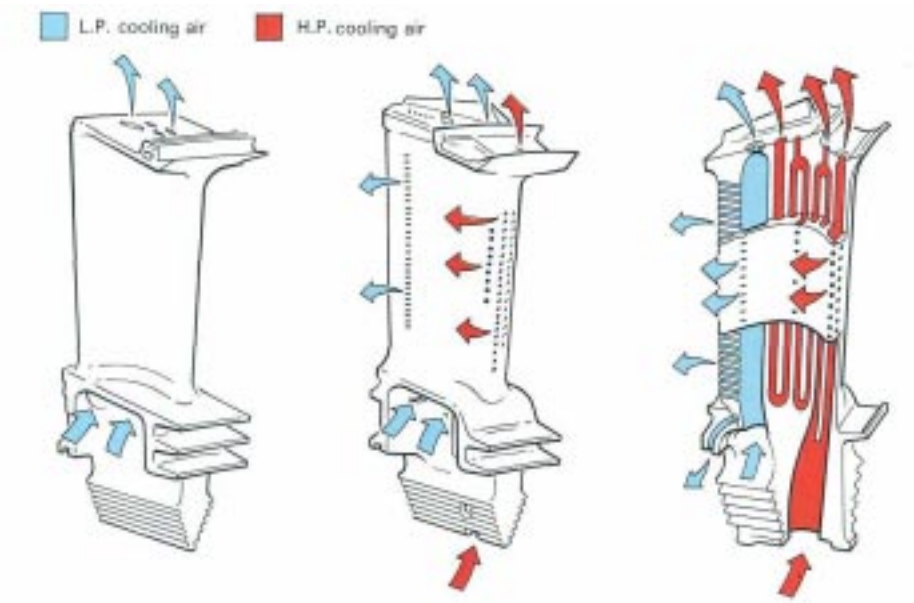

Figure 1.3: Film Cooling Schemes (Courtesy *Rolls-Royce*)

1.2 Motivation

1.2.1 Heat Transfer Coefficient

Turbine heat transfer and film cooling can be described using some important variables. In general, convective heat transfer is described by,

$$q'' = h \cdot (T_{aw} - T_w) \tag{1.1}$$

The first of the important variables in this equation is the heat transfer coefficient, h. The heat transfer coefficient is for the most part dictated by the external flow field. h is a factor that relates a driving temperature difference, $T_{aw} - T_w$, to absorbed heat flux energy, q''. In order to keep blade temperatures low, it is in the best interest of the turbine designer to attempt to minimize heat transfer and consequently, h. In general, the injection of film cooling changes the fluid flow profile around the blade and usually increases the heat transfer coefficient. This increase in h is undesirable as it promotes heat transfer from the hot freestream flow, and good designs of film cooling should attempt to minimize this increase. Obviously, an understanding of exactly how film coolant schemes affect the heat transfer coefficient is important. While the introduction of film cooling has the effect of increasing h slightly, the technique's advantage is realized by a large decrease of the adiabatic wall temperature, T_{aw}.

1.2.2 Film Cooling Effectiveness

Eqn. 1.1 also shows that a second variable of importance that describes heat transfer in engines is the driving temperature difference, $T_{aw} - T_w$. In film cooling schemes, however, it is more convenient to examine a dimensionless form of this driving temperature difference. This dimensionless parameter is defined as the adiabatic

film cooling effectiveness, η.

$$\eta \equiv \frac{T_r - T_{aw}}{T_r - T_c} \tag{1.2}$$

The details of this expression will be discussed at length later in the thesis, but a basic understanding of this variable implies that a higher effectiveness results in the blade surface being protected from the high temperatures of the core flow.

1.2.3 Film Cooling Parameters

This research is an experimental investigation of parameters effecting both the film cooling effectiveness and heat transfer coefficient. In general, η and h are functions of many parameters in an engine environment. The most influential parameters can be grouped into two categories, Aerodynamics and Geometry. Specifically η and h are functions of,

Cooling Geometry...

- Downstream location, $\frac{x}{D}$
- Coolant scheme geometry (hole length, hole spacing, blowing angle, etc.)

Aerodynamics...

- Local Freestream Mach Number, Ma
- Freestream Turbulence, Tu
- Film Cooling Momentum Ratio, I,

$$I \equiv \frac{\rho_c U_c^2}{\rho_\infty U_\infty^2} \tag{1.3}$$

- Film Cooling Blowing Ratio, M,

$$M \equiv \frac{\rho_c U_c}{\rho_\infty U_\infty} \tag{1.4}$$

- Film Cooling Density Ratio, DR,

$$DR \equiv \frac{\rho_c}{\rho_\infty} \tag{1.5}$$

In these experiments the only geometric parameter studied is the downstream distance. This will be investigated by the use of several heat flux gauges staggered along the blade profile. The rest of the coolant geometry is all specified and will remain constant. The blade shape and coolant hole geometries are all fixed to one design.

Furthermore in these experiments, the local Mach number is fixed by the blade design (see Fig 2.8 and Fig. 2.6 for Mach number distributions) and the tunnel operating conditions. For this reason, it will not be varied and studied systematically. Freestream turbulence has been shown to have an influence on heat transfer and film-cooling effectiveness but was not studied in this thesis due to time constraints.

There are several experimental ratios that dictate the manner in which the coolant air leaves the coolant holes. These ratios have been given significant discussion in previous research. One of these, the density ratio, has been shown by Foster et al. [6] and Goldstein et al. [8] to be of secondary importance in determining film cooling effectiveness, at least in the ranges where the current experiments are performed. Furthermore, Goldstein [7] suggests that the parameter of importance in determining whether the coolant film layer lifts off the surface is the momentum ratio.

Since the density ratio has been assumed to be of secondary importance, and only two of the parameters defined in Eqn. 1.3 through Eqn. 1.5 can be varied independently, it was decided to investigate and discuss the results in terms of the

momentum ratio, and the blowing ratio can be backed out from the other two ratios. This decision to control the momentum ratio is also convenient, because the only ratio that can be controlled consistently in the experimental apparatus is the pressure ratio. Because of hardware constraints, the pressure ratio is held to a constant in the course of an experiment, but the temperature ratio varies transiently. From the isentropic flow relations, it can be shown that the temperature dependence cancels out of the formulation of the momentum ratio (See Section 3.3) such that the momentum ratio is purely a function of pressure ratio.

Implied in the outset of this research is Foster's and Goldstein's suggestion that effectiveness is independent of the density ratio (and consequently the temperature ratio). This hypothesis is to be tested with the experiments to see if the effectiveness is truly independent of the density ratio.

This research is an extension to past work done at Virginia Tech on heat transfer measurements. Earlier experiments performed by Smith [22] have developed the technique for measuring heat transfer coefficient and effectiveness in the cascade facility. The extension of the research here involves using this technique to study the influence of pressure ratio (and consequently momentum ratio) on film cooling performance.

1.3 Literature Review

The approaches that have been taken to investigate film cooling phenomenon can be separated into general two areas: experimental and computational. This literature review will concentrate on the experimental side as this is the area where the current research program focuses.

The database of literature on film cooling experiments is very extensive. This short literature review does not profess to be an exhaustive list and discussion of all that has been published in the research area. For the different kinds of research, representative facilities have been selected and discussed where invariably there are multiple researchers performing similar types of experiments with similar conclusions. A reference that provides a nice overview of fundamental film cooling analysis and experiments and the conclusions reached by researchers is given by Goldstein [7].

The most basic of film cooling experiments starts with the flat plate experiment. These types of tests are the simplest to set-up, and detailed measurements of film cooling parameters can be made easily. Experiments done at the University of Minnesota by Goldstein et al. [8] are some of the most basic flat plate discrete hole film cooling experiments. These experiments were performed on both a single coolant hole and one row of coolant holes with a flat plate geometry. Also, these experiments were performed at low speeds rather than at high speeds which are more representative of an engine environment. The thrust of their research was to vary the injection angles and blowing ratios to investigate film cooling effectiveness. These experiments generally showed that the cooling effectiveness was optimized for the hole inclined at 35° to the streamwise direction and that the centerline effectiveness decayed monotonically with distance from the coolant hole. Also, this study showed that at a blowing ratio of approximately 0.5 the centerline cooling effectiveness reached a maximum value. The researchers suggested the decline of effectiveness at higher blowing ratios

was due to the coolant film lifting off the surface and allowing the freestream air to penetrate to the surface.

Compound injection angle schemes (holes angled both in the streamwise and spanwise directions) have been studied at great length and in general have been shown to increase overall cooling effectiveness by better distributing the coolant layer of the surface. Recent studies by Ligrani et al. [16] investigate the possibilities and results of angled injection schemes.

The effect of surface curvature was investigated by Schwartz et al. [21]. Film cooling effectiveness was measured in this research by a mass transfer technique. This research showed that convex surfaces (similar to the suction side of turbine blades) had higher effectiveness values at higher momentum ratios than those of the flat plate experiments. The reason for this is that the pressure gradient held the jet to the surface longer and allowed for better coverage at higher blowing ratios.

Experiments performed by Ekkad et al. [5] investigated the effect of freestream turbulence on heat transfer and film effectivness on a cylindrical model. These experiments used a transient liquid crystal technique which gave high resolution measurements of local heat transfer and film cooling effectiveness. The results from this research showed a maximum effectiveness at a blowing ratio of about 0.4. One important conclusion from this work was that higher values of freestream turbulence reduced film effectiveness at lower blowing ratios, but this effect was diminished at the higher blowing ratios. Also, with the use of the liquid crystal, they were able to show that the location of the highest film effectiveness changes with the increase of blowing ratio. This geometry begins to exhibit the two dimensional and three dimensional nature of film cooling.

From these idealized fundamental geometries, the experiments on realistic blade geometries is developed. Some of the earliest research on realistic geometries

was performed by Ito et al. [13]. These experiments used turbine blades in a low speed ($Ma = 0.065$), cascade wind tunnel with a single row of coolant holes and made measurements using the mass transfer technique. One of the conclusions of this research was that the convex suction side surface provides a pressure gradient that helps to keep the coolant film attached to the blade surface at higher momentum ratios. At the highest of momentum ratios (M >1.5), the film would eventually lift off the surface and the effectiveness would decrease. This work also showed the three dimensional nature of the problem as it illustrated that the blowing ratio where the maximum effectiveness occurred depended on the downstream and spanwise distance from the coolant holes.

Recent research conducted by Bunker et al. [2] from General Electric Aircraft Engines studied a turbine blade and showerhead film cooling geometry representative of actual engine hardware and similar to the geometry used in this research. The experiments were run in a transonic linear cascade wind tunnel. These tests showed a well-behaved, well-mixed film at blowing ratios of 1.2 to 1.4 and density ratios of 1.8 to 2.0. The results showed a general monotonic decrease of both heat transfer coefficient and film cooling effectiveness along the suction side surface. Furthermore, it was seen that the heat transfer coefficient increased significantly with the introduction of film cooling. This research performed measurements only at one design condition of blowing and density ratios.

A closer approximation of engine geometries was accomplished by research at the University of Oxford by Guo et al. [10]. Experiments were performed on heavily film-cooled nozzle guide vanes in a transonic annular cascade facility. These experiments used thin-film gauges to measure a transient surface temperature history and back out the heat transfer coefficient and film cooling effectiveness. The results indicated a scatter of data for both the film cooling effectiveness and heat transfer coefficient profiles. The explanation for the strange profile was that the coolant film lifted off the blade surface. A closer distribution of gauges was needed to understand

the details of the coolant phenomenon.

Another step in experimental approximations to engine environments is a rotating facility. Research was performed by Epstein et al. [1] at Massachusetts Institute of Technology using a fully cooled transonic turbine blade in a short duration rotating facility. Measurements were made with thin film heat flux gauges distributed about the surface of the blade. This showed a notable increase in the heat transfer coefficient between the cooled and uncooled geometries. A comparison was also made between higher blowing ratios (1.24 for the first row of holes) and low blowing ratios (0.96 for the first row of holes). For comparison, our ranges of blowing ratios are from 1.5 to 2.5. The results from this comparison tended to suggest that film liftoff was occurring on the pressure side at the higher blowing ratio but not along the suction side.

Some general conclusions can be drawn from the published literature about both heat transfer coefficient and film cooling effectiveness. The first of these generalizations is that the heat transfer coefficient increases significantly with the introduction of film cooling. Second, film cooling effectiveness generally is reduced with downstream distance from the coolant exits, but in environments that approximate a real engine, effectiveness is inherently a three dimensional phenomenon.

In general, it was difficult to find researchers who were investigating the effect of pressure ratio in a high speed regime with realistic geometries. Epstein et al. [1] did investigate two separate blowing ratios at these realistic conditions.

This literature review attempts to place the Virginia Tech Transonic Wind Tunnel in context with the other experiments that have been performed by the scientific community. The Virginia Tech facility is somewhere in between the most realistic engine approximations (rotating rigs, full coolant scheme) and the more fundamental approximations (flat plate studies, single coolant row).

Chapter 2

Experimental Setup

2.1 Test Conditions

These heat transfer experiments were performed in the Vigrinia Tech Transonic Cascade Wind Tunnel. The test conditions were designed such that they attempted to match relevant engine conditions. A comparison of engine and experimental conditions is summarized in Table 2.1.

Table 2.1: Comparison of Experimental and Engine Conditions

Parameter	Engine	Experiment
Exit Mach Number	Transonic	1.2
Temperature Ratio	2	1.6 ... 2.4
Reynolds Number (based on exit and chord)	5×10^5	3×10^6
Pressure Ratio	1.04	1.02 ... 1.20
Turbulence Level	10% +	1%

The experiments are reasonably close to matching several of the nondimensional parameters of importance. The exit Mach number is transonic as one would expect to see in modern engine designs. The temperature ratio matched for at least

some portion of the tunnel run, and the pressure ratio can be set to reasonable values suggested by General Electric.

It can be seen that the Reynolds numbers are not exactly matched but are close. Perhaps more importantly, the turbulence levels are much lower than one would expect to see in an engine environment. This is a point of note and will be discussed in Chapter 5 as a suggested area of future work.

2.2 Wind Tunnel Facility

All experiments were performed in the Virginia Tech Transonic Cascade Wind Tunnel Facility. This tunnel is a blowdown facility capable of providing run times of approximately 60 sec at the desired test conditions. The wind tunnel provides a freestream flow at 10 psig. Fig. 2.1 is an illustration of the facility.

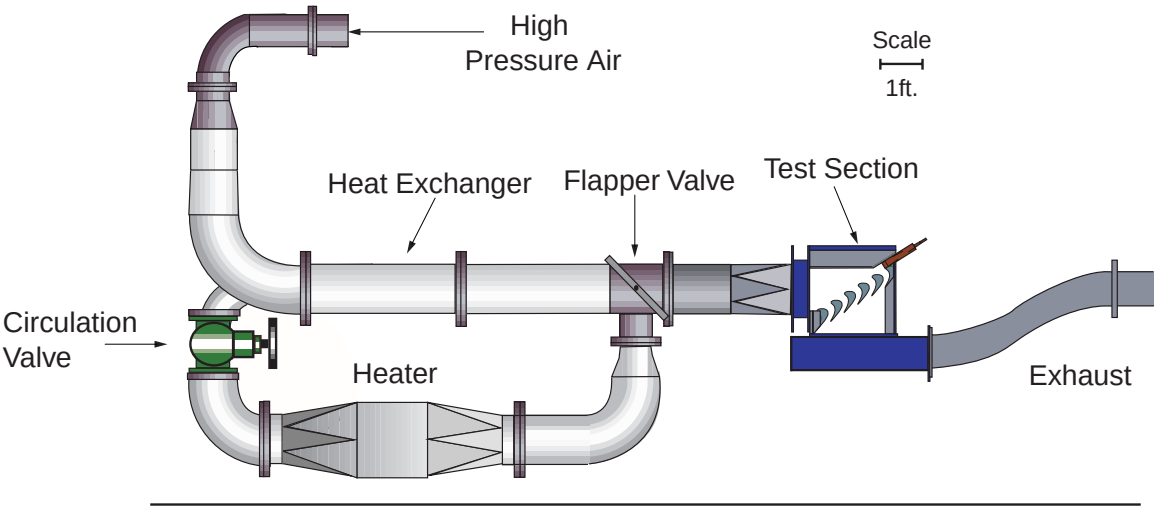

Figure 2.1: Windtunnel Facility

The freestream air for the experiment is provided by two large storage air tanks. The storage tanks are charged to 170 psi by a four-stage Ingersoll-Rand compressor. Before being stored in the tanks, the air is first passed through a dryer to remove water vapor to approximately three percent relative humidity. During a run, the tunnel control value regulates the tank pressure via a tunnel control algorithm to achieve a constant freestream pressure of 10 psig. Before entering the test section, the air is heated as it crosses over a bank of hot copper tubes. After the heated air crosses over the blade cascade it exits to atmosphere.

2.2.1 Heated Flow

The tunnel air is heated by the use of a passive heat exchanger comprised of a bank of copper tubes. This bank of copper tubes is heated before a test run by closing the flapper valve and opening the circulation valve which creates the circulation loop shown in Fig. 2.2. A 36 kW heater and fan then circulates air through this loop. This heats a bank of copper tubes in the upper portion of the loop to a temperature of approximately 130°C. After the tubes have reached this temperature, the heater and fan are turned off and the valves are reopened so the wind tunnel freestream flow can pass through the tubes. During a run, the thermal energy in the tubes is transferred

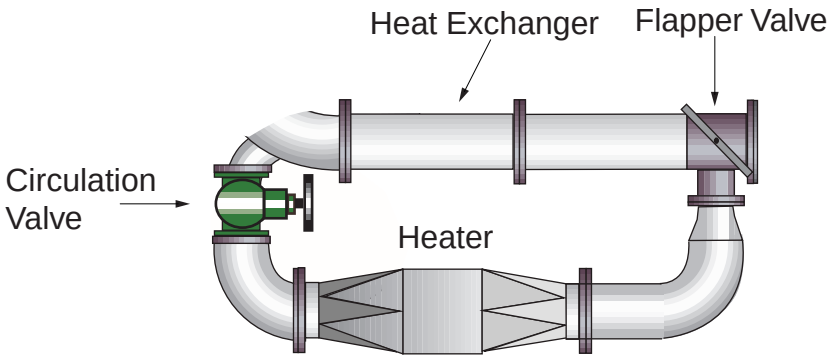

Figure 2.2: Circulation Loop

to the freestream flow. Because the copper tubes cool down during the run, the freestream air also cools. This causes the freestream temperature to vary during a run from about 100°C to 30°C. This changing freestream temperatures provides a range of $\frac{T_\infty}{T_c}$ ratio from about 1.4 to 2.6 during the course of a run.

2.2.2 Tunnel Control

Tunnel control is realized through a control algorithm written in C code. This program utilizes both a feed-back and feed-forward approach. The goal of this algorithm is to maintain the freestream pressure at a desired objective pressure. The objective pressure for all tests was 10 psig. The feed-forward portion of the code determines an initial opening position for the valve and a general profile for value position as a function of time. This general assumed position profile is then corrected via a pressure feedback from a Pitot probe located just before the test section and the objective pressure. This algorithm was able to keep $\frac{P_{obj}}{P_\infty}$ between 0.90 and 1.10 over a duration of approximately 20 seconds. Fig 2.3 is a graph of a pressure control for a typical run.

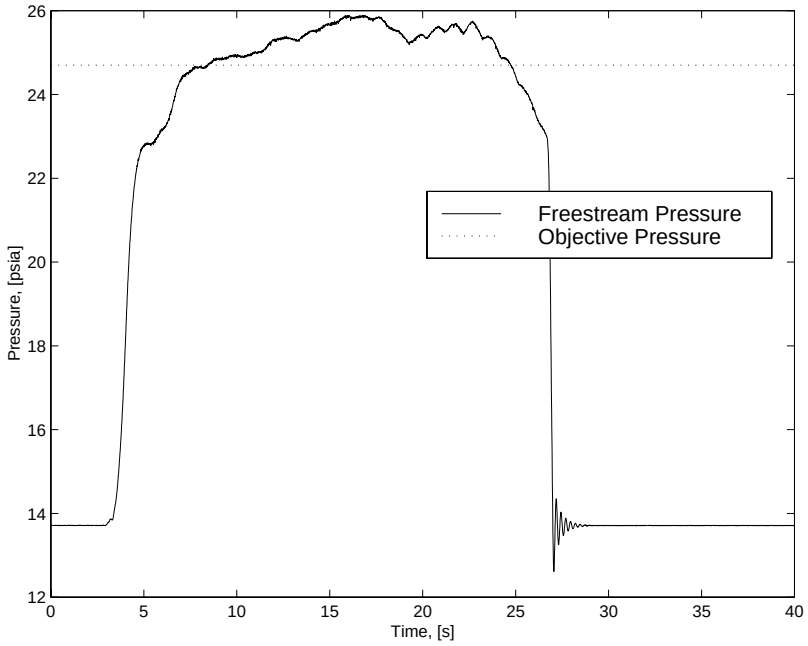

Figure 2.3: Typical Pressure Control During a Run

2.2.3 Test Section

The test section holds four full blades and two half blades for a total of five flow passages. Fig. 2.4 illustrates the blades in place. Only the center blade of the cascade is equipped with instrumentation. The blades have a 13.72 cm (5.4 inch) chord length and a 15.24 cm (6 inch) span. Flow enters the test section at Ma=0.3, goes though a high turning angle of 128°, and exits at Ma=1.3.

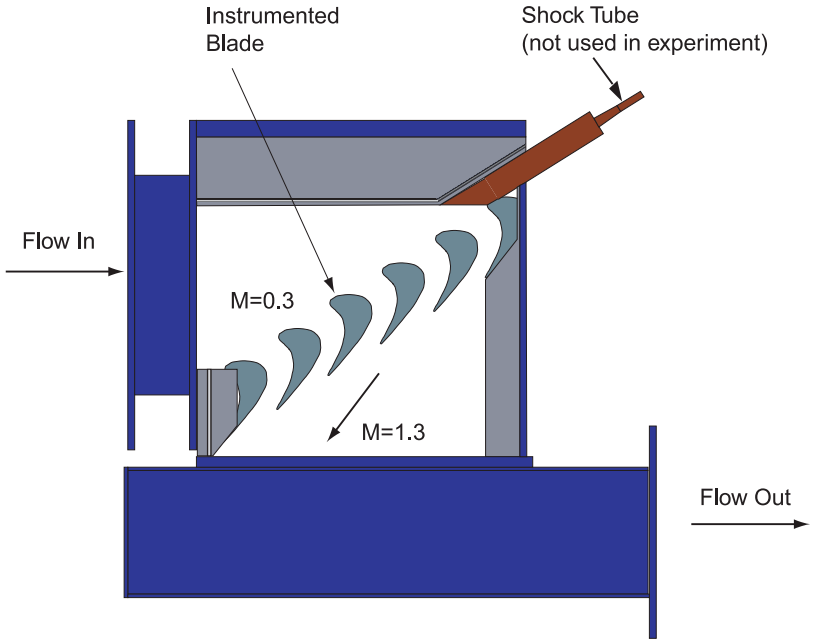

Figure 2.4: Test Section Schematic

The endwalls of the test section are made of one inch thick plexiglas to allow for flow visualization experiments to be performed. These plexiglas endwalls are then reinforced by one inch thich aluminum sidewalls. Fig. 2.5 shows the assembled casacade test section hardware.

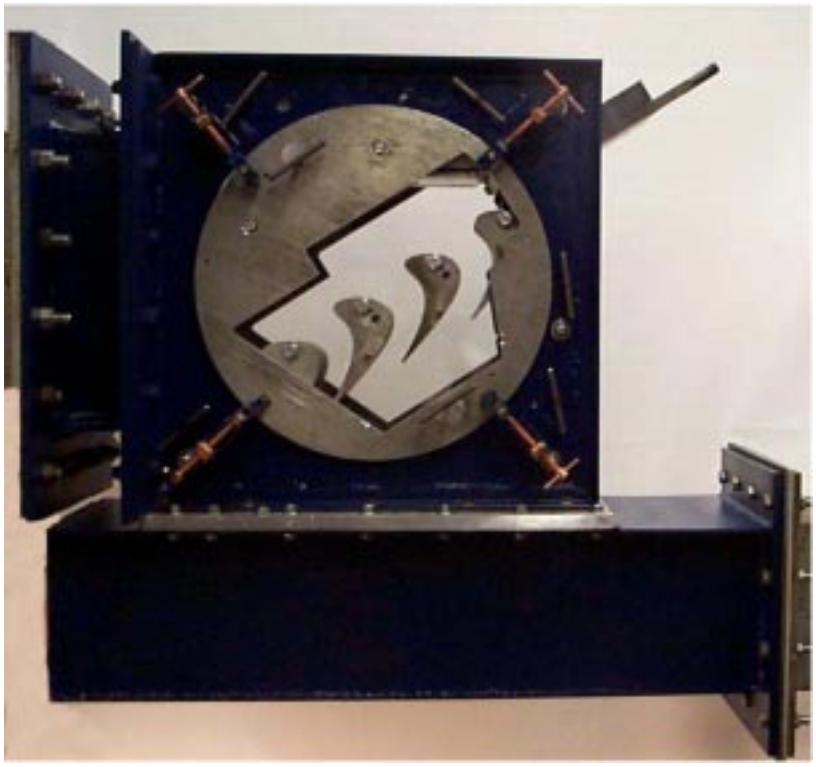

Figure 2.5: Turbine Cascade and Test Section

2.3 Cooling and Blade Design

2.3.1 Blade Design

The blade profile is inspired by a generic General Electric Aircraft Engines first stage turbine blade. Design and measured Mach number profiles are shown in Fig. 2.6.

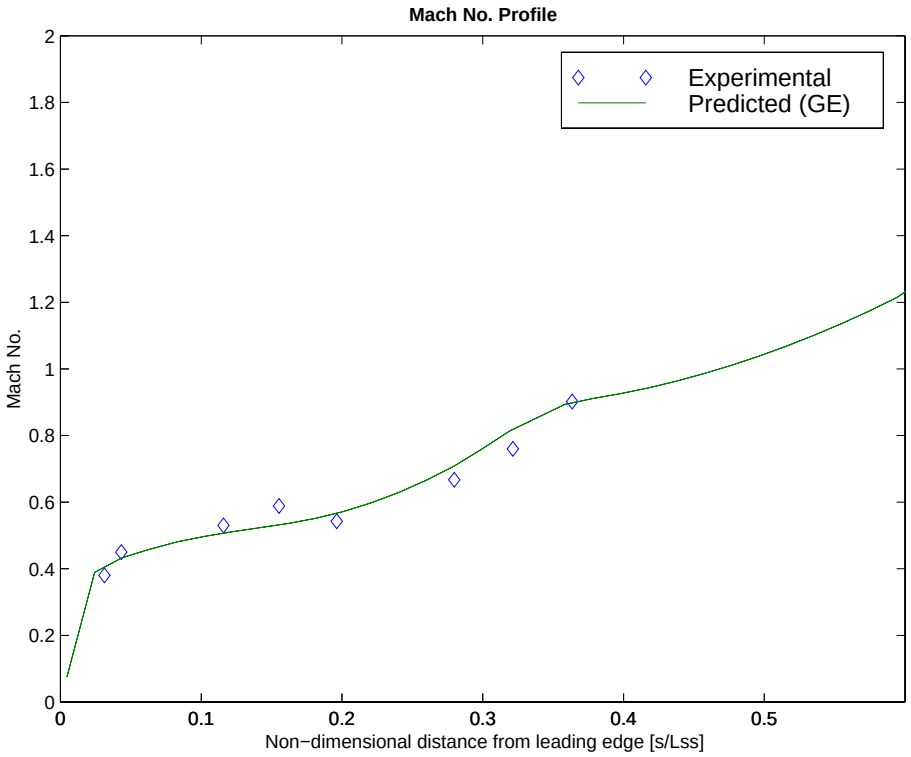

Figure 2.6: Mach Number Profile

The measured Mach numbers are from three pressure taps at the suction side coolant exits and five of the six (transducer 3 was broken) tranducers at the gauge locations. See Sec. 2.4.5 for descriptions of these transducers. The predicted Mach number profile was provided by General Electric for this blade.

Another check that the blade design was operating as expected was performed with shadowgraph visualization. The techniques for the shadowgraph photography are detailed in Sec. 2.4.1. Fig. 2.7 shows the blades without the film coolant running. From this figure it can be seen that the flow is rather periodic in the three full passages.

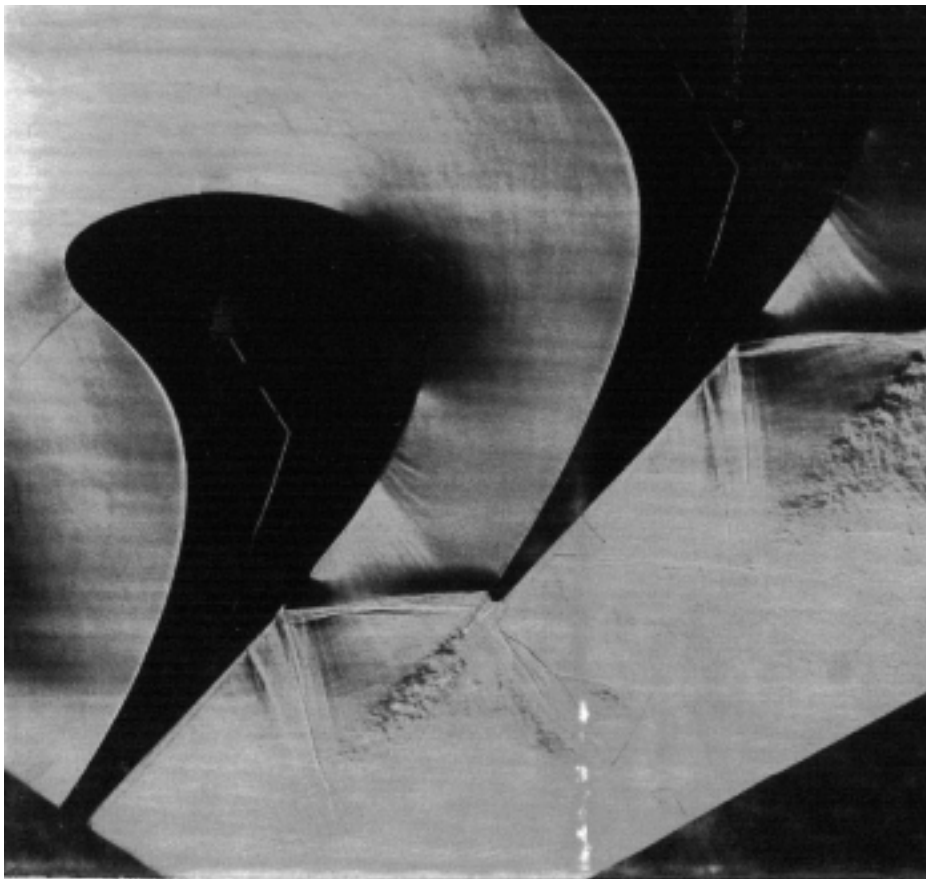

Figure 2.7: Shadowgraph of Blade Passages

Furthermore, the angles of the trailing edge shocks are equal, implying equal exit velocities. The last passage can be seen to have very non-uniform flow, but this is to be expected as it is not a full passage.

2.3.2 Coolant Design

2.3.2.1 Coolant Geometry

The coolant scheme was also inspired by a generic General Electric design. This film cooling scheme consists of six rows of coolant holes. The holes are 10.4 mm (0.041 inches) in diameter with a 91.4 mm (0.360 inches) spacing (a 8.78 $\frac{s}{D}$ ratio). The coolant locations from suction side to pressure side are referred to as Suction Gill (SG), Suction Nose 2 (SN2), Suction Nose 1 (SN1), Nose (N), Pressure Nose (PN), and Pressure Gill (PG) and will be referred to as such from this point. The locations and descriptions are shown in Fig. 2.8. In order to keep the coolant film layer from lifting off the surface of the blade, the coolant holes at locations SN1, SN2, N, and PN are all angled in the spanwise direction by 30°. The coolant holes at locations SG and SN are not angled in the spanwise direction but angled in the streamwise direction by 45° to the surface. Figure 2.9 illustrates the coolant angles.

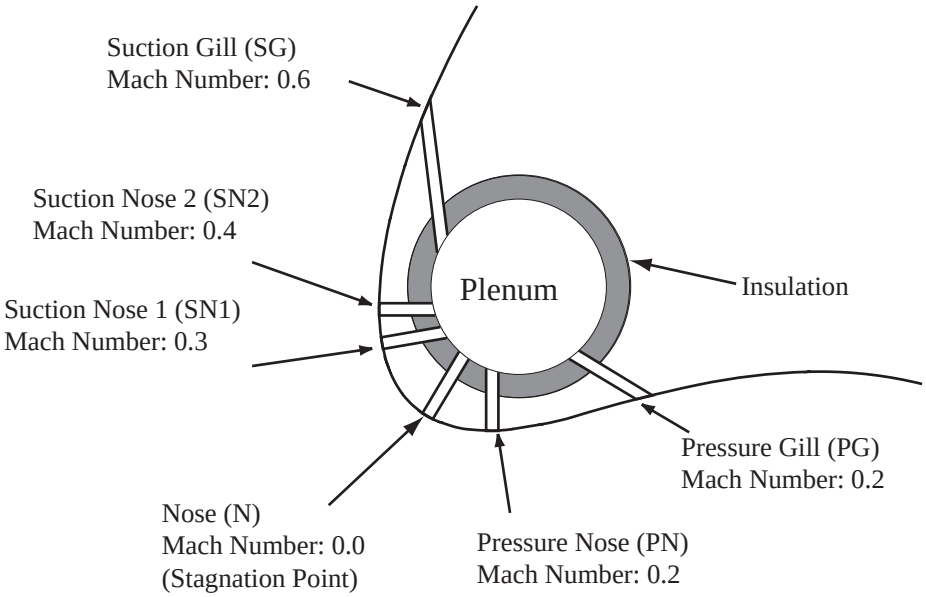

Figure 2.8: Coolant Design

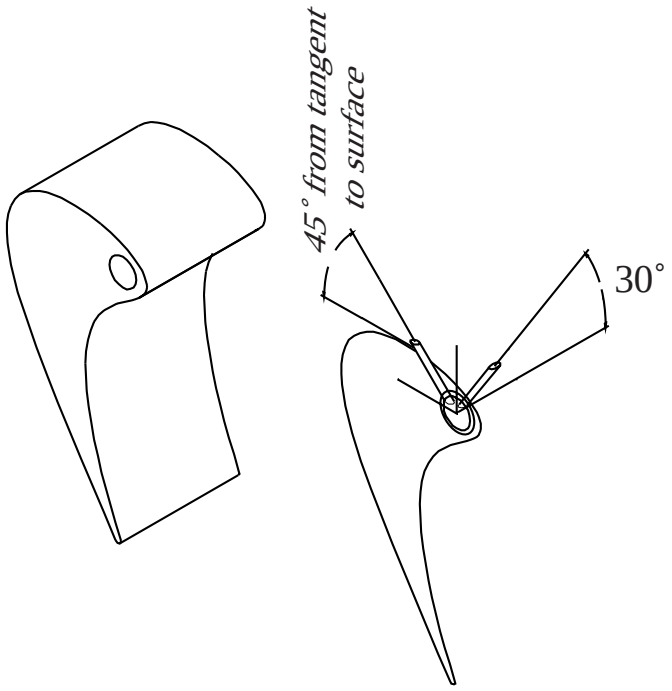

Figure 2.9: Cooling Angles

2.3.2.2 Coolant Air Supply

Coolant air is supplied to the blade by the system of hardware that is illustrated in Fig. 2.10.

The air is supplied to the large storage tank by an Ingersoll Rand compressor, dryer, and filter combination. These three components are pictured in Fig. 2.11. The compressor is an Ingersoll Rand 2475N5 5HP, two stage, reciprocating compressor and provides pressurized air at 175 psi at a rate of 16.8 ambient cubic feet per minute. The dryer is an Ingersoll-Rand HRM regenerative dryer that dries the air to below four percent relative humidity. Finally the air passes through an Ingersoll-Rand filter that removes any dirt particles before being stored in a large storage tank. The exit

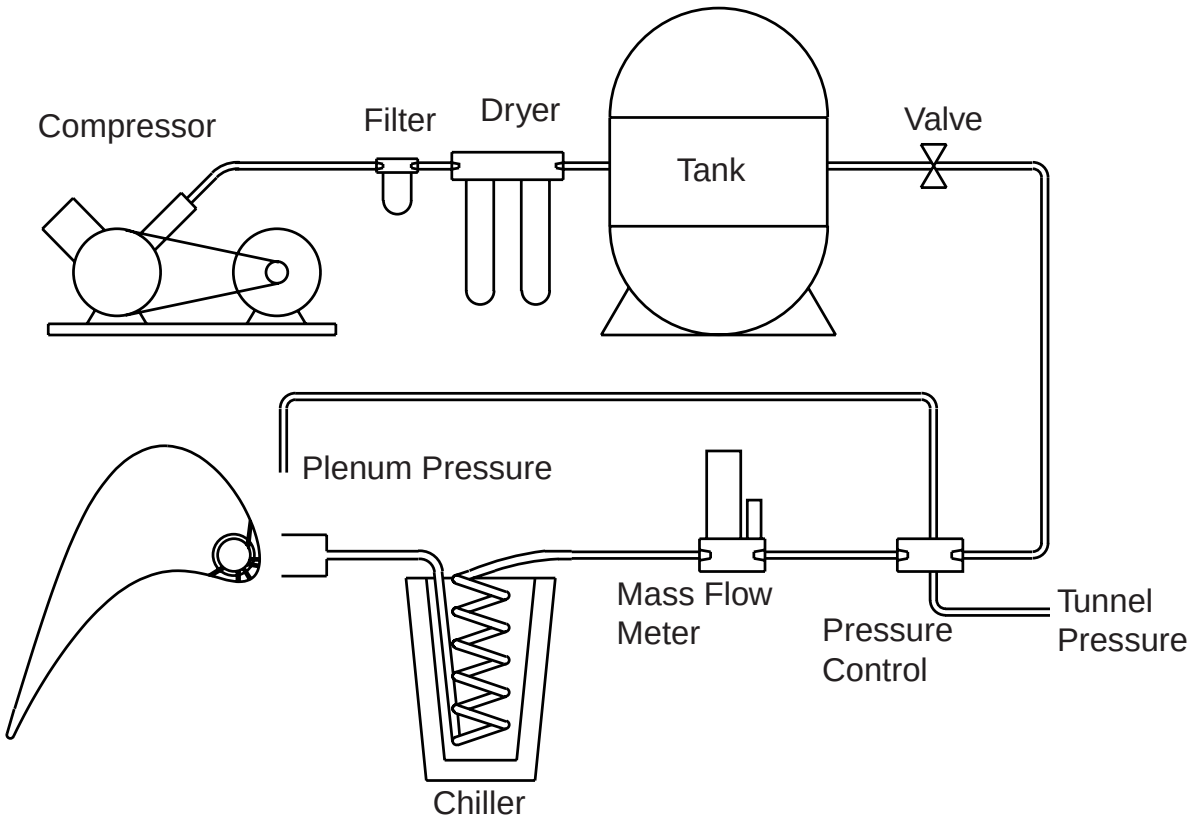

Figure 2.10: Coolant Supply Schematic

flow from the storage tank is regulated by an on/off ball valve.

From the ball valve, the air passes through the coolant pressure control system. The coolant control system was an added improvement from previous research at the same facility. This addition was necessary to be able to control the pressure ratio of the coolant reliably, accurately, and over a wide range of values. A description of this control system is given in Sec. 2.3.2.3.

After the control system, the air passes through an orifice plate to measure the mass flow of coolant. A description of this measurement device is given in Sec. 2.4.6. Next, the air passes through a chiller to cool the air to get the appropriate temperature ratio. The chiller is pictured in Fig. 2.12. It is simply a copper coil emersed in a styrofoam container filled with liquid nitrogen. The level of the nitrogen is regulated manually by a hand valve from the nitrogen supply tank.

Figure 2.11: Compressor, Dryer, Filter combination

Figure 2.12: Liquid Nitrogen Chiller

Lastly, the chilled air enters the plenum and exits the coolant holes on the blade.

2.3.2.3 Coolant Control

The coolant control schematic is shown in Fig. 2.13. This system is what maintains a constant pressure difference between the plenum and freestream total pressures throughout the tunnel run. The heart of this control system is a simple integrating circuit, which was able to maintain the pressure ratio at the values needed.

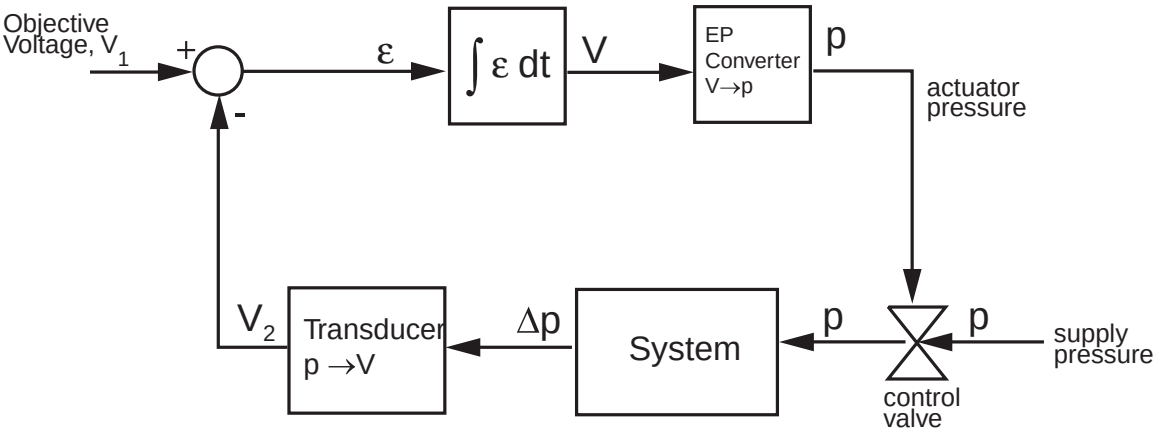

Figure 2.13: Coolant Control System Schematic

The first step in this control schematic is to set the objective delta pressure using the objective voltage, V_1. This voltage is created simply by a battery and a voltage divider circuit with a potentiometer. The signal from the feedback delta pressure,V_2, is given by a transducer which has a linear output where pressure in psi outputs directly as volts. In other words, if the desired delta pressure is 2 psi, the objective voltage is set to 2 V.

This objective voltage is then subtracted from the actual feedback voltage by the use of an op-amp difference amplifier. This difference amplifier is detailed in Fig. 2.14. The first two op-amps in this schematic constitute the difference amplifier portion of the control circuit. This circuit yields the inverted difference between the

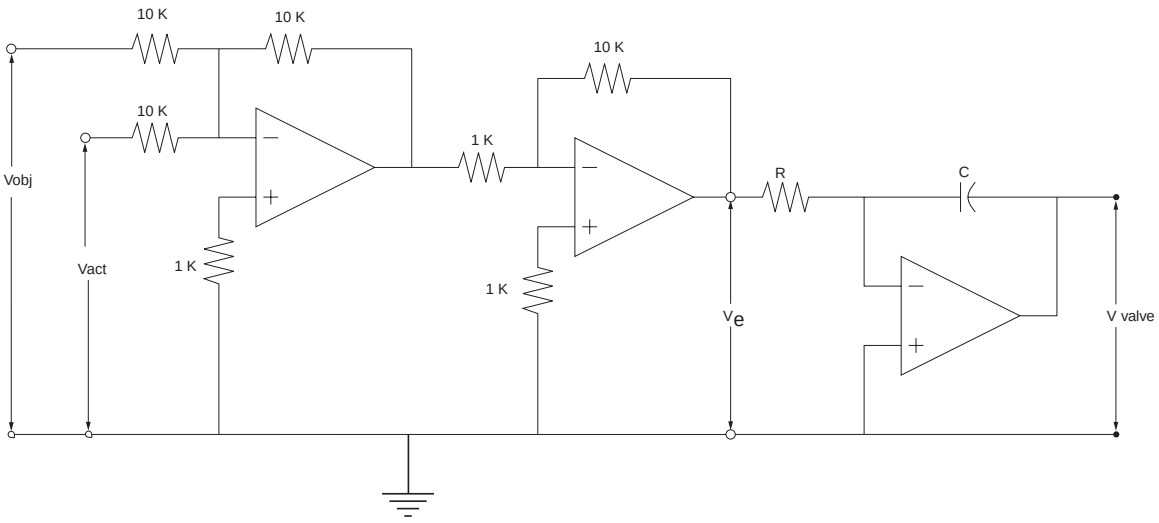

Figure 2.14: Coolant Control Circuit

actual and objective voltages by the simple relationship,

$$V_\varepsilon = -(V_{act} - V_{obj})$$

The second portion of this control circuit is the integrating op-amp circuit. It provides a control voltage for the control valve, V_{valve}. The intergator circuit integrates the error signal by the equation,

$$V_{valve} = \frac{-1}{RC} \int_0^t V_\varepsilon \, dt$$

In this equation, the $\frac{1}{RC}$ term is often referred to as the integrator "gain". This term controls the slope of the control output. In the control apparatus, the value of the integrator gain was adjusted by using a set capacitance and a potentiometer. An appropriate tuning of the control system provided a quick rise time with little overshoot. Both the difference amplifier portion and the integrating portion of this circuit are inverting amplifiers, so the end result is a non-inverted output. Two good references for op-amp designs are Jung [15] and Mims [12]. An example of the control that was achieved is shown in Fig. 2.15. It is important to comment here that this system controls the coolant to freestream pressure difference rather than the pressure ratio. Over the ranges of the tunnel runs, however, this type of control yielded a very constant pressure ratio as well as pressure difference.

Following Fig. 2.13, the integrated error signal is then routed into an electro-pneumatic converter, and the voltage is converted into an actuating pressure for a proportional valve. The proportional valve is a Research Control Valve Model 4 Type B1RA valve from Badger Meter, Inc. This actuator valve is a proportional pneumatically driven valve that regulates the air flow from the large coolant storage tank to the rest of the coolant system. This actuator valve opens or closes in proportion to the pressure supplied to it from the electro-pneumatic converter. After the air leaves the control valve, it enters the rest of the cooling system, namely the chiller and the plenum, which in turns creates a real pressure difference that is measured and used as feedback to close the control loop.

If the feedback pressure is higher than the objective pressure, the error signal is negative, the integrated signal starts to decrease and the actuator valve starts to close. The opposite occurs if the feedback is lower than the objective. An illustration of typical coolant pressure control is shown in Fig. 2.15.

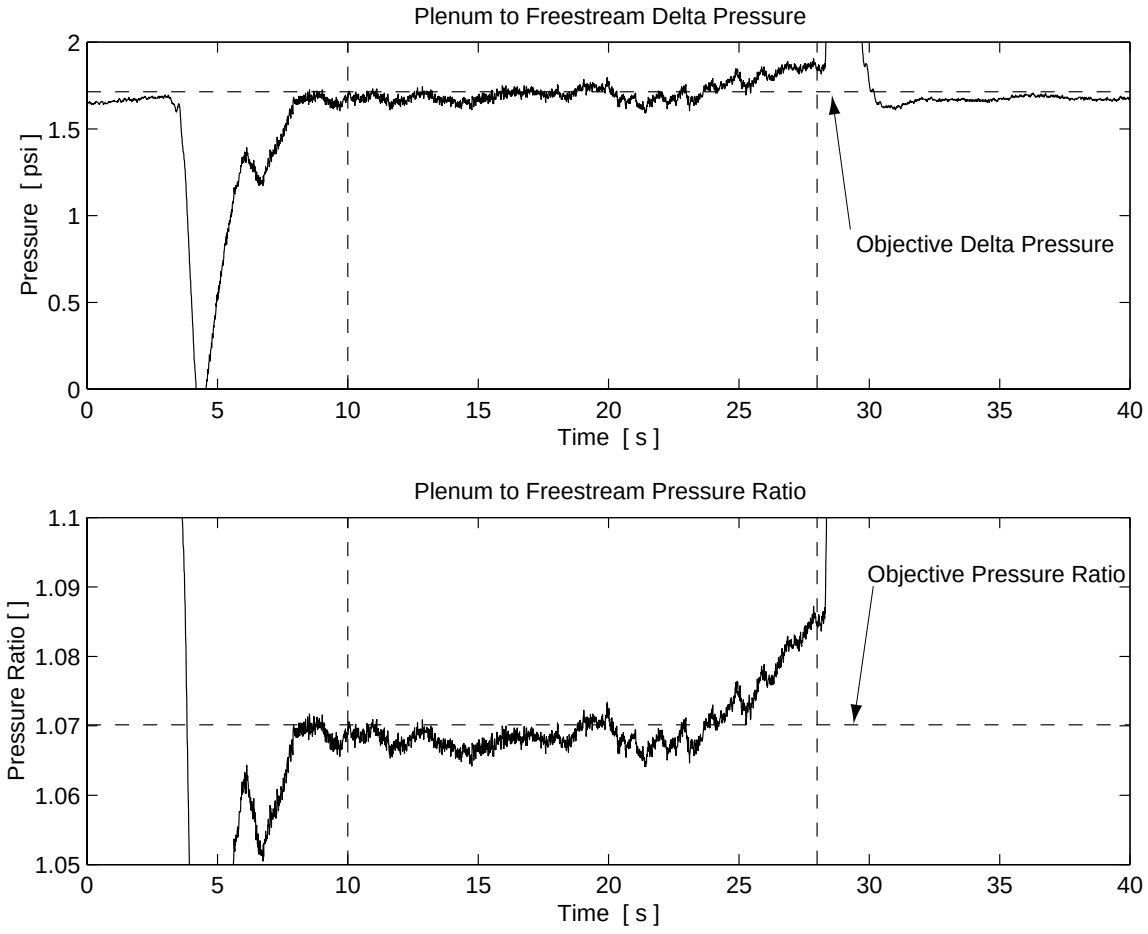

Figure 2.15: Typical Coolant Control

2.4 Instrumentation

2.4.1 Optical Techniques

Two types of optical visualizations were performed; Schlieren and shadowgraphs. A brief overview of the two techniques is given in this section but for a detailed discussion of these and more detailed descriptions of our apparatus see Grabowski [9]. Both techniques use a similar set-up depicted in Fig. 2.16. For the Schlieren pho-

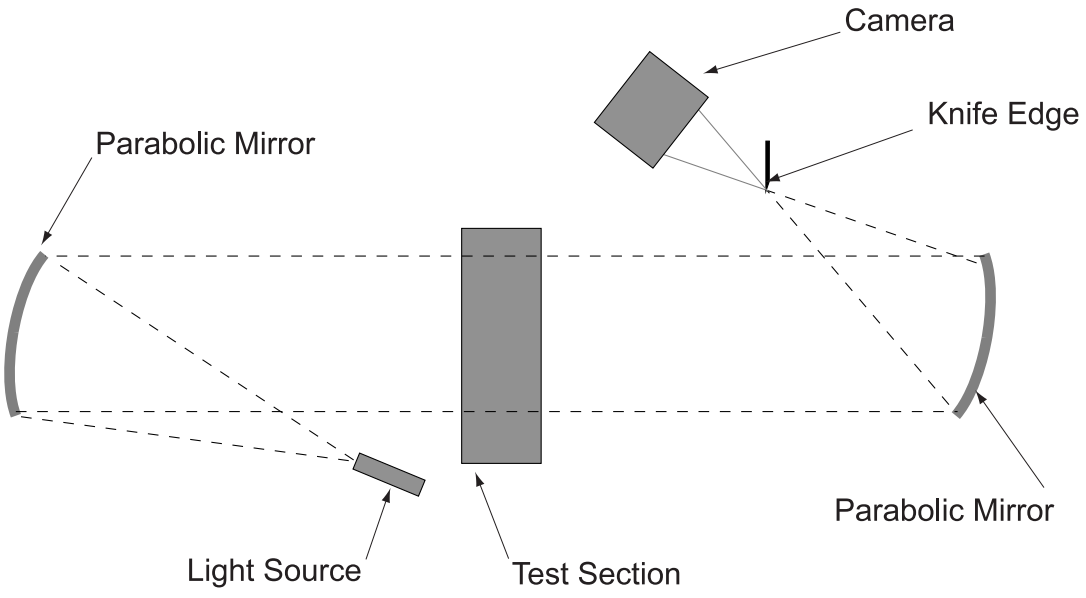

Figure 2.16: Optical Set-up

tographs, the light source is a slot, and a knife edge is placed at the second focal point as shown in this figure. This visualization yields the gradient of density normal to the knife edge direction. The shadowgraph visuaization, on the other hand, uses a point light source and no knife edge. This type of photograph shows the second derivative of density.

2.4.2 On-Blade measurements

The instrumented blade is equipped with numerous transducers. In order to facilitate the installation of all the sensors, the blade was manufactured in two halves. These two halves are pictured in Fig. 2.17. The first half is the pressure side which contains the plenum and cooling passages and instrumentation coolant transducers. The second half is the suction side and it contains six sets of triplet (pressure, heat flux, and temperature) gauges. These triplet gauges are staggered down the chordwise

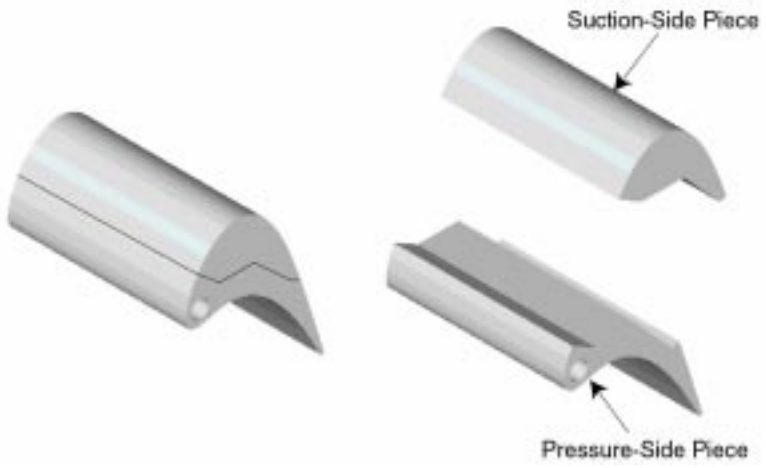

Figure 2.17: Blades Halves

direction at a spacing of 0.41 inches and across the spanwise direction at a spacing of 0.50 inches. The locations of these triplet gauges with respect to the coolant exits and to each other is depicted in Fig. 2.18. A picture of the actual hardware is shown in Fig. 2.19.

A diagram of all of the on-blade measurements is shown in Fig. 2.20. Table 2.2 complements this figure by summarizing the on-blade measurements.

At six separate locations along the chord of the blade (locations 1 through 6) there are triplet gauge groups. The temperature is measured with a K-type surface

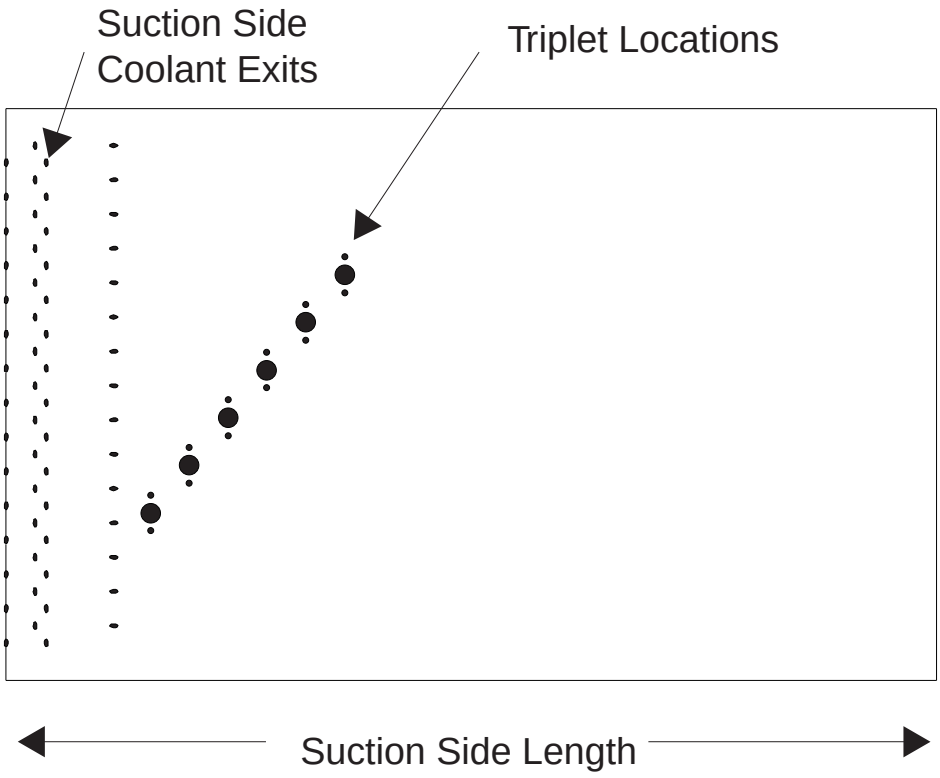

Figure 2.18: Suction Side Plan View

thermocouple mounted flush to the blade surface. The pressure measurement is made with a *Kulite* XCQ-062-50 pressure transducer. Finally, the heat flux measurement is made with a *Vatell* HFM-7 heat flux microsensor.

In addition to these triplet gauges along the blade surface, a number of measurements were made at the coolant exits. At each of the six coolant exit rows, static pressure and coolant exit temperature are measured using *Lucas* NPC-410 pressure sensors. These pressure taps are metal tubes inserted so that they are flush to the blade surface. The tap location is 1 cm (0.39 inches) from the sidewalls. Flow vi-

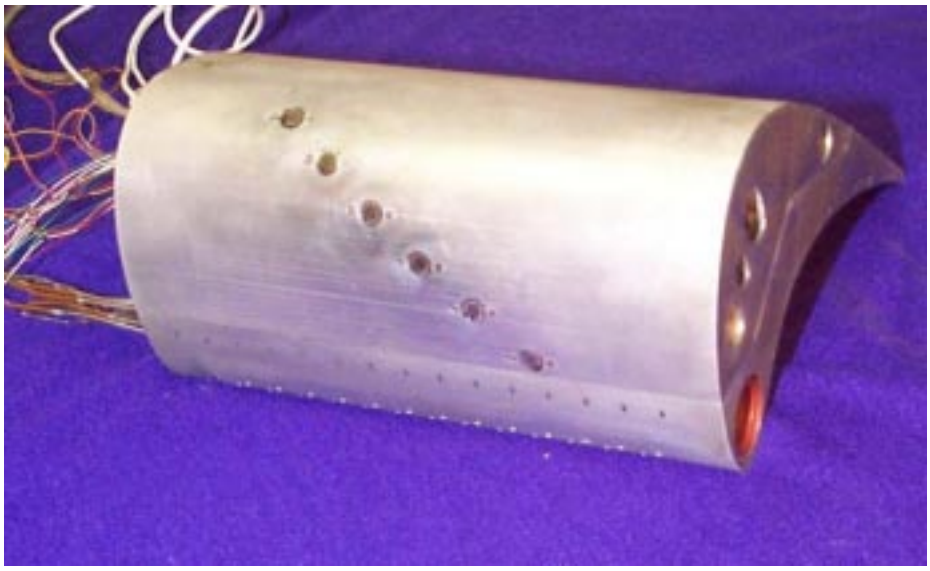

Figure 2.19: Instrumented Blade

sualization experiments showed that this distance is sufficiently outside the endwall secondary flows. The thermocouple measurements are made with a small (36 gauge) K-type thermocouple bead just protruding into the coolant flow passage of the coolant hole closest to the endwall. Fig. 2.21 illustrates this configuration.

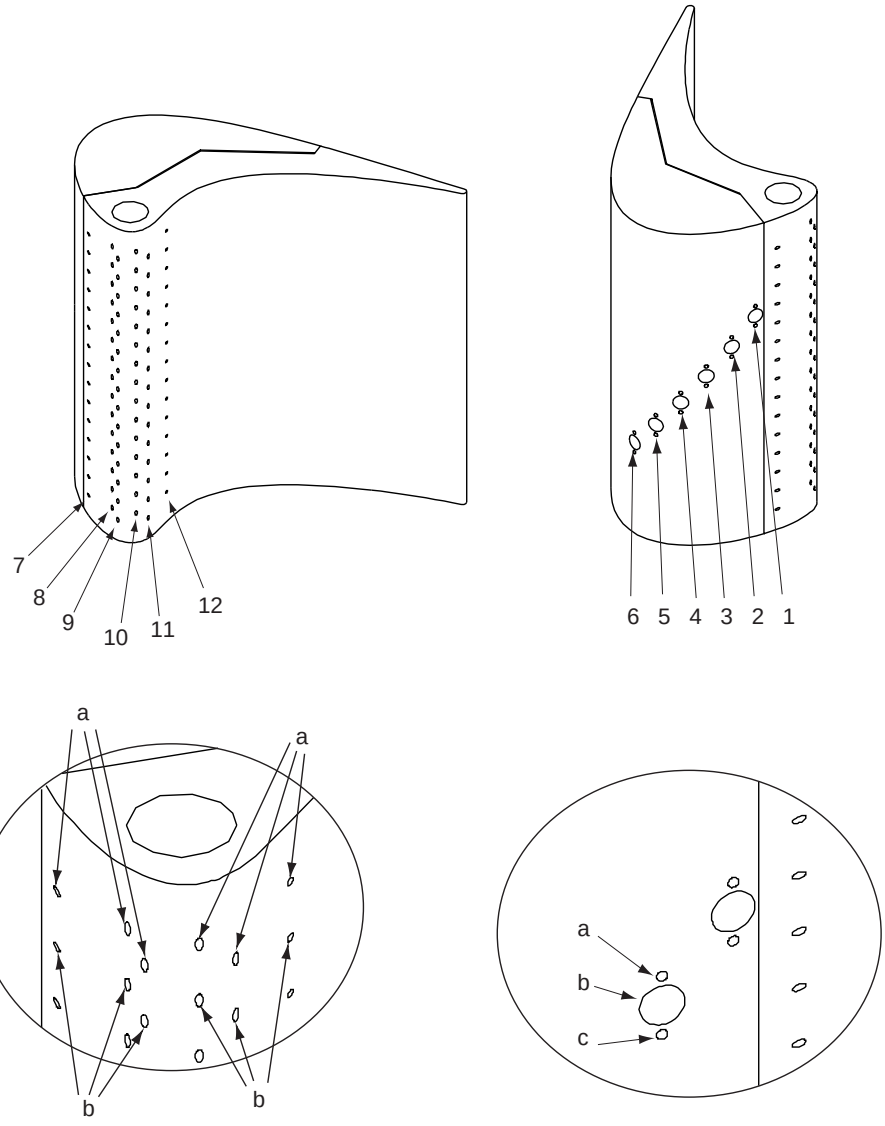

Figure 2.20: Blade Instrumentation Scheme. See Table 2.2 for Location Descriptions

Table 2.2: On-Blade Measurements

Location	Measurement	Device
1a	Heat Flux and Temperature	*Vatell* HFM
1b	Static Pressure	*Kulite* Transducer
1c	Temperature	Thermocouple
2a	Heat Flux and Temperature	*Vatell* HFM
2b	Static Pressure	*Kulite* Transducer
2c	Temperature	Thermocouple
3a	Heat Flux and Temperature	*Vatell* HFM
3b	Static Pressure	*Kulite* Transducer
3c	Temperature	Thermocouple
4a	Heat Flux and Temperature	*Vatell* HFM
4b	Static Pressure	*Kulite* Transducer
4c	Temperature	Thermocouple
5a	Heat Flux and Temperature	*Vatell* HFM
5b	Static Pressure	*Kulite* Transducer
5c	Temperature	Thermocouple
6a	Heat Flux and Temperature	*Vatell* HFM
6b	Static Pressure	*Kulite* Transducer
6c	Temperature	Thermocouple
7a	Static Pressure	Lucas Sensor
7b	Temperature	Thermocouple, AMUX-64T
8a	Static Pressure	Lucas Sensor
8b	Temperature	Thermocouple, AMUX-64T
9a	Static Pressure	Lucas Sensor
9b	Temperature	Thermocouple, AMUX-64T
10a	Static Pressure	Lucas Sensor
10b	Temperature	Thermocouple, AMUX-64T
11a	Static Pressure	Lucas Sensor
11b	Temperature	Thermocouple, AMUX-64T
12a	Static Pressure	Lucas Sensor
12b	Temperature	Thermocouple, AMUX-64T
Plenum	Temperature	Thermocouple, AMUX-64T
Plenum	Total Pressure	Lucas Sensor

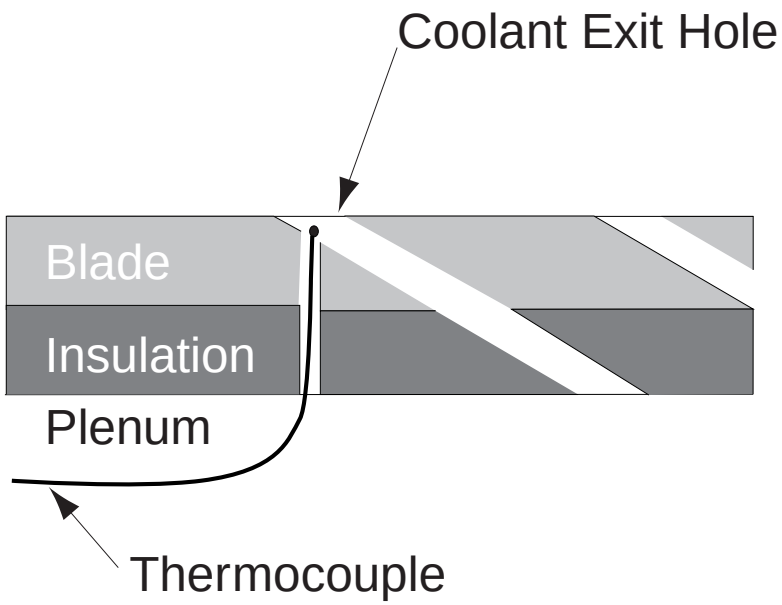

Figure 2.21: Coolant Temperature Thermocouple

2.4.3 Off-Blade Measurements

The off-blade measurements made are summarized in Table 2.3.

Table 2.3: Off-Blade Measurements

Location	**Measurement Device**
Orifice Total Pressure	Lucas Sensor
Orifice Delta Pressure	Lucas Sensor
Orifice Line Temperature	Thermocouple, AMUX-64T
FreeStream Total Pressure	Lucas Sensor
FreeStream Temperature	Thermocouple, AMUX-64T

2.4.4 Heat Flux Measurements

Heat flux measurements were taken by *Vatell* Heat Flux Microsensors (HFM). The active sensor area is 4 mm in diameter. This sensor is actually comprised of two separate devices, a Heat Flux Sensor (HFS) and a Resistance Temperature Sensor (RTS). Figure 2.22 is a picture of the HFM.

Figure 2.22: Heat Flux Microsensor (Courtesy *Vatell*)

A thorough discussion of the phenomenon that comprise this type of heat flux gauge is giver by Diller [4]. A basic understanding of the gauge physics follows. The HFS works by measuring a temperature difference over a thin resistance layer. The differential temperature across the substrate is measured by a thermopile of thermocouples. The thermopile has 280 Nichrome/Constantan thermocouple pairs deposited in a serpentine pattern along the gauge face. Conduction through this

thin-film sensing layer is described by Fourier's Law,

$$q'' = k\frac{\Delta T}{t}$$

where q'' is heat flux, k is the thermal conductivity, t is the thickness, and ΔT is the temperature difference across the sensing layer. A calibration procedure yields a value of $\frac{k}{t}$ so that the measured thermalcouple voltage of ΔT is converted into a heat flux value by using a gauge sensitivity. Over the temperature ranges that our experiments are being performed, it is assumed that the heat flux sensitivity is constant, so that actual heat flux can be calculated using,

$$q'' = \frac{VG}{S}$$

where V is HFS voltage, G is amplifier gain, and S is gauge sensitivity. Over higher temperature ranges the gauges have a sensitivity to temperature. This temperature dependence is typically corrected for with the RTS portion of the HFM, but for our application this effect is ignored. The calibrated coefficients that corrected for the temperature dependence were extremely small and over the ranges of temperature of our experiments were insignificant.

The sensitivities of each gauge are determined by a number of calibration tests. An extensive study of different calibration schemes is given by Smith et al. [23]. The HFS can be essentially modeled as a first-order system having a time constant of 17 μ s. Experiments have been performed to verify this by Popp [20] and Peabody [19].

The second portion of the HFM is the resistance temperature sensor (RTS). The RTS is a thin-film element deposited surrounding the gauge. It works on the principle that its resistance changes repeatably as a function of temperature. This temperature dependence is generally described by a polynomial fit of the form,

$$T = a \cdot R^3 + b \cdot R^2 + c \cdot R + d$$

where T is temperature, R is RTS resistance, and a,b,c, and d are the coefficients of the polynomial. The coefficients for each gauge are determined through calibration.

The gauge is supplied with a 0.1 mA constant current supply and the voltage is measured which yields resistance from Ohm's Law.

The HFM gauges have a thin (2 microns) thick sensing layer and the substrate of the rest of the gauge is made of aluminum nitride. This material was picked so it would have nearly the same thermal properties as that of the aluminum blade to minimize its disturbance of the thermal phenomenon. The installment of the HFM gauges was done by press fitting the sensor into the blade. This was done in the so that the tight fit would provide good thermal contact with the blade, minimizing the contact resistance that might occur.

2.4.5 Pressure Measurements

2.4.5.1 Kulite Transducers

Static pressure measurements at the six gauge triplet locations were made using *Kultite* XCQ-062-50 high frequency pressure transducers. The transducer is pictured in Fig. 2.23. These transducers are 1.7 mm in diameter. The frequency response of the transducers is 25 kHz. The transducer is based on pizeoelectric materials and gives a voltage linearly proportional to its face pressure. The linear output of the gauge is typically near 2 mV/psi. These transducers were then amplified using *Measurements Group* 2310 amplifiers at a gain of 100. These pressure transducers were selected for their high frequency response for some other experiments that were performed by Popp [20] in the same facility. For the experiments presented in this thesis the transducers were used for low speed measurements only.

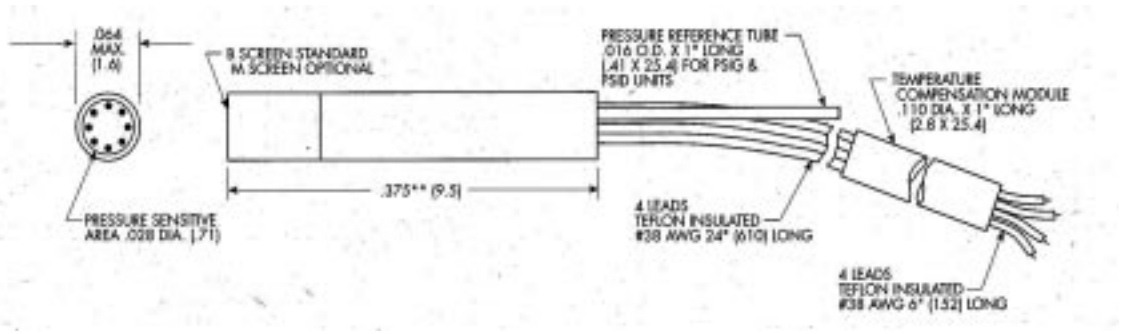

Figure 2.23: *Kulite* Pressure Transducer (Courtesy *Kulite* Inc.)

2.4.5.2 Lucas Transducers

Other low speed pressure measurements of plenum total pressure, freestream total pressure, orifice total pressure, orifice differential pressure, and static pressure were made using a *Lucas* NPC-410 solid state pressure transducer. The transducer

works by the use of a piezoresistive strain gauge integrally formed on a mechanical diaphragm. This resistance is then used as a leg of a wheatstone bridge. Several different transducers with different pressure ranges are used in the experiments.

2.4.6 Coolant Mass Flow

Coolant air mass flow was recorded using an orifice plate pictured in Fig. 2.24. This orifice plate was a Lambda Square orifice plate. In order to use the orifice plate,

Figure 2.24: Orifice Plate

it is necessary to record line temperature, upstream total pressure, and differential plate pressure. These measurements can then be used with the correlation,

$$\dot{m} = C_d A \sqrt{2\rho\Delta p} \tag{2.1}$$

where, C_d is the discharge coefficient, A is the bore area, ρ is the air density (calculated from line temperature and line pressure), and Δp is the differential plate pressure. A value of 0.62 for C_d was used for this model of orifice plate.

2.4.7 Amplifiers

2.4.7.1 AMP-6

The volatge output from the HFM is amplified using *Vatell* AMP-6 amplifiers. The amplifier provides a 0.1 mA signal to the RTS. The amplifier has two separate gains for both the heat flux signal and the temperature signal. Both must be zeroed by the use of a potentiometer. The AMP-6 has RTS gain settings of 1, 100, 200, and 500. For all experiments the RTS gain setting of 100. The AMP-6 has HFS gain settings of 1, 200, 500, 1000, and 5000. All experiments used an HFS gain setting of 100.

2.4.7.2 Measurements Groups 2310

The *Kulite* signals were amplified with a *Measurements Group* 2310 amplifier. These amplifiers provide both an excitation voltage and measurement of gauges in a wheatstone configuration. The 2310's can provide gains from 1 to 11,000. All experiments used a *Kultie* gain setting of 100.

2.4.8 Data Acquisition

All data acquisition was done using a *National Intruments* AT-MIO-16XE-50 digital data acquisition board and a PC. This board provides eight differential channels of input. In order to increase the number of channels acquired, two *National Instruments* AMUX-64T multiplexer boards were used. These boards both mutiplex four channels apiece which expands the channel count to 64 differential channels. Also the AMUX-64T has a built-in ability to acquire thermocouple signals directly with a temperature compensated electronic ice point. This is the device that was used for all thermocouple measurements.

A *Labview* program was written to acquire all channels. The details of this *Labview* program are given by Smith [22].

Chapter 3

Analysis

3.1 Convective Heat Transfer

Convective heat transfer as described by Eqn. 1.1 is repeated here for clarity,

$$q'' = h \cdot (T_{aw} - T_w) \tag{3.1}$$

where q'' is heat flux, h is the convective heat transfer coefficient, T_{aw} is the adiabatic wall temperature, and T_w is the blade wall temperature. This equation illustrates that heat transfer is directly proportional to a heat transfer coefficient and a driving temperature difference. In this analysis, it is assumed, and has been confirmed by experiment [22], that the heat transfer coefficient is a function of the fluid flow field and independent of the temperatures of the blade and fluid.

The second factor in Eqn. 3.1 is the difference between the blade wall temperature, T_w, and the adiabatic wall temperature, T_{aw}. When this temperature difference is zero, there is no heat transfer to the blade, hence the term "adiabatic" wall temperature.

Eqn. 3.1 is a general expression that can be applied to different flow regimes.

3.1.1 Low Speed Convection

In low speed flows, T_{aw} in Eqn. 3.1 is simply replaced by boundary layer edge temperature, T_e.

$$q'' = h \cdot (T_e - T_w) \tag{3.2}$$

In such a flow regime, the heat transfer coefficient can be determined by measuring q'', T_w, and T_e.

3.1.2 High Speed Convection

In high speed flows, however, the true driving temperature difference must be represented using a recovery temperature, T_r for the adiabatic wall temperature. This recovery temperature takes into account the total enthalpy and the viscous dissipation effects which are neglected in low speed flows. Substituting recovery temperature into Eqn. 3.1 results in,

$$q'' = h \cdot (T_r - T_w) \tag{3.3}$$

The recovery temperature is often found by assuming a recovery factor, r, as defined by,

$$r \equiv \frac{T_r - T_e}{\frac{U_e^2}{2C_p}} \tag{3.4}$$

where U_e is the boundary layer edge velocity, and C_p is the specific heat of air. A further simplification commonly used is to estimate the recovery factor as the cube root of the Prandtl Number for turbulent flow. In the following analysis however,

instead of making this approximation, the recovery temperature has been determined for this test section experimentally. Earlier experiments performed by Smith et al. [22] have shown the recovery temperature to be a simple drop from the boundary layer edge temperature denoted by T_d.

$$T_d = T_{t,e} - T_r \tag{3.5}$$

At each location T_d was measured and the results for this are summarized in Sec. B.1. Knowing the recovery temperature is important in order to extend our analysis to film-cooled heat transfer.

3.1.3 Film-Cooled Heat Transfer

In film-cooling heat transfer, it is convenient to use a nondimensionalized temperature difference rather than the adiabatic wall temperature. This nondimensionalized temperature, η, (repeated from Eqn. 1.2) is defined as,

$$\eta \equiv \frac{T_r - T_{aw}}{T_r - T_c} \tag{3.6}$$

The three temperatures in this expression are: recovery temperature, T_r, adiabatic wall temperature, T_{aw}, and the coolant temperature, T_c. Solving this expression for for T_{aw} yields,

$$T_{aw} = T_r - \eta \cdot (T_r - T_c) \tag{3.7}$$

Substituting this expression into Eqn. 3.1 yields,

$$q'' = h \cdot (T_r - T_w - \eta \cdot (T_r - T_c)) \tag{3.8}$$

3.2 Data Reduction

All of the terms in Eqn. 3.8 are measurable quantities except two important parameters: the heat transfer coefficient, h, and film cooling effectiveness, η. The analysis outlined below is a description of how the raw data is reduced to yield these two parameters.

Fig. 3.1 is a sample test run showing the relevant measurements used in the data reduction. The blade wall temperature is simply measured using the blade

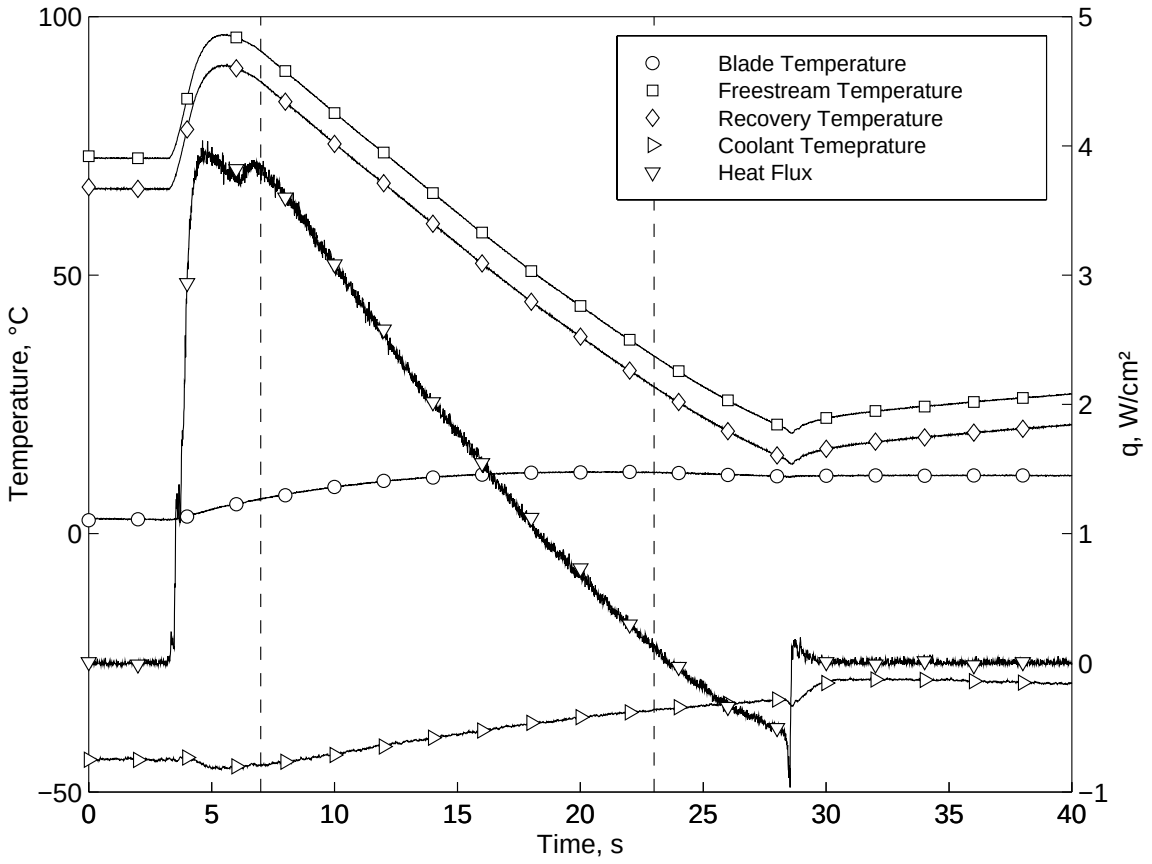

Figure 3.1: Sample Test Run at Gauge 1

thermocouples at each triplet location. The coolant temperature is derived from the coolant exit thermocouples (See Sec. 2.4.2). Since there is a coolant exit thermocouple

for each row of coolant holes, a representative coolant temperature must be found. This was found by using a mass averaged coolant temperature from the exits locations SN1, SN2, and SG. The recovery temperature is found by utilizing Eqn. 3.5 and the data in Appendix B.1. For this representative location on the blade (Gauge 1), the recovery temperature is a drop from the freestream temperature of 6 °C.

It is important to notice that the temperature history is transient. At the beginning of the run the total freestream temperature starts at about 100°C and drops to a final value of about 30°C. The blade temperature stays fairly constant of the course of the run at about 10°C. The coolant temperature also varies somewhat at values near −40°C. This gives a wide range of driving temperature difference to use to evaluate the effectiveness and heat transfer coefficient. In Fig. 3.1 the vertical dashed lines indicate the area over which the analysis is applied. All measured values shown in Fig. 3.1 are from Gauge 1.

The blade wall temperature is simply measured using the blade thermocouples at each triplet location. The coolant temperature is derived from the coolant exit thermocouples (See Sec. 2.4.2). Since there is a coolant exit thermocouple for each row of coolant holes, a representative coolant temperature must be found. This was found by using a mass averaged coolant temperature from the exits locations SN1, SN2, and SG. The recovery temperature is found by utilizing Eqn. 3.5 and the data in Appendix B.1. For this representative location on the blade (Gauge 1), the recovery temperature is a drop from the freestream temperature of 6 °C.

These measured values can now be used to yield the heat transfer coefficient and film cooling effectiveness. In order to do this, it is convenient to rearrange the terms of Eqn. 3.8 by dividing both sides of the equation by $(T_r - T_c)$ to yield,

$$\frac{q''}{T_r - T_c} = h \cdot \left(\frac{T_r - T_w}{T_r - T_c} \right) - h \cdot \eta \tag{3.9}$$

Inspection of this equation shows that it is a linear equation for $\frac{q''}{T_r - T_c}$ and $\frac{T_r - T_w}{T_r - T_c}$ with

a slope of h and y-axis intercept of $h \cdot \eta$. Plotting the data from Fig. 3.1 as in Fig. 3.2 shows the linearity of this relationship. Upon realizing that the experimental data is

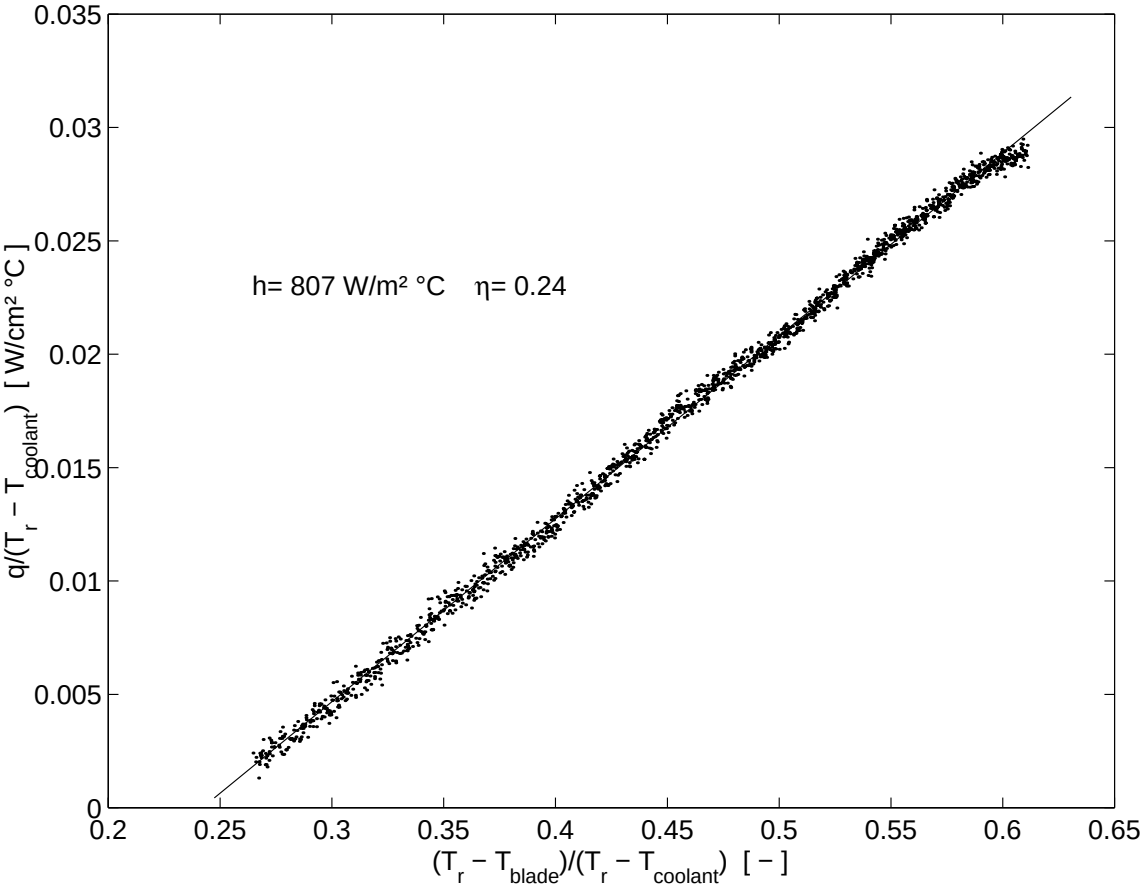

Figure 3.2: Linearized Data at Gauge 1

fairly linear over the range of temperatures, a least-squares regression analysis was applied. The slope of the least-squares fit of the data yields a heat transfer coefficient (807 W / m^2 °C for the example case shown in Fig 3.2) and the x-intercept yields the film cooling effectiveness (0.24 for this example case).

The above outlined method was used to reduce the data from numerous runs at all locations to get both a heat transfer coefficient and a film cooling effectiveness.

After having performed the analysis illustrated in Fig. 3.2, the adiabatic wall

temperature can be determined from Eqn. 3.7. In order to visualize the adiabatic wall temperature over the course of the run it is necessary to assume the film cooling effectiveness is constant. Using this assumption along with Eqn. 3.7 gives rise to the plot of adiabatic wall temperature as shown in Fig. 3.3.

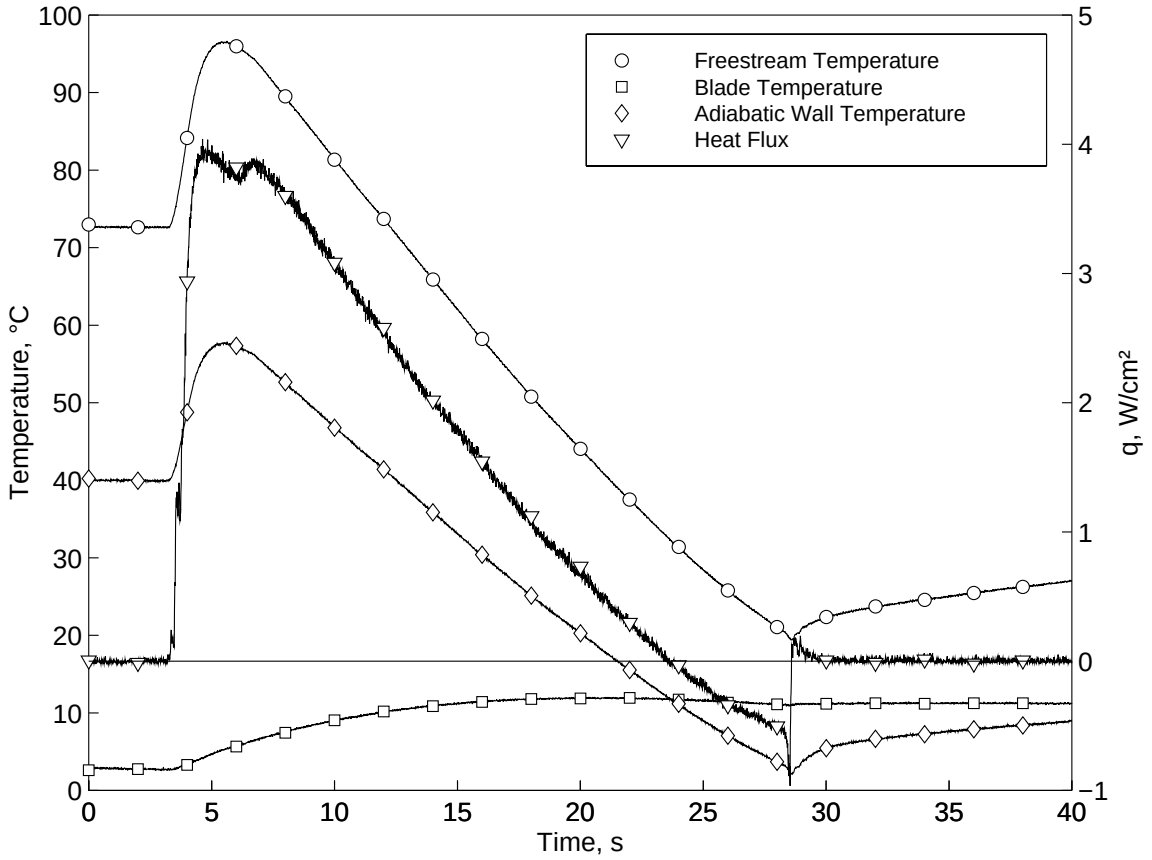

Figure 3.3: Adiabatic Wall Temperature at Gauge 1

This analysis illustrates a few important ideas. The first is that the effect of film cooling is to lower the adiabatic wall temperature significantly. In this sample run, the adiabatic wall temperature is approximately 40°C below the freestream temperature. A second idea illustrated in Fig. 3.3 is that the measured heat flux goes to zero when the adiabatic wall and blade wall temperatures cross. This fact is not surprising but serves as a nice "sanity" check for the data reduction scheme presented.

The analysis illustrated in Fig. 3.2 yields an average heat transfer coefficient over the analysis time. If one still makes the assumption that the film cooling effectiveness is constant, the time varying heat transfer coefficient can backed out from Eqn. 3.8. This yields Fig. 3.4. This figure shows that the heat transfer coefficient is

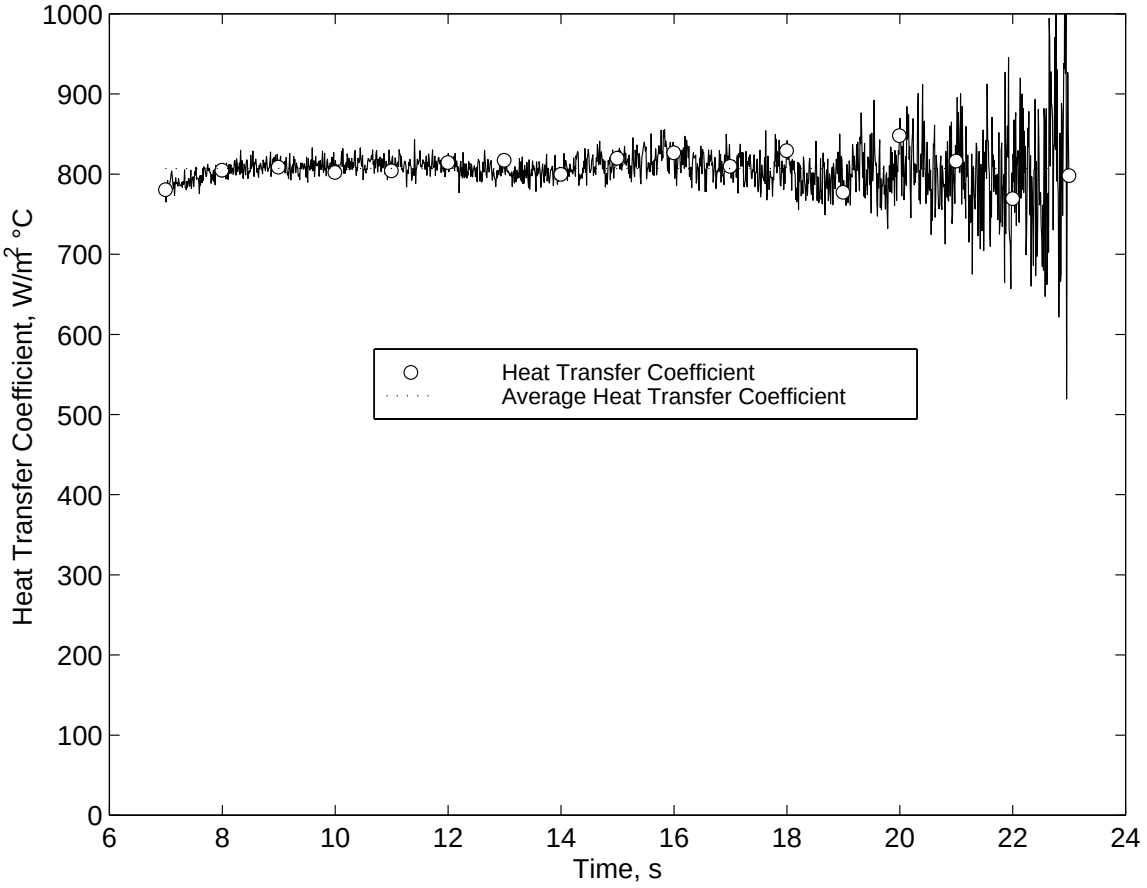

Figure 3.4: Time Varying Heat Transfer Coefficient at Gauge 1

fairly constant over the course of the run. The large amount of noise near 22 seconds is due to the way the heat transfer coefficient is calculated. Eqn. 3.8 shows that h can be calculated by dividing by q'', and as q'' approaches zero, the analysis breaks down. The least squares analysis has the advantage of not being affected by this "division by zero" phenomenon.

The time history of the film-cooling effectiveness can be found in a similar

manner. Assuming a constant h and using Eqn. 3.8 yields Fig. 3.5. This figure shows that the film-cooling effectiveness is constant over the course of a run.

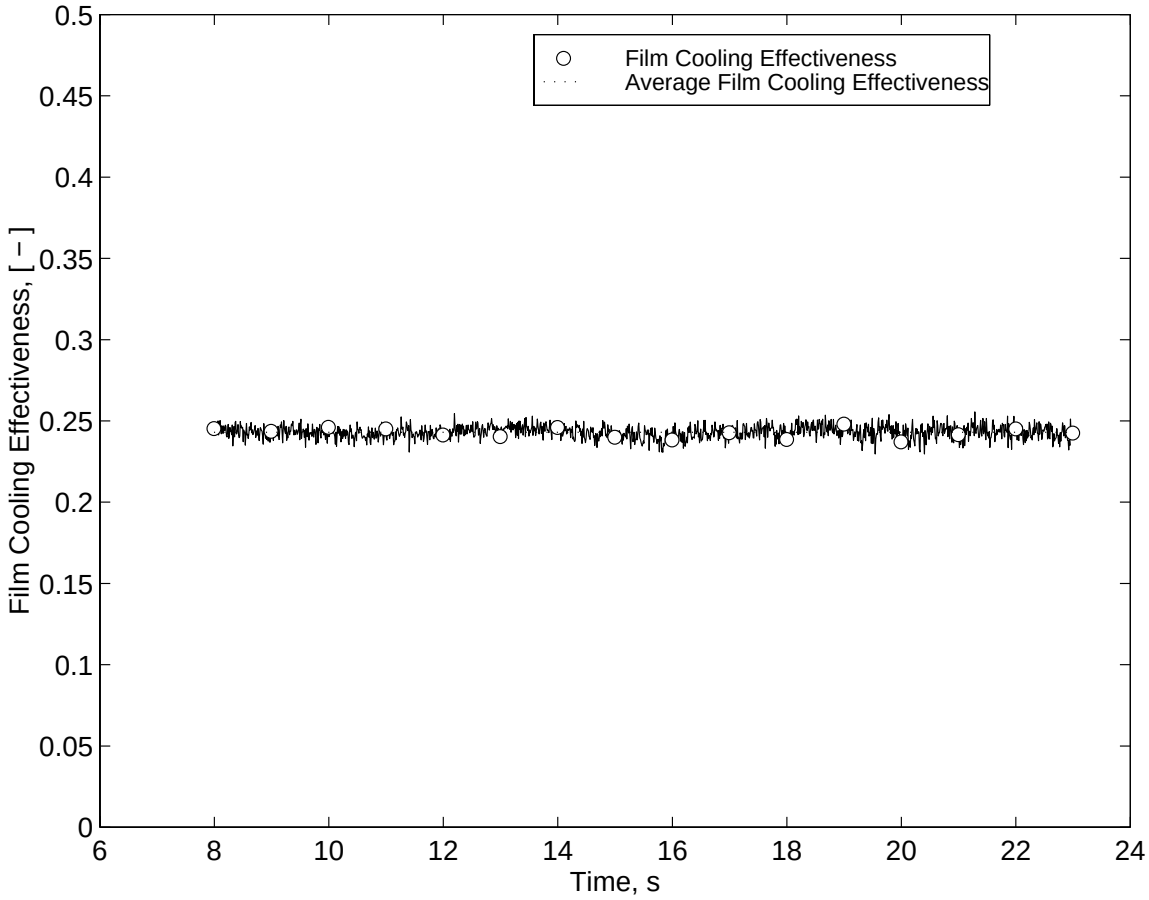

Figure 3.5: Time Varying Effectiveness at Gauge 1

3.3 Calculation of Coolant Ratios

A number of aerodynamic calculations have been made using isentropic relations. The first of these is the Mach number profile. The Mach number, Ma, at location x is calculated from,

$$Ma_x = \sqrt{\frac{2}{\gamma - 1} \cdot \left(\left(\frac{p_{t\infty}}{p_\infty} \right)^{\frac{\gamma-1}{\gamma}} - 1 \right)} \tag{3.10}$$

The coolant ratios defined in Eqn. 1.3 through Eqn. 1.5 are calculated using isentropic relations in the following manner.

$$DR \equiv \frac{\rho_c}{\rho_\infty}$$

$$DR = \frac{T_\infty}{T_c} \cdot \left(\frac{p_{tc}}{p_{t\infty}} \right)^{\frac{\gamma-1}{\gamma}} \tag{3.11}$$

$$I \equiv \frac{\rho_c U_c^2}{\rho_\infty U_\infty^2}$$

$$I = \frac{2}{\gamma - 1} \cdot \frac{1}{Ma^2} \cdot \left(\left(\frac{p_{tc}}{p_{t\infty}} \right)^{\frac{\gamma-1}{\gamma}} \cdot \left(1 + \frac{\gamma - 1}{2} \cdot Ma^2 \right) - 1 \right) \tag{3.12}$$

$$M \equiv \frac{\rho_c U_c}{\rho_\infty U_\infty}$$

$$M = \sqrt{DR \cdot I} \tag{3.13}$$

It can be seen from Eqn. 3.12 that I is a function of only the local freestream Mach number and the pressure ratio. Since the pressure ratio is controlled carefully with this experimental setup, the momentum ratio is consequently controlled. Since the pressure ratio is constant for all coolant exits and the momentum ratio is different for each coolant exit (as a consequence of the Mach number profile), the results of this

study show the film cooling effectiveness and heat transfer coefficient as affected by the pressure ratio. Fig. 3.6 illustrates Eqn. 3.12 over the ranges where this research is concerned.

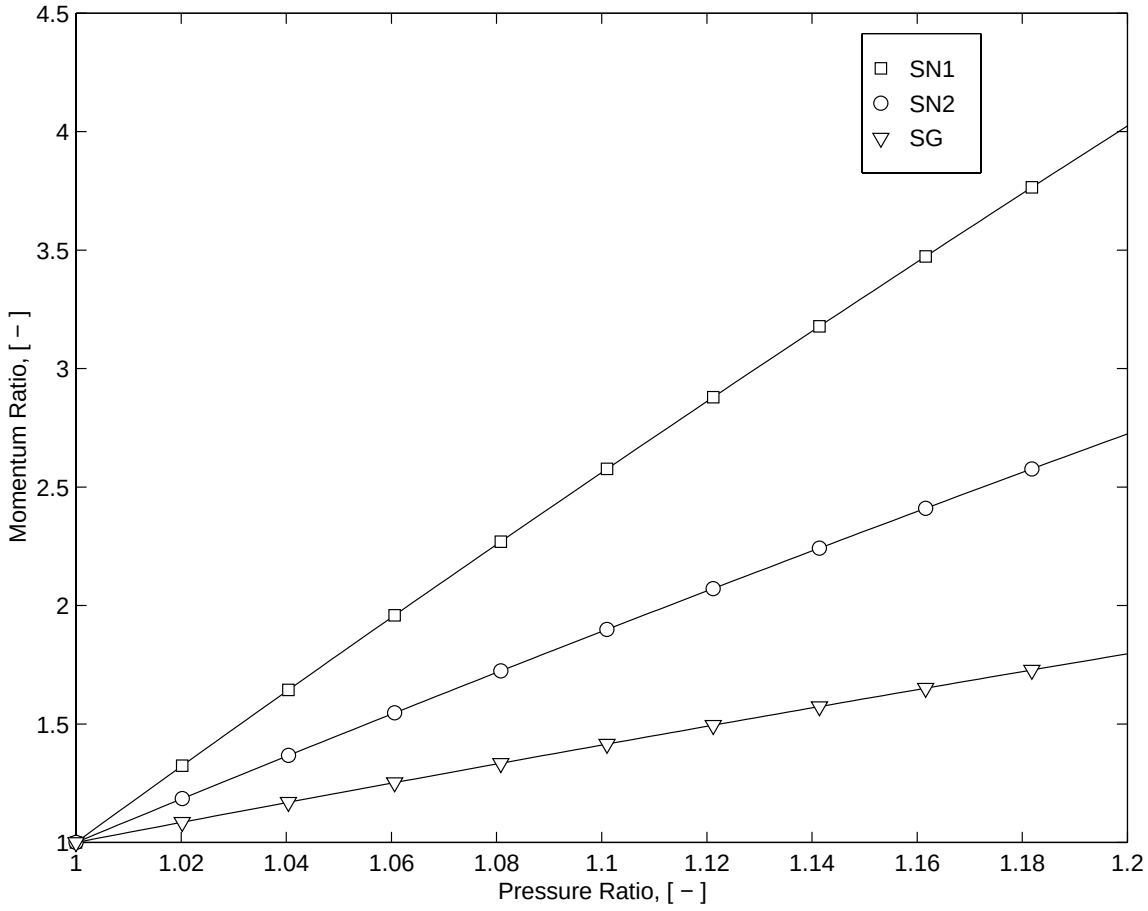

Figure 3.6: The Isentropic Relationship Between Pressure Ratio and Momentum Ratio

It is useful to look at the ratio histories over the duration of one representative run. The data shown in Fig. 3.7 through Fig. 3.9 are from the same sample run as shown in Fig. 3.1. These figures illustrate that the momentum ratio is held fairly constant over the course of the run. The density ratio, however, is shown to vary significantly due to the changing freestream and coolant temperatures and the fact that the density ratio changes with the temperature ratio as shown in Eqn. 3.11.

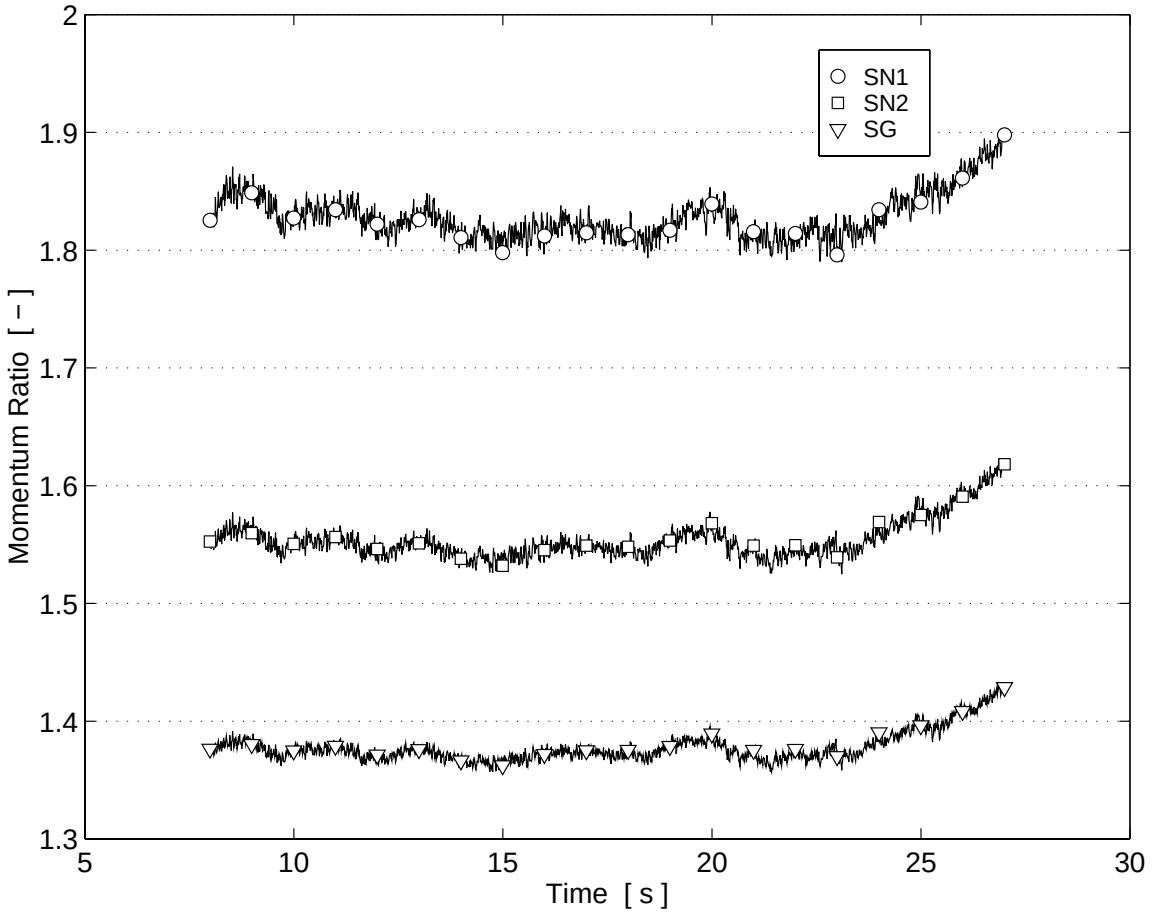

Figure 3.7: Time History of Momentum Ratio During Run

Also, the blowing ratio varies during the run due to the changing temperatures but only as the square root of the temperature ratio as illustrated by Eqn. 3.13.

The assumption that the density ratio has little effect on film cooling effectiveness over our range of interest is somewhat confirmed by these figures. Even though the density ratio is varying significantly, the data shown in Fig. 3.2 shows a very linear trend. This was an important verification of a needed assumption in the analysis.

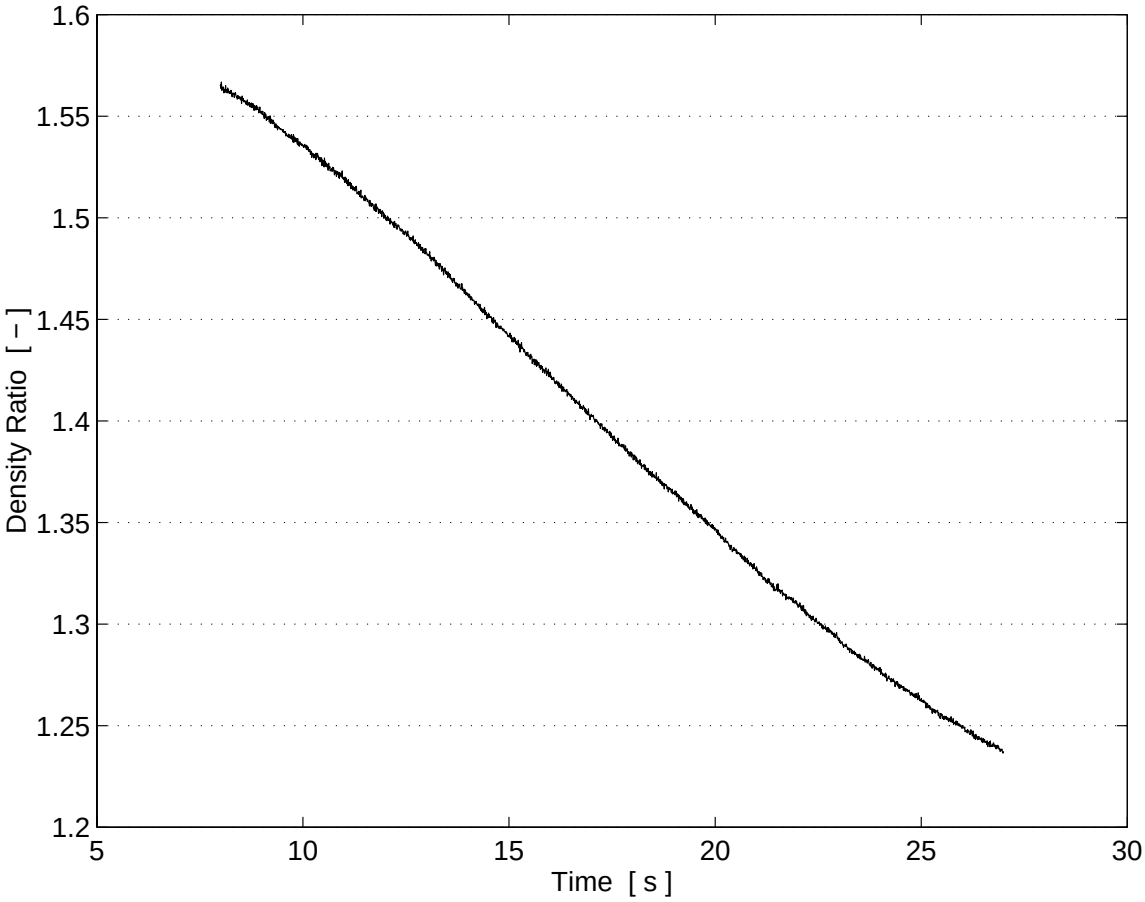

Figure 3.8: Time History of Density Ratio During Run

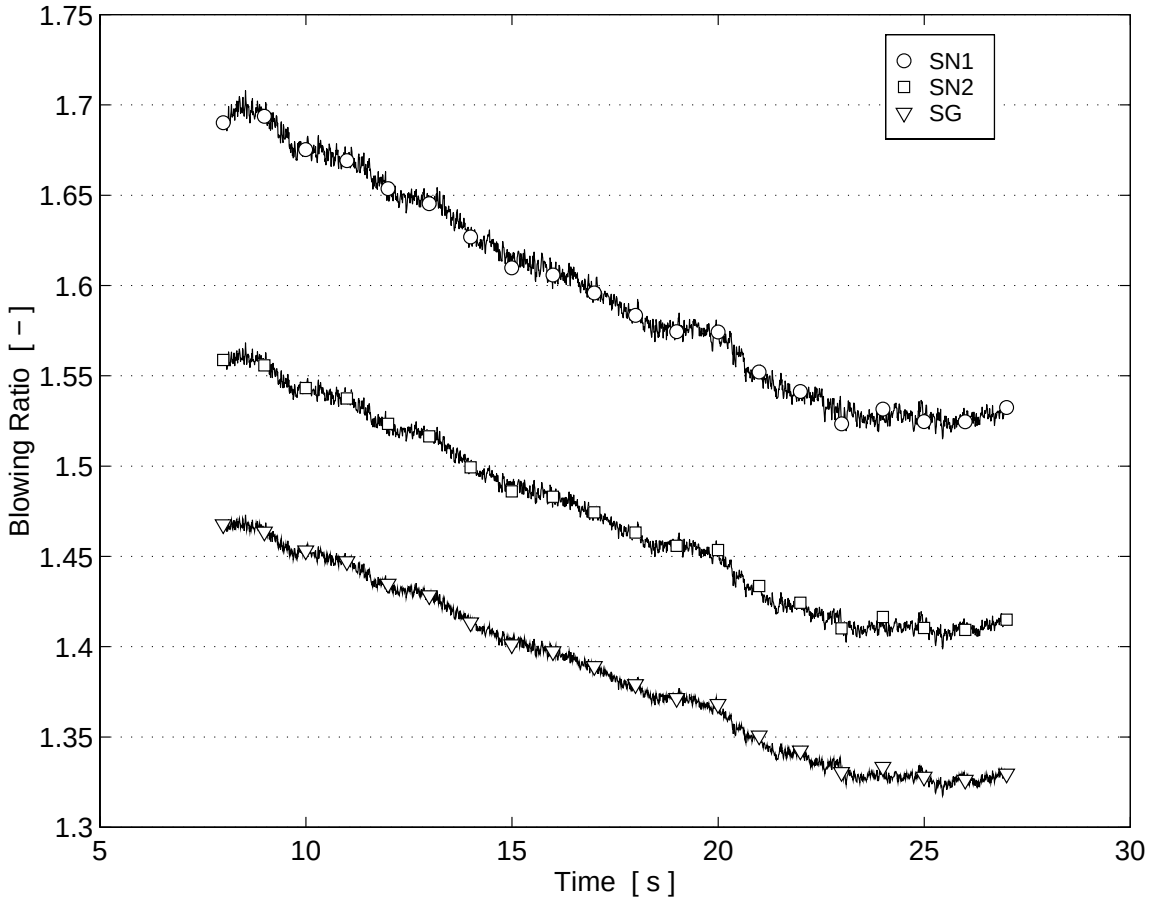

Figure 3.9: Time History of Blowing Ratio During Run

3.4 Measurement Error

There are two issues in measurement error that are important to consider: measurement uncertainty and measurement repeatability. Measurement uncertainty refers to how close the measurements are to the true physical properties. Measurement repeatability, on the other hand, is a measure of how repeatable the tests can be reproduced from run to run and day to day. The first of these matters to address is measurement uncertainty.

3.4.1 Measurement Uncertainty

Within measurement uncertainty there are two categories, bias uncertainty and precision. Bias uncertainty refers to an error that is made consistently from measurement to measurement. These types of errors are typically associated with calibration of the transducers or consistent errors in an acquisition scheme. The precision uncertainty is associated with random errors that vary from measurement to measurement. The first area of uncertainty to address is the bias uncertainty.

For these experiments, The HFM sensors are the main component of bias uncertainty. Reliable measurements of heat flux are directly dependent on the calibrated sensitivity of each sensor. The sensors went through an extensive calibration procedure summarized by Smith et al. [23]. In this study, the gauges were calibrated with both convective and radiative heat flux. At the conclusion of the study, values for the uncertainty for each of the gauge sensitivites are calculated. These uncertainties are specific for each of the gauges installed in the blade, and they are based on several of the convective tests and a 90% confidence interval assuming a student-T distribution. These uncertainties are listed in Table 3.1. The next question to answer is how do these bias errors in heat flux measurements affect the h and η biases. Since the

Table 3.1: HFM Gauge Uncertainties

Gauge	Uncertainty
1	17.0%
2	3.7%
3	5.2%
4	15.2%
5	8.8%
6	10.7%

value of h is the slope of the linearized data and q'' is plotted on the y-axis, these q'' uncertainties go directly into the h values, so that the values in Table 3.1 can be understood directly as bias uncertainties in h. Also, the uncertainty of η is unaffected by uncertainties in the scale of q'' since η is derived from the x-axis intercept of the linearized data. The value of η is solely dependent upon temperature measurements and is unbiased using this data reduction method.

The next area of uncertainty is precision. The thermocouple measurements constitute this type of uncertainty. The kinds of errors that go into precision uncertainty are thermocouple wire difference from junction to junction, acquisition inconsistencies from channel to channel, or a wandering electronic ice point. The three thermocouple measurements that go into the h and η calculations are T_w, T_c, and T_r. Temperature measurements are made with K-Type thermocouples and the AMUX-64T multiplexer board. From the *National Instruments* literature the uncertainty of any individual temperature measurement is estimated to be $\pm$ 1.1°C. The value used for T_r is 1.56°C since it is a derived value from two thermocouple measurements (square root of the sum of the squares).

In order to translate the individual thermocouple precision uncertainties to h and η precision uncertainties, a method was used similar to that suggested by Moffat [18]. The first step of this approach is re-apply the h and η analysis using the nominal values of two of the temperature measurements and an "errored" third temperature measurement consisting of the measurement added to its uncertainty.

The addition or subtraction of this individual uncertainty is done such that it has the greatest influence on the h and η values. Next, this procedure is repeated for each of the other two measurements individually, and the influence of each measurement is computed. Knowing each individual contribution, the total uncertainty, δ, can be calculated as the sum of the squares of all three uncertainties,

$$\delta = \sqrt{\delta_{T_r}^2 + \delta_{T_w}^2 + \delta_{T_c}^2} \tag{3.14}$$

The results vary slightly from gauge to gauge and from run to run. A number of runs over different operating ranges were subjected to this uncertainty analysis and the maximum uncertainty for each gauge is listed in Table 3.2. The raw data for the runs is listed in Appendix C in the MATLAB file "summary.m".

Table 3.2: Precision Uncertainties

Gauge	h **Precision**	η **Precision**
	[W / m^2 °C], [%]	[-], [%]
1	43.5, 5.9%	0.040, 18.5%
2	49.2, 6.1%	0.041, 21.0%
3	35.0, 5.6%	0.036, 13.9%
4	42.5, 5.9%	0.040, 21.3%
5	48.3, 6.0%	0.040, 17.0%
6	49.4, 5.7%	0.034, 11.5%

3.4.2 Measurement Repeatability

Another indication of measurement error is measurement repeatability. This refers to the repeatability of conditions from run to run. Measurement repeatability is an experimental number that reflects the same ideas contained in the more theoretical value of precision (from Sec. 3.4). Measurement repeatability, however, also takes into account the real variations from run to run (e.g. variation of aerodynamic conditions, variations of humidity levels, coolant supply leakage, etc.). These kinds of errors have not been accounted for in the data reduction scheme, and perhaps some of the sources of variation probably have not been even conceived. Because of this, it is important to get this experimental value of measurement repeatability.

In order to quantify the measurement repeatability, a number of runs at approximately the same conditions were compared. The greatest number of runs were performed near the cooling design point of a pressure ratio of 1.04. All of the runs for this pressure ratio are compared in Fig. 3.10 and 3.11.

These measurements were taken from eight different runs on two different days. There was considerable variation noticed from day to day. The different day's runs are shown with different symbols. With these runs, a Student-T distribution with a 90% confidence interval is used. These confidence intervals are shown in Table 3.3.

Table 3.3: Measurement Repeatability

Gauge	h **90% Confidence Interval**	η **90% Confidence Interval**
	[W / m^2 °C], [%]	[-], [%]
1	± 90, ± 11.1%	± 0.049, ± 16.4%
2	± 32, ± 4.0%	± 0.015 ± 8.2%
3	± 34, ± 5.5%	± 0.024, ± 7.1%
4	± 38, ± 5.1%	± 0.034, ± 15.8%
5	± 51, ± 6.7%	± 0.023, ± 12.1%
6	± 63, ± 7.3%	± 0.034, ± 11.4%

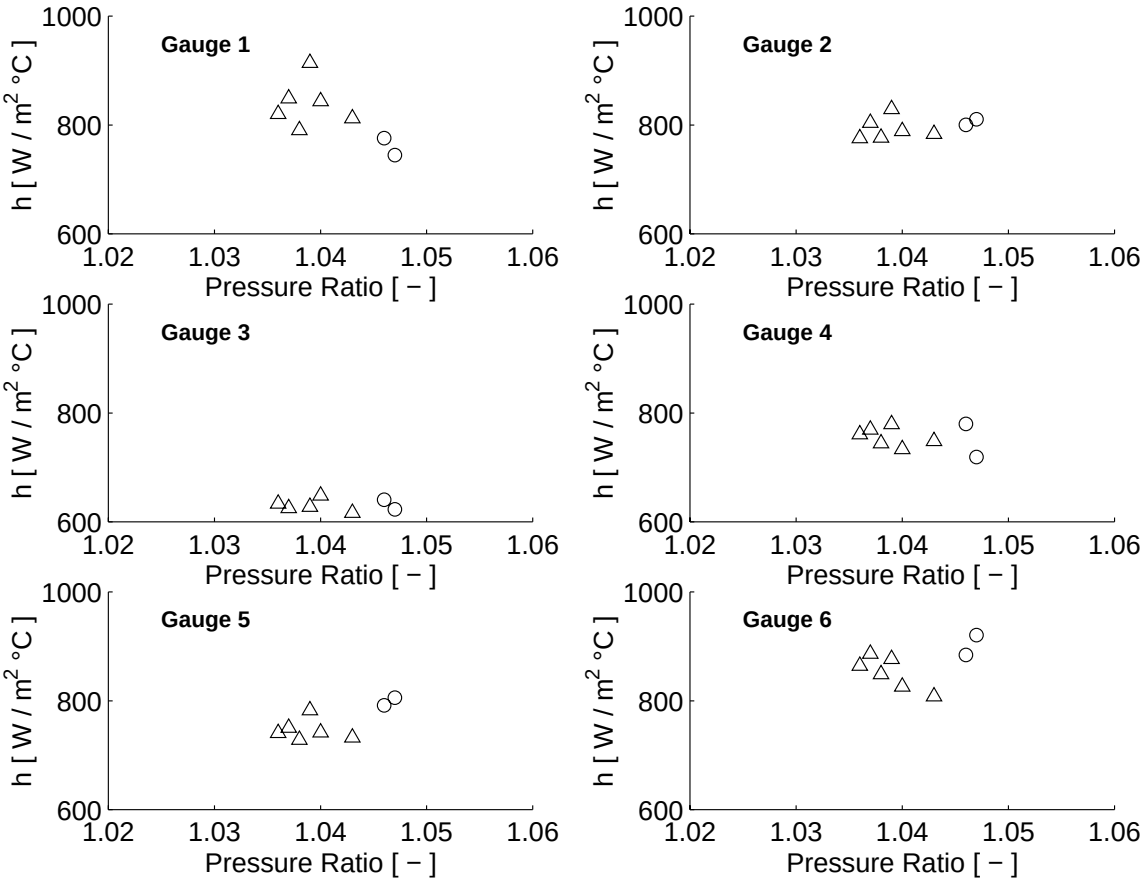

Figure 3.10: Measurement Repeatability of Heat Transfer Coefficient at PR=1.04

The observed measurement repeatability is of approximately the same size as the theoretical precision uncertainty. Gauge 1 is an exception to this generalization as its observed repeatability is higher than its predicted precision. Most likely this is due to the fact that the flow physics around gauge one is extremely unstable because it is so close to the last coolant exit.

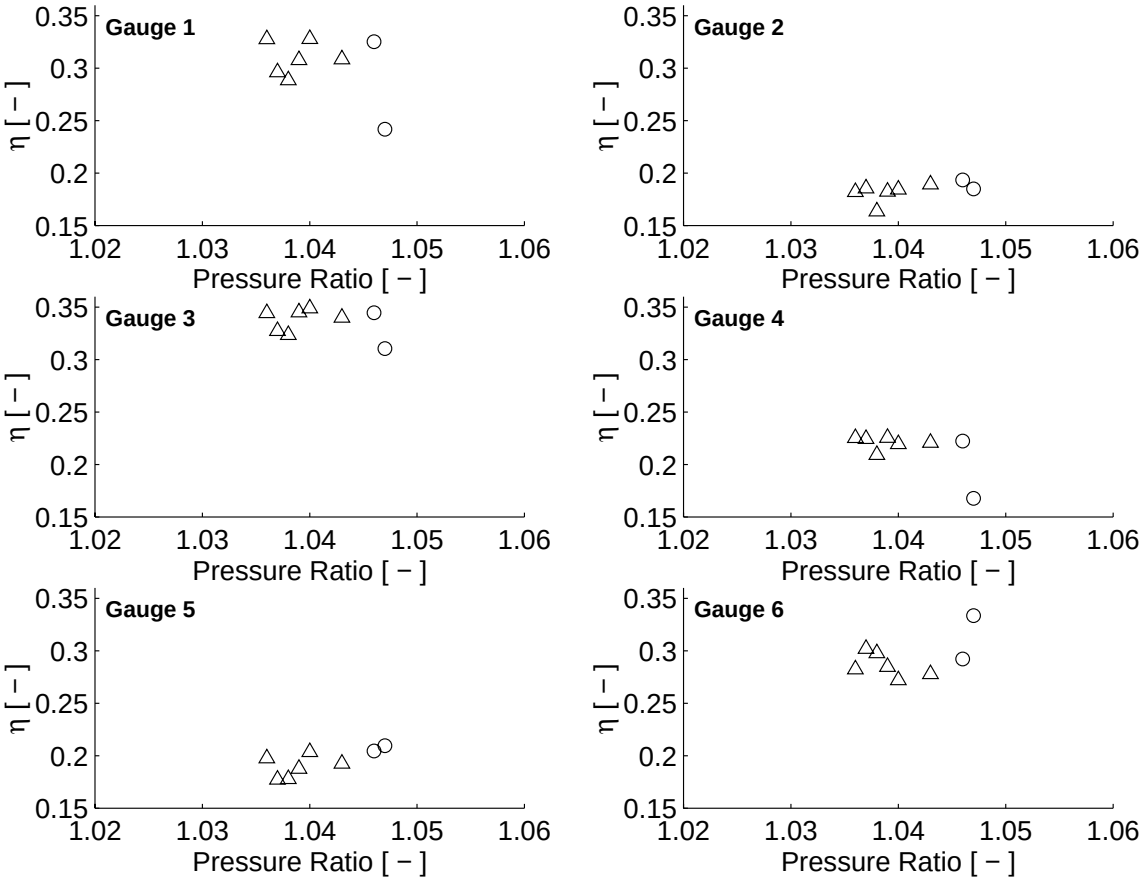

Figure 3.11: Measurement Repeatability of Effectiveness at PR=1.04

3.5 Coolant Mass Flow

The coolant mass flow rates measured using the orifice plate are documented in Fig. 3.12. On the left axis of this figure is the mass flow (g/s) and on the right axis is the fraction of coolant mass flow to the approximate freestream mass flow per passage (2 kg/s). Also shown on this curve is the predicted mass flow from an isentropic calculation and a discharge coefficient of 0.655. As can been seen, the mass flow of coolant is increased at higher pressure ratios. The scatter of this data is

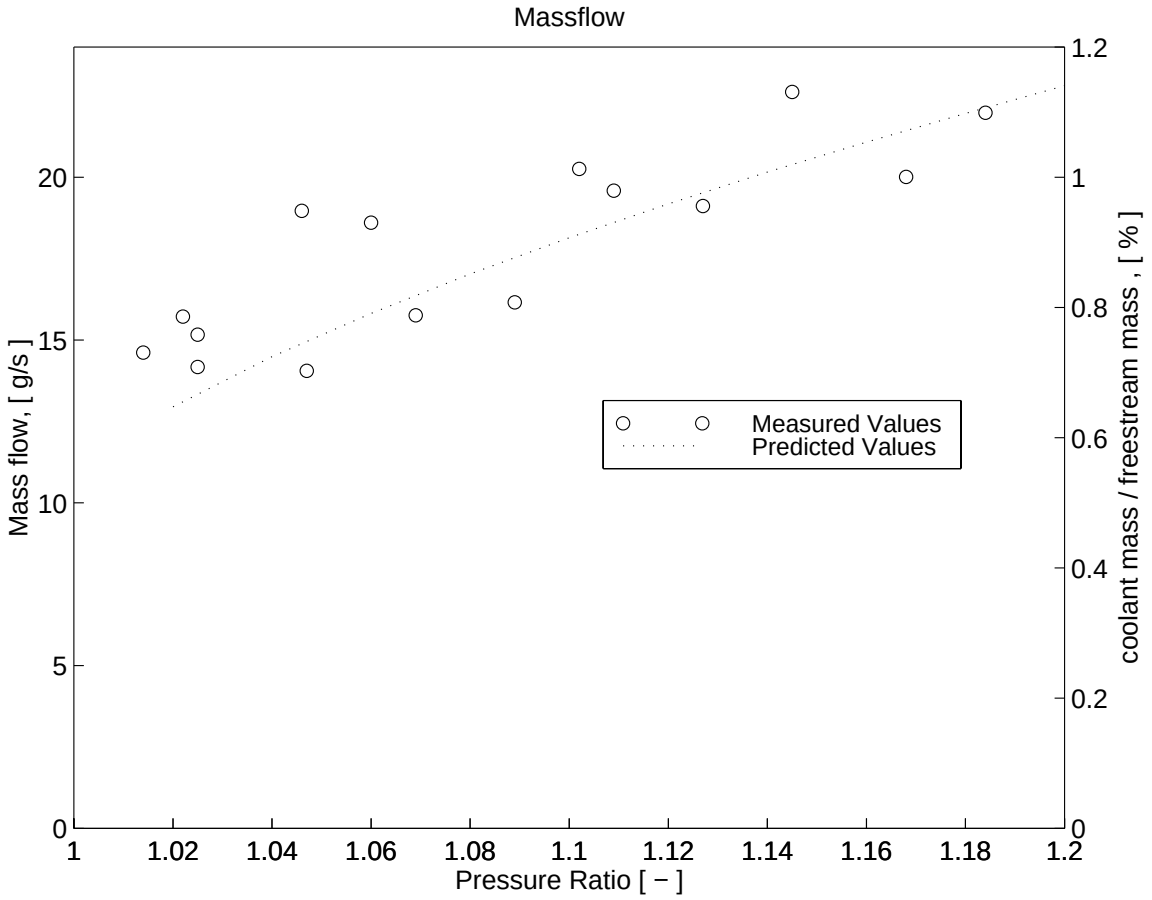

Figure 3.12: Coolant Mass Flow as a Function of Pressure Ratio

most likely due to the lack of control of coolant temperature (and therefore density ratio). In order to evaluate this possibility, it is useful to examine an expression for

the coolant mass flow,

$$\dot{m} = \rho_c \cdot U_c \cdot A$$
$$\dot{m} = M \cdot \rho_\infty \cdot U_\infty \cdot A$$
$$\dot{m} = \sqrt{I \cdot DR} \cdot \rho_\infty \cdot U_\infty \cdot A \tag{3.15}$$

Eqn. 3.15 shows that the mass flow is proportional to the square root of the product of the momentum ratio and density ratio, $\sqrt{I \cdot DR}$. Arbitrarily choosing the Suction Gill exit momentum ratio and plotting $\sqrt{I \cdot DR}$ on top of the measured mass flow is done in Fig. 3.13. This figure suggests a nice correlation between the scatter in the mass flow and the scatter in the density ratio.

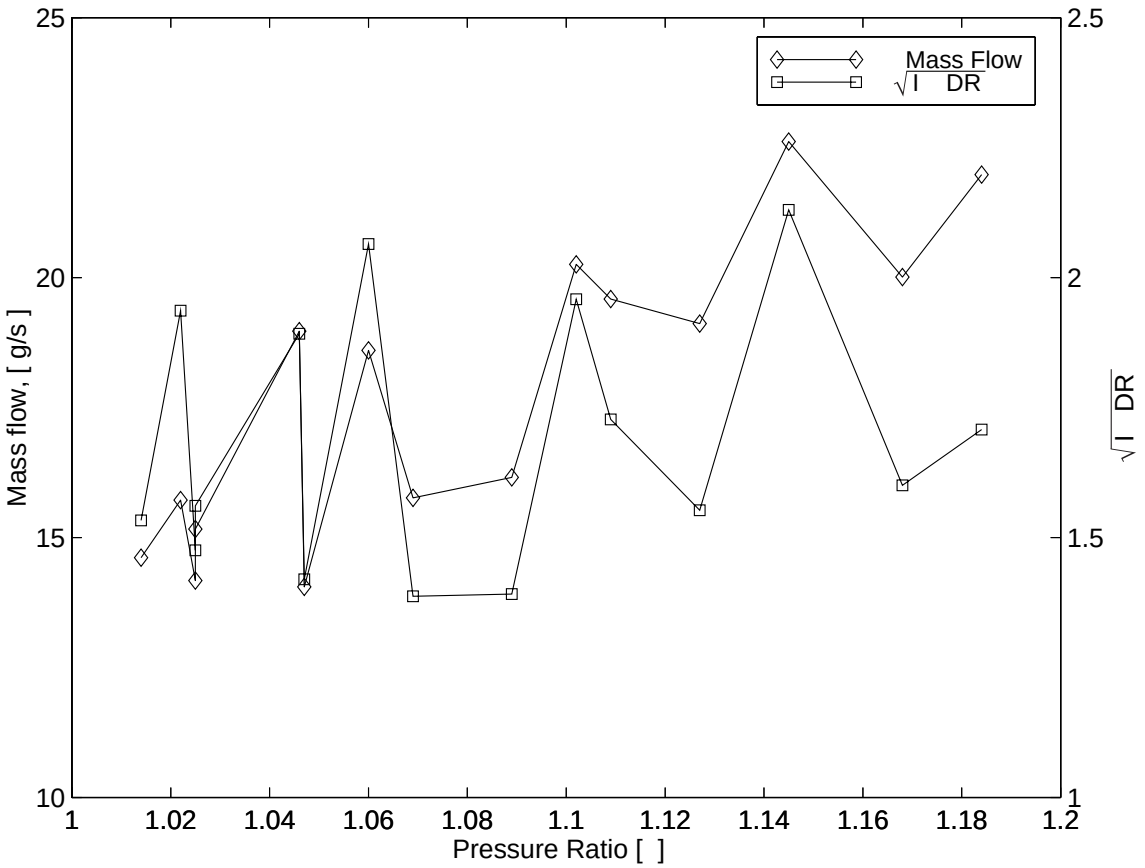

Figure 3.13: Coolant Mass Flow compared to $\sqrt{I \cdot DR}$ for SG

Again, it should be pointed out that the changes in density ratio have been shown earlier to not affect the heat transfer coefficient and film cooling effectiveness significantly (See Section 3.3).

Chapter 4

Results and Discussion

4.1 Shadowgraph Visualization

Shadowgraph photographs of tests with different pressure ratios are shown in Fig. 4.1 through Fig. 4.7. Unfortunately, the quality of these photographs is limited due to the following reasons:

- The abrasive environment of the tunnel gave poor endwall surface quality and lead to Moire patterns.
- Frost was formed near the leading edge on the outside of the endwalls due to the cold coolant.
- The optical set-up distorted the blade shape so the locations of the gauges and coolant geometry shown in Fig 4.1 are all approximate.
- The camera has a reduced resolution compared to that of Polaroid film.

Fig. 4.1 shows a drawing of the blade overlaid on the shadowgraph. This figure orients the photograph with respect to the coolant geometry. Fig. 4.2 shows the blade with no freestream flow and no coolant flow running. This figure can be used as a reference to compare the features of the coolant pictures. Another no-freesream flow picture is shown in Fig. 4.3. In this picture the coolant flow is running at a pressure ratio of 1.04. It can be seen in this picture that, without the presence of a freestream flow, the coolant film shoots directly off the blade surface. This is no surprise but the picture serves as a check that the coolant film can be visualized.

The next figures (4.4 - 4.7) show cases with the main flow and a progression of coolant pressure ratio. The film layer can be seen on these pictures attached to the blade surface. The most striking observance between these photos is that there is no noticeable difference between the appearance of the coolant layers. Never does the coolant seem to lift off the surface, as we had previously anticipated happening. Furthermore, while there appears to be a slight thickening of the film layer from the 1.02 to the 1.04 tests, there is no significant changes from the 1.04 to either of the higher pressure ratios photographs. This observation was surprising.

It is important to realize that these photographs only give a spanwise averaged picture across the flow field as is an inherent feature of al . There might perhaps be some spanwise shifting of the coolant flow or other coolant physics that is not being shown using this visualization method.

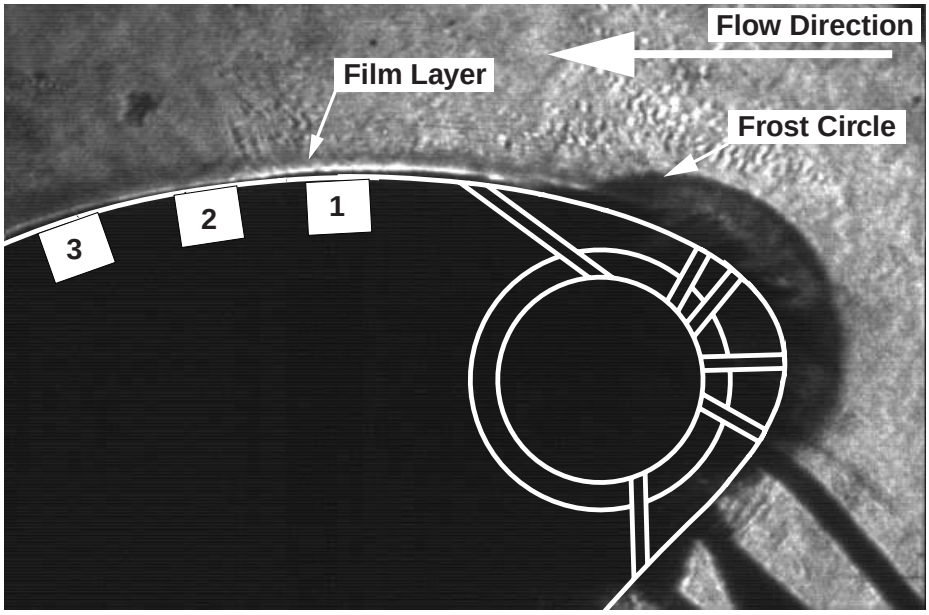

Figure 4.1: Typical Shadowgraph

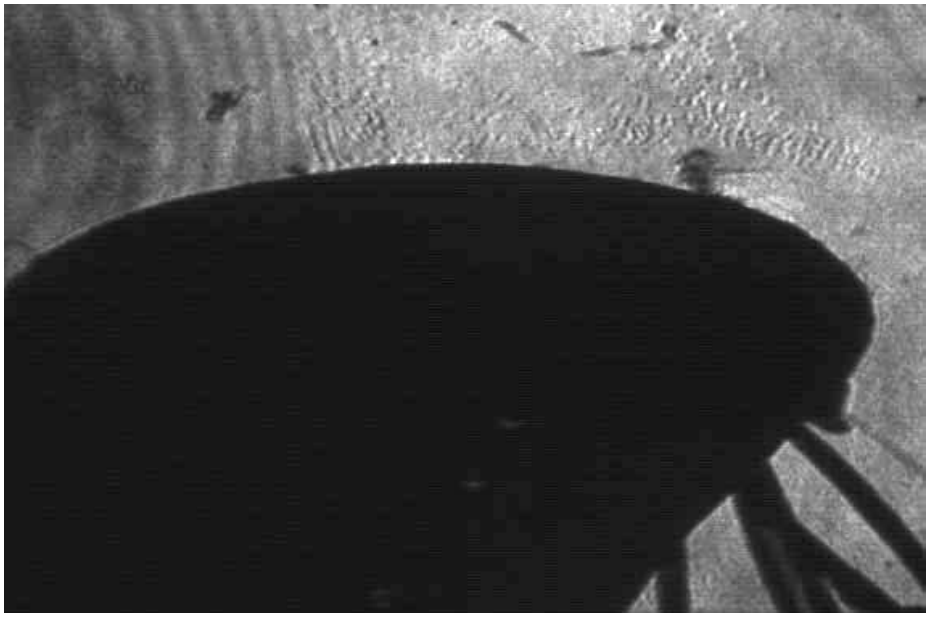

Figure 4.2: Shadowgraph, No Flow, No Coolant

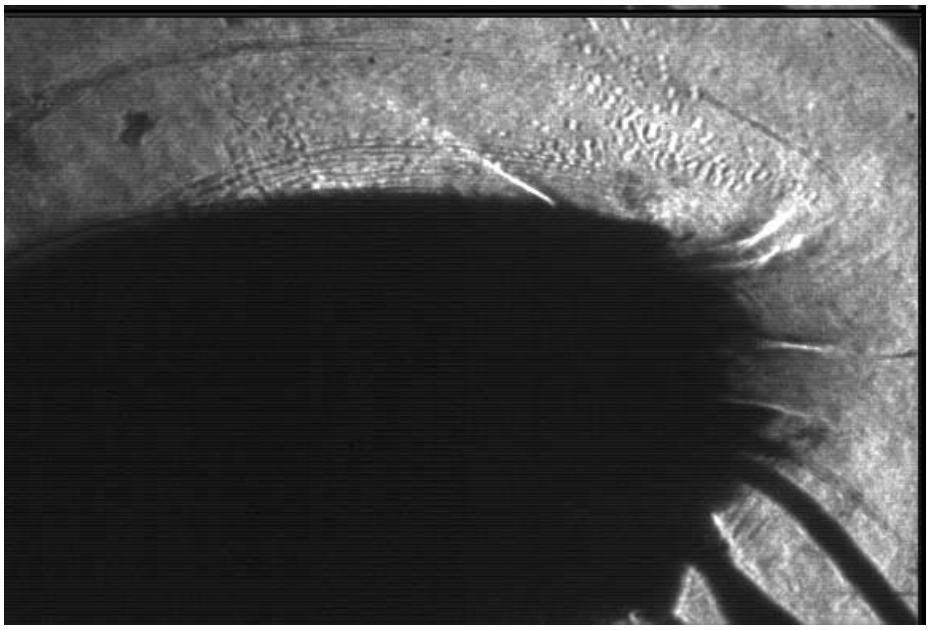

Figure 4.3: Shadowgraph, No Flow, Coolant Running

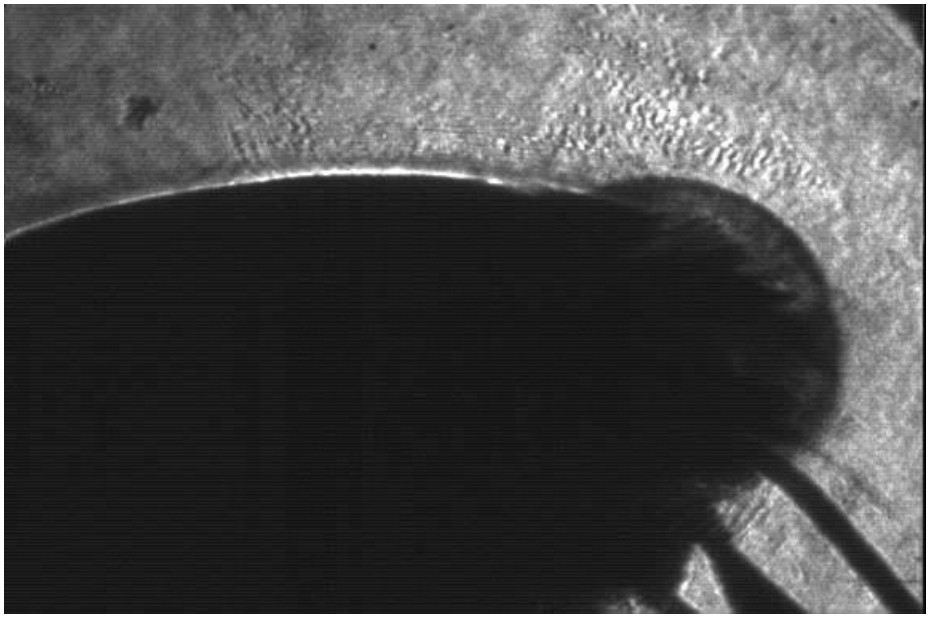

Figure 4.4: Shadowgraph, Pressure Ratio: 1.02

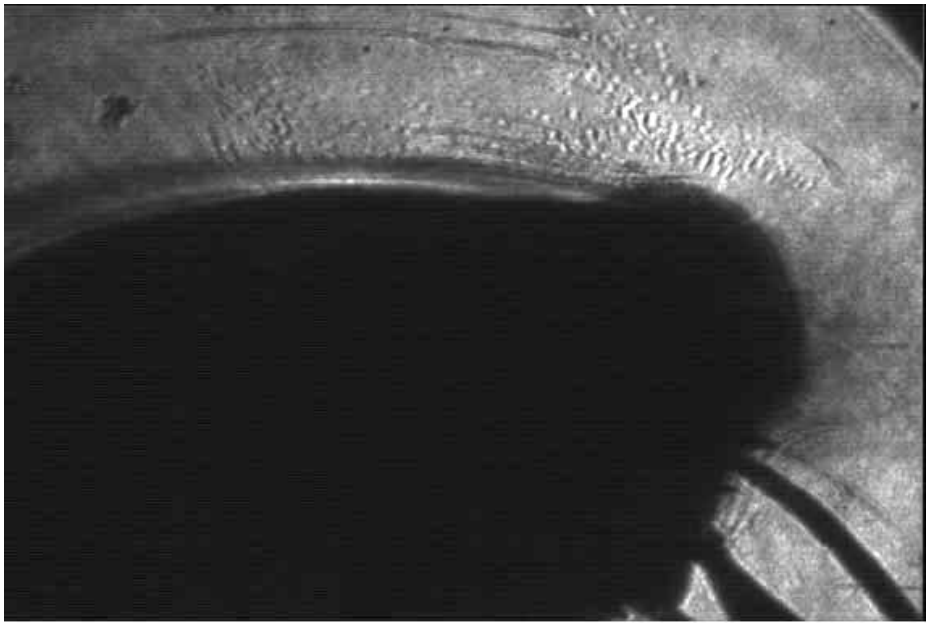

Figure 4.5: Shadowgraph, Pressure Ratio: 1.04

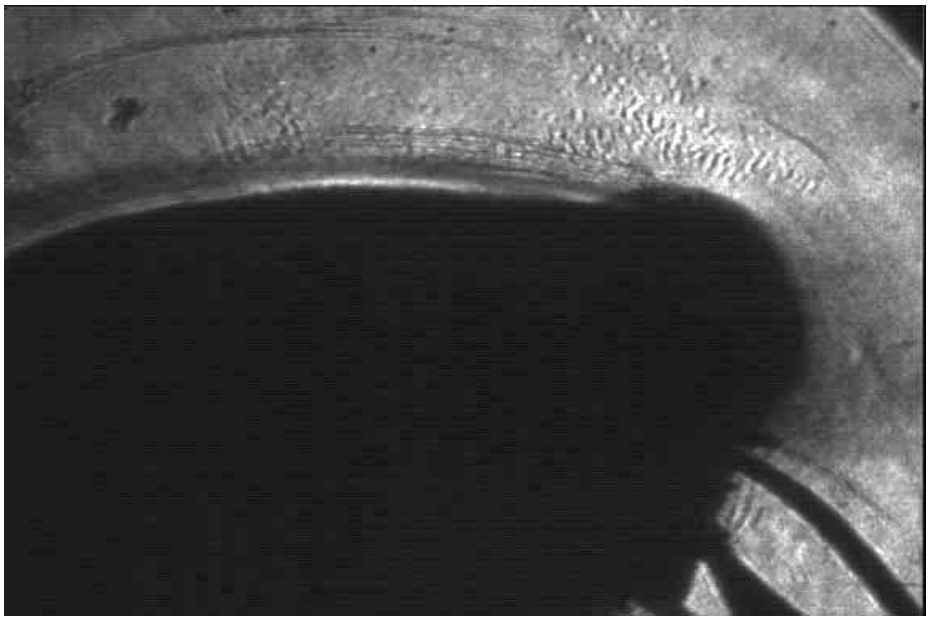

Figure 4.6: Shadowgraph, Pressure Ratio: 1.18

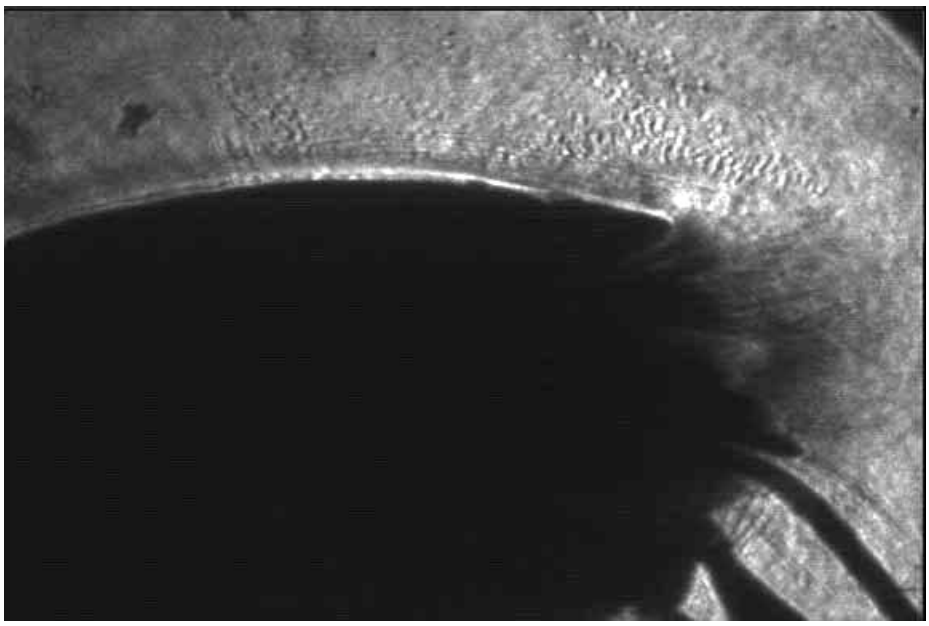

Figure 4.7: Shadowgraph, Pressure Ratio: 1.21

4.2 Effect of Pressure Ratio on Heat Transfer Coefficient

The observed effect of the pressure ratio on the surface heat transfer coefficient is illustrated in Fig. 4.8 through Fig. 4.13. These graphs show the results from a number of runs performed on two different days. The range of pressure ratios covers from about 1.02 to about 1.19. The GE design point for this coolant design is a pressure ratio of 1.04. The error bars shown on these plots are for the 90% confidence bounds on measurement repeatability (these uncertainties are summarized in Table 3.1). It is important to realize that the error bars are representative of measurement repeatability and not measurement accuracy as discussed in Sec. 3.4. Each of the gauges is shown on a different graph to better illustrate the trends of pressure ratio at each different location.

A few observations can be made from looking at these graphs. One noticeable feature is that the data at Gauge 1 has very low repeatability as evidenced by the scatter of the data points and the large error bars. It is suspected that this scatter is due to the fact that Gauge 1 is so close to the last coolant exit. At this close location, the film is most probably very un-mixed and small tunnel variations can create significant changes in the local flow field appearance. This type of situation would result in a very unstable flow physics at this location. The second more general observation, is that the heat transfer coefficient appears to be fairly independent of the pressure ratio.

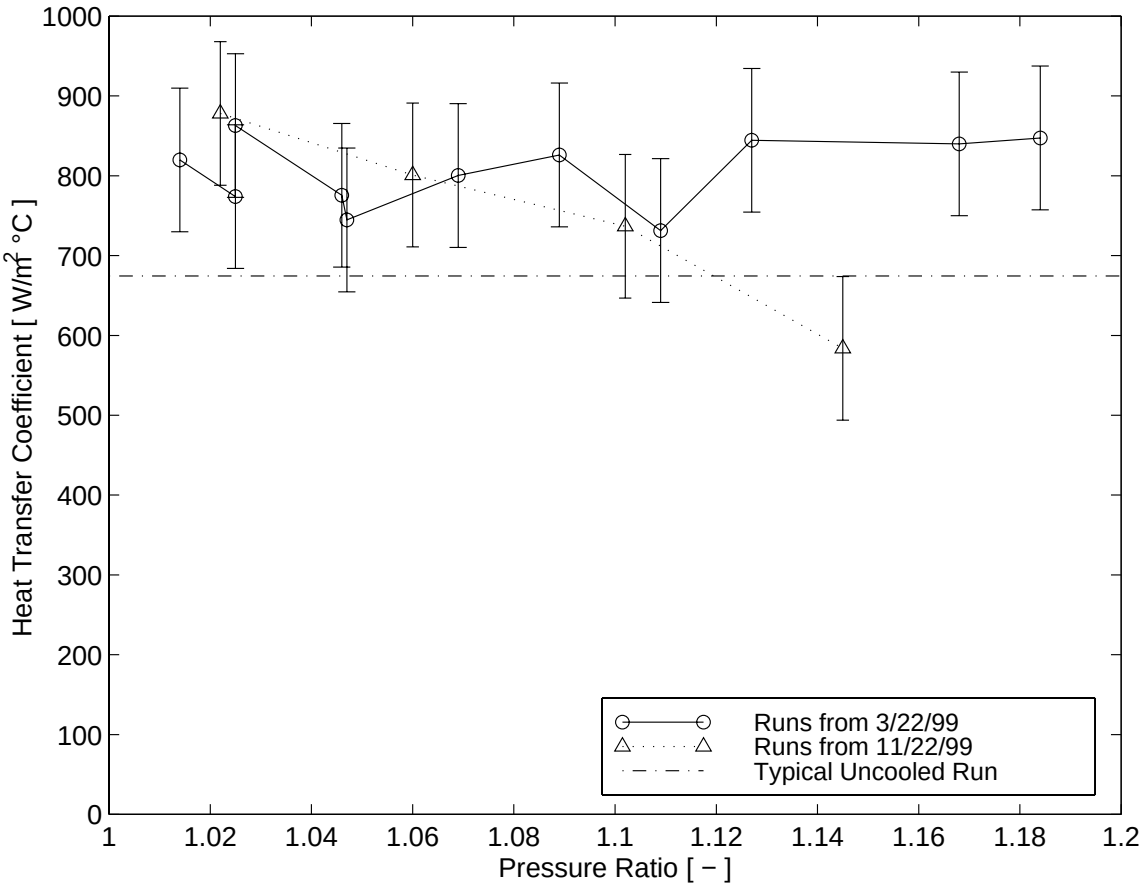

Figure 4.8: Variation of Heat Transfer Coefficient with Pressure Ratio for Gauge 1

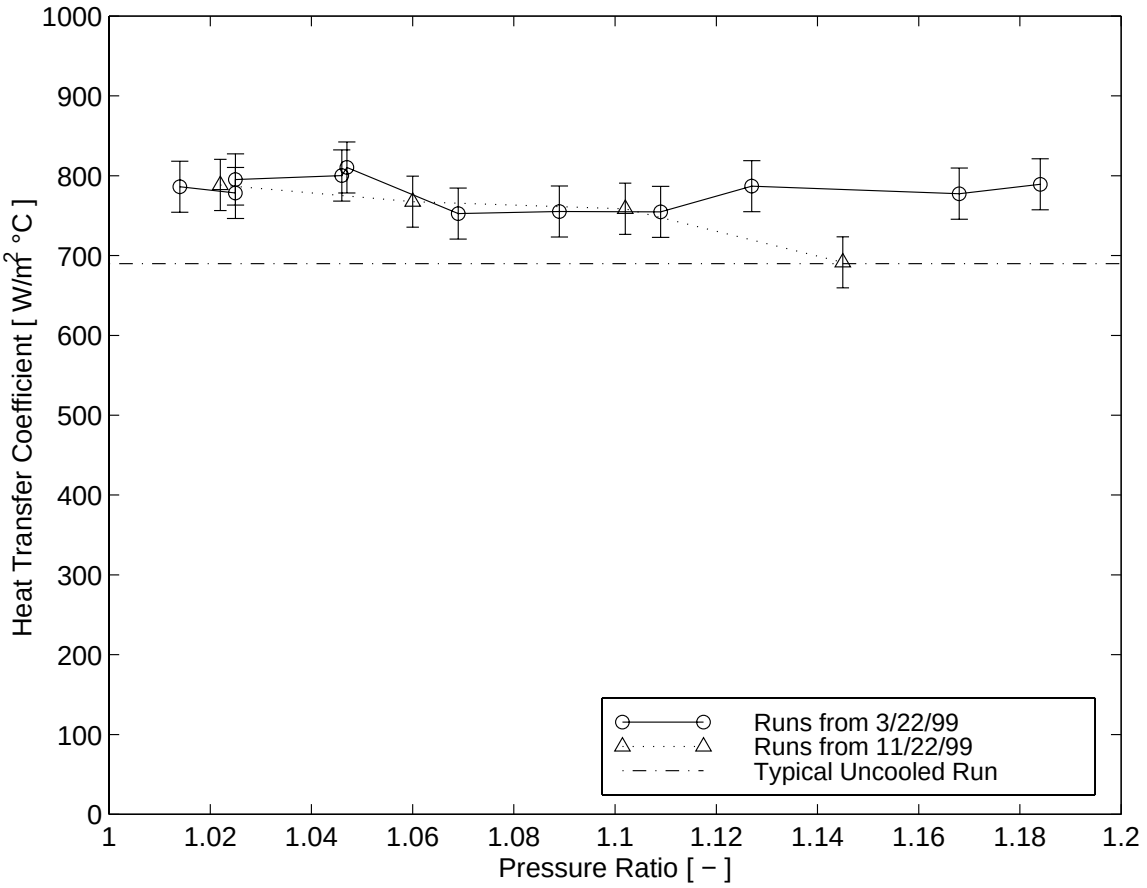

Figure 4.9: Variation of Heat Transfer Coefficient with Pressure Ratio for Gauge 2

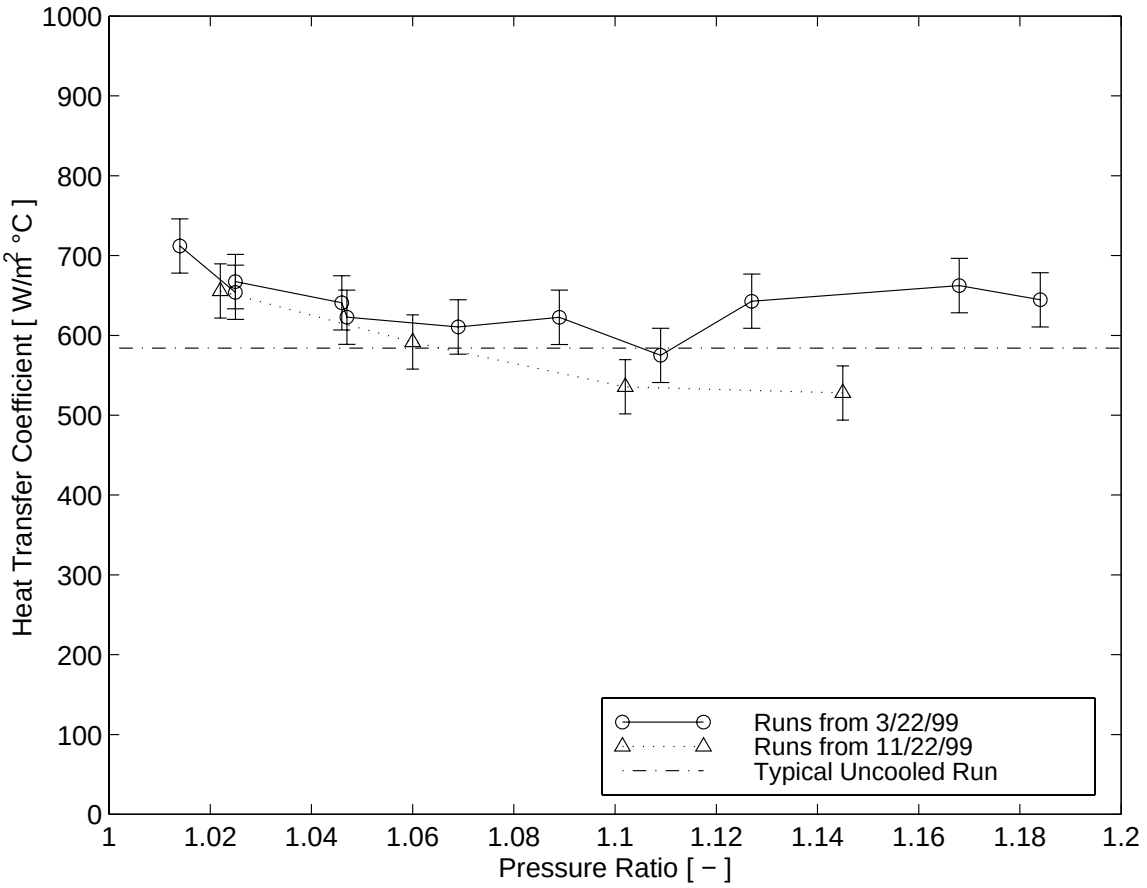

Figure 4.10: Variation of Heat Transfer Coefficient with Pressure Ratio for Gauge 3

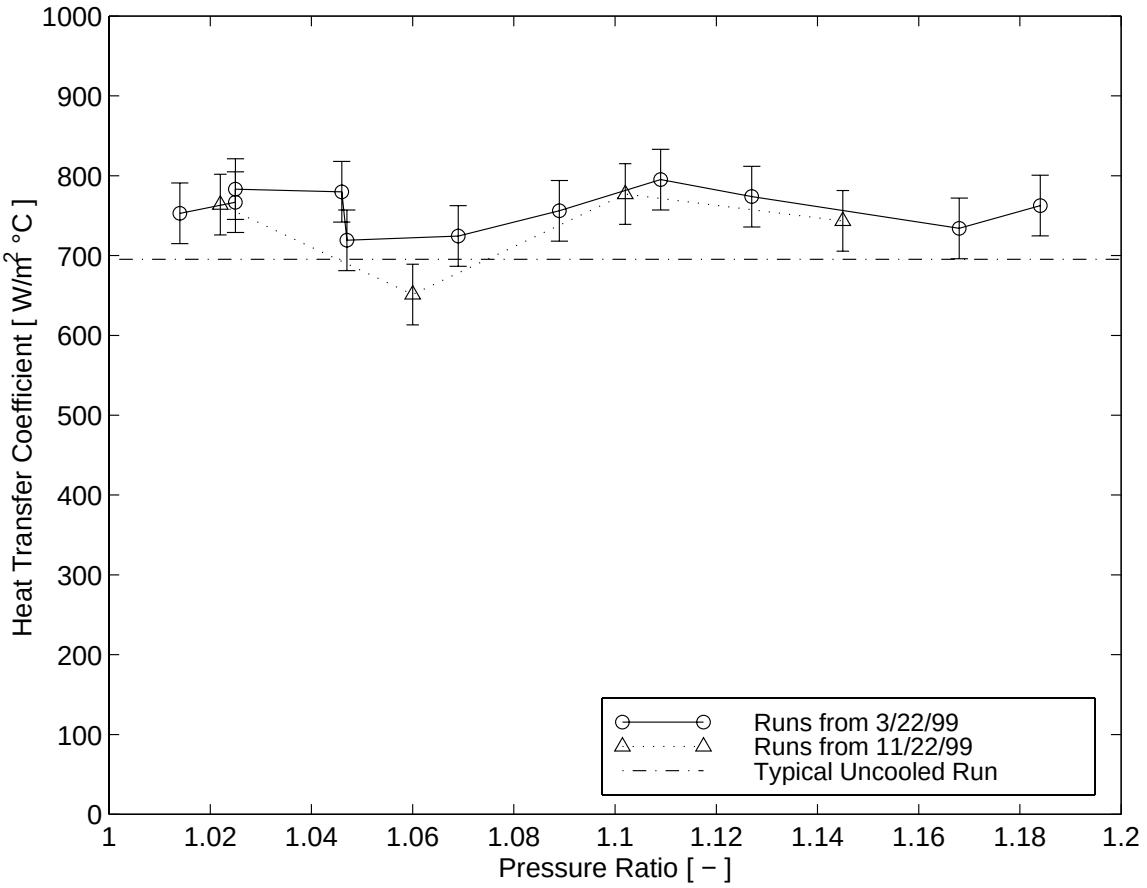

Figure 4.11: Variation of Heat Transfer Coefficient with Pressure Ratio for Gauge 4

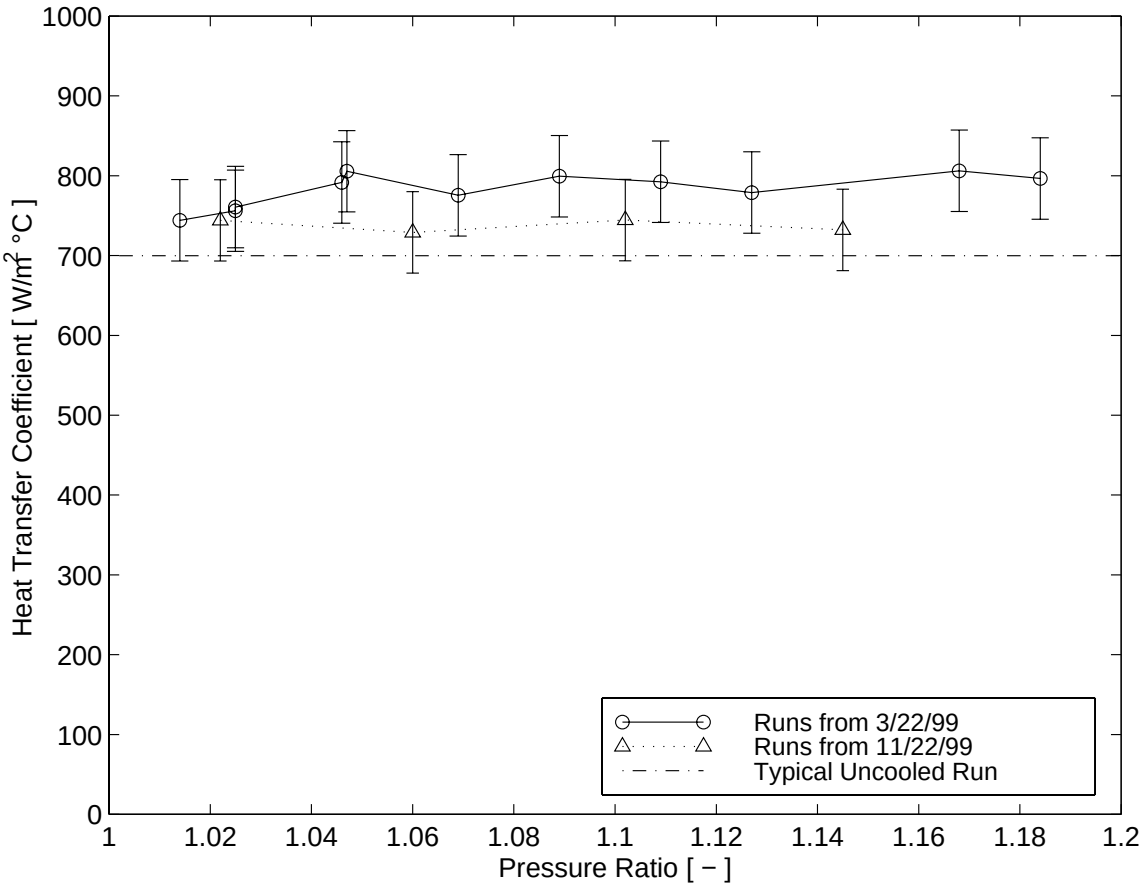

Figure 4.12: Variation of Heat Transfer Coefficient with Pressure Ratio for Gauge 5

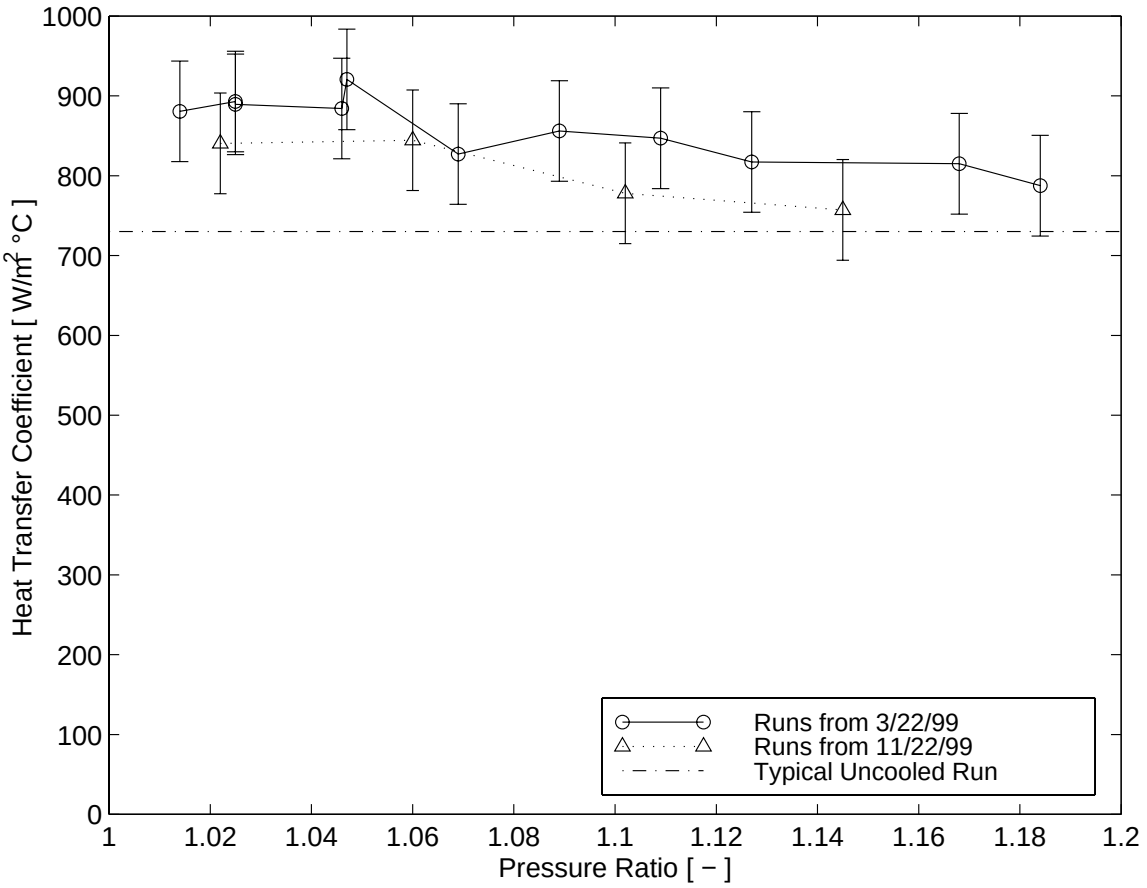

Figure 4.13: Variation of Heat Transfer Coefficient with Pressure Ratio for Gauge 6

4.3 Effect of Pressure Ratio on Effectiveness

The observed effect of the pressure ratio on film cooling effectiveness is illustrated in Fig. 4.14 through Fig. 4.19. These graphs show the results from a number of runs performed on two different days. The range of pressure ratios covers from about 1.02 to about 1.19. The GE design point for this coolant design is a pressure ratio of 1.04. The error bars shown on these plots are for the 90% confidence bounds on measurement repeatability (these uncertainties are summarized in Table 3.1). It is important to realize that the error bars are representative of measurement repeatability and not measurement accuracy as discussed in Sec. 3.4. Each of the gauges is shown on a different graph to better illustrate the trends of pressure ratio at each different location.

At Gauge 1, a high scatter of the data points is observed. It is suspected that this scatter is due to the same reason there is high scatter in the heat transfer coefficient. This reason is that the flow physics in the region so close to the coolant exits is unsteady. The film is not mixed very well and from one run to the next different amounts of film coverage are present resulting in different cooling effectiveness. The uncertainties and overall scatter of the data points outweigh any trends that might be interpreted.

Gauge 2 has much lower scatter and a fairly flat trend of film cooling effectiveness. Gauge 3 has moderate uncertainty and a trend that suggests the film cooling effectiveness is reduced at the higher pressure ratios. Gauge 4 shows little dependence of effectiveness on pressure ratio.

Gauges 5 and 6 show a trend that indicates film cooling effectiveness reduces slightly with higher pressure ratios.

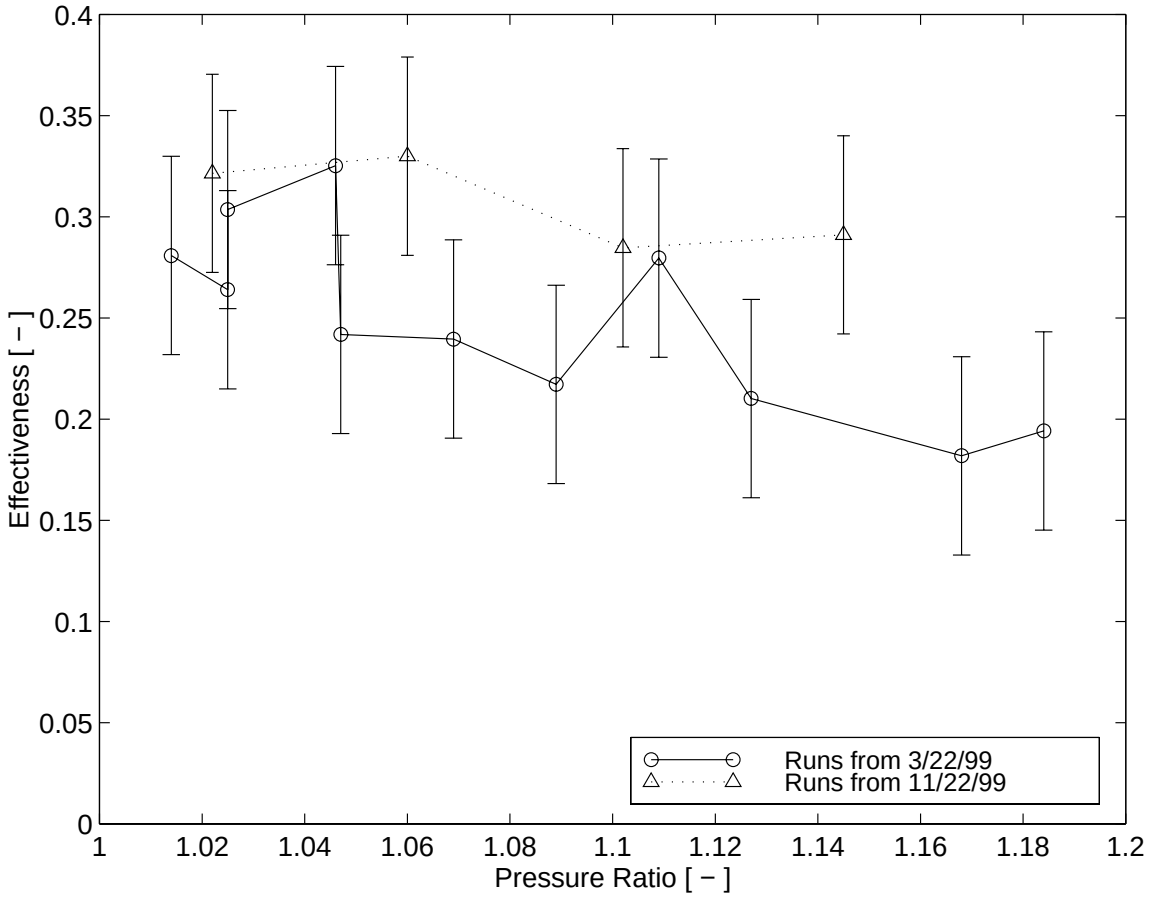

Figure 4.14: Variation of Film Cooling Effectiveness with Pressure Ratio for Gauge 1

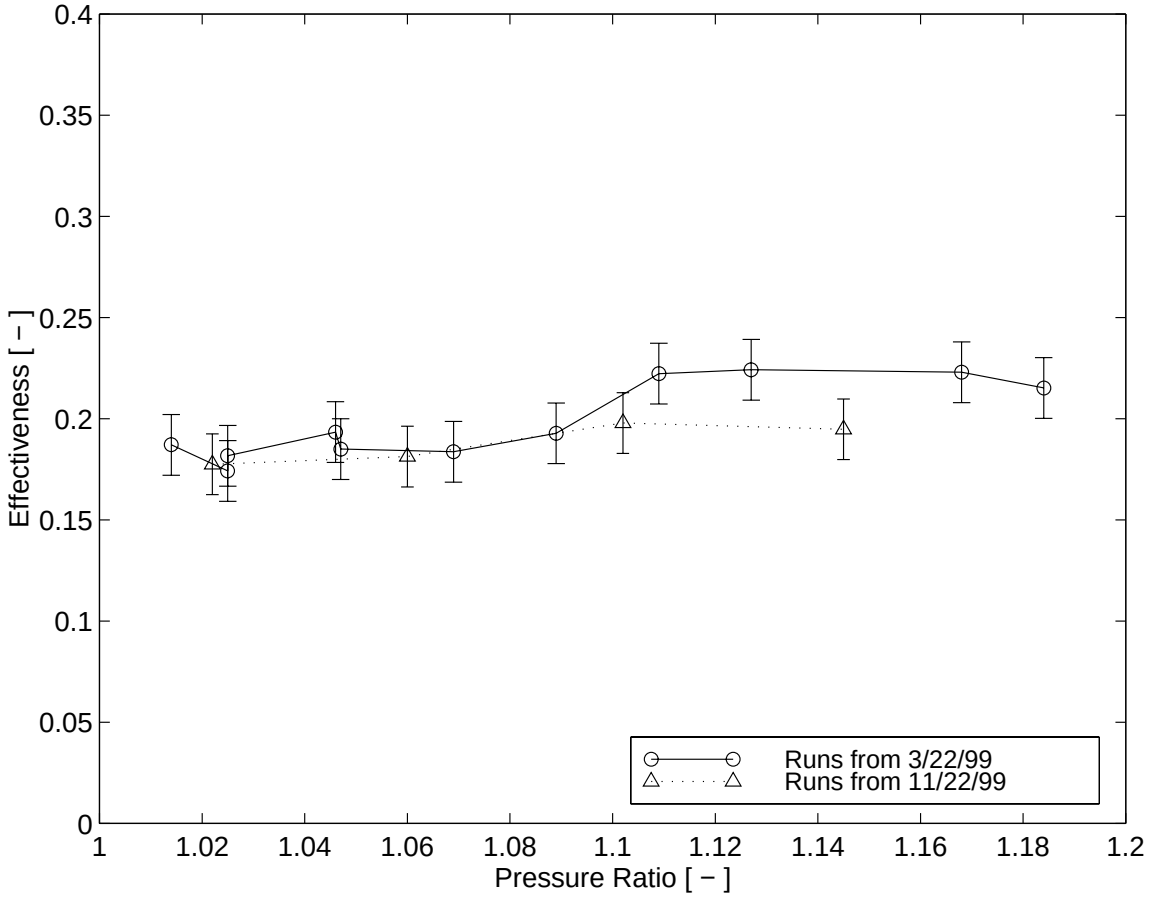

Figure 4.15: Variation of Film Cooling Effectiveness with Pressure Ratio for Gauge 2

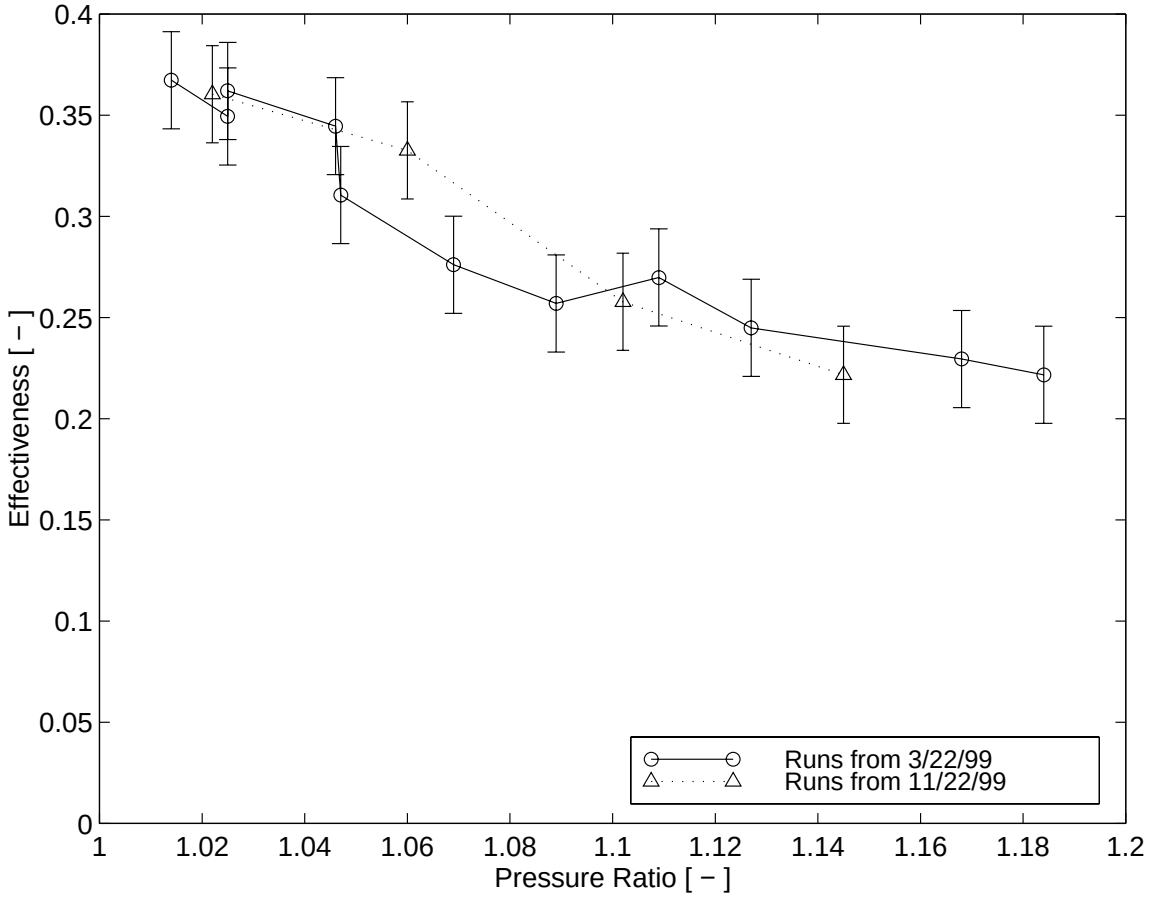

Figure 4.16: Variation of Film Cooling Effectiveness with Pressure Ratio for Gauge 3

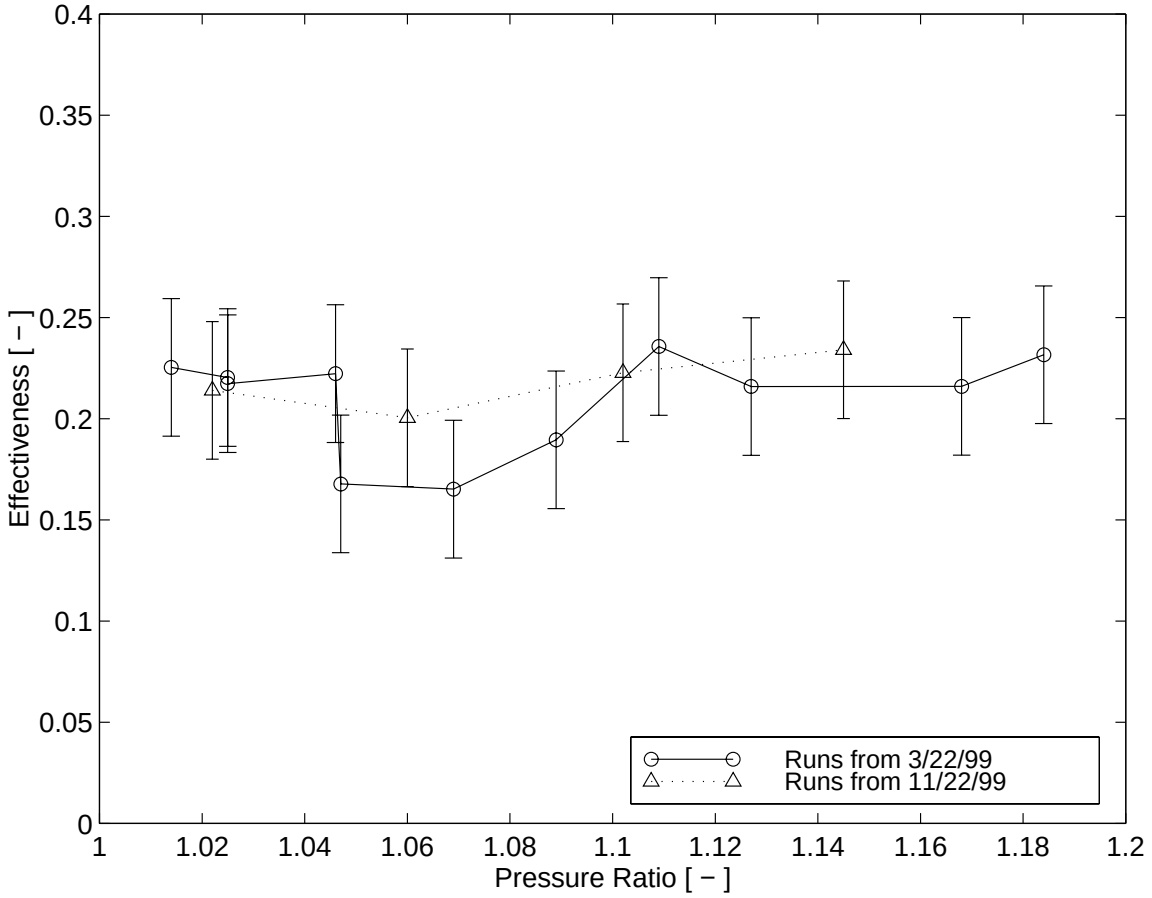

Figure 4.17: Variation of Film Cooling Effectiveness with Pressure Ratio for Gauge 4

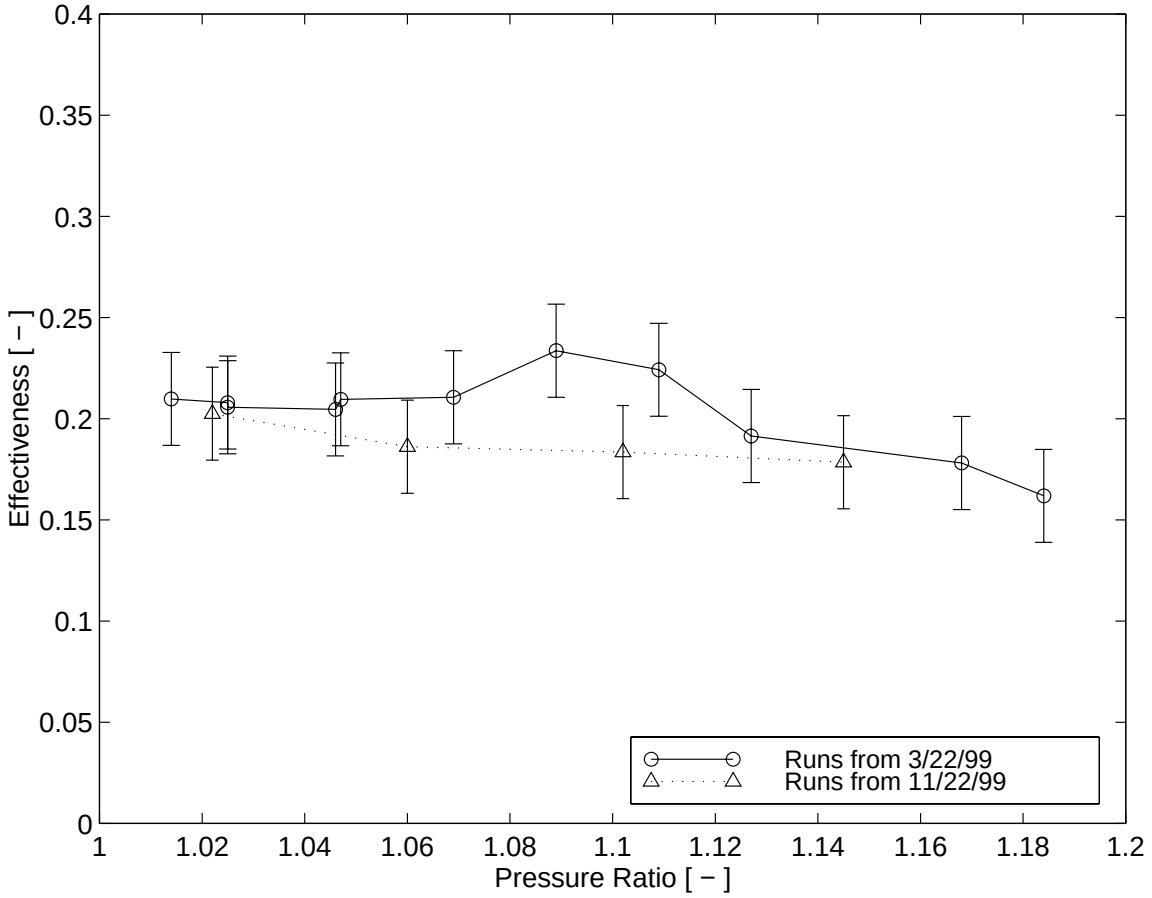

Figure 4.18: Variation of Film Cooling Effectiveness with Pressure Ratio for Gauge 5

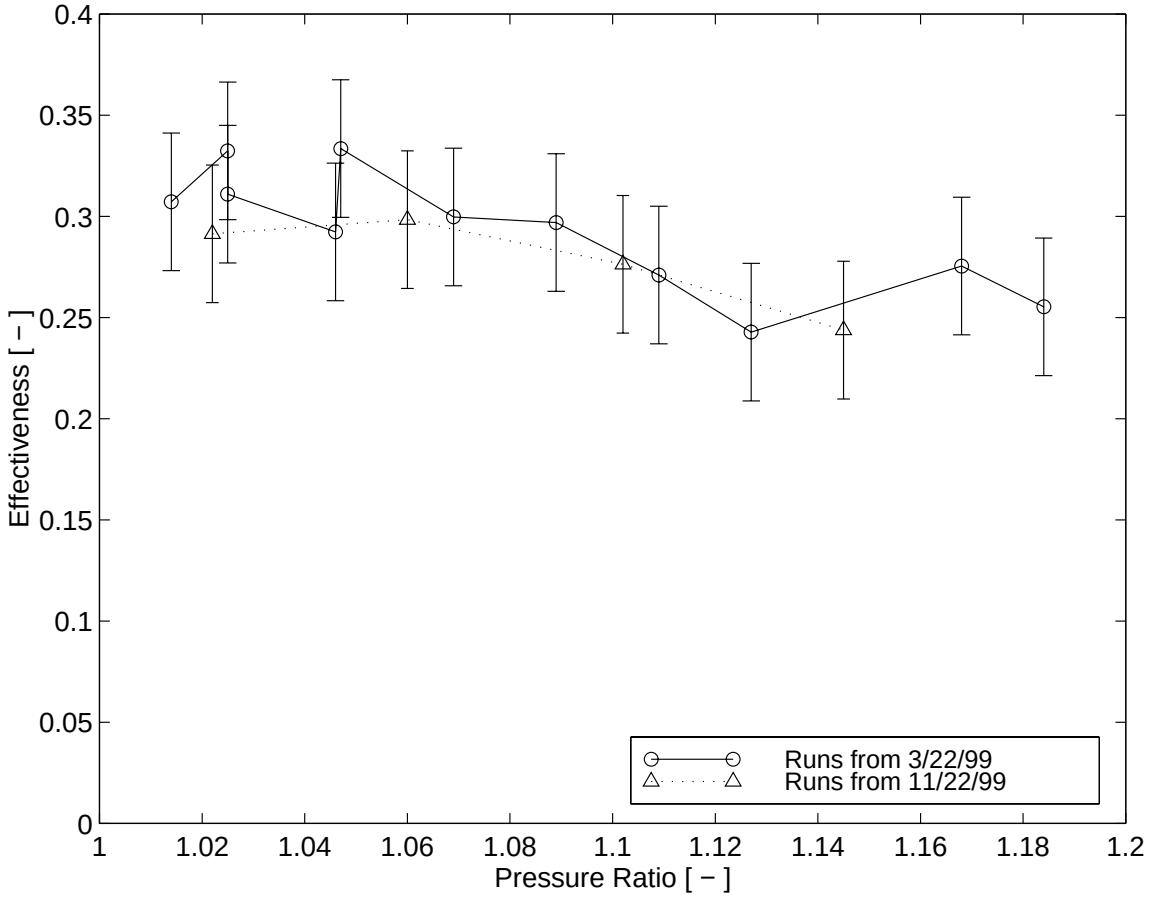

Figure 4.19: Variation of Film Cooling Effectiveness with Pressure Ratio for Gauge 6

4.4 Streamwise Variation of Heat Transfer Coefficient and Effectiveness

4.4.1 Experimental results

One of the objectives at the outset of this research was to measure and to explain the variation of heat transfer coefficient and film cooling effectiveness as a function of the streamwise distance from the coolant holes. These h and η profiles are shown in Fig. 4.20 and Fig. 4.21, respectively. These figures are taken from one representative run, and other runs show a similarly shaped profile.

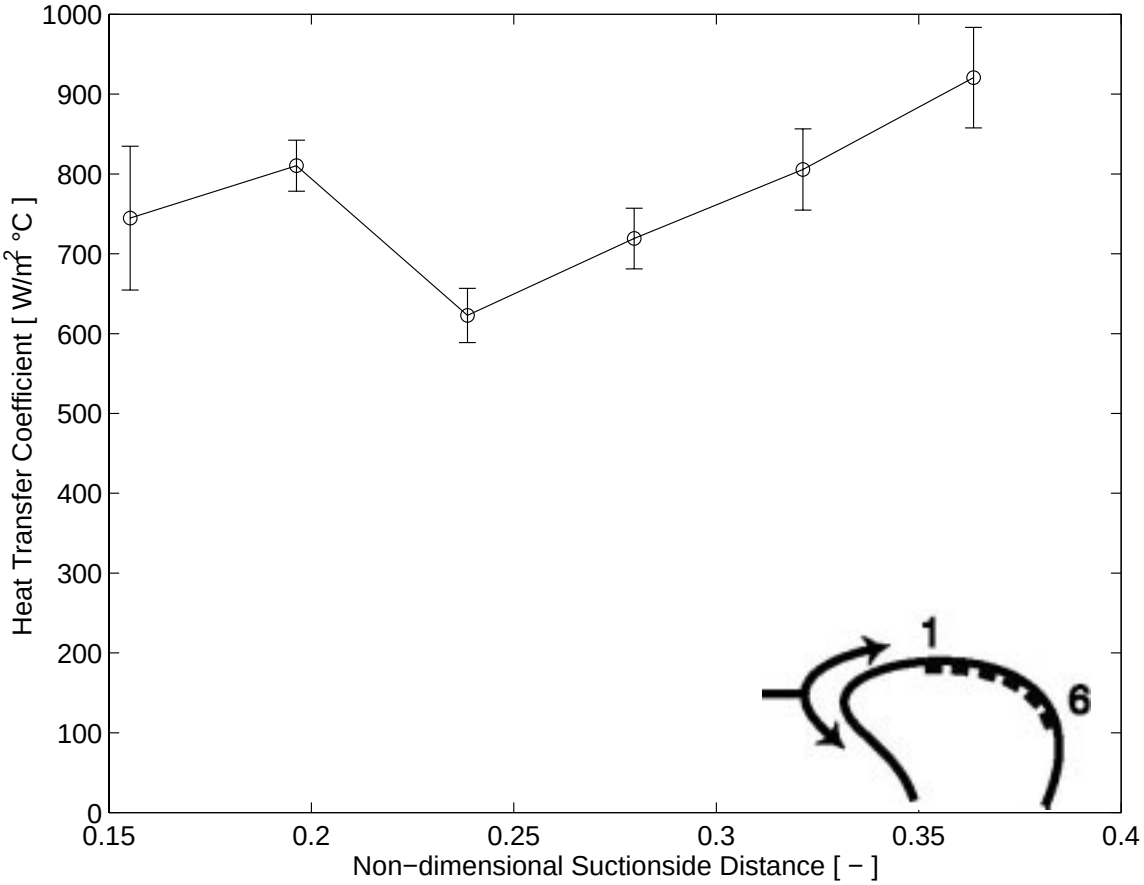

Figure 4.20: Heat Transfer Coefficient Profile at Pressure Ratio of 1.04

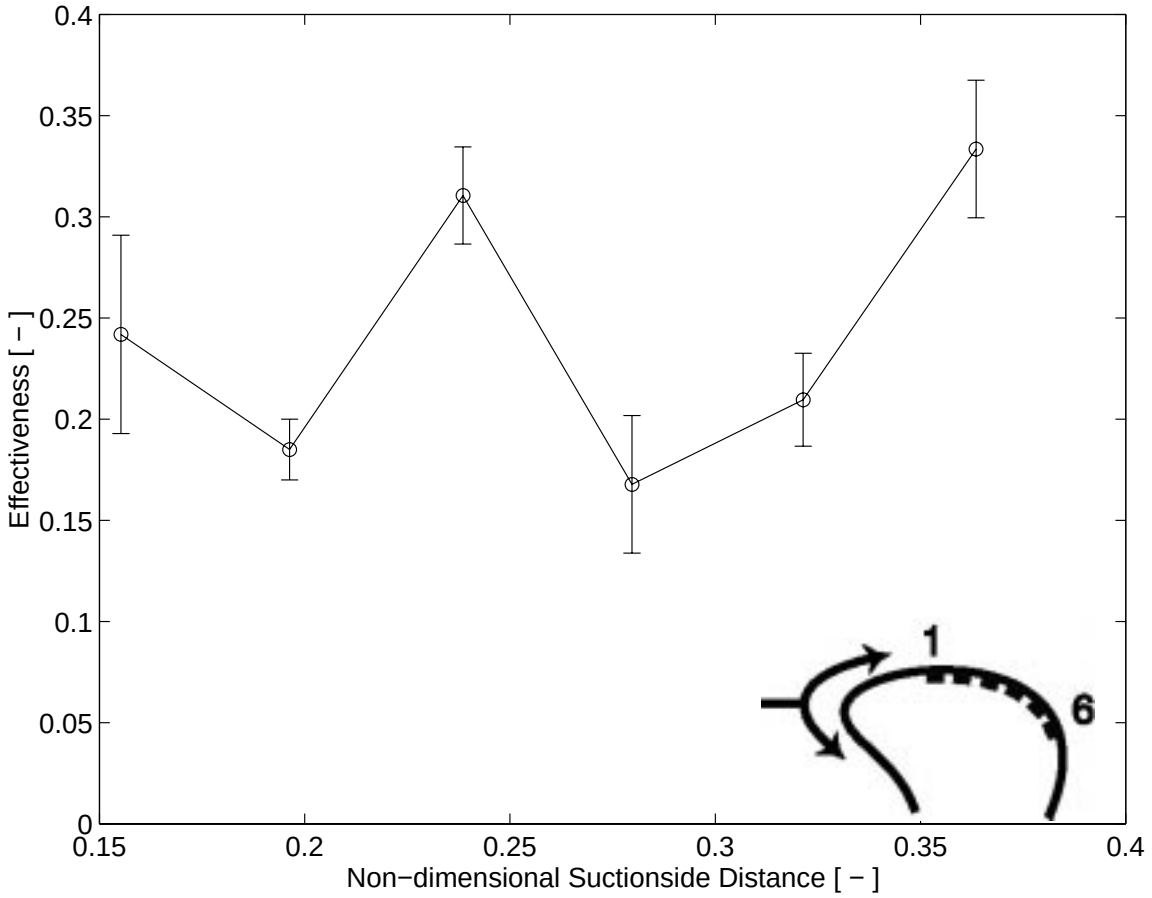

Figure 4.21: Film Cooling Effectiveness Profile at Pressure Ratio of 1.04

As can be seen, both the heat transfer coefficient and film cooling effectiveness vary significantly from location to location. The heat transfer coefficient starts high, decreases until Gauge 3, and then increases until Gauge 6. It is difficult to find a plausible explanation for this streamwise profile. There were several possible explanations proposed for the shape of these profiles, and a number of experiments were performed to investigate each of the possibilities. The next section describes and discusses different ideas that were proposed, the experiments performed to investigate the hypotheses, and the results of these experiments.

1. **Transition**

One thought was that the increase in heat transfer could be caused by transition of the boundary layer from a laminar to turbulent regime. It was somewhat doubtful that this would be the cause, however, since the same trend can be seen on both the non-film-cooled heat transfer data and film-cooled data. Shadowgraph pictures of a film-cooled blade also seemed to show a film layer that was turbulent from the very start. These pictures, however, provide only a spanwise averaged picture, and perhaps the boundary layer outside of the jet plumes (but along the surface of the blade) started laminar and transitioned to turbulent, giving the rise in heat transfer coefficient.

To investigate this possibility, a strip of sand was glued to the front of the blade to trip the boundary layer to turbulent. The sand strip was manufactured with 80 grit sand sealed with Polaroid sealant and the dimensions were in general as suggested by Chandraeskhara [3]. This setup should have insured that the boundary layer was turbulent for the entire length of the blade. A Schlieren picture of the tripped boundary layer without film-cooling is shown in Fig. 4.22. From Fig. 4.22 one can see that the boundary layer is turbulent when compared to that of the laminar un-tripped blade shown in Fig. 4.23. Also, from looking at the tripped picture it does appear that the boundary re-laminarizes far down the length of the blade. This occurs much farther down the blade surface then where the gauges are located. This boundary layer tripping strip did successfully provide a fully turbulent boundary over the region of scrutiny.

The experiment was run without film cooling to see if the heat transfer coefficient trends would become monotonic with surface distance as one might expect in a fully turbulent boundary. The results of this experiment, however, yielded heat transfer curves with the same shape but the heat transfer coefficient rose slightly (approximately 50 W/cm^2 °C) over the laminar case as one would expect.

At the end of this experiment, we felt fairly sure that the cause of the heat

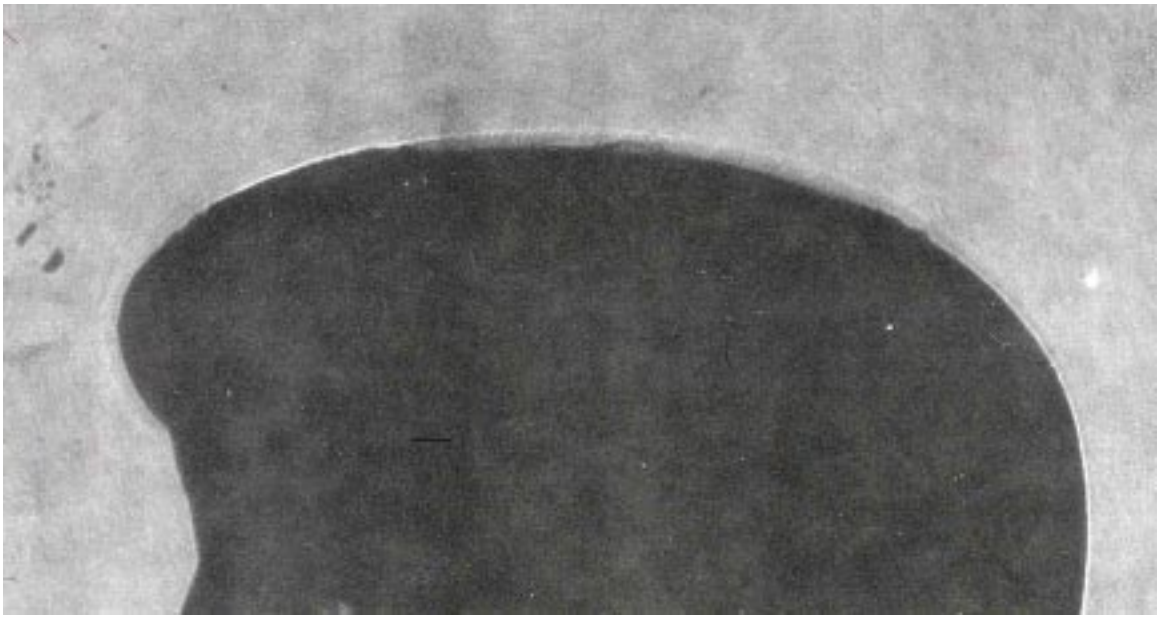

Figure 4.22: Schlieren of Blade with Tripped Boundary Layer (No Film Cooling)

transfer coefficient shape is not transition from laminar to turbulent.

2. **Calibration**

   Another possible cause for the both the peculiar heat transfer coefficient and film effectiveness profiles might be errors in the sensitivities of each HFM gauge. The sensitivities of the gauges have been investigated thoroughly in an attempt to eliminate this as a possible source of error. An in-situ calibration method for the HFM was developed and used as detailed by Smith et al. [23]. This in-situ calibration method provides a way for the gauges to be self calibrated every time the tunnel is run. The data was used from many of the runs and the gauges all have reasonable and repeatable sensitivities for each location. HFM calibration does not seem to be a likely explanation for the strange trends.

3. **Location of the Gauges with Respect to the Coolant Exits**

   As can be seen in Fig. 2.18 the gauges are not located consistently with respect to the coolant holes. Some gauges are located directly behind one

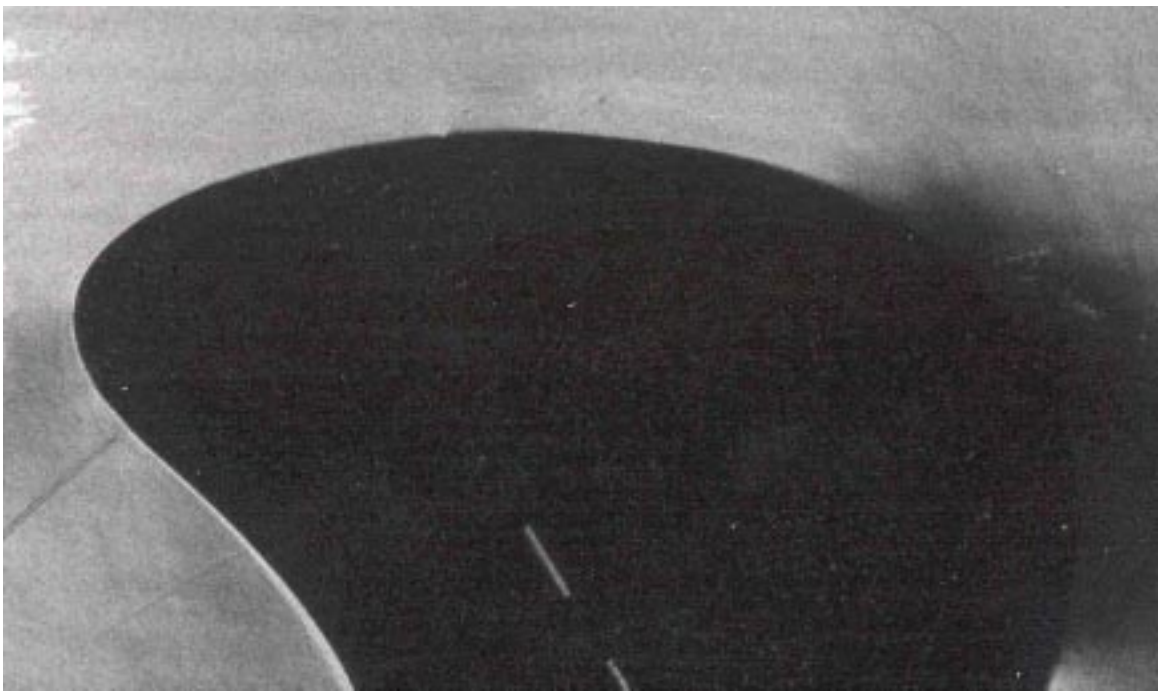

Figure 4.23: Schlieren of Blade with Un-Tripped Boundary Layer (No Film Cooling)

coolant exit, and some gauges have two coolant exits in front of them. The assumption in the experimental design was that the coolant would be sufficiently mixed spanwise by the time it reached the gauges. This might have been a bad assumption especially at Gauge 1 as it is so close to the last coolant exit.

If such were the case, it would explain the strange trends in cooling effectiveness. This hypothesis seems like the most plausible. Film cooling effectiveness can vary considerably if the film layer is not thoroughly mixed.

This hypothesis is a little more troubling to apply to the variations in heat transfer coefficient, however, since similar profiles persists in both the cooled and uncooled data. The only way this hypothesis might apply would be if the very presence of the film cooling holes even without the film coolant air running, was changing the flow field, therefore providing different heat transfer coefficients for different gauges. This is one scenario that may be occurring but it is suspected rather unlikely. The explanation for the h profiles is probably

somewhere else.

4. **Spanwise Variations of Heat Transfer Coefficient and Effectivness**

It is assumed in these experiments that the spanwise variations are secondary to the streamwise variations. Steps were taken to insure that the blade had as close to two dimensional flow as was possible and that the area of the measurements was sufficiently outside any secondary flow regimes. Because such steps had been taken, it was decided to stagger the gauges in the streamwise direction (as shown in Fig. 2.18) so that any effects from a gauge possibly not being flush to the surface (see item 5) would not effect the downstream gauges. Perhaps this assumption that the measurements are being made in a two dimensional portion of the blade is wrong. There might have been some significant spanwise variation that was measured.

In order to investigate this possibility, a simple oil dot surface flow visualization test was performed. This sort of test was inspired by a technical note written by Meyer [17] about oil dot visualization. Essentially, it was shown by Meyer that small oil drops placed on a surface would streak when placed in a wind tunnel. The length of the oil streak is proportional to skin friction, which is proportional to heat transfer. Therefore, the streak length is, at least qualitatively, proportional to the heat transfer on the blade at that location. Realizing this, a matrix of oil dots was placed on the blade before the tunnel was run. After the uncooled tunnel run, the lengths of these oil streaks were measured. Fig. 4.24 is a picture of the oil dots on the blade before the tunnel run, and Fig. 4.25 is a picture of the blade and oil streaks after the tunnel was run.

The results of these few experiments showed a repeatable variation of streak length in the streamwise direction and a rather uniform streak length in the spanwise direction. These results tend to confirm that there is uniform spanwise heat transfer. An attempt was made to correlate the streak length with the heat transfer coefficient in the streamwise direction. Unfortunately however, no

Figure 4.24: Setup of the Oil Streak Experiment

matching trends could be found from these tests.

These experiments added more confidence to ruling out spanwise variations as the cause of the peculiar heat transfer coefficient profiles.

5. **Gauge Offset**

One concern at the outset of this research program was that the flat surface heat flux gauges might not sit perfectly flush with the surface of the blade. Consequently, the lip where the gauge surface meets the blade surface would cause a disturbance in the boundary layer and effect the local heat transfer coefficient. This concern had been addressed earlier by Peabody [19]. He performed a number of tests to quantify the amount of error that both positive and negative gauge offsets introduce into the heat transfer measurements. His results showed that at a gauge offset of 0.010 inches there was a 40% difference in the heat transfer coefficient. Peabody's blades were one third the size of the blades used in this thesis and of the same profile. Since the blades used in this thesis

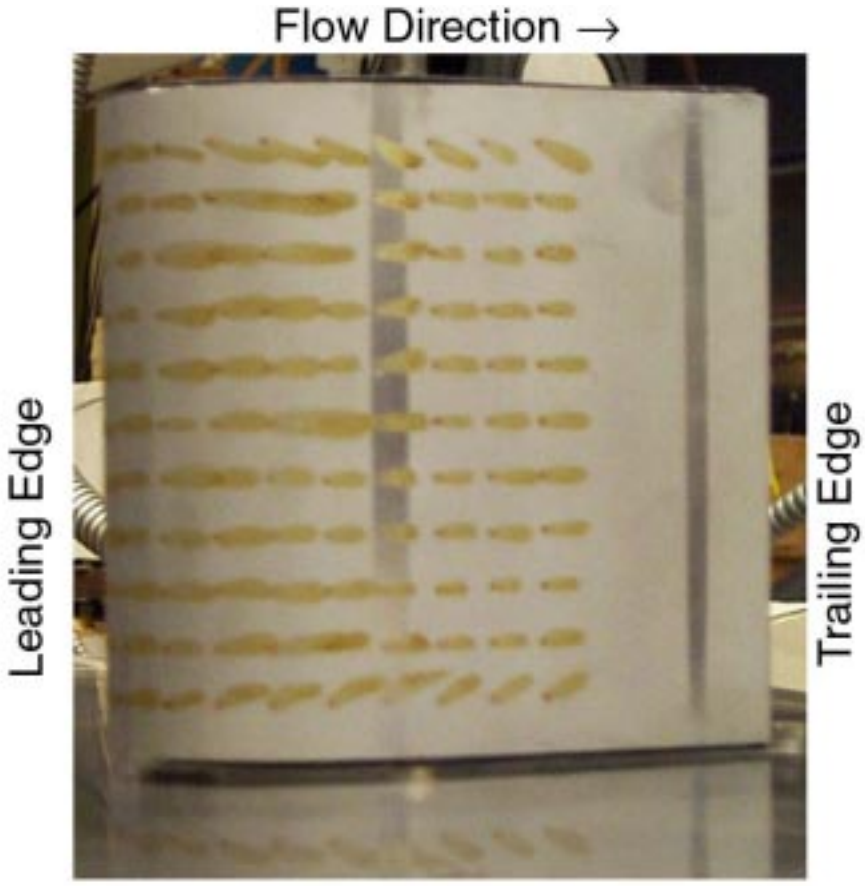

Figure 4.25: Oil Dot Streaks After Tunnel Run

are much larger, the local curvature and thus the offset is much smaller. An estimate of the worst offset of the gauges is about 0.001 inches. This offset may still be a source of error in the heat transfer coefficient measurements, but it is hard to believe it can account for the large changes in heat transfer coefficient.

4.4.2 Comparison to Published Results

An comparison of the Virginia Tech data to other published results is made in the following section . This comparison was made from General Electric data

from a similar conditions and is shown in Fig. 4.26 and Fig. 4.27. As shown,

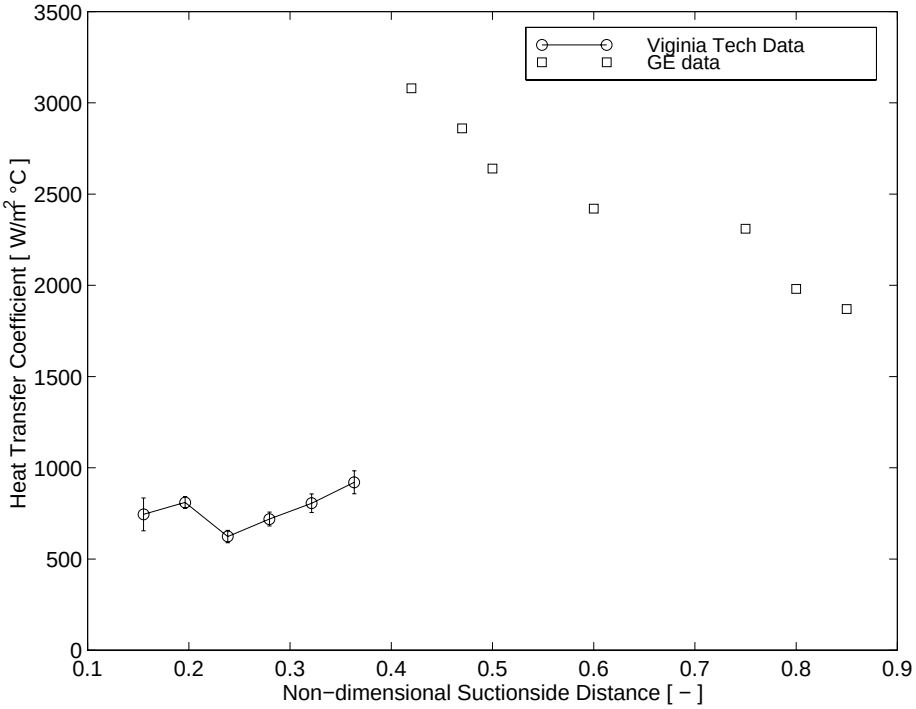

Figure 4.26: Comparison of Heat Transfer Coefficient

both the values of the heat transfer coefficient and the effectiveness are higher. This difference can be partially attributed to the fact the the General Electric blades had a film-cooling showerhead scheme with much more coolant exits. One can see the the General Electric film-cooling effectiveness drops off rapidly as downstream distance increases.

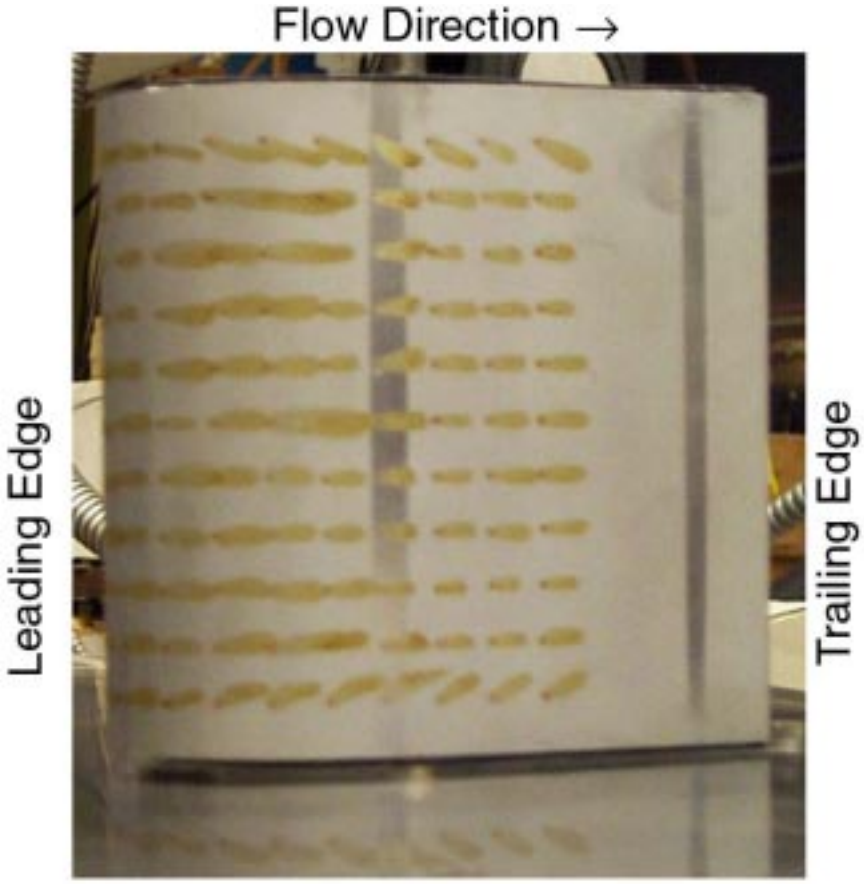

Figure 4.27: Comparison of Film-Cooling Effectiveness

Chapter 5

Conclusions

The primary goal at the outset of this research was to investigate the influence of pressure ratio on the heat transfer coefficient and film cooling effectiveness. The experimental results show that the heat transfer coefficient is nearly independent of the pressure ratio. Previous research at the same facility indicated that the presence of a coolant film increases the heat transfer coefficient when compared to an uncooled blade [22]. This research has extended that observation to state that the value of the increased heat transfer coefficient is independent of pressure ratio and coolant mass flow.

In addition, the film cooling effectiveness has been shown to be relatively independent of the pressure ratio. Film detachment is not seen over the tested range of pressure ratios. This conclusion is supported both by the film cooling effectiveness data and the shadowgraph pictures. Furthermore, this conclusion has been seen in research under similar conditions conducted by Epstein et al. [1].

It was also seen that the film cooling effectiveness has some slight trends at certain gauge locations. Gauges 1, 2, and 4 suggest an independence of pressure ratio

and effectiveness, and Gauge 3, 5, and 6 show a slight decrease in effectiveness with increasing pressure ratio.

In order to have a reasonable explanation for why the effectiveness has a decreasing trend, one must suppose a possible behavior of the three-dimensional flow field. Fig. 5.1 provide a few illustrations of what the flow field might possibly look like. In this figure, parts A and B show how an increase in momentum ratio might

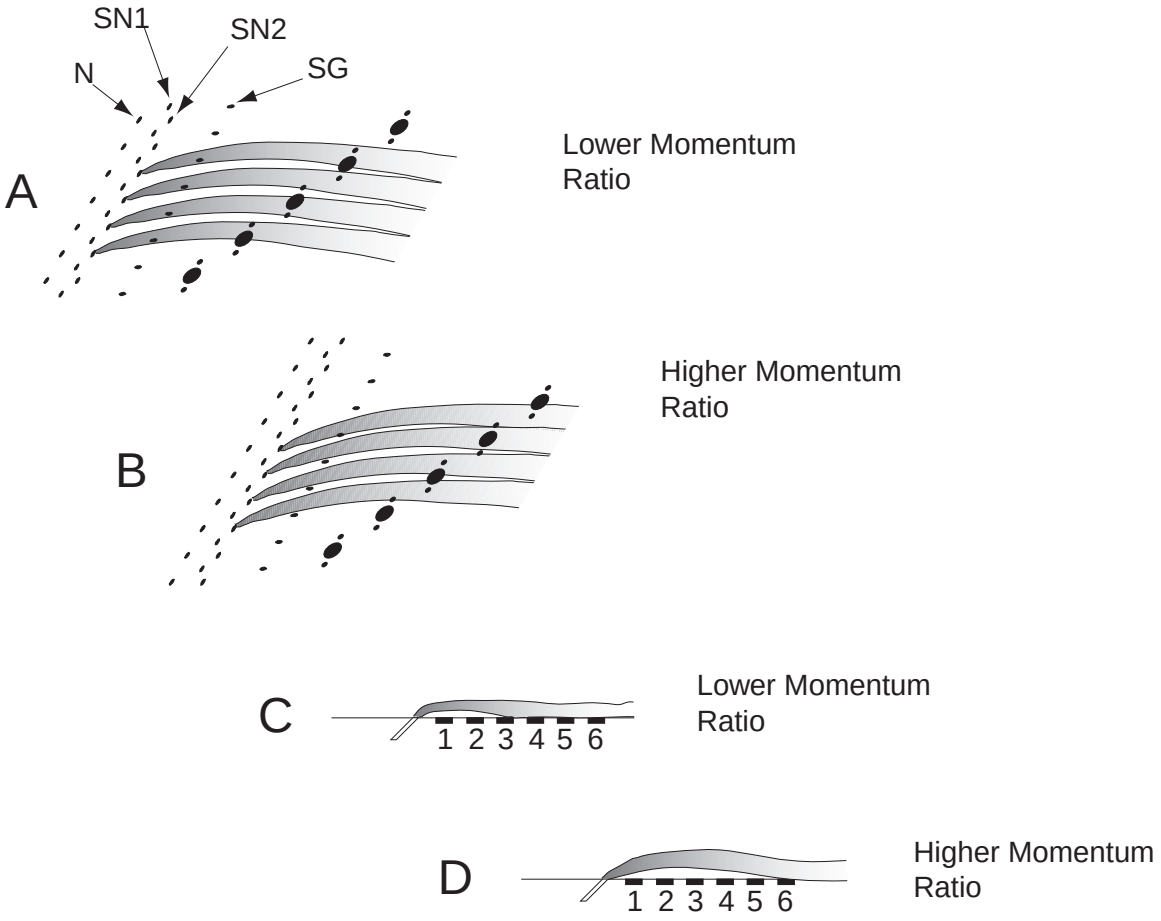

Figure 5.1: Possible Three-Dimensional Coolant Flow Fields

affect the angle SN2 or SN1 holes. In effect, the coolant film might move spanwise on the blade surface resulting in more or less film coverage depending on gauge location. Pictures C and D show a cross-section view of how the SG coolant might behave with

changes in momentum ratio. The increase in momentum ratio might lift the coolant film off the first gauge locations allowing the hot freestream gases to be exposed to the blade surface. The shadowgraph visualizations discussed in Sec. 4.1 tend to indicate that the dynamics in pictures C and D are not present. These Schlieren photographs, however, give only a streamwise averaged picture of the flow.

Perhaps more important than the supposition of reasonable flow dynamics, is the realization that the coolant flow is not one-dimensional or even two-dimensional. The flow in this area is very three-dimensional and very complicated. In order to really understand how it behaves, additional measurement techniques need to be used (liquid crystals, LDV's, a tighter spacing of gauges, etc.).

The sort of scenarios described above are possible if the coolant film is not well mixed over the gauge area. In continuing research it would be advisable to increase the number of coolant holes either by increasing the number of holes or decreasing the s/D spacing. This might provide a more evenly mixed film layer that would be better for study.

Another area of future study is an investigation of freestream turbulence. As suggested in Sec. 1.2.3, freestream turbulence has an effect of film cooling effectiveness and heat transfer coefficient. The turbulence levels for these tests are also much lower than is seen in a real engine environment. An expansion of this research to higher turbulence levels would certainly be an interesting endeavor.

A last area of recommended research would to be to investigate similar effects on the pressure side of the blade. Past research (Ito [13] for example) has shown the pressure side of turbine blades to be much more sensitive to film lift-off.

Bibliography

[1] R. S. Abhari and A. H. Epstein. An experimental study of film cooling in a rotating transonic turbine. *ASME Journal of Turbomachinery*, 116, 1994.

[2] N. Abuaf and R. Bunker. Heat tansfer and film cooling effectiveness in a linear airfoil cascade. *ASME Journal of Turbomachinery*, 119, 1997.

[3] M.S. Chandraeskhara, M.C. Wilder, and L.W. Carr. Boundary layer tripping studies of compressible dynamic stall flow. In *AIAA 25th Fluid Dynamics Conference*, number 94-2340, 1994.

[4] T. E. Diller. *Advances in Heat Flux Measurements*, volume 23. Academic Press, Inc, 1993.

[5] V. Ekkac, Srinath, Hui Du, and Je-Chin Han. Local heat transfer coefficent and film effecitveness distributions on a cylindrical leading edge model using a transient liquid crystal image method. Presented at the ASME International Mechanical Engineering Congress and Exposition, 1995.

[6] N. W. Foster and D. Lampard. Effects of density and velocity ratio on descrete hole film cooling. *AIAA Journal*, 13, 1975.

[7] R. J. Goldstein. Film cooling. In *Advances in Heat Transfer*. Academic Press, Inc, 1971.

[8] R. J. Goldstein, E. R. G. Eckert, V. L. Ericksen, and J. W. Ramsey. Film cooling following injection through inclined circular tubes. *Israel Journal of Technology*, 8, 1970.

[9] Hank Grabowski. An optical study of a film cooled turbine blade. Master's thesis, Virginia Polytechnic Institute and State University, 1999.

[10] S. M. Guo, T. V. Jones, and G. D. Lock. Gas turbine heat transfer measurements with engine simulated film cooling. In *2nd Annual European Conference on Turbomachinery Fluid Dynamics and ThermoDynamics*, 1996.

[11] David Holmberg. *Frequency Domain Analysis of Surface Heat Transfer/Free-Stream Turbulence Interations in a Transonic Turbine Cascade.* PhD thesis, Virginia Polytechnic Institute and State University, 1996.

[12] Forrest M. Mimms III. *Engineer's Mini-Notebook.* Siliconepts, second edition, 1994.

[13] S. Ito, R. J. Goldstein, and E. R. G. Eckert. Film cooling of a gas turbine blade. *The ASME Journal for Engineering Power*, 100, 1978.

[14] Venkit Iyer. Computer program bl2d for solving two-dimensional and axisymmetric boundary layers. Contractor Report CR-4668, National Aeronautics and Space Administration, 1995.

[15] Walter G. Jung. *IC Op-Amp Cookbook.* SAMS, third edition, 1986.

[16] P. M. Ligrani, S. Ciriello, and D. T. Bishop. Heat transfer, adiabatic effectiveness, and injectant ditributions downstream of a single row and two staggered rows of compound angle film-cooling holes. *ASME Journal of Turbomachinery*, 114, 1992.

[17] R. F. Meyer. A note on a technique of surface flow visualisation. Aeronautical Report LR-457, Canada National Research Council, 1966.

[18] R. J. Moffat. Describing uncertainties in experimental results. In *Experimental Thermal and Fluid Science*. Elsevier Science Publishing Co., Inc., 1988.

[19] Hume Peabody. Evaluation of a heat flux microsensor in a transonic turbine cascade. Master's thesis, Virginia Polytechnic Institute and State University, 1997.

[20] Oliver Popp. *Steady and Unsteady Heat Transfer in a Film Cooled Transonic Turbine Cascade*. PhD thesis, Virginia Polytechnic Institute and State University, 1999.

[21] S. G. Schwarz, R. J. Goldstein, and E. R. G. Eckert. The influence of curvature on film cooled performance. *The ASME Journal of Turbomachinery*, 113, 1990.

[22] Dwight Smith. Evaluation of heat transfer coefficient and film cooling effectiveness in a transonic turbine cascade. Master's thesis, Virginia Polytechnic Institute and State University, 1999.

[23] Dwight Smith et al. A comparison of radiation versus convection calibration of thin-film heat flux gauges. In *The ASME Ad-Hoc Committee on Heat Flux Measurement*, 1999.

[24] Angela Wesner. *An Interferometric Study of Unsteady Passing Shock Flow in a Turbine Cascade*. PhD thesis, Virginia Polytechnic Institute and State University, 1996.

Appendix A

Author's Published Research

A.1 Steady and Unsteady Heat Transfer in a Transonic Film Cooled Turbine Cascade

Presented at the 44th ASME Gas Turbine and Aeroengine Technical Congress, Exposition and Users Symposium as Paper Number ASME 99-GT-259.

STEADY AND UNSTEADY HEAT TRANSFER IN A TRANSONIC FILM COOLED TURBINE CASCADE

O. Popp, D. E. Smith, J. V. Bubb, H. C. Grabowski III, T.E. Diller, J. A. Schetz, Wing-Fai Ng
Virginia Polytechnic Institute and State University
Blacksburg, VA 24061

ABSTRACT

This paper reports on an investigation of the heat transfer on the suction side of a transonic film cooled turbine rotor blade in a linear cascade. Heat transfer coefficient and film effectiveness are first determined for steady conditions. The unsteady effects of a passing shock on the heat transfer are then investigated. The film cooling pattern used is a showerhead design with three rows on the suction side, one row at the stagnation point and two rows on the pressure side. The experiments were performed at engine representative temperature and pressure ratios using air as coolant. Heat transfer measurements are obtained using a Heat Flux Microsensor, and surface temperature is monitored with a surface thermocouple. Static pressure is monitored with a Kulite pressure transducer. The shock emerging from the trailing edge of the NGV and impinging on the rotor blades is modeled by passing a shock wave along the leading edges of the cascade blades. The steady-state heat transfer coefficient is 8% higher with film cooling than without film cooling. Shock heating of the freestream flow is determined to be the major contribution to the unsteady variation of heat flux, leading to an increase of about 30°C to 35°C in recovery temperature and adiabatic wall temperature.

NOMENCLATURE

Symbols

B	blowing ratio $(\rho u)_c/(\rho u)_f$
d	cooling hole diameter (1 mm)
c_p	specific heat of air, 1005 J/(kg K) in Eq.(3)
h	heat transfer coefficient w/o film cooling
h_c	heat transfer coefficient w/ film cooling
I	momentum ratio $(\rho u^2)_c/(\rho u^2)_f$
M	density ratio ρ_c/ρ_f
p	static pressure
Pr	Prandtl Number (0.71 in Eq.(9))
q	heat flux per unit area
q'_{max}	peak value of the unsteady component of heat flux
q_ε	bias in heat flux measurement (Eq.(8))
r	recovery factor in Eq.(3) and Eq.(6)
T_{aw}	local adiabatic wall temperature
T_c	coolant exit temperature
T_d	T_t-T_r Eq.(3)
T_d^*	real value of measured T_d
T_p	coolant temperature in the cooling plenum
T_r	local recovery temperature
T_t	freestream total temperature
T_w	local wall or blade temperature
T_ε	bias in temperature measurement (T_r-T_w) (Eq.(5))
u	local freestream velocity in Eq.(3)
η	film effectiveness defined in Eq.(7)

Superscripts

´	unsteady variation

Subscripts

c	coolant or w/ film cooling
f	freestream

INTRODUCTION

The efficiency of a gas turbine engine increases with turbine inlet temperature. In the ongoing effort to raise the turbine inlet temperature the gas stream temperature is made to greatly exceed the operating temperatures of blade materials, requiring elaborate blade cooling techniques to be developed. One of these methods is to spread a thin layer of cold air between the hot gas and the surface to be protected, referred to as film cooling. The quest for higher thrust to weight ratios in the development of aero-engines has led to the design of nozzle guide vanes (NGV) with supersonic exit velocities. The rotor blades consequently are not only subject to wake but also shock impingement as they pass behind the NGV's at very high speed. The effect of this unsteady process on the heat transfer to the rotor blade has been the topic of a variety of research programs.

The vast majority of results have been presented by the research team led by Schultz and Jones at the University of Oxford. Johnson et

al. (1990) investigated the unsteady heat flux on rotor blades in a linear cascade simulating the wake and shock with a rotating bar mechanism upstream of the cascade. They found a turbulent spot forming on the leading edge produced after the collapse of the shock induced separation. Travelling along the suction side, this turbulent spot increases the heat transfer. Boundary layer transition due to wake impingement was observed to further enhance unsteady heat flux. Moss et al. (1997) performed tests in a rotating annular cascade indicating that the unsteady disturbances caused by the NGV's have little influence on the heat transfer coefficient and the time averaged heat flux. They indicate that the unsteady heat flux is caused mostly by the time variation in relative total temperature. The mean heat transfer level therefore is not strongly affected by the presence of the NGV's. None of these experiments involved rotor blade film cooling. Film cooling experiments have been done on the same blade geometry (Horton et al. 1985) but did not include unsteady effects.

Hilditch et al. (1995) performed time resolved heat transfer measurements on an axial turbine rotor and compared his results with data from the University of Oxford and MIT. The rotor blades were not cooled and no analysis was done to discriminate shock and wake effects.

Similarly, Abhari and Epstein (1992) measured unsteady heat flux on a film cooled rotor in a rotating transonic turbine stage. They observed large fluctuations of heat transfer over a blade passing period but did not distinguish between the effects of shocks and wakes.

Heidmann et al. (1997) experimentally and numerically investigated the effect of wake passing on the time-averaged heat flux in a film cooled annular cascade, modeling the wake using a rotating bar mechanism.

Hale et al. (1997) modeled the effect of wake passing in a quasi-steady way using a stationary strut. Increases in heat transfer coefficient were measured for a number of locations on the blade, particularly on the pressure side.

Nix et al. (1997) analyzed in detail the progression of a shock through the same cascade and its effect on the unsteady heat transfer. When averaged over a 200µs blade passing event, a maximum increase of heat flux of 60% was measured due to shock passing.

The intent in the present study is to measure and interpret the unsteady heat transfer due to an isolated shock, as opposed to a combination of wake and shock. The focus of the research has been extended to film cooled blades.

EXPERIMENTAL APPARATUS

Wind Tunnel Facility, Cascade and Shock Apparatus

The experiments necessary for this investigation were performed in the transonic blowdown wind tunnel at Virginia Tech. A passive heating device is available to achieve high (120°C) inlet temperatures to the cascade. It consists of many copper tubes that are preheated prior to running the tunnel. Fig. 1 shows the wind tunnel with the heating loop. With the present cascade, the facility allows run times of up to 35 seconds with the inlet pressure controlled. The test-section and cascade built for this investigation are shown in Fig. 2. The cascade consists of four full and two half blades forming five passages (see Fig. 2). The blade design is a generic, high-turning, first stage rotor geometry. It is scaled up three times to accommodate the cooling scheme and instrumentation. The span is 15.3 cm (6") and the aerodynamic chord is 13.6 cm (5.4"). Pitch and axial chord are 11.4 cm (4.5"). The Reynolds Number based on aerodynamic chord and exit conditions is about $6 \cdot 10^6$. The Mach Number distribution was shown to correspond to design conditions. To simulate the shock emerging from the trailing edge of a NGV, a shock tube creates a shock wave which is sent along the leading edges of the cascade (see Fig. 2). The shock strength can be varied to obtain realistic pressure ratios. For the present investigation a shock strength of 1.08 (ratio of local static pressure behind shock and local static pressure before shock impact) was chosen. Accordingly, the shock Mach number is about 1.03 relative to the freestream flow.

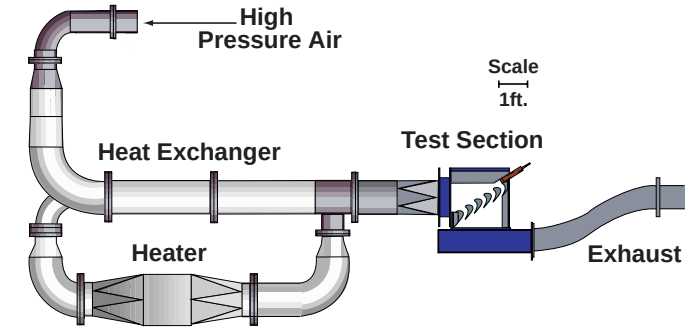

Figure 1: Wind Tunnel Facility

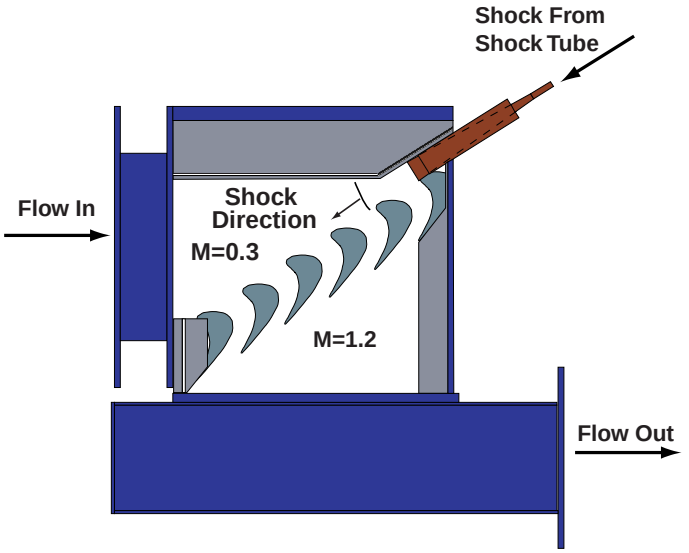

Figure 2: Cascade and Shock Apparatus

Cooling Pattern

A schematic of the showerhead film cooling design is shown in Fig. 3. All coolant holes are cylindrical and straight. The pressure and suction side gill holes form angles with the local chordwise tangent of 45° and 30°, respectively, and have no inclination in the radial direction. All other rows of holes are normal to the local chordwise tangent but angled 60° in the radial direction. Each row consists of 14 holes with a diameter of 1.04 mm (0.041") and a spacing of 9.14 mm (0.360"). The rows are staggered half the spacing with respect to the neighboring rows, yielding an overall pitch/diameter ratio of 4.39. Length/diameter ratios vary from 11.5 for the suction side gills to 4.4 for the suction side nose #2 row. Only the suction side gills and the suction side rows #1 and #2 actually affect the suction side heat transfer. The coolant ejected through the stagnation point row actually flows along the pressure side as observed from shadowgraph pictures. That means that in spite of pressure measurements locating the stagnation point right at the stagnation point row exit, it must be shifted towards the suction side.

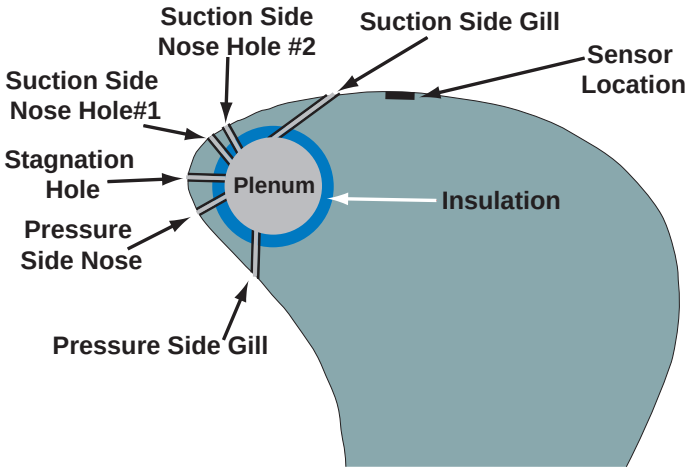

Figure 3: Blade Cooling Scheme

The nominal ratio of coolant to freestream total pressure for these experiments is 1.04. Therefore, the Momentum Ratio for each row of holes is kept constant while Density Ratio and Blowing Ratio vary with coolant temperature as shown later in section 'Steady-State Data Analysis and Results, With Film Cooling'. The temperature ratio T_t/T_c decreases from about 1.9 early in the experiment to about 1.5 late in the run. Homogeneous blowing through the cooling holes was checked by traversing a total and static pressure probe along the centerline of the cooling plenum. The resulting linear velocity distribution indicated uniform blowing. Coolant exit temperatures are measured with very small exposed junction thermocouples protruding into the exit of the last set of cooling holes. Conduction errors in those measurements were investigated experimentally. It was determined that these errors were negligible for the application in the blade. For the experiments without film cooling the plenum is fully plugged with a tightly fitting Nylon rod. The coolant supply is shown in Fig. 4. The two stage reciprocating compressor provides pressurized air at 12 bar (160 psig) to the storage tank. The dryer lowers the humidity to below three percent relative humidity.

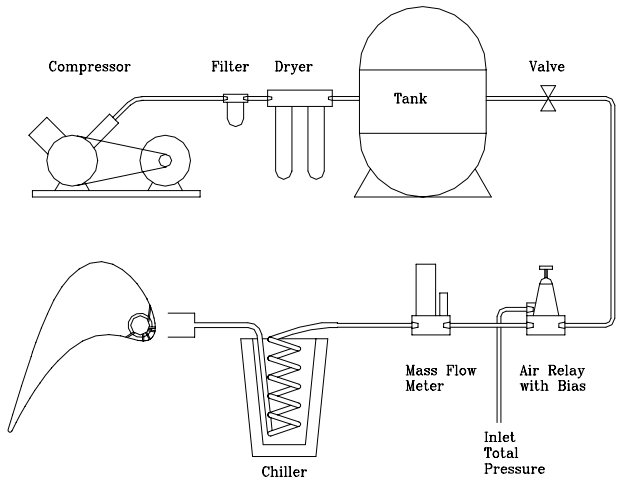

Figure 4: Coolant Supply

In order to control the difference between coolant and freestream total pressure, an air relay is used with the freestream total pressure as the signal and an adjustable bias. The chiller is a copper tube heat exchanger immersed in liquid nitrogen. It provides coolant temperatures down to –100°C in the plenum.

Sensors

The measurement location in this investigation is indicated in Fig. 5. Three different sensors are placed staggered in the spanwise direction. A surface thermocouple monitors the local blade temperature. It was designed to have thermal properties similar to the surrounding blade material (aluminum), and it is press fit to provide good thermal contact. The surface static pressure is measured with a Kulite pressure transducer, so that pressure variations due to the shock passing can be captured. Heat flux is measured using a heat flux microsensor. This sensor is described in detail in Diller (1993).

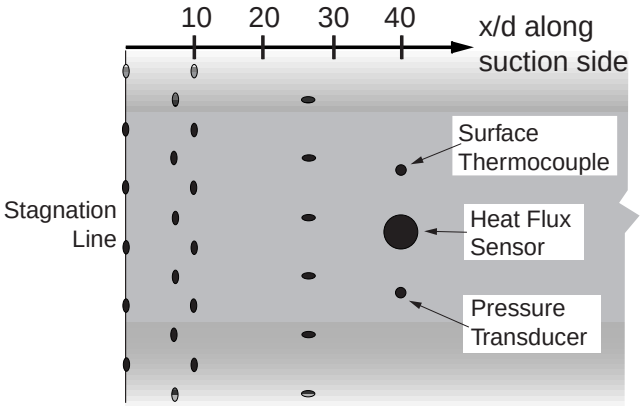

Figure 5: Plan View of a Section of the Suction Side Showing Sensor Locations and Coolant Exits

It behaves similar to a first-order system with a time constant of about 6µs. Therefore, it is capable of tracing rapid changes like a shock passing with sufficient accuracy. The substrate material of the sensor is aluminum nitride which has thermal properties similar to aluminum but is electrically insulating. Consequently, the temperature history of the gauge should closely follow the local blade temperature. The active diameter of the gage is 5.3 mm (0.21"). Accordingly the gauge extends from 10 to 15 cooling hole diameters downstream of the suction side gills. The relative size and location of the sensor are expected to provide a spatially averaged value of heat flux. For the steady-state investigation, all signals are sampled at 100 Hz and filtered at 50 Hz. Both pressure and heat flux signal are sampled at 1 MHz and filtered at 40 kHz for the unsteady investigation.

Optical Access

To monitor the state of the cooling film and to visualize the shock passing process, shadowgraph pictures were taken either using Polaroid film (steady-state) or a high speed digital camera (shock passing). The digital camera is capable of taking four successive pictures with a frequency of up to 1 MHz. The high speed capability is necessary to investigate in detail the effect of the passing shock.

STEADY-STATE DATA ANALYSIS AND RESULTS

Without Film Cooling

The general definition of the heat transfer coefficient used here is

$$q = h \cdot (T_{aw} - T_w) \tag{1}$$

With no cooling film present, the adiabatic wall temperature is the recovery temperature. Therefore

$$q = h \cdot (T_r - T_w) \tag{2}$$

The difference between the freestream total temperature and the recovery temperature is a function of the freestream velocity and the recovery factor

$$T_d = T_t - T_r = (1 - r) \cdot \frac{u^2}{2 \cdot c_p} \tag{3}$$

This difference T_d is a constant throughout the run. Therefore Eq. (2) can be written as

$$q = h \cdot (T_t - T_w) - h \cdot T_d \tag{4}$$

Eq. (4) is a linear equation with the independent variable $(T_t\text{-}T_w)$ and the dependent variable q. The slope is the heat transfer coefficient h, and T_d is the intercept at q=0 as illustrated in Fig. 6. The temperatures T_t, T_w, and the heat flux q vary during the experiment, since the passive heating device is cooling down as the freestream air is drawing heat from the copper tubes. The blade temperature is increasing during the tunnel run, so the overall temperature difference $(T_t\text{-}T_w)$ and the heat flux q decrease (see Fig. 7). Assuming that h is not a function of the temperatures involved, one can obtain the heat transfer coefficient and T_d by fitting Eq. (4) to the data. A typical graph illustrating this technique is shown in Fig. 6. The data shows linear behavior as expected. The difference between the freestream total and wall temperatures never actually reaches zero. It typically spans the range from 70°C down to 10°C. The intercept at q=0 is, therefore, an extrapolation which seems justified. The corresponding time history of heat transfer coefficient (h) and recovery temperature obtained using the calculated T_d is shown in Fig. 7 along with the total temperature (T_t), the blade temperature (T_w), and the heat flux (q) during a run.

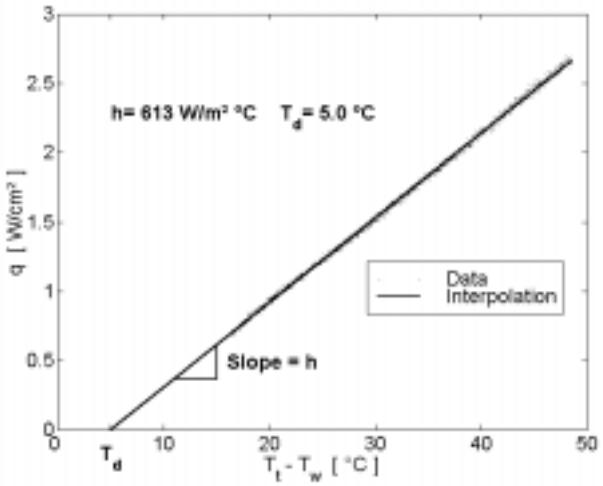

Figure 6: Interpolation for h and T_d (Uncooled Run #6)

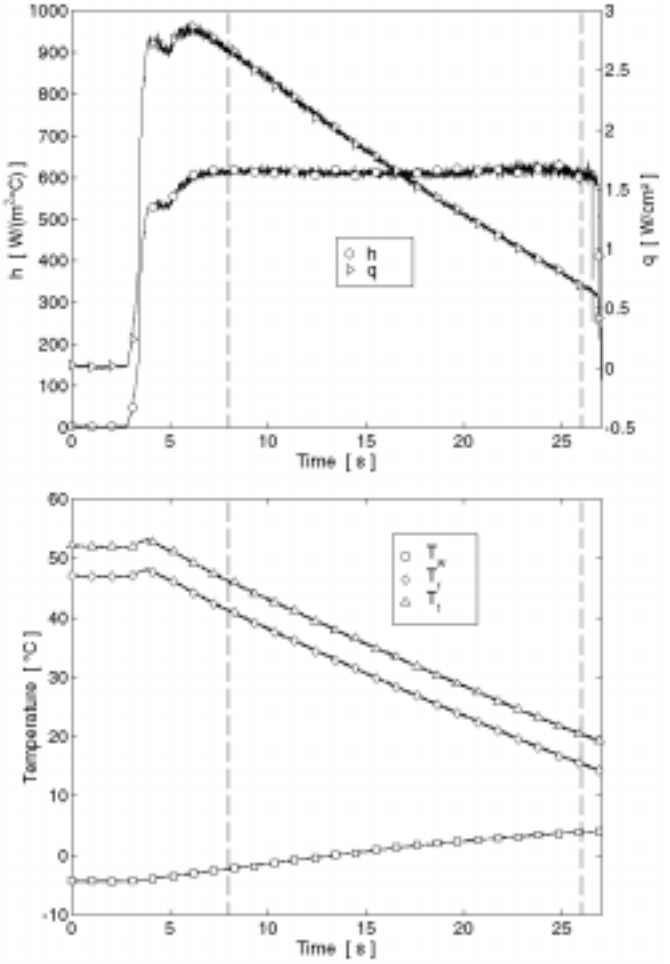

Figure 7: Time History of T_t, T_r, T_w, h, q (Uncooled Run #6)
(Dashed Lines Indicate Range of Useful Data)

An error analysis shows that bias errors in both the heat flux and the temperature measurement do not affect the resulting heat transfer coefficient. This is because an offset of the data in either the x or y-direction ($(T_r\text{-}T_w)$ and q respectively) does not change the slope of the curve. Accordingly, the experimental scatter for the heat transfer coefficient is small. T_d on the other hand is more severely affected by measurement uncertainty. A bias error in both temperature and heat flux measurement transfers directly into an error in recovery temperature

$$T_d = T_d^* - T_\varepsilon + \frac{q_\varepsilon}{h} \tag{5}$$

Therefore, the scatter is larger. The experimental results for several repeating runs are shown in Table 1. The difference between total and recovery temperature based on

$$r = \sqrt{Pr} \tag{6}$$

and the local Mach Number of 0.6 would yield a value of T_d of 4.2°C, assuming an average T_t. Shadowgraph and Schlieren pictures had

shown that the boundary layer at the blade location of interest is laminar. It needs to be stated that all the experimental results of T_d are higher than the ones based on isothermal flat plate calculations. The reason for this is either in the measurement accuracy (Eq.(5)) or in the steep pressure gradient.

Run #	1	2	3	4	5	6	7	8	9
h [W/m²°C]	635	620	639	654	664	613	625	623	637
T_d [°C]	6.9	8.6	7.0	7.7	8.8	5.0	6.9	7.3	4.7

Table 1: Run-to-Run Variation of h and T_d

With Film Cooling

To indicate the state of the cooling film, shadowgraphs and Schlieren pictures are taken both with Polaroid film and the high-speed digital camera. The shadowgraph in Fig. 8 shows that the film is attached to the surface showing turbulent structures. The pressure side is hidden by instrumentation outside of the cascade.

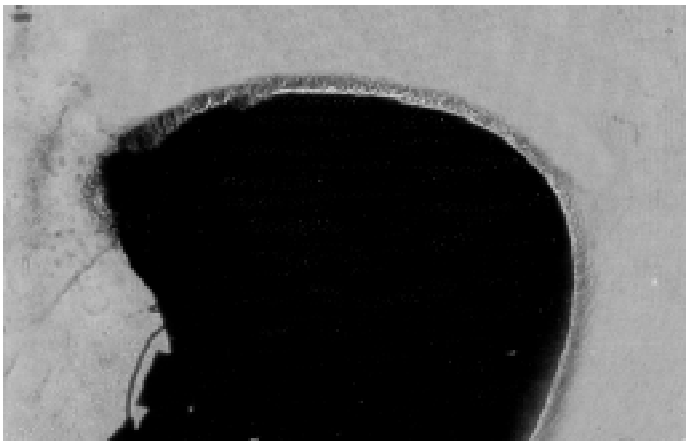

Figure 8: Shadowgraph Showing Attached Film

With film cooling, the adiabatic wall temperature is usually expressed in terms of the film effectiveness.

$$\eta = \frac{T_{aw} - T_r}{T_c - T_r} \quad \text{or} \quad T_{aw} = T_r - \eta \cdot (T_r - T_c) \tag{7}$$

Substituting Eq. (5) into Eq. (1) yields

$$q = h_c \cdot (T_r - T_w - \eta \cdot (T_r - T_c)) \tag{8}$$

Dividing by (T_r-T_c) yields

$$\frac{q}{T_r - T_c} = h_c \cdot \frac{T_r - T_w}{T_r - T_c} - h_c \cdot \eta \tag{9}$$

Since the temperatures and heat flux levels change considerably during the experiment, a wide range of values is obtained, as illustrated in Fig. 9. Assuming that h_c and η are not functions of temperatures, Eq. (9) is a linear relation between the fraction on the left hand side and the temperature ratio on the right hand side. The slope is the heat transfer coefficient, and the intercept at q=0 is the film effectiveness. The recovery temperature is calculated by subtracting the average T_d of 6.9°C from the freestream total temperature. The coolant temperature is determined using the mass flow averaged exit coolant temperatures from the three rows of cooling holes affecting the suction side. A representative example is shown in Fig. 9. Since the data follows the linear interpolation closely, it can be stated that the assumptions leading up to this interpretation of the data are correct. Specifically, the heat transfer coefficient and the film effectiveness do not vary significantly throughout the run.

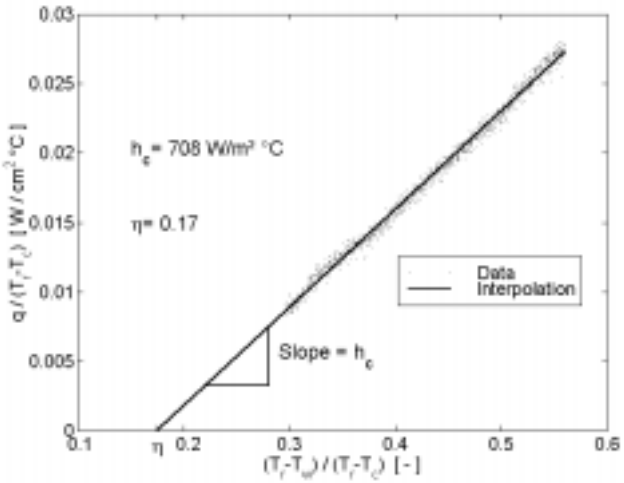

Figure 9: Interpolation for h_c and η (Run #5)

Fig. 10 a) shows the time history of the heat transfer coefficient calculated using the film effectiveness in Fig. 9. The heat transfer coefficient determined this way is very uniform throughout the time window used for the data analysis. In Fig. 10 b) all temperatures involved during this particular experiment are shown. T_{aw} is based on the film effectiveness determined in Fig. 9. It is evident that the coolant exit temperature is significantly higher than the coolant total temperature in the plenum indicating high heat transfer rates in the cooling holes. Fig. 10 c) gives the Density Ratio, Blowing Ratios and Momentum Ratios for all three cooling hole locations of interest. Since the Density Ratio is not a function of the local freestream Mach Number it is the same for all coolant exit locations. Since the total pressure ratio is kept relatively constant throughout the run, the Momentum Ratios are close to uniform. Even though the Momentum Ratios are repeatable, the coolant total temperature varies somewhat from run to run, since there was no physical control for this parameter. As shown in Fig. 10 b) the freestream total temperature changes with time. That causes the decrease of Density Ratio and Blowing Ratio shown in Fig. 10 c). All Ratios are based on isentropic flow through the holes. Realistically, it would be hard to analyze the flow through the cooling holes since not only frictional effects but also high heat transfer rates (see Fig. 10 b)) would have to be taken into account. Based on coolant mass flow measurements an average discharge coefficient of 0.66 for all cooling holes was determined.

The average heat transfer coefficient with film cooling (686 W/(m²°C)) is 8% higher than h without film cooling (634 W/(m²°C)). Using a thermal conductivity of 0.030 W/mK and the axial chord (0.114 m) to obtain the Nusselt number, yields values of 2410 and 2610 for the experiments without and with film cooling, respectively. The average film effectiveness of 15.3% appears to be rather low.

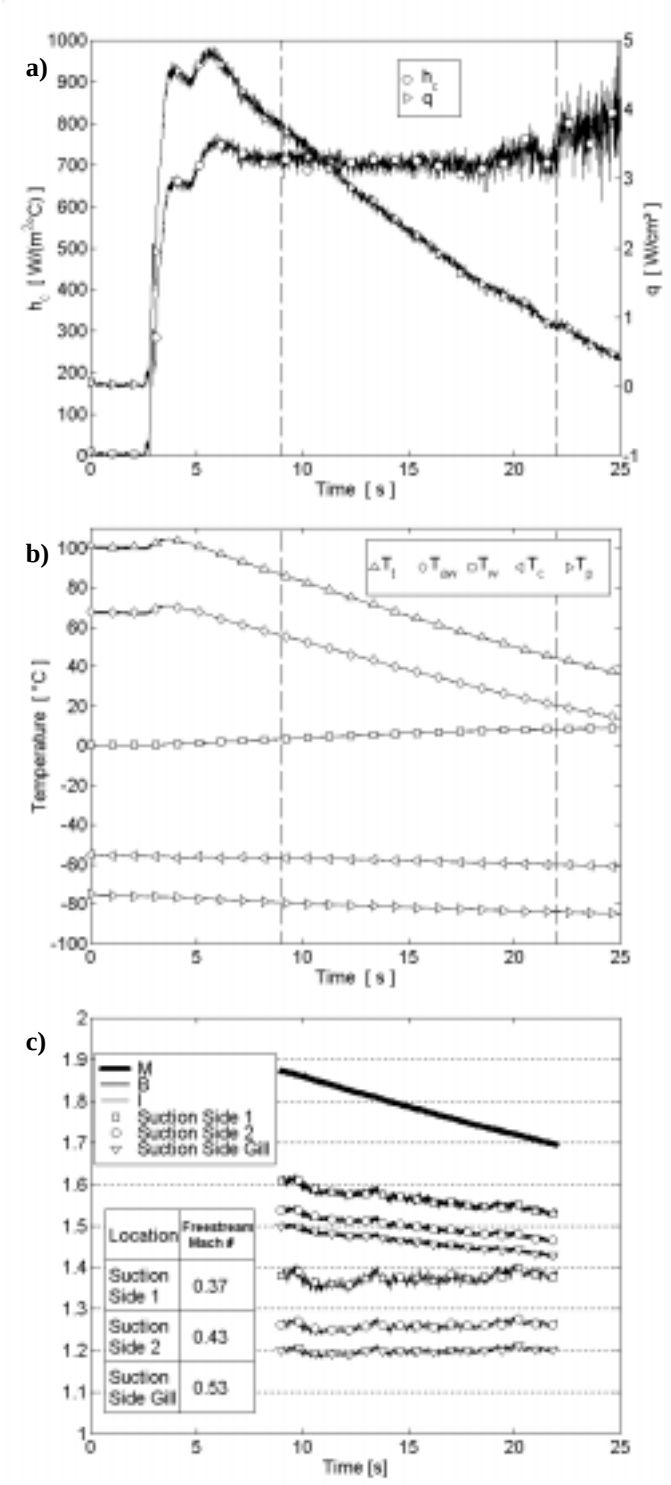

Figure 10: Time Histories from Cooled Run #5
a) Heat Transfer and Heat Transfer Coefficient
b) All Relevant Temperatures
c) Density Ratio, Blowing Ratio, Momentum Ratio
(Dashed Lines Indicate Range of Useful Data)

In low speed cascade tests with one closely spaced row of holes on the suction side of a large scale blade model, Ito et al. (1978) found comparably low values for film effectiveness for similar Momentum Ratios and gauge locations. Values between about 4% and 17% are found for gauge locations between x/D=10 and x/D=15 and Momentum Ratios between 1.0 and 2.3.

An error analysis for the method presented shows that the heat transfer coefficient is sensitive to bias errors in temperature and heat transfer measurement. Therefore, a larger scatter in the experimental results can be expected. The film effectiveness is also subject to higher scatter, as it is calculated from the intercept and the heat transfer coefficient. Results for heat transfer coefficient and film effectiveness are shown in Table 2. If the theoretical value for T_d (4.2°C) was used instead of the experimental value (6.9°C) the results for h_c and η would be a few percent higher.

Run #	11	12	13	14	15	16	17	18
h_c [W/m^2°C]	709	623	672	715	708	704	685	675
η [%]	16.6	12.0	17.0	16.6	16.8	14.6	15.1	13.5

Table 2: Run-to-Run Variation of h_c and η

SHOCK PASSING DATA ANALYSIS AND RESULTS

Shock Passing without Film cooling

For the analysis of the passing shock event Eq. (2) will be rewritten in such a way that all properties that are a function of time will be broken down into a mean value before shock impact (no superscript) and a time varying component (superscript ´). The unsteady heat flux during the event of a passing shock can then be expressed in terms of mean and fluctuating components:

$$q + q' = (h + h') \cdot (T_r + T_r' - T_w) \qquad (10)$$

The wall temperature does not change during the short duration of the shock passing. Expanding the right hand side of Eq. (10) yields:

$$q + q' = h \cdot (T_r - T_w) + h' \cdot (T_r - T_w) + h \cdot T_r' + h' \cdot T_r' \qquad (11)$$

Subtracting the mean heat flux on both sides yields the fluctuating component of heat transfer:

$$q' = h' \cdot (T_r - T_w) + h \cdot T_r' + h' \cdot T_r' \qquad (12)$$

The goal of this investigation is to determine the time variation of heat transfer coefficient (h´) and recovery temperature (T_r´) during the shock event which constitute the three components of unsteady heat transfer on the right hand side of Eq. (12). In Fig. 11, the traces of heat flux during a shock passing event are shown for different runs. The numbering corresponds to the run numbers in the steady state experiments (Table 1). The different levels of heat flux before the run are due to the fact that the shock is purposely initiated at different times during the run, i.e. at different temperature levels. Run #10 is not listed in Table 1 since the temperature differences were intentionally kept very small for this particular experiment. Therefore h and T_d could not be determined from this run. The time history of heat flux for times later than about 400 µs is of no interest since it is dominated by the interaction of shock reflections and later the contact surface emerging from the shock tube. These phenomena are not observed in the engine. Therefore, this investigation focuses on the impact of the first shock front primarily.

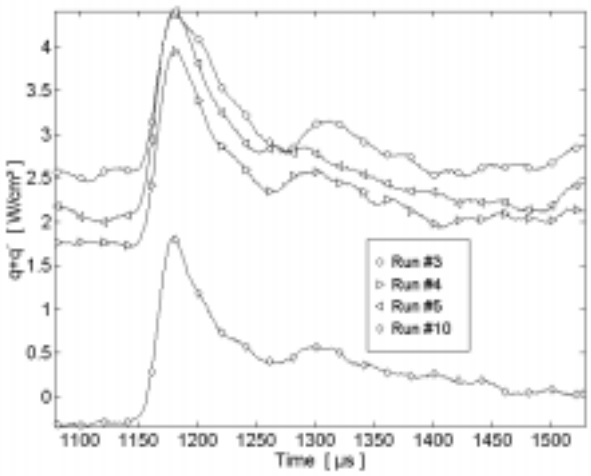

Figure 11: Heat Flux Traces from all Uncooled Experiments

In Fig. 12, the mean components of heat flux have been removed, leaving the traces of q´ indicated on the left y-axis. Apparently, all the fluctuating components of heat flux are similar.

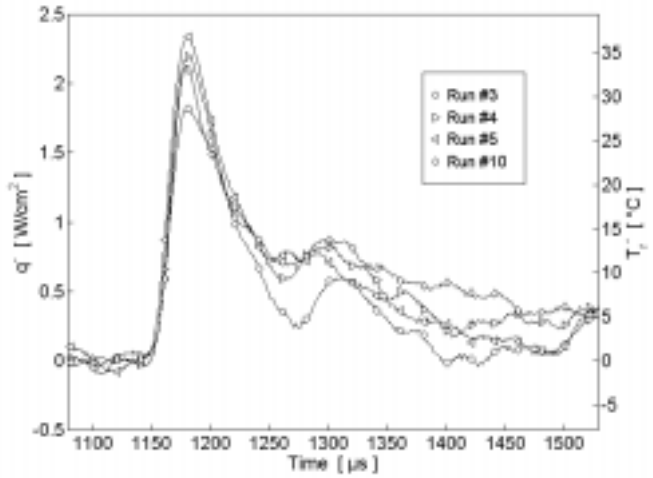

Figure 12: Unsteady Heat Flux and Recovery Temperature from all Uncooled Experiments

The first term on the right hand side of Eq. (12), $h' \cdot (T_r - T_w)$, indicates that the unsteady heat flux (q´) is a function of the overall temperature difference (T_r-T_w) if h´ is significant. If q´ is a function of (T_r-T_w), then the maximum or peak heat flux (q'_{max}) would also have to be a function of this temperature difference. In Fig. 13 the peak heat flux q'_{max} is plotted versus (T_r-T_w).

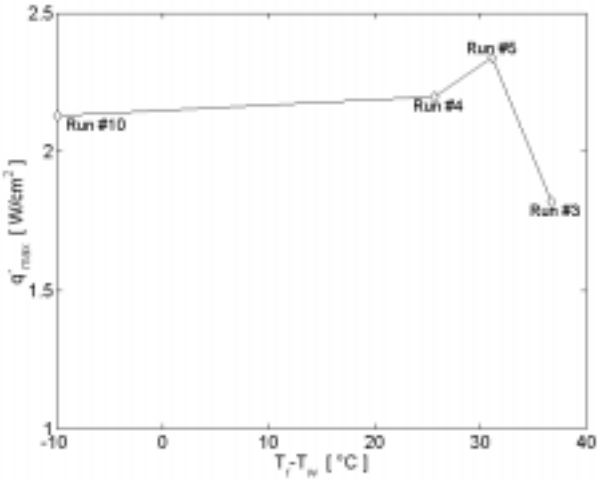

Figure 13: Peak Heat Flux vs. (T_r-T_w) from all Uncooled Experiments

There is no clear correlation between the two variables. Hence, q'_{max} does not strongly dependent on (T_r-T_w). This can only be the case if h´ is much smaller than h. Assuming h´ to be negligible and dropping all the terms containing h´ on the right hand side of Eq. (12), leaves an equation for the unsteady change of recovery temperature

$$T'_r = \frac{q'}{h} \tag{13}$$

Fig. 12 shows the time histories of this temperature variation indicated on the right y-axis. The heat transfer coefficient used here is the mean of the results of all the steady experiments. Since the scatter is relatively small, an average time variation of recovery temperature is used in the analysis of the experiments with film cooling.

Shock Passing with Film cooling

When film cooling is present, Eq. (12) still applies with the recovery temperature now replaced by the adiabatic wall temperature

$$q' = h'_c \cdot (T_{aw} - T_w) + h_c \cdot T'_{aw} + h'_c \cdot T'_{aw} \tag{14}$$

Analogous to the analysis for the uncooled case, it is the aim of this investigation to quantify the contribution of T'_{aw} and h'_c to the overall variation of heat flux. T'_{aw} can be expressed in terms of fluctuating components of recovery temperature (T'_r) and film effectiveness (η')

$$T'_{aw} = T'_r \cdot (1-\eta) - \eta' \cdot (T_r - T_c) - \eta' \cdot T'_r \tag{15}$$

A further question of interest is how much the change in recovery temperature and film effectiveness affect the variation of T_{aw}. The time variation of recovery temperature is one of the results of the uncooled unsteady investigation. It is the goal of this investigation to determine the contributions of T'_r, h'_c, and η' to the unsteady heat transfer. The coolant temperature is considered to be a constant.

Fig. 14 shows the pressure traces recorded by the blade mounted Kulite pressure transducer for representative experiments with and without film cooling. All the time histories of static pressure are very repeatable, asserting that the comparison of different runs is possible.

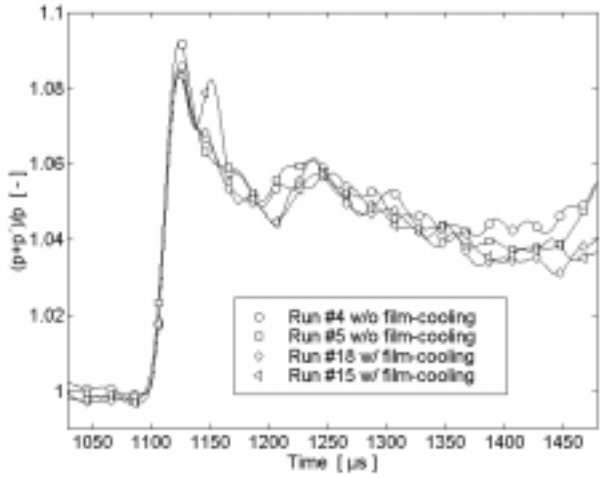

Figure 14: Pressure Traces from Representative Experiments with and without Film cooling

In Fig. 15, all the heat flux traces at shock impact are shown. Again, the differences in heat flux level are due to different temperature levels at the time of the shock release. Run #19 is not listed in Table 2. Intentionally, the temperature differences were kept very small and neither heat transfer coefficient nor film effectiveness could be determined from this experiment.

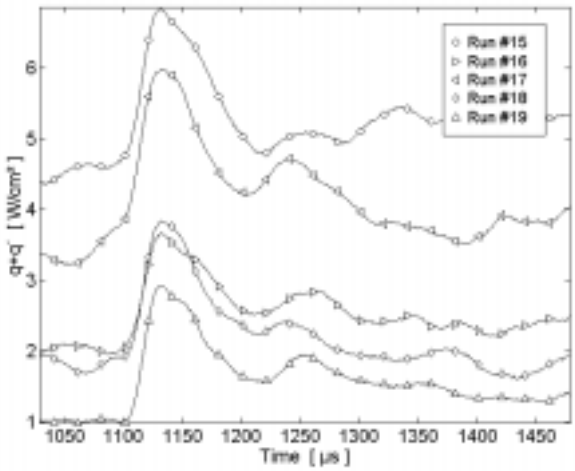

Figure 15: Heat Flux Traces from all Cooled Experiments

In Fig. 16, the same traces are shown after their mean values before shock impact have been removed. The traces of unsteady heat flux with and without film cooling (Figs. 16 and 12, respectively) are very similar in terms of magnitude and shape. Hence, the modes of heat transfer for both cases must be similar. The shock does not seem to influence the heat transfer coefficient or the mixing in the boundary layer (η) in any significant manner, otherwise these time histories would have to appear different for the cases with and without film cooling. Furthermore, pictures taken with the high-speed camera indicate that the cooling-film is not severely affected by the passing shock.

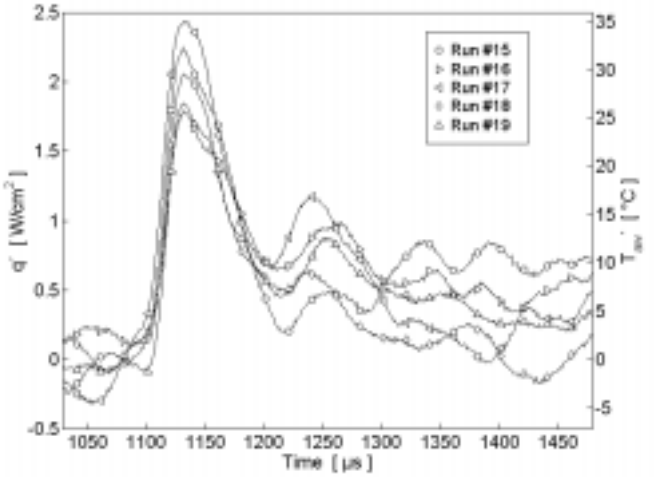

Figure 16: Variation of Heat Flux and Adiabatic Wall Temperature from all Cooled Experiments

The unsteady heat flux as expressed in Eq. (14) contains the term $h'_c \cdot (T_{aw}-T_w)$. It represents the first-order term of the contribution of h'_c to the unsteady heat flux. If h'_c is significant, the unsteady heat flux and the peak unsteady heat flux q'_{max} should correlate with $(T_{aw}-T_w)$. In Fig. 17 the peak heat flux is plotted against $(T_{aw}-T_w)$.

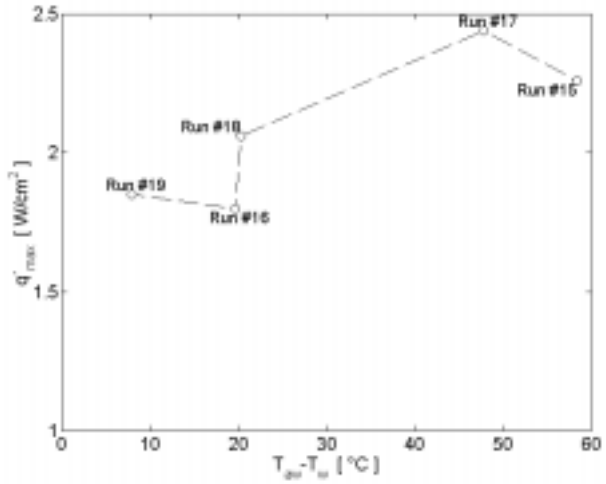

Figure 17: Peak Heat Flux vs. $(T_{aw}-T_w)$ from all Cooled Experiments

There is no strong dependency between q'_{max} and $(T_{aw}-T_w)$ evident. This can only be the case if h'_c is of minor significance. Neglecting all the terms containing h'_c in Eq. (14) yields a relation between the fluctuating components of T_{aw} and q

$$T'_{aw} = \frac{q'}{h_c} \tag{16}$$

The traces of adiabatic wall temperature calculated from Eq. (16) for all the runs are shown in Fig. 16 scaled on the right y-axis. The similarity of the fluctuations seems to allow for an ensemble averaging of the different runs, shown in Fig. 18. Eq. (15) contains an expression for the contribution of T'_r to the variation of the adiabatic wall temperature

$$T'_{aw} = T'_r \cdot (1-\eta) - \eta' \cdot (T_r - T_c) - \eta' \cdot T'_r \tag{15}$$

The averaged time variation of T_{aw} and the first term on the right side of Eq. (14) ($T_r' \cdot (1-\eta)$) are shown in Fig. 18. For the time variation of recovery temperature, the ensemble average from the uncooled tests are used. The film effectiveness used is the averaged result from the steady film cooled experiments.

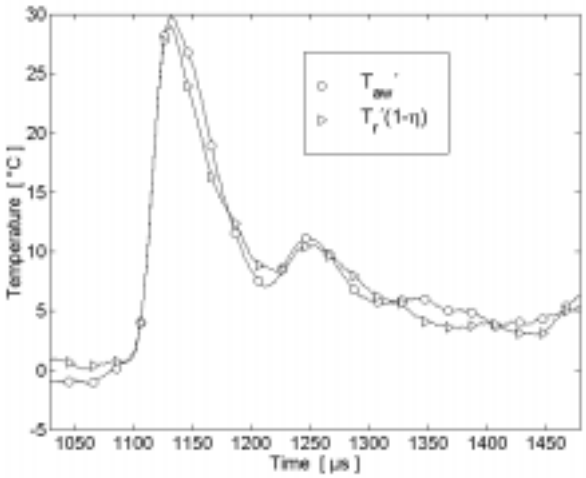

Figure 18: Variation of T_{aw} and the Contribution of T_r

The two traces are of very similar magnitude and shape. This suggests that the remaining terms on the right side of Eq. (14) ($\eta' \cdot (T_r - T_c)$ and $\eta' \cdot T_r'$) are small and consequently η' is small. It has to be concluded that the major contribution to the unsteady heat flux is the change of recovery temperature. The variations of h, h_c, and η have to be considered secondary effects. For the uncooled case this has been stated before by Moss et al. (1995). They performed on-rotor measurements of pressure and heat flux. Calculating the change of relative total temperature from the pressure measurement and assuming a constant heat transfer coefficient to calculate heat transfer, they found very good agreement between this calculation and the actual measurement. The present study suggests that this observation is also true for film cooled blades. Extrapolating to engine application, this implies that the time-averaged increase of heat transfer caused by passing shocks is small, since the relative total temperature is by definition varying around its mean value.

CONCLUSIONS

An experimental setup for the investigation of steady and unsteady heat transfer on film cooled transonic turbine blades was designed and built. For uncooled blades, one experiment in the transient facility was shown to be sufficient for the determination of heat transfer coefficient and recovery temperature. For film cooled blades, a method was presented to obtain heat transfer coefficient and film effectiveness from one experiment.

An analysis of the time resolved shock passing event with and without film cooling showed that the major contribution to the unsteady heat transfer is due to the fluctuation of recovery temperature caused by the shock. Heat transfer coefficient and film effectiveness were shown not to vary significantly during the interaction of the shock with the blade surface.

ACKNOWLEDGMENT

This work was supported by the Air Force Office of Scientific Research (AFOSR) under grant F08671-9601062, monitored by Dr. Jim M. McMichael and Dr. Mark Glauser. We would like to thank Messrs. Scott Hunter, Monty Shelton and Mark Pearson of General Electric Aircraft Engines for their collaboration on this project.

REFERENCES

Johnson, A.B., Oldfield, M.L.G., Rigby, M.J., Giles, M.B., 1990, "Nozzle Guide Vane Shock Propagation and Bifurcation in a Transonic Turbine Rotor", ASME 90-GT-310

Moss, R.W., Sheldrake, C.D., Ainsworth, R.W., Smith, A.D., Dancer, S.N., 1995, "Unsteady Pressure and Heat Transfer Measurements on a Rotating Blade Surface in a Transient Flow Facility", AGARD CP-571 pp. 22.1-22.9

Moss, R.W., Ainsworth, R.W., Garside, T., 1997, "Effects of Rotation on Blade Surface Heat Transfer: An Experimental Investigation", ASME 97-GT-188

Horton, F.G., Schultz, D.L., Forest A.E., 1985, "Heat Transfer Measurements With Film Cooling on a Turbine Blade Profile Cascade", ASME 85-GT-117

Hilditch, M.A., Smith, G.C., Anderson, S.J., Chana, K.S., Jones, T.V., Ainsworth, R.W., Oldfield, M.L.G., 1995, "Unsteady Measurements in an Axial Flow Turbine" AGARD CP-571 pp. 24.1-24.8

Abhari, R.S., Epstein, A.H., 1992, "An Experimental Study of Film Cooling in a Rotating Transonic Turbine", ASME 92-GT-201

Heidmann, J.D., Lucci, B.L., Reshotko, E., 1997, "An Experimental Study of the Effect of Wake Passing on Turbine Blade Film Cooling", ASME 97-GT-255

Hale, J.H., Diller, T.E., Ng, W.F., 1997, "Effects of Wake on Turbine Blade Heat Transfer in a Transonic Cascade", ASME 97-GT-130

Nix, A.C., Reid, T., Peabody, H., Ng, W.F., Diller, T.E., Schetz, J.A., 1997, "Effects of Shock Wave Passing on Turbine Blade Heat Transfer in a Transonic Cascade", AIAA-97-0160

Diller, T.E., 1993, "Advances in Heat Flux Measurement", Advances in Heat Transfer, Vol. 23, Ads, J.P., Hartnett et al., Academic Press, Boston, 1993, pp. 279-368

Ito, S., Goldstein, R.J., Eckert, E.R.G.,"Film Cooling on a Gas Turbine Blade", Journal of Engineering for Power, 1978, Vol. 100, pp. 476-481

A.2 Comparison of Radiation versus Convection Calibration of Thin-Film Heat Flux Gauges

Submitted to the ASME ad-hoc Committee on Heat Transfer

A COMPARISON OF RADIATION VERSUS CONVECTION CALIBRATION OF THIN-FILM HEAT FLUX GAUGES

D. E. Smith, J. V. Bubb, O. Popp, T.E. Diller
Virginia Polytechnic Institute and State University
Blacksburg, VA 24061

Stephen J. Hevey
Vatell Corporation
Christiansburg, VA 24073

ABSTRACT

A transient, in-situ method was examined for calibrating thin-film heat flux gauges using experimental data generated from both convection and radiation tests. Also, a comparison is made between this transient method and the standard radiation substitution calibration technique. Six Vatell Corporation HFM-7 type heat flux gauges were mounted on the surface of a 2-D, first-stage turbine rotor blade. These gauges were subjected to radiation from a heat lamp and in a separate experiment to a convective heat flux generated by flow in a transonic cascade wind tunnel. A second set of convective tests were performed using jets of cooled air impinging on the surface of the gauges. Direct measurements were simultaneously taken of both the time-resolved heat flux and surface temperature on the blade. The heat flux input was used to predict a surface temperature response using a one-dimensional, semi-infinite conduction model into a substrate with known thermal properties. The sensitivities of the gauges were determined by correlating the semi-infinite predicted temperature response to the measured temperature response. A finite-difference code was used to model the penetration of the heat flux into the substrate in order to estimate the time for which the semi-infinite assumption was valid. The results from these tests showed that the gauges accurately record both the convection and radiation modes of heat transfer. The radiation and convection tests yielded gauge sensitivities which agreed to within ±11%.

NOMENCLATURE

Symbols

C	specific heat of substrate (J/kg·°C)
HFM	heat flux microsensor (temperature and heat flux)
HFS	heat flux sensor
RTS	resistance temperature sensor
S_{conv}	convection tests gauge sensitivity ($\mu V/W/cm^2$)
S_{sub}	standard substitution gauge sensitivity ($\mu V/W/cm^2$)
$S_{rad,blade}$	radiation tests gauge sensitivity ($\mu V/W/cm^2$)
$S_{rad,bench}$	transient tests gauge sensitivity ($\mu V/W/cm^2$)
S_{jet}	impinging jet tests gauge sensitivity ($\mu V/W/cm^2$)
$S_{in\text{-}situ}$	in-situ tests gauge sensitivity ($\mu V/W/cm^2$)
T_{calc}	calculated temperature (°C)
T_{exp}	experimental temperature (°C)
k	thermal conductivity of substrate (W/m·°C)
q_{calc}	calculated heat flux (W/cm^2)
q_{exp}	experimental heat flux (W/cm^2)
t	time (s)
ε	emissivity of coating applied to gauges
ρ	density of the substrate (kg/m^3)
τ	time allowance for semi-infinite assumption (s)

INTRODUCTION

The accurate measurement of heat flux into a surface is very important to researchers concerned with thermal systems. For example, information about the steady and unsteady heat transfer into turbine blades is in high demand by the turbine industry and its thermal designers. However, the difficulties involved in measuring high-speed thermal phenomena limit the available information. Another area where heat flux measurements are necessary is in the determination of material properties. If the incident heat flux on a material and the corresponding temperature rise are known, the thermal properties of that material may be determined. These are only two of the many areas in which heat flux measurements are critical. The accurate measurement of heat flux is usually a challenge, however.

One difficulty is that the installation of a gauge on a surface will always result in a disturbance to the thermal system being investigated. This disturbance can be minimized if the thermal resistance of the gauge is similar to that of the material in which it is embedded, and if the area to thickness ratio of the gauge is large enough to promote one-dimensional conduction through the gauge. Another difficulty in measuring heat flux is the calibration of the gauges. Moffatt (1995) said that errors in the estimate of gauge sensitivities on the order of ±10% are reasonable due to the difficulties involved with calibration. Moreover, it is often difficult or impossible to calibrate a gauge once it has been mounted in an experimental setup.

One of the present methods for calibrating heat flux gauges consists of a substitution technique where a reference gauge is subjected to an incident radiation heat flux. The gauge to be calibrated is then put in its place and subjected to matched conditions and a calibration is made by comparison with the known gauge. In addition to the substitution calibration, a transient in-situ technique can be used with gauges which have a fast response time provided the temperature is known as well [Hager et al., 1994]. It has been shown (Baker and Diller, 1993) that the surface temperature time history can be calculated from the time history of the measured heat flux. This calculated temperature can then be compared with the transient measured surface temperature to calibrate the heat flux gauges.

For this study, six heat flux microsensor (HFM) thin-film gauges, produced by Vatell, Inc., were mounted on the surface of a first-stage turbine rotor blade made of aluminum. The gauges were used to measure, simultaneously, the local time-resolved heat flux and surface temperature. Because it is difficult to use the substitution technique on these gauges while they are in the blade, the transient calibration method was used. A different set of free-standing gauges were exposed to a radiative flux and the data was used to perform calibrations using both the substitution and the transient techniques. A comparison was then made between the two calibration methods for both convection and radiation.

INSTRUMENTATION

Heat Flux Microsensors

The HFM is composed of two separate sensors, a resistance temperature sensor (RTS) and a heat flux sensor (HFS). The HFS uses a passive differential thermopile made up of 280 thermocouple pairs to generate a voltage proportional to the incident heat flux. The active area of the HFM is 4mm in diameter, two microns thick, and is deposited on an aluminum-nitride substrate, an electrically insulating material with thermal properties close to those of the aluminum blade. The heat flux gauge has been shown to have a time response on the order of 10μs [Holmberg, 1995]. The small thickness-to-area ratio and the thermal properties of the substrate ensure that the thermal disruption caused by the gauge will be minimal.

Two different types of HFM's were used in this work: HFM-7's and HFM-6's. The difference between the two types is in the material which is used to form the thermocouple pairs. The HFM-6 gauge uses a Nichrome/Platinum thermocouple pair and has a lower sensitivity ($S \approx 30 \mu V/W/cm^2$) than the HFM-7 which uses a Nichrome/Constantan pair ($S \approx 150 \mu V/W/cm^2$). All of the gauges use the same material for the substrate, however. The six gauges mounted in the aluminum blade are all HFM-7's and will hereafter be referred to as gauges B1 through B6. Of the five gauges used in the substitution experiments, two are HFM-7's and three are HFM-6's. These gauges will hereafter be referred to as gauges G7/1, G7/2, and G6/1 through G6/3, respectively.

Blade Instrumentation

The six HFM gauges were all mounted on the suction side surface of a generic two-dimensional, high-turning, first-stage turbine rotor blade. The gauges were staggered along the chord of the blade as well as along its span. Each of the gauges was press-fitted flush with the surface of the blade. The curvature of the blade made using the substitution technique extremely difficult and the press-fit meant that the gauges could not be removed from the blade without a very high possibility of incurring damage to the gauges. Therefore, the transient technique was used in-situ to calibrate the six HFM's embedded in the blade.

SUBSTITUTION CALIBRATIONS OF UNMOUNTED GAUGES

The substitution calibration is widely used in research and industry for the calibration of heat flux gauges. Its use in the calibration of HFM's was documented by Hager et al. (1994). The known heat flux is applied to the gauge and the voltage output can be directly calibrated using equation (1).

$$S_{HFS} = \frac{V_{HFS}}{Q_{REF}} \tag{1}$$

The reference gauge, a circular-foil gauge, was calibrated by Vatell Corp. using a primary standard gauge which was calibrated by Nist. After calibration, the reference gauge has an expanded uncertainty (95% confidence level) quoted as ± 3%.

The substitution technique is a steady-state calibration which uses a reference heat flux gauge to measure the incident flux from a heat lamp and then substitutes an un-calibrated gauge for the known assuming the conditions are the same. An accurate calibration using the substitution method cannot be made with the six gauges that were already embedded in the blade. The curvature of the blade makes it difficult to position the heat lamp the same with respect to both the reference gauge and the embedded HFM. Small changes in the relative positions of the two gauges to the lamp can result in large calibration errors, since the incident heat flux differs with the exact orientation of the lamp. Therefore, five HFM gauges which had not been mounted in the blade were tested instead (G7/1-2 and G6/1-3). The sensitivities of three of these gauges (G6/1-3) was smaller due to the different materials used to make the thermocouple pairs for the HFS and RTS, but the accuracy of the sensitivity estimate was unaffected.

The reference gauge, a circular-foil heat flux gauge painted with a high emissivity coating (0.94), was exposed to a heat lamp to determine the amount of heat flux generated by the lamp. Typical heat flux levels were on the order of 14 W/cm^2. Both the lamp and the circular-foil gauge were mounted in a fixture that maintained their relative orientation and positioning. The five HFM gauges were also coated, mounted in the fixture, and then exposed to the heat lamp as is shown in Fig. 1. Six tests were performed on each gauge. The data generated by each HFM were recorded at 2000Hz. Sensitivities determined using data from this test will be referred to as S_{sub}. Because all gauges, including the reference gauge, were coated with the same paint, the value of the emissivity did not affect the calibrations.

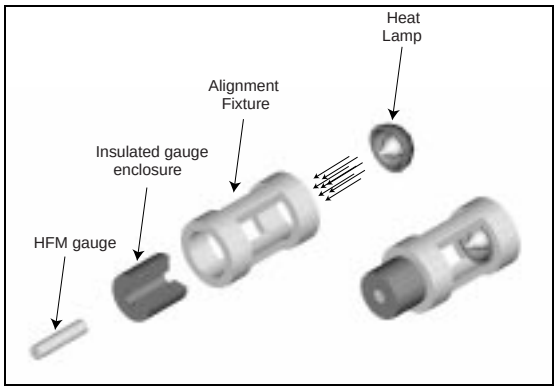

Figure 1: Radiation Tests for Substitution Method

TRANSIENT CALIBRATIONS

Mathematical Model

The transient method of calibrating heat flux gauges was used to analyze the data generated by all of the tests described earlier, including the substitution bench tests. The transient calibration makes use of the fact that for very short time periods, the surface heat flux can be easily calculated from the surface temperature if a one-dimensional, semi-infinite model is assumed [Diller, 1993]. The time period is usually a fraction of a second, and so time-resolved temperature measurements must be taken in order to use this method of calibration. The time response of the HFM gauge is on the order of 10μs, so it is capable of providing these time-resolved measurements for both the surface temperature and the heat flux simultaneously. Baker and Diller (1993) developed a method of determining surface temperature from heat flux using a Green's function approach. By assuming the substrate to be initially at a uniform temperature, T_o , and treating the series of heat flux data points, q_j , as impulses, the surface temperature time history can be reconstructed using equation (2),

$$T_{calc}(t_n) - T_o = \frac{2}{\sqrt{\pi}\sqrt{k\rho C}} \sum_{j=0}^{n-1} q_j \left[\sqrt{t_n - t_j} - \sqrt{t_n - t_{j+1}} \right] \qquad (2)$$

Equation (2) shows that the transient technique requires that the thermal properties of the substrate be known. An algorithm was written to determine the sensitivity of the HFS by minimizing the temperature difference between the measured and calculated temperature histories, T_{exp} - T_{calc}.

Validity of 1-D, Semi-infinite Assumption

The use of the transient method is dependent upon the validity of the one-dimensional, semi-infinite conduction model. Therefore, it is necessary to determine how long this assumption may be considered valid. The active area of the HFM gauge is a circle 4mm in diameter; the HFS (heat flux sensor) occupies the center of that area and the RTS (resistance temperature sensor) is laid down in a ring surrounding it. The HFS and the RTS are located close enough to each other that it might be assumed that they measure the same thermal phenomena. The two-dimensional heat transfer effects, however, are felt first at the edge of the sensor. Therefore, the difference of the temperature at this location from the one-dimensional model is the limiting case for the transient calibration technique. A two-dimensional finite difference conduction code was written to model the penetration of a step input of heat flux into the substrate. The code was used to determine the maximum time, τ, for which the one-dimensional, semi-infinite assumption was valid.

The parameters used in the code are shown in Fig. 2. The heat flux step input of 10^5 W/m^2 used is typical of the levels measured during heated runs in the transonic blowdown wind tunnel and of the heat lamp used in the radiation bench tests. The step input was applied to a circular area with a diameter approximately four times that of the HFM gauge. This area is the same size as that of the heat lamp, which is the limiting case in this study since the wind tunnel provides a flux over a larger area and two-dimensional heat transfer effects are felt much later in time. The code used cylindrical coordinates to accurately model the gauge, and the thermal properties shown in the figure were used for both the gauge and the surrounding material. The code was discretized in time as well as space; a mesh size of 0.4mm and a time step of 0.005s were chosen.

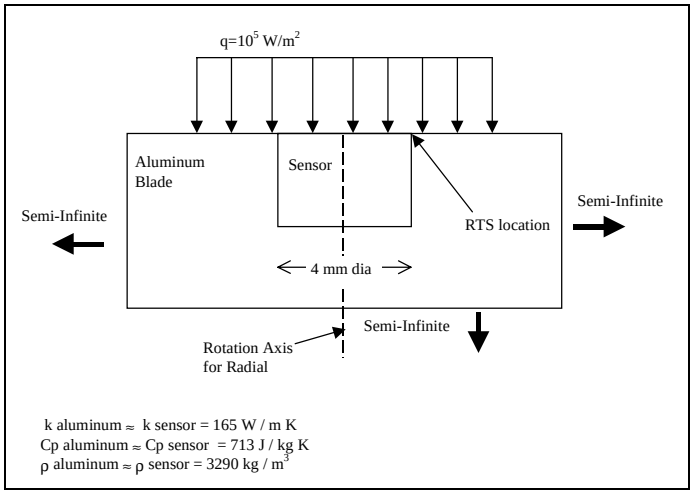

Figure 2: Finite Difference Model

The time history of the RTS surface temperature along with the solution of the one-dimensional, semi-infinite conduction model can be seen in Fig. 3. As time progresses, two-dimensional effects (radial heat transfer) are seen to become more important as the RTS temperature diverges from the one-dimensional model. A time, τ, was chosen such that the error in calculated heat flux from the one-dimensional, semi-infinite model was less than 5%. For the parameters shown in Fig. 2., τ was found to be 125ms.

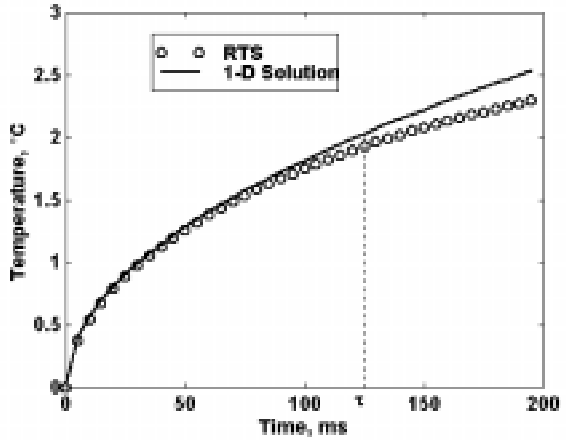

Figure 3: Determination of Time Allowance, τ

Experiments

In-situ Transonic Convection Tests

The mounted HFM's were used to investigate the convective heat transfer into a turbine blade, using the convection experiments performed in the transonic blowdown wind tunnel at Virginia Tech. A set of resistance heaters are used to preheat copper tubes located in the path of the main flow upstream of the test section. The tubes act as a passive heat exchanger and allow the flow to be heated to higher (120°C) temperatures before entering the cascade. Figure 4 shows the wind tunnel with the heating loop and the cascade test section. The cascade test section contains four full blades and two half blades, or five flow passages. Figure 5 shows the location of the instrumented blade in the cascade test section. The heated flow passing over the instrumented blade provides a large convective heat flux to the gauges. Six tunnel runs were made and the data generated by each gauge was recorded simultaneously. The HFM's were sampled at 100Hz and filtered using a low-pass, one-pole filter. The wind tunnel is capable of running for up to 35s with the inlet total pressure controlled, but only a very small fraction of the data recorded by the HFM's is needed for the transient calibration. An important point to note is that the transient calibration technique can be used to perform an in-situ calibration each time a tunnel experiment is performed. The calibration performed at the beginning of an experiment can then be compared to the manufacturer's calibration to determine if the gauge's calibration has drifted. Sensitivities determined using data from this test will be referred to as $S_{in\text{-}situ}$.

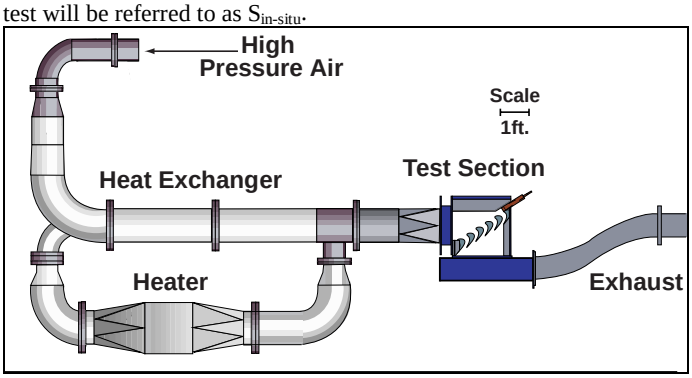

Figure 4: Wind Tunnel Facility

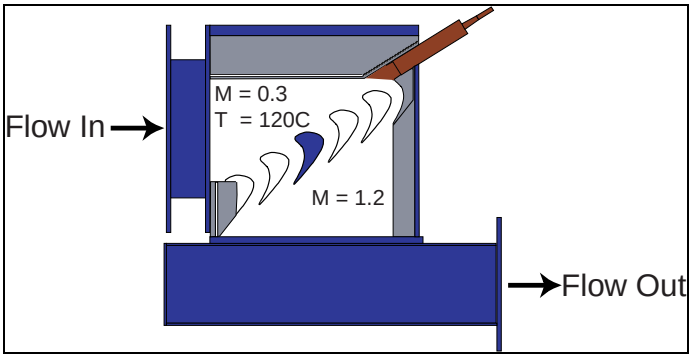

Figure 5: Cascade Test Section

Impinging Jet Bench Tests

In addition to the transonic convection experiments, which were performed in the blowdown wind tunnel, an impinging jet with cold (-100°C) air was used to provide a large negative incident heat flux to the gauges. These experiments required that the blade be taken out of the cascade test section. The jet was 0.5 inches in diameter and was mounted eight diameters from the blade as is shown in Fig 6. A large tank was loaded to 150 psi and used to supply pressurized air for the impinging jet. For the transient technique, the incident heat flux need not be known if it is assumed to be uniform, so it was not necessary to measure the velocity of the jets. For each test, a shutter placed between the gauge and the jet was manually removed to provide a quick increase in the level of heat flux. The response of the HFM to the jet was recorded at 1000Hz and filtered at 50Hz. Separate tests were performed for each gauge. Sensitivities determined using data from this test will be referred to as S_{jet}.

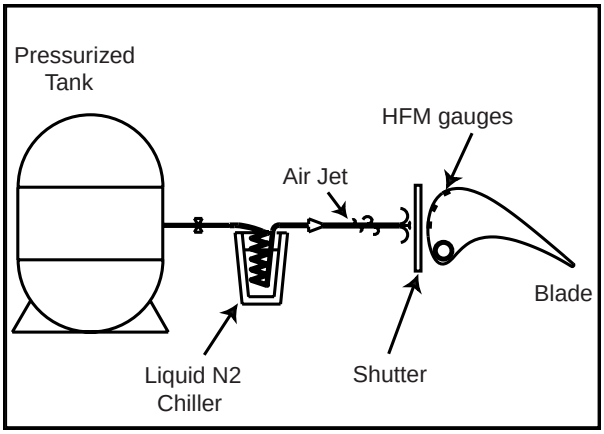

Figure 6: Jet Impingement on Blade

Radiation Bench Tests of Gauges in Blade

Another set of radiation bench tests was performed on the gauges in the instrumented blade after it had been removed from the cascade test section. All of the gauges were painted with a high emissivity coating ($\varepsilon = 0.94$), and a heat lamp was used to subject each gauge to an incident heat flux as shown in Fig. 7. The heat lamp was positioned directly over each gauge and the radiative heat flux was made to simulate a step input by using a manual shuttering mechanism; once the lamp had reached its full illumination, the shutter was quickly removed and the gauge was exposed to the incident flux. Again, it should be noted that when using the transient calibration, the incident heat flux does not need to be a known value. It is therefore not necessary to position the lamp in the exact same orientation over each gauge as was required with the substitution method. This test was performed once on each gauge and the data generated by each HFM was recorded at 2000Hz, unfiltered. Sensitivities determined using data from this test will be referred to as S_{rad}.

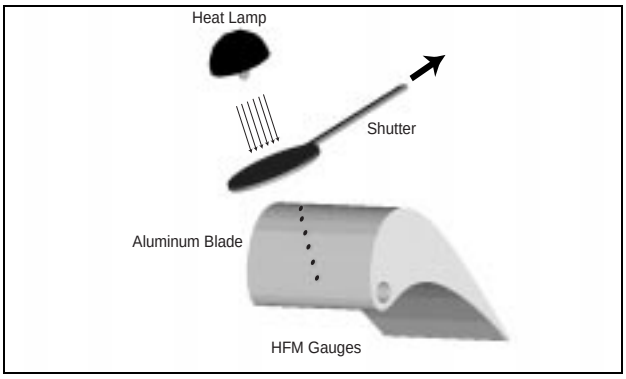

Figure 7: Transient Radiation Tests

Radiation Bench Tests of Unmounted Gauges

The data generated by applying radiative heat flux to the unmounted gauges as described earlier in the substitution experiments section can also be analyzed using the transient method. To do this, data was sampled at 2000Hz, unfiltered, in order to record the initial response of the HFM to the incident heat flux. Sensitivities determined using data from this test will be referred to as S_{trans}.

RESULTS

A comparison of the substitution calibration method with the transient method was done first to determine if the transient method is viable as a calibration technique. The data generated in the substitution experiments were analyzed using both the substitution technique and the transient technique. The material properties ($[k\cdot\rho\cdot C]^{1/2}$ = 19,670 in SI units) used in the transient technique are 10% higher than those shown in Fig. 2 due to a change in the aluminum nitride supplier. Six tests were performed for each gauge. The calibration results for both methods can be seen in Table 1. As mentioned earlier, gauges G6-1 through G6-3 are of a different HFM type and so the magnitude of their sensitivities are smaller than those of the other gauges. The difference in the magnitude of sensitivity between HFM-7's and HFM-6's is solely a function of the thermocouple materials used. The percentage difference between the substitution and the transient sensitivities were all less than 13%. Experimental uncertainty for each gauge was calculated by establishing a 90% confidence interval around the mean of the six tests performed using a student-t distribution.

Table 1: Results of Radiation Calibrations

Gauge Number	S_{sub} ($\mu V/W\cdot cm^2$)	S_{trans} ($\mu V/W\cdot cm^2$)
G6-1	18.01	17.91 ±1.3%
G6-2	15.33	16.58 ±7.3%
G6-3	25.50	28.72 ±5.1%
G7-1	108.6	111.33 ±9.7%
G7-2	189.05	191 ±9.2%

These results show that the transient calibration technique is in excellent agreement with the substitution technique used in most calibrations of heat flux gauges.

Since the transient method is a viable calibration method, the suitability of convection tests, as opposed to the radiation tests commonly used, was investigated. To do this, two different sets of convection tests were performed and compared to a radiation bench test. All three sets of tests were performed on the HFM's embedded in the blade. One set of tests was performed in the Virginia Tech transonic cascade wind tunnel. The blade was then removed from the test section and the two bench tests, convection using a cold impinging jet and radiation using a heat lamp, were performed. The data from all three sets of tests were analyzed according to the transient calibration outlined earlier. Figure 8 is a plot of the measured heat flux and surface temperature along with the calculated surface temperature for a sample radiation bench test. The calculated temperature history is a smooth curve underlying the noisier history of the measured surface temperature. The calculated temperature has less noise due to the integration process used to construct it (Baker and Diller, 1993). Figure 8 shows the strength of the transient calibration method; the time histories of the measured surface temperature and the calculated temperature are in excellent agreement, which they should be if an accurate calibration is done.

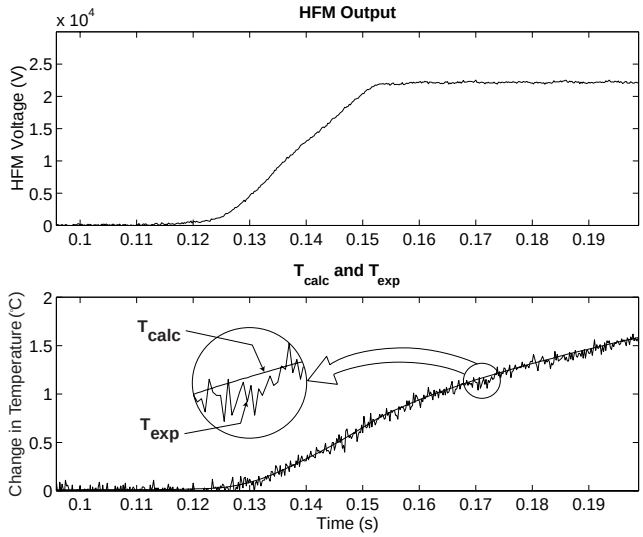

Figure 8: Results of Transient Calibration

The results of the calibrations performed on all three sets of tests can be seen in Table 2. The results for S_{rad}, $S_{in\text{-}situ}$, and S_{jet} are the mean values over all tests for each gauge. A comprehensive method of determining the uncertainty for both the transient radiation and convection calibration was sought. In order to remove the effects of the variations in mean sensitivities of the six gauges, the entire data set for each gauge (S_{rad}, $S_{in\text{-}situ}$, and S_{jet} [$\mu V/W\cdot cm^2$]) was divided by the common mean in order to obtain a percentage. This procedure was performed on all six gauges. A normal distribution was assumed, and the uncertainty in the transient calibration at the 95% level of confidence was found to be ± 11%.

Table 2: Results of Transient Calibration

Gauge	S_{rad}	$S_{in\text{-}situ}$	S_{jet}
B1	264	233	274
B2	114	105	102
B3	148	147	146
B4	150	129	152
B5	177	176	177
B6	155	153	143

CONCLUSIONS

Accurate calibrations are necessary in order to investigate the thermal phenomena reported by heat flux gauges. These calibrations are difficult to make and often impossible to repeat once the gauge has been installed in an experimental setup. A transient method of calibrating thin-film heat flux gauges with fast time responses has been shown to be a viable calibration technique. The strengths of the transient calibration technique are that it can be performed in-situ, the incident heat flux need not be known, and that gauge calibrations can be performed at the start of each run if an appropriate level of heat flux is present. It has been shown that the transient method is capable of using either radiation or convection as the mode of heat transfer.

ACKNOWLEDGMENT

This work was supported by the Air Force Office of Scientific Research (AFOSR) under grant F08671-9601062, monitored by Dr. Jim M. McMichael and Dr. Mark Glauser. We would like to thank Messrs. Scott Hunter, Monty Shelton and Mark Pearson of General Electric Aircraft Engines for their collaboration on this project.

REFERENCES

Baker, K.I., and Diller, T.E., 1993, "Unsteady Surface Heat Flux and Temperature Measurements." ASME 93-HT-33.

Diller, T.E., 1996, “Methods of Determining Heat Flux From Temperature Measurements”, ISA 0227-7576.

Hager, J.M., Terrell, J.P., Silverston, E., Diller, T.E., 1994, “In-Situ Calibration of a Heat Flux Microsensor Using Surface Temperature Measurements”, ISA 94-1034.

Holmberg, D.G., Diller, T.E., 1996, “High-Frequency Heat Flux Sensor Calibration and Modeling”, ASME *Journal of Fluids Engineering*, Vol. 117, pp. 659-664.

Johnson, L.P., Diller, T.E., 1995, “Measurements With a Heat Flux Microsensor Deposited on a Transonic Turbine Blade,” IEEE 95CH3482-7.

Moffat, R.J., and Danek, C., 1995, "Calibrating Heat Flux Gauges for Convection Applications", NIST/NSF Workshop on Heat Flux Transducer Calibration.

Schultz, D.L. and Jones, T.V., 1973, "Heat-Transfer Measurements in Short-Duration Hypersonic Facilities", AGARD AG-165.

A.3 Investigation of Heat Transfer in a Film Cooled Transonic Turbine Cascade, Part I: Steady Heat Transfer

Submitted to the 45th ASME Gas Turbine and Aeroengine Technical Congree, Exposition and Users Symposium, May 2000

AN INVESTIGATION OF HEAT TRANSFER IN A FILM-COOLED TRANSONIC TURBINE CASCADE, PART I: STEADY HEAT TRANSFER

D. E. Smith, J. V. Bubb, O. Popp, H. Grabowski III, T.E. Diller, J.A. Schetz, W.F. Ng
Virginia Polytechnic Institute and State University
Blacksburg, VA 24061

ABSTRACT

Experiments were performed in a transonic cascade wind tunnel to investigate the film effectiveness and heat transfer coefficient on the suction side of a high-turning turbine rotor blade. There are six rows of staggered, discrete cooling holes on and near the leading edge of the blade in a showerhead configuration. Cold air was used as the coolant in order to match the density ratios found in engine conditions. Six high-frequency heat flux gauges were installed downstream of the cooling holes on the suction side of the blade. Preliminary work on this blade with a single gauge was presented in "Steady and Unsteady Heat Transfer on a Film Cooled Transonic Turbine Cascade," ASME 99-GT-259. In the present paper, the experimental technique was refined and more detailed measurements were made. Experiments were performed with and without film cooling on the surface of the blade and the coolant to freestream total pressure ratio was varied from 1.02 to 1.19. In order to simulate real engine flow conditions, the exit Mach number was set to 1.2 and the exit Reynolds number was set to $5x10^6$. The freestream turbulence was approximately 1%. The heat transfer coefficient was found to increase with the addition of film cooling an average of 14% overall and to a maximum of 26% at the first gauge location. The average film cooling effectiveness along the chord-wise direction of the blade is 25%. Both the heat transfer coefficient and the film cooling effectiveness were found to have only a weak dependence upon the coolant to freestream total pressure ratio at the gauge locations used in this study.

NOMENCLATURE

Symbols

B	blowing ratio $(\rho u)_c/(\rho u)_f$
d	cooling hole diameter (1 mm)
C	specific heat of air, 1005 J/(kg K) in Eq.(?)
h	heat transfer coefficient w/o film cooling
h_c	heat transfer coefficient w/ film cooling
I	momentum ratio $(\rho u^2)_c/(\rho u^2)_f$
M	density ratio ρ_c/ρ_f
p	static pressure
Pr	Prandtl Number (0.71 in Eq.(?))
q	heat flux per unit area
r	recovery factor in Eq.(?) and Eq.(?)
T_{aw}	local adiabatic wall temperature
T_c	coolant exit temperature
T_d	T_t-T_r Eq.(?)
T_r	local recovery temperature
T_t	freestream total temperature
T_w	local wall or blade temperature
u	local freestream velocity in Eq.(?)
η	film effectiveness defined in Eq.(?)

Subscripts

c	coolant or w/ film cooling
f	freestream

INTRODUCTION

At present, there is a strong demand from both the military and the industrial sectors to develop gas turbine engines which can operate at higher efficiencies. In order to meet this demand, the inlet temperature to the turbine must be raised. However, hot gas temperatures widely exceed the operating temperatures of the materials presently being used in the construction of turbine blades. In order to raise turbine inlet temperatures without decreasing the life of the blades it is necessary to employ some sort of blade cooling scheme. One such cooling scheme is film cooling, in which cool air drawn from the compressor is forced through holes on the surface of the turbine blade in order to insulate the blade from the hot engine environment. Since this air is seen as a loss of work for the engine, it is necessary for the thermal designer to gain an understanding of the

physics of film cooling and the parameters that affect it in order to minimize the air drawn from the compressor.

In an attempt to provide information about the heat transfer into turbine blades which employ film cooling, many flat plate experiments have been performed. These experiments allowed researchers to amass a great deal of information about the parameters that affect heat transfer into a film-cooled surface. A good compilation of the experimental work done on flat plates was put together by Goldstein (1971).

Schwarz et al. (1990) investigated the effects of curvature and blowing ratio on the film cooling effectiveness of a convex surface. They found that curved surfaces had better film cooling effectiveness than flat plates. Also, Schwarz et al. found that at low blowing rates, film cooling is more effective on the suction side of the blade than on the pressure side. This work was an intermediate step between flat plates and investigations of heat transfer into realistic blade geometries.

Horton et al. (1985) investigated the heat transfer into a realistic turbine blade profile mounted in a linear cascade. Thin-film resistance sensors were used in a short duration blow down tunnel to capture the transient surface temperature history. Horton et al. were able to obtain measurements of the heat transfer coefficient at several locations along both the pressure and suction sides of the blade.

In 1995, researchers at G. E. Aircraft Engines performed heat transfer measurements on a film-cooled inlet nozzle guide vane (NGV) in a linear cascade with realistic flow conditions [Abuaf et al., 1995]. Thermocouples embedded in a thin-walled turbine blade were used to measure the transient surface temperature. Heat transfer coefficient and effectiveness profiles were obtained for both sides of the blade. Also in 1995, Ekkad et al. investigated the effects of freestream turbulence on the heat transfer into a film-cooled turbine blade. Thermotropic liquid crystals (TLC's) were used to obtain the transient surface temperature history. They concluded that high freestream turbulence leads to an increase in heat transfer coefficient.

Researchers at Oxford University used thin-film gauges to study the heat transfer into a heavily film-cooled NGV [Guo et al., 1996 and 1997]. Their measurements were performed in an annular cascade with attempts made to simulate realistic engine conditions. A mixture of SF_6 and Argon was used as a coolant. The heat transfer coefficient and film cooling effectiveness profiles were determined for the pressure side of the NGV.

In 1998, Drost et al. used TLC's to record the transient surface temperature history of an NGV airfoil exposed to a step input in heat transfer while in a linear cascade. They used a foreign gas as a coolant to obtain a realistic density ratio. They concluded that the film cooling effectiveness was higher near the cooling holes and that the mainstream turbulence level had a weak effect on suction side effectiveness, but that it increased suction side heat transfer coefficients.

EXPERIMENTAL APPARATUS

Transonic Wind Tunnel

The experiments described in this paper were all performed in the Virginia Tech transonic wind tunnel, an intermittent blow down facility with an open discharge. A reciprocating compressor is used to load a high-pressure tank that serves as the supply for the mainstream flow. When released, air flows at a rate of approximately 10 kg/s through the system of pipes shown in Fig. 1. A fast-acting control valve is used to maintain the tunnel's total pressure upstream of the test section at a constant value. The Virginia Tech wind tunnel also has the capacity for heated flows by utilizing the lower loop shown in Fig. 1. In the bottom of the loop there are two 36 kW resistance heaters which heat the air. This heated air is then circulated over a bank of copper tubes in the top of the loop by a small fan. The heated copper tubes act as a passive heat exchanger and heat the tunnel's mainstream flow.

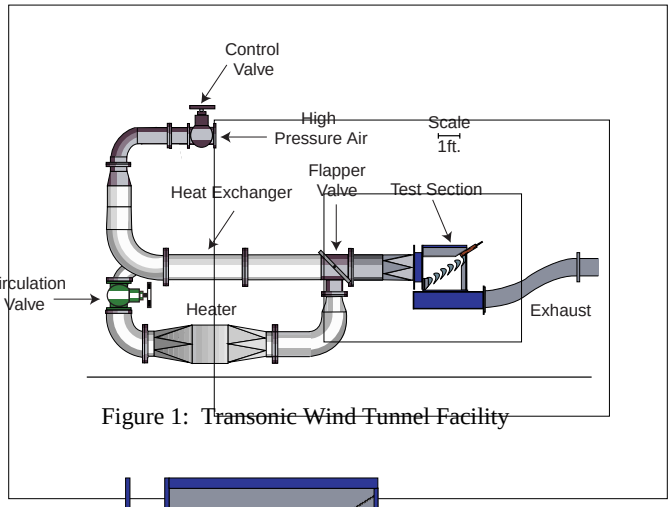

Figure 1: Transonic Wind Tunnel Facility

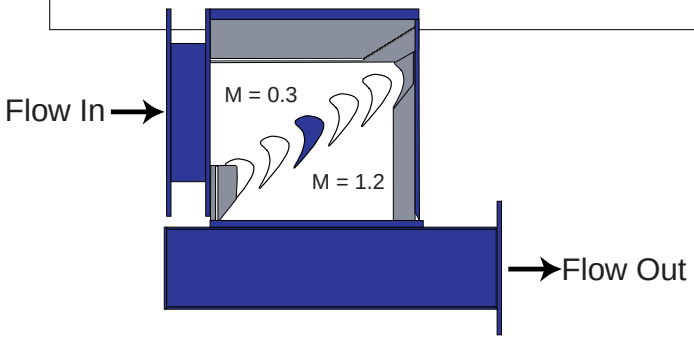

Figure 2: Schematic of Cascade Test Section

Cascade Test Section

The test section used to mount the rotor blades was constructed of aluminum with clear-acrylic side walls. The side walls give optical access to the flow in the passages and allow shadowgraph and Schlieren photography to be performed. A cut-a-way of the test section can be seen in Fig. 2. The test section contains four full blades and two half blades, a total of five flow passages. Flow enters the test section at Mach 0.3, is turned 128º while passing over the blades, and exits the test section at Mach 1.2. The shaded blade was instrumented and used to acquire all of the data presented in this paper.

Turbine Blade Design

The blade profile used in this study was a generic design donated by GE Aircraft Engines and was made from aluminum. Six rows of cooling holes are located near the leading edge in a showerhead arrangement, as can be seen in Fig. 3. All of the holes have a diameter of 1 mm and the spacing between holes is approximately 9.1 hole diameters. The four rows of cooling holes nearest the leading edge are all aligned normal to the streamwise tangent and are inclined at an angle of 30º to the surface where they emerge. The two rows of coolant holes farthest from the leading edge are both aligned parallel to the streamwise tangent. The gill holes on the suction side are inclined at an angle of 30º to the surface where they emerge, while the

gill holes on the pressure side are inclined at an angle of 45° to the surface where they emerge.

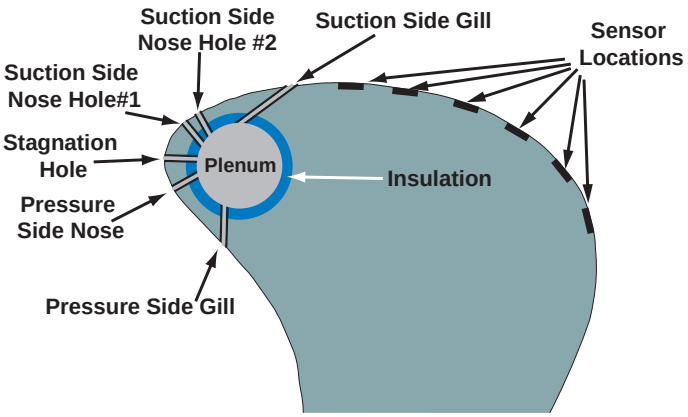

Figure 3: Blade cooling scheme

Sensors

Six sets of gauges were press-fitted into the blade downstream of the last row of cooling holes on the suction side as can be seen in Fig. 4. Figure 4 is a plan view of the suction side of the blade showing the locations of the cooling hole exits and gauge locations. Each set of gauges is composed of a high-speed pressure transducer (Kulite XCQ-062-50a), a high-speed heat flux and temperature sensor (HFM-7), and a surface-mounted thermocouple. The Kulite transducers are used to acquire high-speed static pressure measurements on the blade surface. The HFM-7's acquire separate, direct and simultaneous measurements of both the local heat flux and wall temperature. The HFM-7 has a gauge diameter of 5mm and an active diameter of 4mm. A detailed discussion of these gauges can be found in Diller, ????. The surface-mounted thermocouple is used as a calibration tool for the HFM-7's temperature sensor. The first set of gauges was mounted approximately 9.1 hole diameters downstream of the last row of cooling holes and the subsequent sets of gauges were staggered along the span and in the streamwise direction. All of the gauges were mounted within a three inch wide section of the blade span which surface oil flow visualizations had shown to be free of endwall effects.

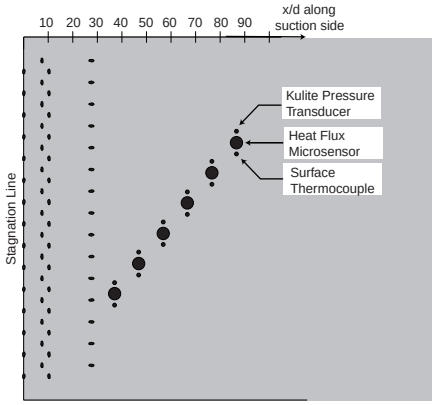

Figure 4: Plan View of Blade Instrumentation

Coolant Supply System

A schematic of the coolant system is shown in Fig. 5. Air is supplied to the insulated plenum of the instrumented blade from a large storage tank. The coolant supply storage tank is fed by a 5 hp compressor with a filter and dryer system attached. When air is released from the storage tank it passes through a coolant control system. This coolant control maintains the plenum-to-freestream total pressure ratio over the course of the run via an integral feedback control. Controlling the pressure ratio allows the momentum ratio to be controlled, but the density and blowing ratios vary over a run. The air then flows through an orifice plate, where the mass flow rate is monitored, and into a chiller which uses liquid nitrogen as a coolant. The cold air is then fed into the insulated plenum of the blade.

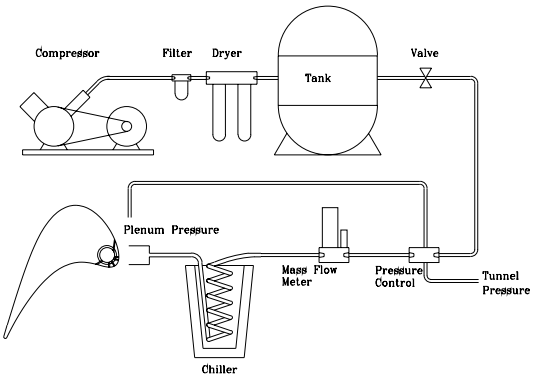

Figure 5: Schematic of Coolant System

DATA ANALYSIS AND RESULTS

Uncooled Data Analysis and Results

The dominant mode of heat transfer in gas turbines is convection, and the convection heat transfer coefficient is defined by the equation,

$$q = h \cdot \left(T_{aw} - T_w\right) \tag{1}$$

where the difference between the adiabatic wall temperature, T_{aw}, and the wall temperature, Tw, is the driving force of the heat transfer. For high-speed flows with no film injection, T_{aw} is equivalent to the recovery temperature and equation (1) can be rewritten as,

$$q = h \cdot \left(T_r - T_w\right) \tag{2}$$

where T_r is the recovery temperature. The recovery temperature can be related to the freestream total temperature by the recovery factor and the freestream velocity as shown in the equation,

$$T_t - T_r = \left(1 - r\right) \cdot \frac{u^2}{2 \cdot C} = T_d \tag{3}$$

where r is the recovery factor, u is the freestream velocity, and C is the specific heat of air. The difference between the freestream total temperature and the recovery temperature is a constant during the run and will hereafter be referred to as T_d. The recovery factors for laminar and turbulent flows are usually considered to be $Pr^{1/2}$ and $Pr^{1/3}$, respectively [Kays and Crawford, 1993]. Substituting equation (3) into (2) yields,

$$q = h \cdot \left(T_t - T_w\right) - h \cdot T_d \tag{4}$$

In equation (4), the local heat flux, q, is the dependent variable and the temperature difference, $T_t - T_w$, is the independent variable. The heat transfer coefficient is the slope in this equation and T_d is equal to the temperature difference, $T_t - T_w$, when q = 0 (i.e. the x-axis intercept). It was shown by Popp et al. (1999) that the heat transfer coefficient and T_d did not significantly depend upon the temperatures involved in equation (4). Therefore, for the uncooled case, the heat transfer coefficient and the temperature difference T_d can be obtained

by measuring the freestream's total temperature, the blade's wall temperature, and the local heat flux into the blade over the course of an experiment.

When the experimental data was fitted to equation (4), the result was a linear trend as can be seen in Fig. 6. Figure 6 is a typical result of the analysis performed on data gathered at the first gauge location. A regression analysis can easily be performed in order to fit a line through this data. The heat transfer coefficient can be obtained from the slope of this line, and the temperature difference T_d can be determined from the x-axis intercept.

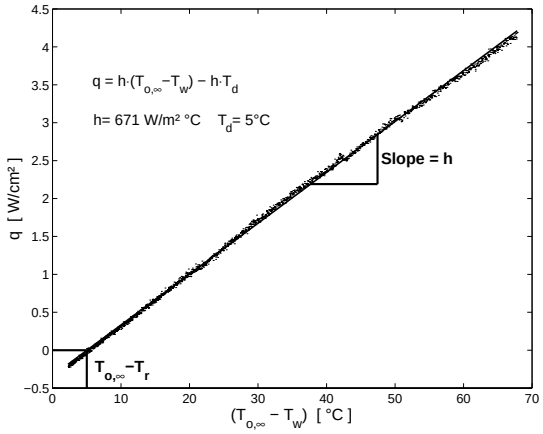

Figure 6: Uncooled Data Analysis

A typical time history of the temperatures and heat flux recorded at location 1 from an uncooled run can be seen in Fig. 7. Figure 7(a) shows all the temperatures of interest, including the recovery temperature, which was calculated by subtracting the value of T_d found at location 1 from the total temperature of the freestream. The freestream's total temperature is seen to vary significantly over the course of the experiment. Typically, it varies from 100ºC to 30ºC as the passive heat exchanger cools down. The blade wall temperature rises approximately 8ºC over the course of the run. Figure 7(b) shows a typical time history of the local heat flux and heat transfer coefficient at location 1. The heat transfer coefficient's time history was calculated by using the previously determined recovery temperature in equation (2). Figure 7(b) shows that after the initial transient caused by the starting of the wind tunnel the heat transfer coefficient is fairly constant. Comparing 7(a) with 7(b), it can be seen that the heat flux into the blade approaches zero as the recovery and wall temperatures converge, which is consistent with the definition of heat flux in equation (2). Figure 7(c) shows the blowing ratios and momentum ratios for the three coolant holes that affect the suction side of the blade. In addition, Fig. 7(c) also shows the coolant-to-freestream density and pressure ratios. All of these ratios were determined assuming isentropic flow conditions.

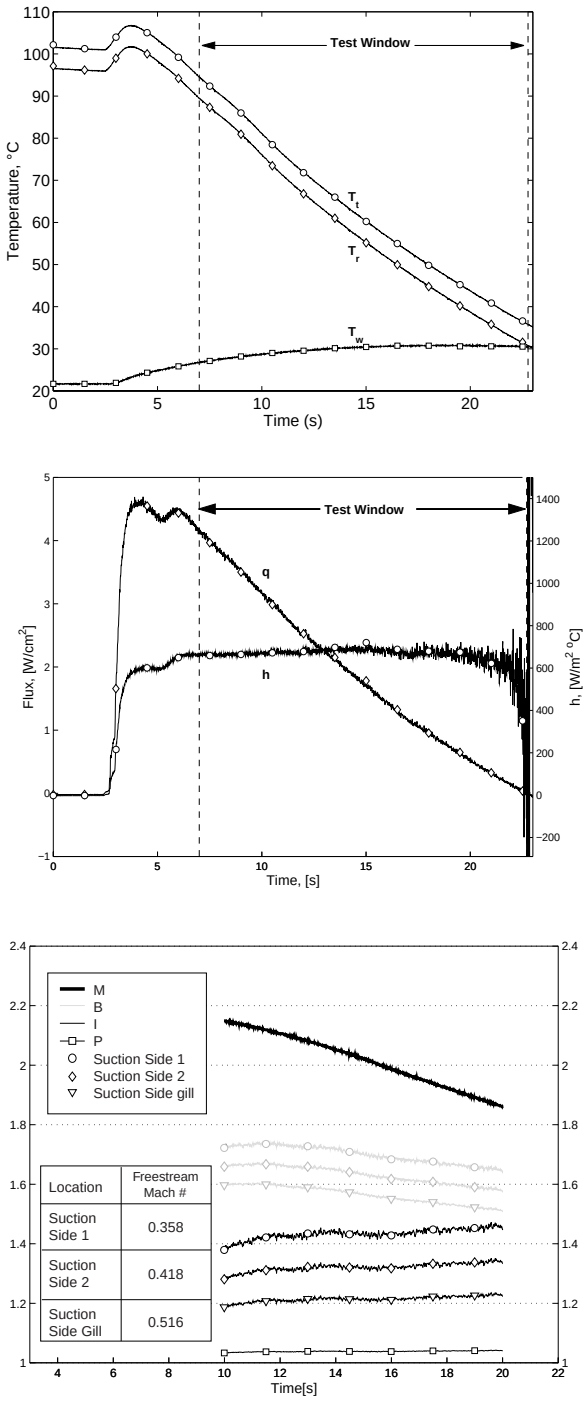

Figure 7: Heat flux and heat transfer coefficient time history

Six experiments were performed without film cooling, and the results of these experiments can be seen in Fig. 8. Figure 8 shows the heat transfer coefficients determined at each gauge location for all six experiments. The average level of the heat transfer coefficient over the region of interest was 700 $W/m^2 \cdot ºC$. This average value of the heat transfer coefficient will be used in investigating the unsteady effects of shocks on the heat transfer into the blade in the next paper on this work.

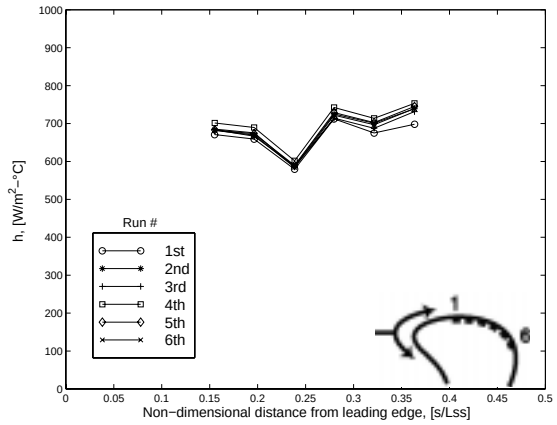

Figure 8: Heat transfer coefficient profile

Film-cooled Data Analysis and Results

For the film-cooled experiments, it was important to be able see the condition of the coolant film. The optical access of the cascade test section allowed both shadowgraph and Schlieren photographs to be made in order to visualize the film-cooling layer. A high-speed digital camera was used to capture the shadowgraph shown in Fig. 9. The coolant film is clearly attached and turbulence is evident in the film layer. The photograph shows that the stagnation point has shifted slightly towards the suction side, causing the coolant jets exiting the nose holes to be diverted entirely to the pressure side. Therefore, only the three rows of coolant holes on the suction side provide protection for the suction side of the blade. The pressure side of the blade is obscured by equipment outside of the test section.

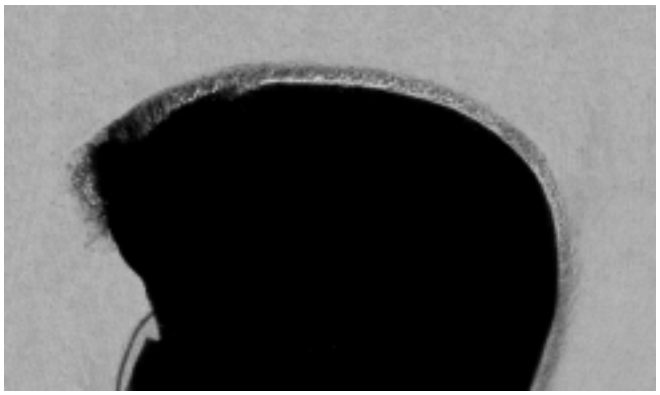

Figure 9: Shadowgraph of Cooling Film

With the addition of film cooling to the surface of a turbine blade in a high-speed flow, the governing equation of convection heat transfer is once again equation (1). However, in such cases the adiabatic wall temperature is usually non-dimensionalized using the adiabatic film effectiveness defined as,

$$\eta = \frac{T_{aw} - T_r}{T_c - T_r} \tag{5}$$

where η is the adiabatic film effectiveness. Equation (5) can be solved for T_{aw} and then substituted into equation (1) which will yield,

$$\frac{q}{T_r - T_c} = h \cdot \left[\frac{T_r - T_w}{T_r - T_c} \right] - h \cdot \eta \tag{6}$$

The dependent variable in equation (6) is now the heat flux divided by a temperature difference and the independent variable is a ratio of two temperature differences. The slope of equation (6) is the heat transfer coefficient and the x-axis intercept is the adiabatic film effectiveness. Once again, Popp et al. (1999) showed that neither the heat transfer coefficient nor the adiabatic film effectiveness have a significant dependence on the temperatures used in equation (6). Using the values of T_d determined for each gauge position in the uncooled case, the recovery temperatures at each location can then be calculated from the freestream total temperature. The only unknowns in equation (6), then, are the heat transfer coefficient and the film effectiveness.

The experimental data from a typical film-cooled run were fitted to equation (6) and the result is a linear trend, which is displayed in Fig. 10. A regression analysis was performed and a line was fit through the data. The film-cooled heat transfer coefficient was determined from the slope of the line and the adiabatic film effectiveness was obtained from the x-axis intercept. For the same gauge location as shown earlier in the uncooled case, the heat transfer coefficient has increased to 950 W/m^2·ºC, while the effectiveness is 31%.

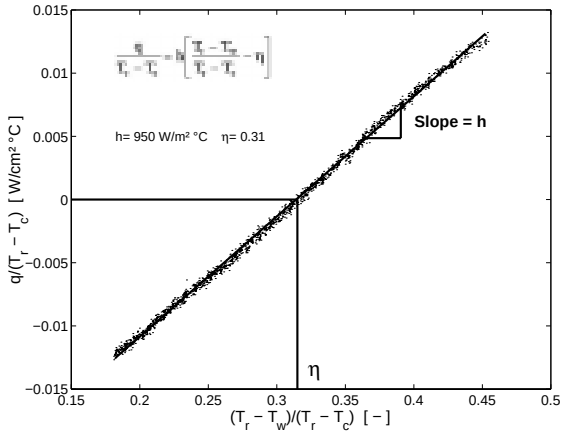

Figure 10: Film-cooled Data Analysis

A sample time history of a film-cooled run can be seen in Fig. 11. The test window indicates the limits of the data set that were used in the film-cooled analysis. The traces in Fig. 11a are similar to those in Fig. 7a except for the addition of a mass-averaged coolant temperature. The adiabatic wall temperature is calculated using the film effectiveness determined from Fig. 10 and equation (5). The freestream temperature again falls from around 100ºC to 30ºC, while the blade temperature rises from near 0ºC to about 10ºC. The liquid nitrogen heat exchanger allows the coolant temperature to be maintained at temperatures ranging between –120ºC and –150ºC. In comparing Figs. 11a and 7a, it should be noted that the driving temperature of the heat transfer is lower for the film-cooled case than for the uncooled case. Figure 11b shows that even though the heat transfer coefficient at location 1 increases, the adiabatic wall temperature is lowered enough that the peak level of the heat flux actually decreases from 4.5 W/cm^2 to 3.5 W/cm^2. The adiabatic wall temperature can be used in equation (1) along with the heat flux and wall temperature to generate the time history of the film-cooled heat

transfer coefficient seen in Fig. 11b. A singularity occurs in the calculation of the film-cooled heat transfer coefficient when T_{aw} and T_w converge. Aside from the singularity, the film-cooled heat transfer coefficient is fairly constant over the course of the experiment.

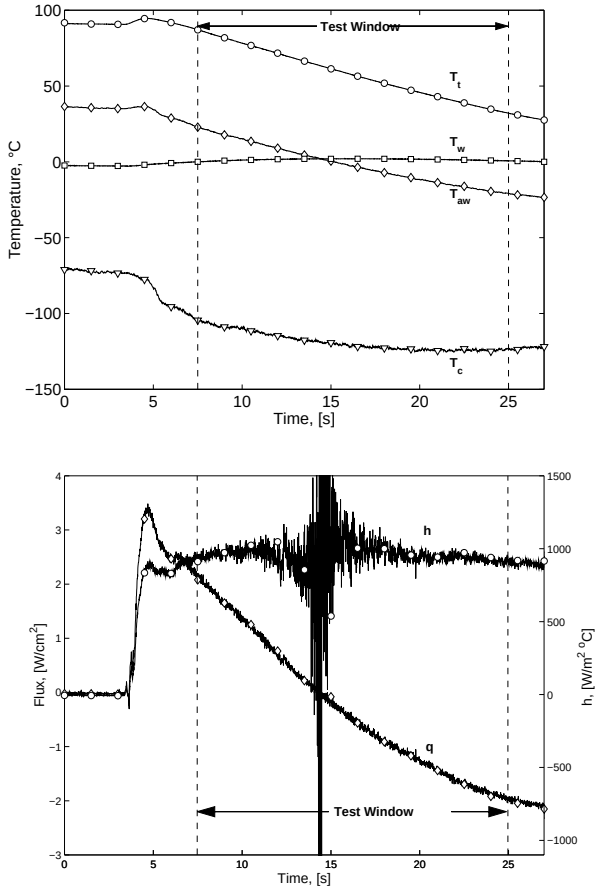

Figure 11: (a) Temperature time history, (b) Heat flux and heat transfer coefficient time history

Six film-cooled experiments were performed and analyzed in the manner just described. Figure 12 shows the results in heat transfer coefficient and film effectiveness for all six runs. The average level of the heat transfer coefficient for the film-cooled case was found to be 850 W/m^2·°C, a 21% increase over the uncooled experiments. Over the same region, the film had an average adiabatic effectiveness of 25%. These experiments provide a basis for the unsteady work that will be investigated in Part 2 of this paper.

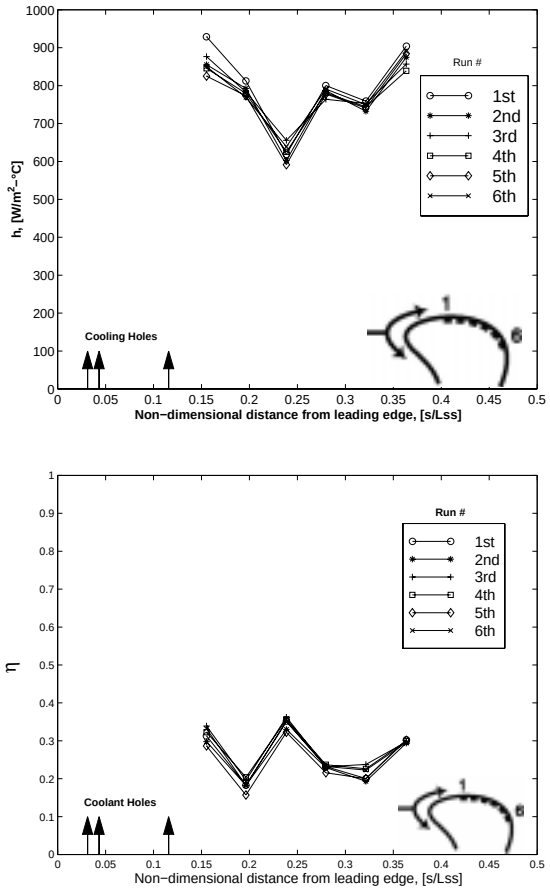

Figure 12: Film-cooled experiments (a) heat transfer coefficient, (b) adiabatic film effectiveness

UNCERTAINTY IN h AND η

The theoretical uncertainty for the h and η measurements are divided into two categories; bias and precision uncertainties. The bias uncertainty is composed entirely of the calibration of the heat flux microsensors. The uncertainties for these six gauges are detailed in a paper by Smith et. al. (Smith 1999) and can be translated directly into heat transfer coefficient bias uncertainties. Table 1 details these bias uncertainties (based on a 90% confidence interval of a student-T distribution).

Gauge	Bias Uncertainty
1	17.0 %
2	3.7 %
3	5.2 %
4	15.2 %
5	8.8 %
6	10.7 %

Table 1: Heat Transfer Coefficient Bias Uncertainties

These gauge bias uncertainties do not effect the bias uncertainty in η since η is determined solely from temperature measurements (i.e. the x-axis intercept in Fig. 10).

Precision uncertainties are comprised of the theoretical variations of temperature measurements and a scheme outlined by Moffat (Moffat 1988) for calculations involving complex computer

algorithms. Based on an individual temperature uncertainty of 1.1°C, this type of analysis yields the precision uncertainties detailed in Table 2.

Gauge	h Precision Uncertainty	η Precision Uncertainty
1	5.9 %	18.5 %
2	6.1 %	21.0 %
3	5.6 %	13.9 %
4	5.9 %	21.3 %
5	6.0 %	17.0 %
6	5.7 %	11.5 %

Table 2: Precision Uncertainties

Another indication of measurement uncertainty is an experimental value of measurement repeatability. This repeatability value was determined from a number of different experiments performed at the same test conditions. The results shown in Table 3 are based on 8 runs at a pressure ratio of 1.04 and a 90% confidence bounds using a student-T distribution.

Gauge	h Repeatability	η Repeatability
1	11.1 %	16.4 %
2	4.0 %	8.2 %
3	5.5 %	7.1 %
4	5.1 %	15.8 %
5	6.7 %	21.1 %
6	7.3 %	11.4 %

Table 3: Measurement Repeatability

THE INFLUENCE OF PRESSURE RATIO ON h AND η

Experiments were performed using the above data reduction technique to determine the influence of the plenum to freestream total pressure ratio on both h and η. Using the coolant control feedback system, the pressure ratio was varied from run to run over the ranges of about 1.02 to 1.19. The results from a number of runs are shown in Fig. 13 and Fig. 15. The error bars on these plots indicate the measurement repeatablilty shown in Table 3.

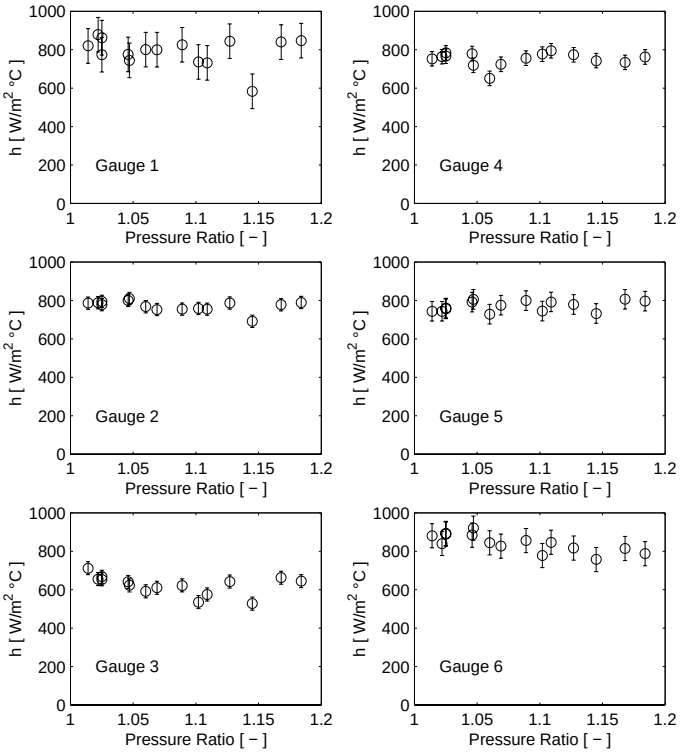

Figure 13: The Influence of Pressure Ratio on the Heat Transfer Coefficient

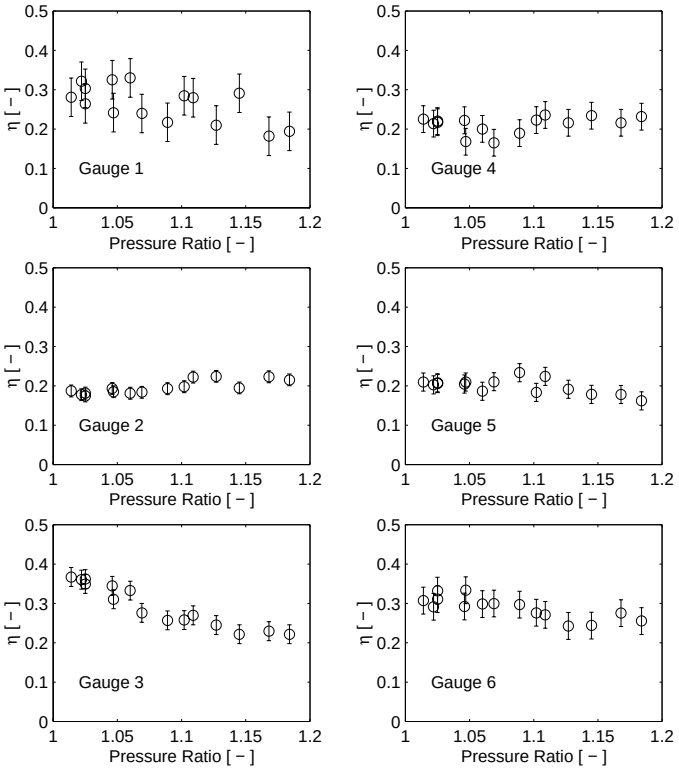

Figure 14: The Influence of Pressure Ratio on Film Cooling Effectiveness

From Fig. 13 can be seen that, in general, the heat transfer coefficent is fairly independent of the pressure ratio. Also Fig. 14 shows a independence of pressure ratio and effectiveness for gauge locations 2,

4, 5, and 6 and a slight decrease of effectiveness at locations 1 and 3. The slight decrease at these locations is suspected to be attributed to spanwise shifting of the coolant at higher pressure ratios which yielded lower film coverage at these locations.

CONCLUSIONS

An experimental setup to investigate the steady heat transfer into a film-cooled transonic turbine rotor blade was made. Experiments were performed with and without film cooling at the nominal plenum to freestream pressure ratio of 1.04. A method that allowed for the determination of both the heat transfer coefficient and either the recovery temperature (in uncooled runs) or the film cooling effectiveness (film-cooled runs) from one transient run was used. For the nominal pressure ratio, an average increase in the heat transfer coefficient of 21% was seen with the addition of film cooling. Varying the pressure ratio in the range from 1.02 to 1.19 had only a weak effect on the heat transfer coefficient and slightly decreased the film effectiveness at some gauge locations.

ACKNOWLEDGMENT

This work was supported by the Air Force Office of Scientific Research (AFOSR) under grant F08671-9601062, monitored by Dr. Jim M. McMichael and Dr. Mark Glauser. We would like to thank Messrs. Scott Hunter, Monty Shelton and Mark Pearson of General Electric Aircraft Engines for their collaboration on this project.

REFERENCES

Abuaf, N., Bunker, R., Lee, C.P., G.E. Aircraft Engines, 1995, "Heat Transfer and Film Cooling Effectiveness in a LInear Cascade, " 40th IGTI Conference, ASME 95-GT-3.

Drost, U., Bölcs, A., Swiss Federal Institute of Technology, 1998, "Investigation of Detailed Film Cooling Effectiveness and Heat Transfer Distributions on a Gas Turbine Airfoil," ASME 98-GT-20.

Ekkad, S.V., Hui Du, and Je-chin Han, Texas A& M University, 1995, "Local Heat Transfer Coefficient and Film Effectiveness Distributions on a Cylindrical Leading Edge Model Using a Transient Liquid Crystal Image Method," ASME 95-WA/HT-3.

Goldstein, R.J., “Measurements in Heat Transfer,” Hemisphere Pub. Corp., 1976.

Guo, S.M., Lai, C.C., Jeong, J.H., Jones, T.V., and Oldfield, M.L.G., University of Oxford, 1997, "Use of Liquid Crystal Techniques to Measure Film Cooling Heat Transfer and Effectiveness," 90th Symposium of the Propulsion and Energetics Panel, AGARD 20-24.

Guo, S.M., Jones, T.V., University of Oxford, and Lock, G.D., University of Bath, 1996, "Gas Turbine Heat Transfer Measurements with Engine Simulated Film Cooling," 2nd European Conference on Turbomachinery Fluid Dynamics and Thermodynamics, Technological Institute, Section on Aeronautics.

Horton, F.G., Shultz, D.L., Forest, A.E., University of Oxford, 1985, "Heat Transfer Measurements with Film Cooling on a Turbine Balade Profile in Cascade," ASME 95-GT-117.

Kays, W.M., Crawford, M.E., “Convective Heat and Mass Transfer,” McGraw-Hill Inc., pp 380-388, 1993.

Moffat, R. J., 1988, “Describing Uncertainties in Experimental Results”, Experimental and Thermal Fluid Science, Elsevier Science Publishing Co., Inc.

Popp, O., et al., 1999, “Steady and Unsteady Heat Transfer in a Film-Cooled Transonic Turbine Cascade,” ASME 99-GT-259.

Schwarz, S.G., Goldstein, R.J., Eckert, E.R.G., Tulane University/University of Minnesota, 1990, "The Influence of Curvature on Film Cooling Performance," 35th IGTI Conference, ASME 90-GT-10.

Smith, D., et al., 1999, “A Comparison of Radiation Versus Convective Calibration of Thin-Film Heat Flux Gauges”, The ASME Ad-Hoc Committee on Heat flux Measurements.

A.4 Investigation of Heat Transfer in a Film Cooled Transonic Turbine Cascade, Part II: Unsteady Heat Transfer

Submitted to the 45th ASME Gas Turbine and Aeroengine Technical Congree, Exposition and Users Symposium, May 2000

INVESTIGATION OF HEAT TRANSFER IN A FILM COOLED TRANSONIC TURBINE CASCADE, PART II: UNSTEADY HEAT TRANSFER

O. Popp, D. E. Smith, J. V. Bubb, H. C. Grabowski III, T.E. Diller, J. A. Schetz, Wing-Fai Ng
Virginia Polytechnic Institute and State University
Blacksburg, VA 24061

ABSTRACT

This paper reports on an investigation of the heat transfer on the suction side of a transonic film cooled turbine rotor blade in a linear cascade. A shock wave is generated in a shock tube and passes into the cascade upstream of the blade row to simulate the interaction of a shock emerging from the trailing edge of an upstream nozzle guide vane on the downstream rotating blade row. The unsteady heat transfer caused by the shock wave passing over the suction side of the rotor blade is analyzed and compared to predictive models published in the literature. The investigation includes experiments with and without film cooling and a variation of the most relevant physical parameters. From the analysis and the comparison of the unsteady heat flux it is concluded that the heat transfer coefficient is not affected strongly by the passing shock. Most of the unsteady heat transfer is induced by the variation of temperature caused by the shock wave.

NOMENCLATURE

Symbols

c_p	specific heat of air
h	heat transfer coefficient w/o film cooling
h_c	heat transfer coefficient w/ film cooling
k	thermal conductivity of air
m	counter in Eq. 9
n	counter in Eq. 9
p	static pressure
q	heat flux per unit area
q_c	unsteady component of heat flux (in Rigby's Model)
q_h	unsteady component of heat flux (in Rigby's Model)
q_M	unsteady component of heat flux (in Moss' Model)
s	variable in Laplace domain
T_{aw}	local adiabatic wall temperature
T_c	coolant exit temperature
T_h	unsteady component of temperature (in Rigby's Model)
T_M	unsteady component of temperature (in Moss' Model)
T_r	local recovery temperature
T_t	freestream total temperature
T_w	local wall or blade temperature
Δt	time between data points
η	film effectiveness defined in Eq.(7)

Superscripts

´	unsteady variation

INTRODUCTION

The efficiency of a gas turbine engine increases with turbine inlet temperature. In the ongoing effort to raise the turbine inlet temperature the gas stream temperature is made to greatly exceed the operating temperatures of blade materials, requiring elaborate blade cooling techniques to be developed. One of these methods is to spread a thin layer of cold air between the hot gas and the surface to be protected, referred to as film cooling. The quest for higher thrust to weight ratios in the development of aero-engines has led to the design of nozzle guide vanes (NGV) with supersonic exit velocities. The rotor blades consequently are not only subject to wake but also shock impingement as they pass behind the NGV's at very high speed. The effect of this unsteady process on the heat transfer to the rotor blade has been the topic of a variety of research programs.

Researchers at Texas A&M (Ou et al. (1994), Mehendale et al. (1994), Du et al. (1997)) published time averaged results from a low speed cascade with and without film cooling. Wakes were produced using a spoked wheel rotating upstream of the linear cascade. It was concluded that the presence of the wakes increases the heat transfer coefficient only on the downstream suction side by affecting the transitional behavior of the boundary layer. With the introduction of film cooling on the suction side the, the boundary layer is tripped early, and the effect of the wakes decreases accordingly.

Heidmann et al. (1997) presented experimental work on a stationary annular cascade consisting of rotor blades with an inlet Mach Number of 0.27. Wakes were generated using a rotating bar mechanism rotating in front of the cascade. Time averaged film cooling effectiveness was measured for a showerhead film cooling scheme with two rows of holes on the suction side and the pressure side and one row in the geometric stagnation point. The wake induced

mixing decreased the film cooling effectiveness all along the blade. The effect was more pronounced on the suction side since the swirl generated by the rotating rods shifted the stagnation point. Therefore, more coolant was available on the pressure side, almost outweighing the decrease in film effectiveness due to the increased mixing.

The last in a series of publications on heat flux and pressure measurements in a full stage rotating turbine done at the Calspan-UB Research Center featured phase-locked measurements of heat flux on the rotor blades (Dunn (1989)). No on-rotor pressure measurements were provided to relate the heat flux to the flowfield. On the shroud both pressure and heat flux data was recorded. The fluctuations of heat flux and pressure were shown to be in phase and of similar shape.

In Guenette et al. (1989) a fist set of time-resolved on-rotor heat flux and pressure data from a full stage blowdown turbine. The mid section of the rotor blade profile was identical to the blade tested in a linear cascade at the University of Oxford. While the flow field in this turbine naturally featured shocks and wakes, those had to be modeled in the linear cascade. The data from both setups were compared and showed reasonable agreement. In 1996 Abhari et al. (1996) compared the heat flux results from a steady state code to time averaged measurements on a film cooled blade. The presence of the wakes and shocks seemed to decrease the heat transfer on the suction side and increase it on the pressure side.

The most comprehensive body of research was published by the University of Oxford. In 1985 Doorly et al.(1985) were the first to report on time resolved heat transfer measurements in a linear cascade. A combination of wakes and weak shocks was produced using a rotating bar mechanism. Turbulent spots and bubbles created by shock and wakes were shown to be responsible for an increase of heat flux. Johnson et al. (1988) used slightly modified blades and increased the rotational speed of the bars to create stronger shock waves. The modified blades were the same ones used by Guenette et al. (1989). The direct impact of the shock wave was observed to be the major contribution to the unsteady heat flux. A first version of a predictive model linking isentropic shock heating and one dimensional conduction in the fluid to the unsteady heat flux showed fairly good agreement with measured heat flux data. Rigby et al. (1989) modified this model and gave a thorough derivation. In 1990 Johnson et al. (1990) found that while the prediction yielded good agreement on the suction side, the pressure side unsteady heat was underpredicted. The reason for this was found in a "Vortical Bubble" created by the shock wave and traveling down the pressure side. Rigby et al. (1990) first included film cooling in the cascade setup. The shock wave signature was found to change with the introduction of film cooling. Data recorded in an entirely new full stage rotating turbine was first published in 1995 by Moss et al. (1995). Time resolved on-rotor heat flux and pressure measurements were presented. It was shown that the unsteady heat flux could be predicted by multiplying a constant heat transfer coefficient and a temperature variation calculated from the unsteady pressure based on an isentropic assumption. In 1997 Moss et al. (1997) compared time averaged heat flux measurements on the rotor with the presence of upstream wakes and a flowfield undisturbed by the nozzle guide vanes. The values of time averaged heat transfer with and without the presence of upstream disturbances were nearly identical, thus proving the assumption of a constant heat transfer coefficient valid.

Hale et al. (1997) modeled the effect of wake passing in a quasi-steady way using a stationary strut. Increases in heat transfer coefficient were measured for a number of locations on the blade, particularly on the pressure side. Nix et al. (1997) analyzed in detail the progression of a shock wave through the same cascade and its effect on the unsteady heat transfer. When averaged over a 200µs blade passing event, a maximum increase of heat flux of 60% was measured due to shock passing. Popp et al. (1999) presented time resolved heat flux and pressure data from one measurement location on the suction side of a large scale film cooled transonic rotor cascade. It was shown that the heat transfer coefficient as well as the film cooling effectiveness were not affected significantly by the passing shock wave.

The intent in the present study is to extend the investigation to a larger number of measurement locations and to verify the conclusions for a variety of physical parameters. The unsteady heat flux will be analyzed to find the relative magnitudes of unsteady heat transfer coefficient, unsteady temperature and film effectiveness and their contributions to the overall unsteady heat flux. Also, the experimental data will be compared to predictive models developed by Rigby et al. (1989) and Moss et al. (1995).

EXPERIMENTAL APPARATUS

Wind Tunnel Facility, Cascade and Shock Apparatus

The experiments necessary for this investigation were performed in the transonic blowdown wind tunnel at Virginia Tech. A passive heating device is available to achieve high (120°C) inlet temperatures to the cascade. It consists of many copper tubes that are preheated prior to running the tunnel. Fig. 1 of Part I (Smith et al. (2000)) shows the wind tunnel with the heating loop. With the present cascade, the facility allows run times of up to 35 seconds with the inlet pressure controlled. The test-section and cascade built for this investigation are shown in Fig. 2 of Part I (Smith et al. (2000)). The cascade consists of four full and two half blades forming five passages. The blade design is a generic, high-turning, first stage rotor geometry. It is scaled up three times to accommodate the cooling scheme and instrumentation. The span is 15.3 cm (6") and the aerodynamic chord is 13.6 cm (5.4"). Pitch and axial chord are 11.4 cm (4.5"). The Reynolds Number based on aerodynamic chord and exit conditions is about $6 \cdot 10^6$. The Mach Number distribution was shown to correspond to design conditions. To simulate the shock emerging from the trailing edge of a NGV, a shock tube creates a shock wave which is sent through flexible tubing and along the leading edges of the cascade (see Fig. 1). The shock strength can be varied to obtain realistic pressure ratios by mounting diaphragms of different thickness between the driver and driven section of the shock tube.

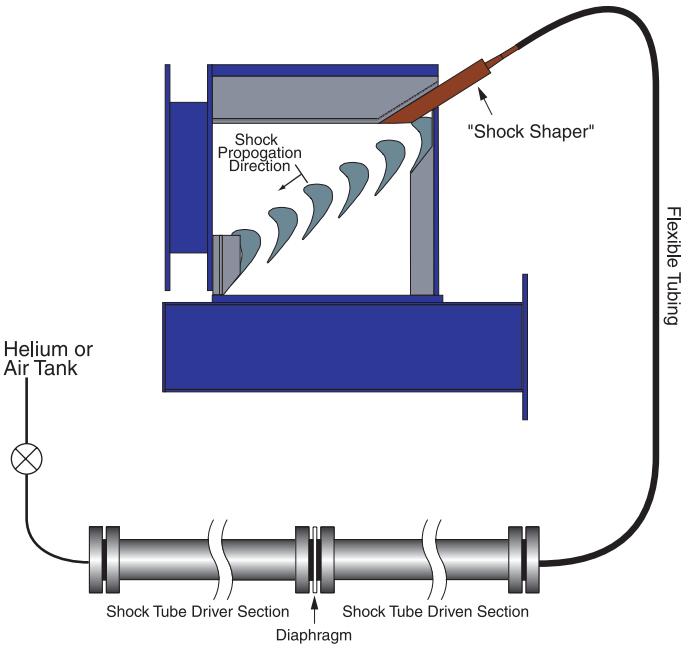

Figure 1: Cascade and Shock Apparatus

Cooling Design

A schematic of the showerhead film cooling design is shown in Fig. 3 in Part I. The design is a generic showerhead layout with four rows of holes close to the leading edge and a row of "gill" holes on both pressure and suction side. The rows around the leading edge are normal to the chordwise tangent and inclined 30° with respect to the spanwise direction. The "gill" row on the suction side is normal to the spanwise direction and inclined 30° with respect to the chordwise tangent while the "gill" row on the pressure side emerges at an angle of 45°. All holes are fed by a common plenum which is insulated to reduce internal heat transfer. The coolant supply and coolant pressure control is shown in Fig. 5 in Part I. This setup allows to control the ratio of coolant total pressure to freestream total pressure. This corresponds to the Momentum Ratio, since air is used as coolant. The objective temperature ratio T_t/T_c was 2, but was not controlled effectively. Therefore, the Density Ratio and Blowing Ratio vary throughout the experiment, while the Momentum Ratio is kept constant.

Sensors

The six measurement locations are shown in Figures 3 and 4 in Part I. At each measurement location a triplet of gauges is installed. A *Kulite* Pressure Sensor XCQ-062-50a is monitoring static surface pressure. A *Vatell* HFM-7/L Heat Flux Microsensor gives a direct reading of surface heat flux and of surface temperature. A surface thermocouple is used as a calibration tool for the resistance temperature device of the HFM-7/L. For the high speed measurements of surface pressure and heat flux, the dynamic characteristics of the heat flux and pressure sensors had to be known. In a shock tube experiment, the transfer function of the *Kulite* XCQ-062-50a pressure sensor with B-screen was found to be modeled well as a second order system in the frequency range of up to 100 kHz. The transfer function of the heat flux sensors was experimentally determined to be of first order with a time constant of about 17μs.

Data Acquisition and Signal Processing

Both surface static pressure and heat flux were recorded at 500 kHz with a *LeCroy* High Speed Waveform Recorder. The signals were filtered at 102.4 kHz using *Frequency Devices* Model 9064 8-Pole Butterworth Low-Pass Filters. Since the transfer functions of both pressure and heat flux sensors show significant signal attenuation and phase shift in the frequency range below the cut-off frequency, the recorded signals had to be corrected. The transfer functions that had been determined experimentally were inversely applied to the pressure and heat flux data.

To find the mean heat flux before shock impact, a time window of 5 μs before the sudden rise in heat flux was used for averaging.

Test Matrix

A technique for the analysis of the transient heat transfer due to shock passing was presented in Popp et al. (1999). This technique will be applied to heat flux time histories in section "Unsteady Decomposition". The analysis was done with and without film cooling and under a wide variety of parameters. Without film cooling two parameters were varied: Shock strength and heat flux before shock impact. The shock strength was varied in two steps. In terms of peak static pressure ratio at gauge #2 the values of shock strength were 1.2 and 1.3. Those values may not be indicative of the "real" shock strength since the pressure signal was filtered at 25 kHz for this test series, which is too slow to actually capture the shock peak. The level of heat flux before shock impact was varied by triggering the shock at different times during the tunnel run. As seen in Figures 7 b and 11 b in Part I, the heat flux level changes during the test. It was attempted to obtain three different levels of initial heat flux (high, medium, low). The two values of shock strength and the three values of heat flux yield a test matrix of six experiments without film cooling. For the tests with film cooling one additional parameter was varied. The ratio of coolant total pressure to freestream total pressure was set to the nominal value (1.04) and a high value (1.2). With the shock strength and the initial level of heat flux varied as in the case without film cooling, this resulted in a test matrix of twelve experiments with film cooling. In section "Unsteady Decomposition" only sample experiments are shown. The conclusions drawn there have been verified for all conditions tested in these test matrices.

The predictive models published in the literature all use the static pressure time history to calculate the unsteady heat flux. For this purpose pressure and heat flux time histories need to be sampled and filtered at the same frequencies, and the signals have to be corrected in order to have the same signal attenuation and phase. This was done according to the procedure described briefly in section "Data Acquisition and Signal Processing". For the comparison of the data with these models a reduced number of gauges and parameters varied were investigated. Pressure and heat flux were only recorded at measurement locations #1 and #2. Two tests with film cooling and one test without film cooling were done at the higher shock strength. Since the frequency content of the pressure data is much wider in these tests (102.4 kHz compared to 25 kHz), the peak unsteady pressure ratio measured at gauge #2 is about 1.5 (compared to 1.3 in the tests with the lower cut-off frequency), while the "real" shock strength is identical. For the two experiments with film cooling, the ratio of coolant total pressure to freestream total pressure was set to the nominal value of 1.04. In section "Comparison with Rigby's Model" and "Comparison with Moss' Model", one test with and one without film cooling are presented.

RESULTS AND DISCUSSION

General Observations

A series of Shadowgraphs taken with a high-speed camera showed no particularly strong interaction between the shock wave and the layer of cooling air. No film detachment or separation were observed. Also no "Separation Bubble" nor "Vortical Bubble" were seen. Figure 2 shows a sample Shadowgraph of the shock passing process with the shock just above gauge #1.

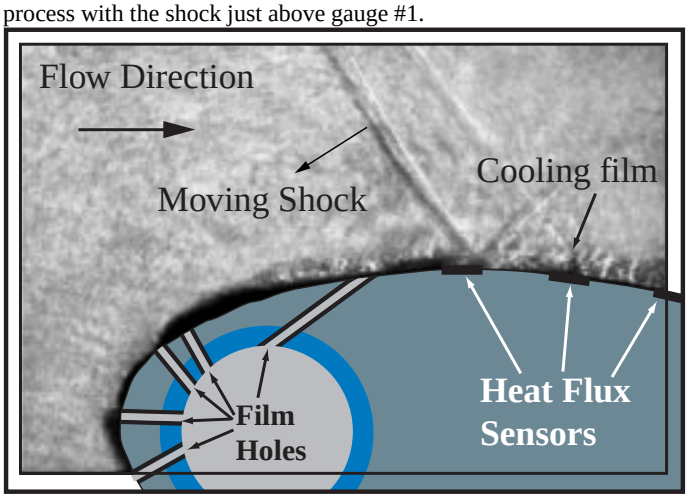

Figure 2: Sample Shadowgraph Illustrating the Interaction between Passing Shock and Layer of Coolant Air

In the upper graph in Figure 3 the heat flux traces of a sample experiment without film cooling are shown for gauges #1 through #5. The lower graph in the same figure shows the pressure traces from gauges #2 #4, #5 and #6 from the same experiment. Note that the pressure time histories shown in this figure were filtered at 25 kHz as explained in section "Test Matrix", and do not provide the best possible representation of the physical event. The x-axes on the two graphs are identical to illustrate the time history of the passing shock as it passes over the gauges. The y-axes on each graph are also identical to allow for a comparison of the relative strength of the shock on each gauge. The time mean value of heat transfer before shock impact was removed to show only the unsteady component of the heat flux for better comparison. This figure illustrates that the time histories of pressure and heat flux are in phase and similar in shape. Higher values of pressure fluctuations correspond to higher values of unsteady heat flux.

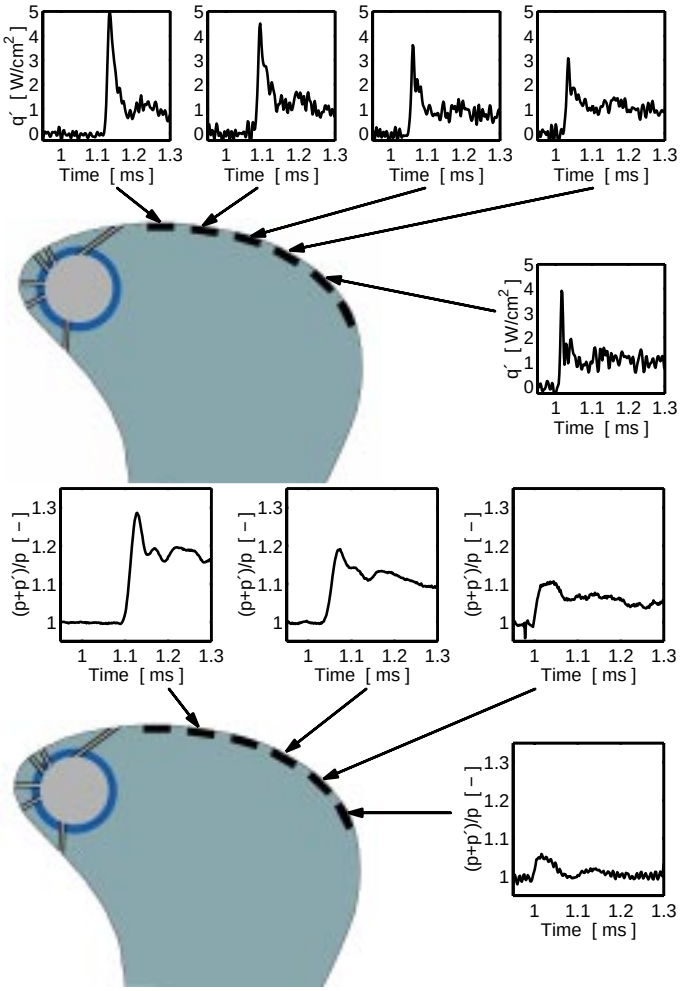

Figure 3: Traces of Unsteady Heat Flux (Upper Graph) and Unsteady Pressure (Lower Graph) Due to Shock Passing Without Film Cooling

The same observation can be made for the experiments with film cooling. The unsteady pressure and heat flux histories from one experiment with film cooling are shown in Figure 4. When comparing Figures 3 and 4 it can also be seen that the traces of unsteady pressure and heat flux with and without film cooling appear similar in shape and phase. This is in contradiction to the statement by Rigby et al. (1990), who concluded that "the unsteady shock wave signature changes when film cooling is introduced". For the front suction surface they observed similar but reduced traces of unsteady Nusselt Number with the introduction of film cooling. This observation is supported by Figures 3 and 4. Even though the pressure traces with and without film cooling are nearly identical the heat flux signatures with film cooling are about 20 to 30% lower.

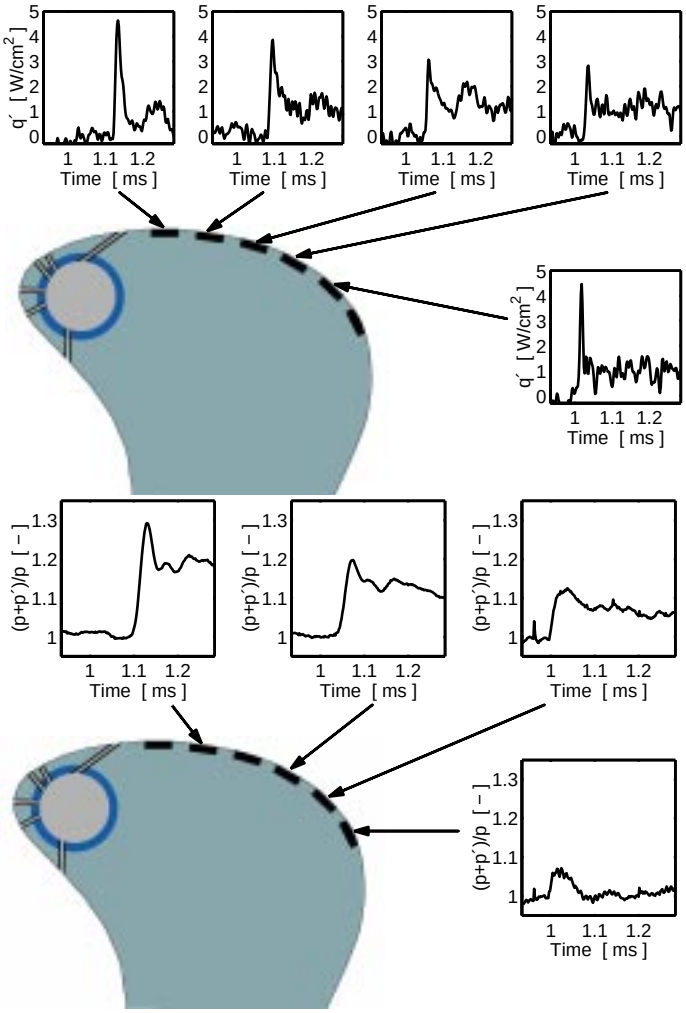

Figure 4: Traces of Unsteady Heat Flux (Upper Graph) and Unsteady Pressure (Lower Graph) Due to Shock Passing With Film Cooling

"Unsteady Decomposition"

The unsteady component of heat flux due to shock passing can be analyzed by a general decomposition of all parameters involved (Popp et al. (1999)). The expression for the unsteady heat flux as a function of all time dependent parameters is then:

$$q' = h' \cdot (T_{aw} - T_w) + h \cdot T'_{aw} + h' \cdot T'_{aw} \qquad (1)$$

The superscript ´ refers to the unsteady component of the physical parameter while the variables without the superscript refer to the value of the variable before shock impact. In the case without film cooling the adiabatic wall temperature T_{aw} and its time varying component T'_{aw} can be replaced by the recovery temperature and its corresponding time varying function. The first term on the right hand side of Eq. 1 shows that the contribution of the unsteady heat transfer coefficient, h´, to the overall unsteady heat flux depends on the temperature difference T_{aw}-T_w before shock impact, or equivalently the heat transfer before shock impact. It can be shown, though, that the overall unsteady heat flux is independent of the value of heat flux before shock impact. This implies that the unsteady component of heat transfer coefficient is not contributing significantly to the overall unsteady heat flux. If h´ was of the same order of magnitude as the value of heat transfer coefficient before shock impact, it would have to contribute to the unsteady heat flux by an amount of the order of the value of heat flux before shock impact. This is clearly not the case as seen in Figures 5 and 6. Figure 5 shows heat flux data from three different shock passing experiments without film cooling at different levels of initial heat flux (higher shock strength). For each of the five gauges the upper graph shows the sum of the steady and unsteady heat flux due to shock passing. The different levels of q before shock impact can be found in these graphs. In the lower graphs the values of heat flux before shock impingement were removed, yielding the unsteady component of heat flux q´. Figure 6 shows the same arrangement for three experiments with film cooling (higher shock strength, coolant to freestream total pressure ratio=1.2). It can be seen that the three traces of unsteady heat flux collapse in both cases. This illustrates that the unsteady component of heat flux is independent of the initial level of heat flux before shock impingement, thereby proving that the contribution of the unsteady heat transfer coefficient to the overall unsteady heat flux is small both w ith and without film cooling.

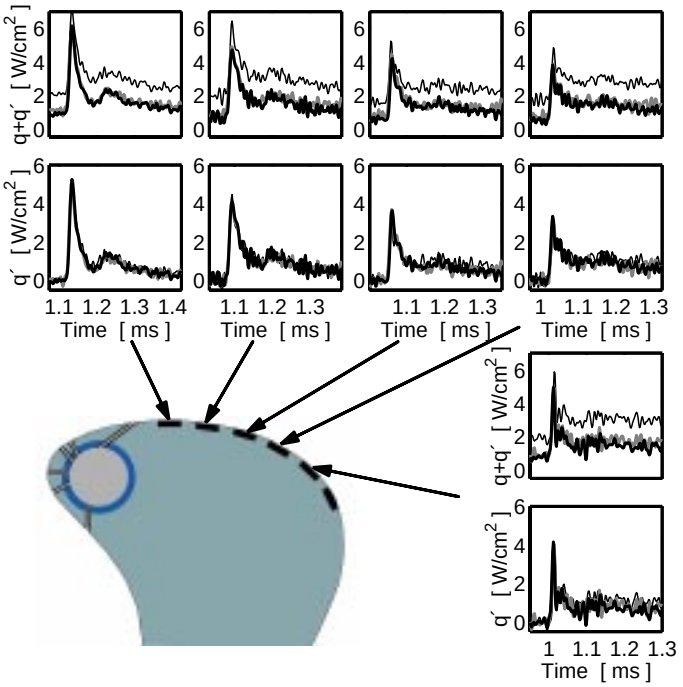

Figure 5: Heat Flux and Unsteady Heat Flux Due to Shock Passing.
Upper Graphs: Overall Unsteady Heat Flux During Shock Impact.
Lower Graphs: Heat Flux Before Shock Impact Removed.
Three Experiments without Film Cooling.

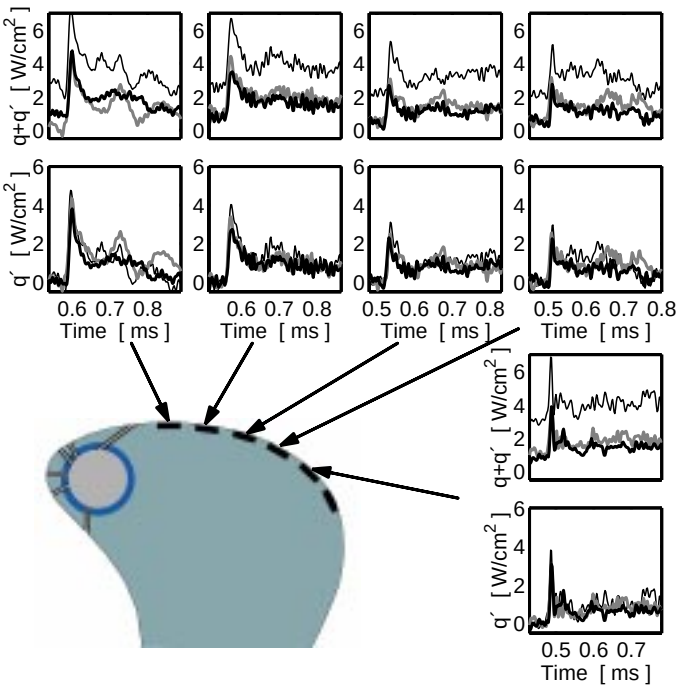

Figure 6: Heat Flux and Unsteady Heat Flux Due to Shock Passing.
Upper Graphs: Overall Unsteady Heat Flux During Shock Impact.
Lower Graphs: Heat Flux Before Shock Impact Removed.
Three Experiments with Film Cooling.

The terms containing h´ in Eq. 1 can be dropped based on this conclusion. For the experiments without film cooling this yields the following relation between the unsteady variation of recovery temperature and unsteady heat flux:

$$q' = h \cdot T_r' \qquad \text{or} \qquad T_r' = \frac{q'}{h} \tag{2}$$

For the experiments with film cooling the corresponding relation is:

$$q' = h_c \cdot T_{aw}' \quad \text{or} \qquad T_{aw}' = \frac{q'}{h_c} \tag{3}$$

These equations imply that all the unsteady heat flux is caused by a temperature variation induced by the passing shock, which follows from the conclusions drawn above. The effect of the passing shock on the film effectiveness can be analyzed by decomposing the unsteady variation of adiabatic wall temperature according to Popp et al.(1999):

$$T_{aw}' = T_r' \cdot (1-\eta) - \eta' \cdot (T_r - T_c) - \eta' \cdot T_r' \tag{4}$$

Or rearranged:

$$\eta' \cdot \left[(T_r - T_c) + T_r' \right] = T_r' \cdot (1-\eta) - T_{aw}' \tag{5}$$

The difference between the variation of the recovery temperature scaled by (1-η) and the variation of adiabatic wall temperature is a measure for the magnitude of η´. The scaling factor for η´ on the left hand side of Eq. 5 is always a relatively high number since the difference between the recovery and the coolant temperature is of the order of 150°C. To estimate the magnitude of η´, the two terms on the right hand side of Eq. 5 are plotted in Figure 7. T'_r is calculated from an uncooled experiment shown in Figure 5 using Eq.2. The results for T'_r are so similar for the three experiments that a separate comparison is not necessary and a representative trace of T'_r can be used. The value of η used for each gauge location is the local mean value of η from all three experiments. The actual values were determined according to the procedure explained in Smith et al. (2000).

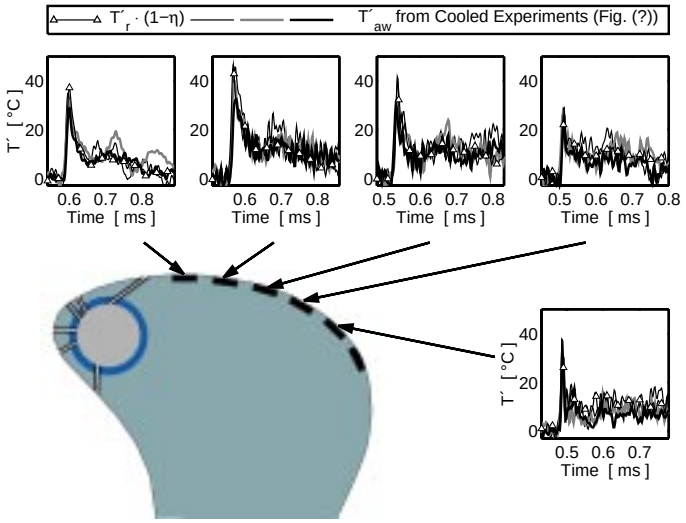

Figure 7: Comparison of $T'_r(1-\eta)$ and T'_{aw} for Three Different Cooled Experiments. T'_r Determined from one Representative Experiment Without Film Cooling

It can be seen from Figure7 that the difference between $T'_r(1-\eta)$ and T'_{aw} does not exceed 7°C at all times in all three experiments and the five gauge locations. With $[(T_r-T_c)+T'_r]$ on the order of 150°C this will yield values of η´ not exceeding 5%. This value is relatively small compared to the value of η (on the order of 20% to 30%). The variation of the film effectiveness can therefore be considered a secondary effect in the heat transfer process due to shock wave passing.

Comparison with Rigby's Model

In 1989 Rigby et al. (1989) published a modified version of a model for the prediction of unsteady heat transfer first developed by Johnson et al.(1988). The two models are very similar but the later version came with a more thorough derivation. Therefore, Rigby's model will be used for comparison with the data presented here. The reader is referred to Rigby et al. (1989) for the detailed derivation. Two components of unsteady heat flux are identified. One of them is caused by isentropic compression of the entire temperature field due to a pressure perturbation:

$$q_c = q \cdot \left(\frac{p + p'}{p} \right) \tag{6}$$

The equation for the second component of unsteady heat flux is caused by transient conduction in the fluid close to the wall. Neglecting convective and viscous terms and analyzing the remaining terms in the boundary layer equation it is found that the one-

dimensional heat conduction equation can be applied to this component of heat flux. The following solution is found :

$$\overline{q}_h = \sqrt{k \cdot \rho \cdot c_p}_{gas} \cdot \overline{T}_h(0,s) \cdot \sqrt{s} \tag{7}$$

The overlines denotes the Laplace transform of the function and s is the variable in the Laplace domain. The discrete temperature history

$$T_h(0,t) = T_w \cdot \left[\left(\frac{p + p'}{p} \right)^{\frac{\gamma-1}{\gamma}} - 1 \right] \tag{8}$$

is decomposed in piecewise linear elements, transformed into the Laplace domain and substituted in Eq. 7. q_h is obtained after retransformation into the time domain:

$$q_h(t_m) = \frac{2 \cdot \sqrt{k \cdot \rho \cdot c_p}_{gas}}{\sqrt{\pi \cdot \Delta t}} \cdot \sum_{n=2}^{m-1} \left(T_{n+1} - 2 \cdot T_n + T_{n-1} \right) \cdot \sqrt{m - n} \tag{9}$$

The overall heat flux can be calculated using:

$$q + q' = q_c + q_h \tag{10}$$

The method is illustrated in Figure 8 for an experiment without film cooling. Only data from gauges #1 and #2 are available for this type of comparison. The graphs on the left hand side of Figure 8 show data from gauge #1, while the right column of graphs show data from gauge #2. The top graphs show the pressure time history and the time history $T_h(0,t)$ calculated according to Eq. 8. The second row of graphs show the time history of q_h and q_c determined according to Eqs. 9 and 6 respectively. The last row of graphs shows the direct comparison of the measured and predicted heat flux.

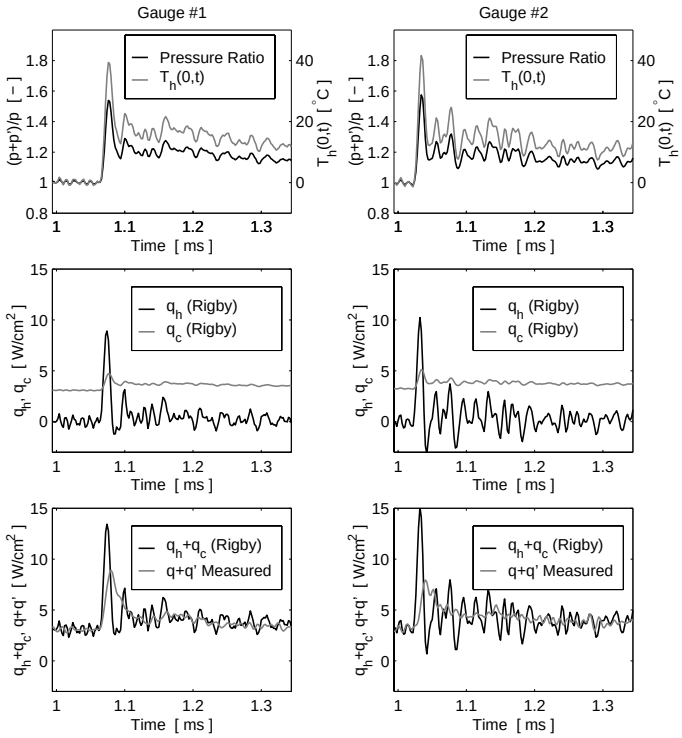

Figure 8: Comparison of Measured Heat Flux and Heat Flux Predicted According to Rigby's Model (Experiment without Film Cooling).
Left Column: Gauge #1.
Right Column: Gauge #2.
Top Row: Time Histories of Pressure and $T_h(0,t)$.
Middle Row: q_h and q_c.
Bottom Row: Comparison of Measured and Predicted Heat Flux.

From the second row of graphs it is clear that q_h outweighs q_c by far for the levels of q and the pressure ratios encountered in these experiments. The last row of graphs showing the direct comparison between the measured and predicted heat flux illustrates that the model does not provide a good prediction of unsteady heat flux due to shock passing. The reason for this must be that at least one of the three major simplifications made in the derivation of the model was not justified (neglecting convective and viscous terms, dropping the term containing the time derivative of pressure in Eq. (14) of Rigby et al. (1989)). Figure 9 shows the same comparison presented in Figure 9 for an experiment with film cooling. The time histories of pressure are nearly identical with and without film cooling. Therefore, the traces of $T_h(0,t)$ and q_h are also similar. Rigby's model was not originally developed for a situation with film cooling. The derivation suggests, though, that it can be applied to this situation. The measured heat flux data supports the model in so far as the time histories of heat flux are indeed similar with and without film cooling. On the other hand the comparison between actual data and predicted heat flux is as poor with film cooling as it was shown to be without film cooling.

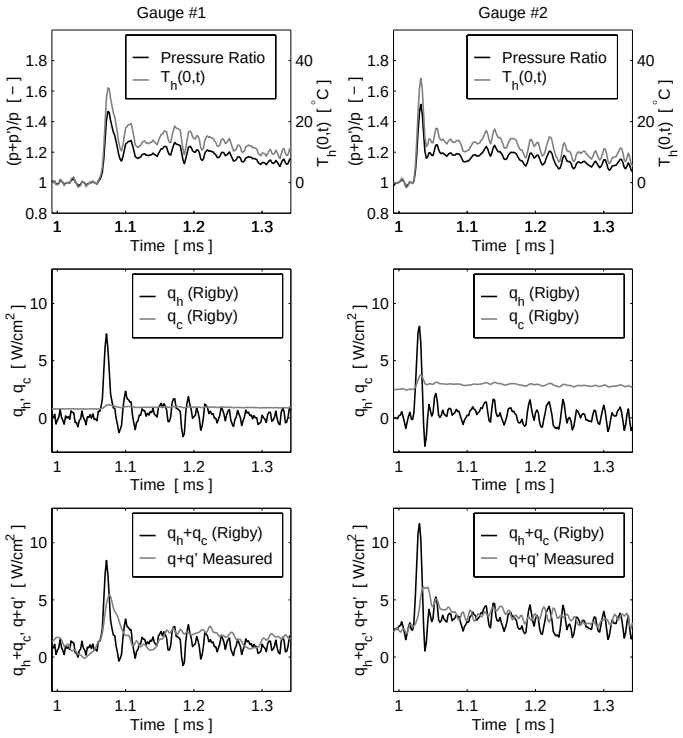

Figure 9: Comparison of Measured Heat Flux and Heat Flux Predicted According to Rigby's Model (Experiment with Film Cooling).
Left Column: Gauge #1
Right Column: Gauge #2
Top Row: Time Histories of Pressure and $T_h(0,t)$
Middle Row: q_h and q_c
Bottom Row: Comparison of Measured and Predicted Heat Flux

Comparison with Moss' Model

In 1995 Moss et al. (1995) published ensemble averaged heat flux and pressure data from a rotating turbine facility. Using Johnson's model – which is almost identical to Rigby's model – they predicted heat flux from the pressure time histories and found reasonable agreement. By simply assuming a constant heat transfer coefficient and predicting the heat transfer from a temperature variation induced by isentropic compression, an even better prediction could be found:

$$q_M = h \cdot T_M \quad \text{with} \quad T_M = T \cdot \left[\left(\frac{p + p'}{p} \right)^{\frac{\gamma-1}{\gamma}} - 1 \right] \tag{11}$$

The temperature T was not specified by Moss et al. (1995). For the comparison in this investigation, the f reestream static temperature will be used. Figures 10 and 11 demonstrate the method and compare the predicted heat flux to the data shown in the last section for an experiment without and with film cooling respectively.

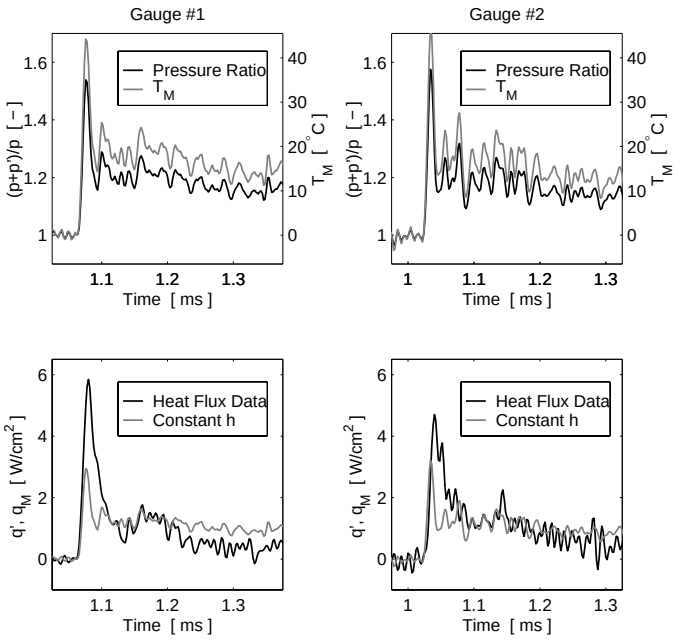

Figure 10: Comparison of Heat Flux Data with Moss' Assumption of a Constant h (Experiment Without Film Cooling).
Left Column: Gauge #1.
Right Column: Gauge #2.
Top Row: Pressure and Temperature Time Histories
Bottom Row: Comparison of Measured and Predicted Heat Flux

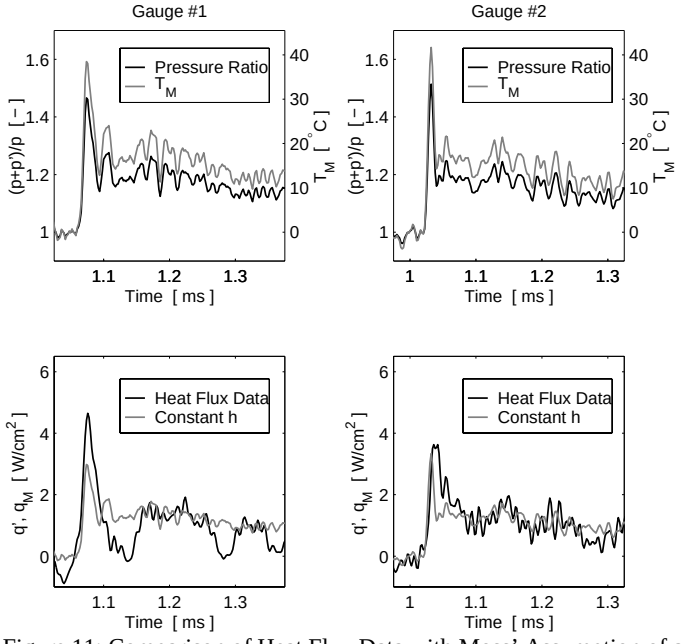

Figure 11: Comparison of Heat Flux Data with Moss' Assumption of a Constant Heat Transfer Coefficient (Experiment With Film Cooling).
Left Column: Gauge #1
Right Column: Gauge #2
Top Row: Pressure and Temperature Time Histories
Bottom Row: Comparison of Predicted and Measured Heat Flux

Even though the agreement is not perfect, Moss' prediction matches the measured heat flux much better in terms of magnitude and

shape than Rigby's model presented in the last section. The conclusion from section "Unsteady Decomposition" is supported by this observation. The contribution of the variation of the heat transfer coefficient to the overall unsteady heat flux proves to be small compared to the unsteady heat transfer caused by the variation of temperature induced by the passing shock.

CONCLUSIONS

The unsteady heat transfer caused by a passing shock wave on the suction side of a transonic turbine blade was investigated with and without film cooling. Heat flux data was analyzed by means of a mathematical decomposition and by comparison with predictive models available in the literature. The mathematical and comparative analysis leads to the conclusion that the unsteady heat transfer is mostly driven by the temperature fluctuation induced by the passing shock wave. Heat transfer coefficient and film effectiveness are not affected enough to contribute significantly to the overall unsteady heat transfer. This conclusion was verified on six locations on the suction side for shocks of different strength and for different coolant blowing rates. Since the temperature in an actual engine is fluctuating around its mean value, the time mean heat transfer in the presence of shocks is expected not to differ significantly from the time mean heat flux without the disturbance of the shock.

ACKNOWLEDGMENT

This work was supported by the Air Force Office of Scientific Research (AFOSR) under grant F08671-9601062, monitored by Dr. Jim M. McMichael and Dr. Mark Glauser. We would like to thank Messrs. Scott Hunter, Monty Shelton and Mark Pearson of General Electric Aircraft Engines for their collaboration on this project.

REFERENCES

Ou, S., Han, J.-C., Mehendale, A.B., Lee, C.P., 1994,"Unsteady Wake Over a Linear Turbine Blade Cascade With Air and CO2 Film Injection: Part I – Effect on Heat Transfer Coefficients", ASME Journal of Turbomachinery, Vol. 116, pp. 721-729

Mehendale, A.B., Han, J.-C., Ou, S., Lee, C.P., 1994, "Unsteady Wake Over a Linear Turbine Blade Cascade With Air and CO2 Film Injection: Part II – Effect on Film Effectiveness and Heat Transfer Distributions", ASME Journal of Turbomachinery, Vol. 116, pp 730- 737

Du, H., Han, J.-C., Ekkad, S.V., 1997, "Effect of Unsteady Wake on Detailed Heat Transfer Coefficient and Film Effectiveness Distributions for a Gas Turbine Blade", ASME 97-GT-166

Heidmann, J. D., Lucci, B.L., Reshotko, E., 1997, "An Experimental Study of the Effect of Wake Passing on Turbine Blade Film Cooling", ASME 97-GT-255

Dunn. M.G., 1989, "Phase and Time-Resolved Measurements of Unsteady Heat Transfer and Pressure in a Full-Stage Rotating Turbine", ASME 89-GT-135

Guenette, G.R., Epstein, A.H., Giles, M.B., Haimes, R., 1989, "Fully Scaled Transonic Turbine Rotor Heat Transfer Measurements", ASME Journal of Turbomachinery, Vol. 111, pp. 1-7

Abhari, R.S, 1996,"Impact of Rotor-Stator Interaction on Turbine Blade Film Cooling", ASME Journal of Turbomachinery, Vol. 118, pp. 123-133

Doorly, D.J., Oldfield, M.L.G., 1985,"Simulation of the Effects of Shock Passing on a Turbine Rotor Blade", ASME 85-GT-112

Johnson, A.B., Rigby, M.J., Oldfield, M.L.G., Ainsworth, R.W., Oliver M.J., 1988, "Surface Heat Transfer Fluctuations on a Turbine Rotor Blade Due to Upstream Shock Wave Passing", ASME 88-GT-172

Rigby, M.J., Johnson, A.B., Oldfield, M.L.G., Jones, T.V., 1989,"Temperature Scaling of Turbine Blade Heat Transfer with and without Shock Wave Passing", International Symposium on Air Breathing Engines ISABE 89-7070

Johnson, A.B., Oldfield, M.L.G., Rigby, M.J., Giles, M.B., 1990, "Nozzle Guide Vane Shock Wave Propagation and Bifurcation in a Transonic Turbine Rotor", ASME 90-GT-310

Rigby, M.J., Johnson, A.B., Oldfield, M.L.G., 1990, "Gas Turbine Rotor Blade Film Cooling With and Without Simulated NGV Shock Waves and Wakes", ASME 90-GT-78

Moss, R.W., Sheldrake, C.D., Ainsworth, R.W., Smith, A.D., Dancer, S.N., 1995, "Unsteady Pressure and Heat Transfer Measurements on a Rotating Blade Surface in Transient Flow Facility", AGARD CP-571, pp. 22-1 – 22-9

Moss, R.W., Ainsworth, R.W., Garside T., 1997, "Effects of Rotation on Blade Surface Heat Transfer: An Experimental Investigation.", ASME 97-GT-188

Hale, J.H., Diller, T.E., Ng, W.F., 1997, "Effects of Wake on Turbine Blade Heat Transfer in a Transonic Cascade", ASME 97-GT-130

Nix, A.C., Reid, T., Peabody, H., Ng, W.F., Diller, T.E., Schetz, J.A., 1997, "Effects of Shock Wave Passing on Turbine Blade Heat Transfer in a Transonic Cascade", AIAA-97-0160

Popp, O., Smith, D.E., Bubb, J.V., Grabowski, H.C. III, Diller, T.E., Schetz, J.A., Ng, W.F., 1999, "Steady and Unsteady Heat Transfer in a Transonic Film Cooled Turbine Cascade", ASME 99-GT-259

Appendix B

Data Runs

B.1 Recovery Temperature Experimental Results

The details of the experiments that determined the recovery temperature drop can be found in Smith et al [22]. These experiments use and expression for recovery temperature given by Eqn. 3.5 and not the approximation given by Eqn. 3.4. For a complete set of this data see that reference. The results are summarized in Table B.1.

Table B.1: Recovery Temperature Difference

Gauge	T_d
1	5.95 °C
2	5.15 °C
3	5.78 °C
4	9.03 °C
5	10.18 °C
6	16.33 °C

B.2 Heat Transfer Coefficient and Film-Cooling Effectivness Results

A summary of h and η data is given in one MATLAB file etitled "summary.m". Instead of repeating this data here, the reader is refered to Appendix C.3.

Appendix C

M-Files

The following pages list the important MATLAB m-files I used to do the major part of my data reduction and analysis. A summary of each of the files follows,

data032299b.m	Performs the data reduction from the raw data. A similar file, data032299.m, is also used where the column numbers are changed for a different acquisition scheme.
outrawout.m	Output and analysis of data that has been reduced from data032299b.m.
summary.m	Summary of the results from many different runs, mostly reduced using data032299b.m and outrawout.
summaryout.m	Output of the data from summary.m Also performs the uncertainty analysis.

C.1 data032299b.m

```
% data032299b.m
% Data Ananylsis for Turbine Heat Transfer Group
% 6 triplet blade analysis
% O. Popp 12/03/98, J. Bubb 03/22/99
%

close all;
format short g;
clear all;

% ---- Input Data Files ------------
% This is the section you change...
%
% typeflag = 0   No Coolant Flow
%                h = q / (Tfree - Tblade)
%                 Tdrop = (1-r)*u^2/2Cp
%
% typeflag = 1   Cold Coolant Flow (using measured Tdrop)
%                h = ( q / (Tr - Tcool) ) / ( (Tr - Tblade)/(Tr - Tcool) )
%                n = (Taw - Tr) / (Tcool - Tr)
%                 Tr = Tfree - Tdrop (Tdrop=6.9C)
%
% typeflag = 2   Cold Coolant Flow (using Pr approx for Tr)
%                h = ( q / (Tr - Tcool) ) / ( (Tr - Tblade)/(Tr - Tcool) )
%                n = (Taw - Tr) / (Tcool - Tr)
%                 Tr = Tfree - Pr^.33 (Tdrop=0.89C)
% front,back     Analysis window for each data set
%
% data           data(time,column#, run#)
```

```
%

loadnew=input('Reload Data? (1=Yes) ');
if loadnew==1
   gub=path;
   j=gub(1);

   names    = [ j ':\afosr\data\03_22_99\run10.asc'];
   typeflag = 1;
   front    = 800;
   back     = 2600;
   qoffset  = 0;
   To       = 20;
   Po       = 13.7;
   times    = 2040;   %Time of shock impact *100


   % ---- OK now stop changing things from here on out  -------
   % ---- The rest is golden.... ----------------------------

   disp('Loading data files...')
   [datanames,data]=loadset(names);
   disp('Performing Analysis...')
   NF=size(data,3);                                    %Number of Data Files

   Torr     = data(:,29);
   Tfree        = data(:,7);
   Tplen        = data(:,13);
   RTS5     = data(:,10);
   RTS6     = data(:,11);
   HFS6     = data(:,12);
     HFS6      = HFS6 - mean(HFS6(1:100));   % Zeroed the data
```

```
  [b,a]=ellip(4,.5,20,.5);              % Create Elliptical Filter
  HFS6=filter(b,a,HFS6);                % Apply filter
Tsg       = data(:,14);
Tsn2      = data(:,15);
Tsn1      = data(:,23);
Tn       = data(:,32);
Tpn      = data(:,24);
Tpg      = data(:,16);
Tblade6   = data(:,22);
Tblade5   = data(:,5);
Tblade4   = data(:,30);
Tblade3   = Tblade4;
Tblade2   = data(:,31);
Tblade1   = data(:,6);
Psg       = data(:,34);
Psn2      = data(:,35);
Psn1      = data(:,36);
Pn        = data(:,37);
Ppn       = data(:,38);
Ppg       = data(:,39);
Pdp       = data(:,40);
Pup       = data(:,41)+Po;
Pfree     = data(:,43);
RTS4      = data(:,45);
RTS3      = data(:,46);
RTS2      = data(:,47);
RTS1      = data(:,48);
Pplen     = data(:,52);
Kul6      = data(:,58);
Kul5      = data(:,57);
Kul4      = data(:,56);
Kul3      = data(:,55);
```

```
Kul2      = data(:,54);
Kul1      = data(:,53);
HFS5      = data(:,62);
HFS4      = data(:,63);
HFS3      = data(:,59);
HFS2      = data(:,60);
HFS1      = data(:,61);


len       = length(Tn);
t         = linspace(0,len/100,len)';

%Correctios Section:  Check this Always!!
%Tblade1   = Tblade1 - 12.5;
%Tblade5   = Tblade5 - 5.5;
%Tblade2   = Tblade1;

%Tfree-Trec for all locations from uncooled runs
Tdrop1    = 5.95;
Tdrop2    = 5.15;
Tdrop3    = 5.78;
Tdrop4    = 9.03;
Tdrop5    = 10.18;
Tdrop6    = 16.33;


%Sensitivity vector
%   S=[234 105 145 130 171 153];
%   S=[264 114 153 150 191 162];
%    S=[214 99  133 122 154 128];
S=[242 104 146 135 173 151];
```

```
%HFS #1 CALIBRATION
HFSGain1 = 100;
g1       =  0;          % V/((W/cm^2)C)
hcal1    = S(1);         % V/(W/cm^2)
RTSGain1 = 500;
c1       = 3.93326;     % C/Ohm
d1       = -495.849;    % C
e1       = 0.261826;    % Ohm/C
f1       = 125.7314;    % Ohm
Ro1      = f1+To*e1;

%HFS #2 CALIBRATION
HFSGain2 = 100;
g2       =  0;
hcal2    = S(2);
RTSGain2 = 500;
c2       = 2.57488;
d2       = -518.276;
e2       = 0.39751;
f2       = 200.8981;
Ro2      = f2+To*e2;


%HFS #3 CALIBRATION
HFSGain3 = 100;
g3       =  0;
hcal3    = S(3);
RTSGain3 = 500;
c3       = 3.9724;
d3       = -480.423;
e3       = 0.255602;
```

```
f3       = 120.7617;
Ro3      = f3+To*e3;


%HFS #4 CALIBRATION
HFSGain4 = 100;
g4       =  0;
hcal4    = S(4);
RTSGain4 = 500;
c4       = 3.89763;
d4       = -488.813;
e4       = 0.261826;
f4       = 125.1414;
Ro4      = f4+To*e4;

%HFS #5 CALIBRATION
HFSGain5 = 100;
g5       =  0;
hcal5    = S(5);
RTSGain5 = 1;
c5       = 2.4478;
d5       = -477.73;
e5       = 0.415353;
f5       = 194.8265;
Ro5      = f5+To*e5;

%HFS #6 CALIBRATION
HFSGain6 = 1;
g6       =  0;
hcal6    = S(6);
RTSGain6 = 1;
c6       = 4.13174;
```

```
d6       = -476.724;
e6       = 0.243154;
f6       = 115.3224;
Ro6      = f6+To*e6;

%Kulite Sensitivities
KS1      = 1.688;    % mV/psi
KS2      = 1.696;
KS3      = 1.727;
KS4      = 1.743;
KS5      = 1.724;
KS6      = 2.000;

%Kulite Gains
KG1      = 10;
KG2      = 10;
KG3      = 10;
KG4      = 10;
KG5      = 10;
KG6      = 10;

%Flux at all locations
q1   = HFS1.*1000000./(HFSGain1.*(g1.*Tblade1+hcal1));
q2   = HFS2.*1000000./(HFSGain2.*(g2.*Tblade2+hcal2));
q3   = HFS3.*1000000./(HFSGain3.*(g3.*Tblade3+hcal3));
q4   = HFS4.*1000000./(HFSGain4.*(g4.*Tblade4+hcal4));
q5   = HFS5.*1000000./(HFSGain5.*(g5.*Tblade5+hcal5));
q6   = HFS6.*1000000./(HFSGain6.*(g6.*Tblade6+hcal6));

%RTS Temperature at all locations
RTS1 = c1.*(Ro1+RTS1./(RTSGain1*100E-6))+d1;
RTS2 = c2.*(Ro2+RTS2./(RTSGain2*100E-6))+d2;
```

```
RTS3 = c3.*(Ro3+RTS3./(RTSGain3*100E-6))+d3;
RTS4 = c4.*(Ro4+RTS4./(RTSGain4*100E-6))+d4;
RTS5 = c5.*(Ro5+RTS5./(RTSGain5*100E-6))+d5;
RTS6 = c6.*(Ro6+RTS6./(RTSGain6*100E-6))+d6;

Pfree=Pfree+Po;
Pplen=Pplen+Pfree;
Pratio=Pplen./Pfree;
Tratio=(Tfree+273.15)./(Tplen+273.15);

%Pressures and Mach Numbers at all locations
Kul1 = Kul1*1000/(KG1*KS1)+Po;
Kul2 = Kul2*1000/(KG2*KS2)+Po;
Kul3 = Kul3*1000/(KG3*KS3)+Po;
Kul4 = Kul4*1000/(KG4*KS4)+Po;
Kul5 = Kul5*1000/(KG5*KS5)+Po;
Kul6 = Kul6*1000/(KG6*KS6)+Po;
M1   = (5*((Pfree./Kul1).^(2/7)-1)).^0.5;
M2   = (5*((Pfree./Kul2).^(2/7)-1)).^0.5;
M3   = (5*((Pfree./Kul3).^(2/7)-1)).^0.5;
M4   = (5*((Pfree./Kul4).^(2/7)-1)).^0.5;
M5   = (5*((Pfree./Kul5).^(2/7)-1)).^0.5;
M6   = (5*((Pfree./Kul6).^(2/7)-1)).^0.5;

%Free-Stream Mach Number at all coolant exit locations
Mpg  =real((5*((Pfree./(Pfree-Ppg)).^(2/7)-1)).^0.5);
Mpn  =real((5*((Pfree./(Pfree-Ppn)).^(2/7)-1)).^0.5);
Mn   =real((5*((Pfree./(Pfree-Pn)).^(2/7)-1)).^0.5);
Msn1 =real((5*((Pfree./(Pfree-Psn1)).^(2/7)-1)).^0.5);
Msn2 =real((5*((Pfree./(Pfree-Psn2)).^(2/7)-1)).^0.5);
Msg  =real((5*((Pfree./(Pfree-Psg)).^(2/7)-1)).^0.5);
```

```
    %Density Ratio at all coolant exit locations (the same for all locations)
    DR   =Pratio.^(2/7).*Tratio;    %coolant/freestream

    %Momentum Ratio at all coolant exit locations
    MRpg  =5*(Pratio.^(2/7).*(1+0.2*Mpg.^2)-1)./Mpg.^2;   %coolant/freestream
    MRpn  =5*(Pratio.^(2/7).*(1+0.2*Mpn.^2)-1)./Mpn.^2;
    MRn   =5*(Pratio.^(2/7).*(1+0.2*Mn.^2)-1)./Mn.^2;
    MRsn1 =5*(Pratio.^(2/7).*(1+0.2*Msn1.^2)-1)./Msn1.^2;
    MRsn2 =5*(Pratio.^(2/7).*(1+0.2*Msn2.^2)-1)./Msn2.^2;
    MRsg  =5*(Pratio.^(2/7).*(1+0.2*Msg.^2)-1)./Msg.^2;

    %Blowing Ratio at all coolant exit locations
    BRpg  =(DR.*MRpg).^0.5;    %coolant/freestream
    BRpn  =(DR.*MRpn).^0.5;
    BRn   =(DR.*MRn).^0.5;
    BRsn1 =(DR.*MRsn1).^0.5;
    BRsn2 =(DR.*MRsn2).^0.5;
    BRsg  =(DR.*MRsg).^0.5;

    %Massflow ratios
    mr    =real(Msn1./(1+0.2*Msn1.^2).^3);
    mrsn1 =mean(mr(front:back));
    mr    =real(Msn2./(1+0.2*Msn2.^2).^3);
    mrsn2 =mean(mr(front:back));
    mr    =real(Msg./(1+0.2*Msg.^2).^3);
    mrsg  =mean(mr(front:back));
    ms    =mrsn1+mrsn2+mrsg;
    mrsn1 =mrsn1./ms;
    mrsn2 =mrsn2./ms;
    mrsg  =mrsg./ms;

end
```

```
% ---- Average Values, Cold Coolant  ----

coolant=mrsg*Tsg+mrsn2*Tsn2+mrsn1*Tsn1;

if typeflag == 1                    %Cooled Analysis

   Tr1    = Tfree - Tdrop1;
   Tr2    = Tfree - Tdrop2;
   Tr3    = Tfree - Tdrop3;
   Tr4    = Tfree - Tdrop4;
   Tr5    = Tfree - Tdrop5;
   Tr6    = Tfree - Tdrop6;

   deltaT1  = (Tr1 - Tblade1)./(Tr1 - coolant);
   deltaT2  = (Tr2 - Tblade2)./(Tr2 - coolant);
   deltaT3  = (Tr3 - Tblade3)./(Tr3 - coolant);
   deltaT4  = (Tr4 - Tblade4)./(Tr4 - coolant);
   deltaT5  = (Tr5 - Tblade5)./(Tr5 - coolant);
   deltaT6  = (Tr6 - Tblade6)./(Tr6 - coolant);

   qprime1  = q1./(Tr1 - coolant);
   qprime2  = q2./(Tr2 - coolant);
   qprime3  = q3./(Tr3 - coolant);
   qprime4  = q4./(Tr4 - coolant);
   qprime5  = q5./(Tr5 - coolant);
   qprime6  = q6./(Tr6 - coolant);

   [p1,S1] = POLYFIT( deltaT1( front:back ), qprime1( front:back ) , 1);
   [p2,S2] = POLYFIT( deltaT2( front:back ), qprime2( front:back ) , 1);
   [p3,S3] = POLYFIT( deltaT3( front:back ), qprime3( front:back ) , 1);
   [p4,S4] = POLYFIT( deltaT4( front:back ), qprime4( front:back ) , 1);
```

```
[p5,S5] = POLYFIT( deltaT5( front:back ), qprime5( front:back ) , 1);
[p6,S6] = POLYFIT( deltaT6( front:back ), qprime6( front:back ) , 1);

h1=10000*p1(1);
h2=10000*p2(1);
h3=10000*p3(1);
h4=10000*p4(1);
h5=10000*p5(1);
h6=10000*p6(1);

n1=-p1(2)./p1(1);
n2=-p2(2)./p2(1);
n3=-p3(2)./p3(1);
n4=-p4(2)./p4(1);
n5=-p5(2)./p5(1);
n6=-p6(2)./p6(1);

mass    = 3.9941*sqrt(75.0437.*Pdp.*(Pup+Po)./(460+(Torr*9/5)+32));

%  ----  Average values of things:

Amass   = mean(mass( front:back ));
APratio = mean(Pratio( front:back ));
ABRpg   = mean(BRpg ( front:back ));
ABRpn   = mean(BRpn ( front:back ));
ABRn    = mean(BRn ( front:back ));
ABRsn1  = mean(BRsn1 ( front:back ));
ABRsn2  = mean(BRsn2 ( front:back ));
ABRsg   = mean(BRsg ( front:back ));
AMRpg   = mean(MRpg ( front:back ));
AMRpn   = mean(MRpn ( front:back ));
AMRn    = mean(MRn ( front:back ));
```

```
    AMRsn1  = mean(MRsn1 ( front:back ));
    AMRsn2  = mean(MRsn2 ( front:back ));
    AMRsg   = mean(MRsg ( front:back ));
    ADR     = mean(DR ( front:back ));

    %  ----  Display Summary of h and eta  ----

    disp(' ');
    disp(' ');
    disp('Location          h          eta');
    disp(['   1           ', num2str(h1,5),'      ', num2str(n1,4)]);
    disp(['   2           ', num2str(h2,5),'      ', num2str(n2,4)]);
    disp(['   3           ', num2str(h3,5),'      ', num2str(n3,4)]);
    disp(['   4           ', num2str(h4,5),'      ', num2str(n4,4)]);
    disp(['   5           ', num2str(h5,5),'      ', num2str(n5,4)]);
    disp(['   6           ', num2str(h6,5),'      ', num2str(n6,4)]);
    disp(['Mass flow : ', num2str(Amass,5)]);
    disp(' ');
    disp(['DR:  ',num2str(ADR,4)]);
    disp(['PR:  ',num2str(APratio,4)]);
    disp('Average Values at sn1')
    disp(['BR:  ',num2str(ABRsn1,4)]);
    disp(['MR:  ',num2str(AMRsn1,4)]);
    disp('Average Values at sn2')
    disp(['BR:  ',num2str(ABRsn2,4)]);
    disp(['MR:  ',num2str(AMRsn2,4)]);
    disp('Average Values at sg')
    disp(['BR:  ',num2str(ABRsg,4)]);
    disp(['MR:  ',num2str(AMRsg,4)]);

end
```

```
if typeflag == 0                %Uncooled Analysis
   deltaT1 = Tfree - Tblade1;
   deltaT2 = Tfree - Tblade2;
   deltaT3 = Tfree - Tblade2;
   deltaT4 = Tfree - Tblade5;
   deltaT5 = Tfree - Tblade5;
   deltaT6 = Tfree - Tblade6;

   qprime1=q1;
   qprime2=q2;
   qprime3=q3;
   qprime4=q4;
   qprime5=q5;
   qprime6=q6;

   [p1,S1] = POLYFIT( deltaT1( front:back ), qprime1( front:back) , 1);
   [p2,S2] = POLYFIT( deltaT2( front:back ), qprime2( front:back) , 1);
   [p3,S3] = POLYFIT( deltaT3( front:back ), qprime3( front:back) , 1);
   [p4,S4] = POLYFIT( deltaT4( front:back ), qprime4( front:back) , 1);
   [p5,S5] = POLYFIT( deltaT5( front:back ), qprime5( front:back) , 1);
   [p6,S6] = POLYFIT( deltaT6( front:back ), qprime6( front:back) , 1);

   h1=10000*p1(1);
   h2=10000*p2(1);
   h3=10000*p3(1);
   h4=10000*p4(1);
   h5=10000*p5(1);
   h6=10000*p6(1);

   Tdrop1=-p1(2)/p1(1);
   Tdrop2=-p2(2)/p2(1);
```

```
    Tdrop3=-p3(2)/p3(1);
    Tdrop4=-p4(2)/p4(1);
    Tdrop5=-p5(2)/p5(1);
    Tdrop6=-p6(2)/p6(1);

    disp(' ');
    disp(' ');
    disp('Location          h          Tdrop');
    disp(['   1           ', num2str(h1,5),'      ', num2str(Tdrop1,4)]);
    disp(['   2           ', num2str(h2,5),'      ', num2str(Tdrop2,4)]);
    disp(['   3           ', num2str(h3,5),'      ', num2str(Tdrop3,4)]);
    disp(['   4           ', num2str(h4,5),'      ', num2str(Tdrop4,4)]);
    disp(['   5           ', num2str(h5,5),'      ', num2str(Tdrop5,4)]);
    disp(['   6           ', num2str(h6,5),'      ', num2str(Tdrop6,4)]);
    disp(' ');
    disp(' ');

end
```

C.2 outraw.m

```
% outrawout.m
% Used to output graphs loaded from data032299b.m
% J. Bubb 6/1/99
%

close all;
format short g;

   disp(' ');
   disp('Location          h          eta');
   disp(['   1           ', num2str(h1,5),'      ', num2str(n1,4)]);
   disp(['   2           ', num2str(h2,5),'      ', num2str(n2,4)]);
   disp(['   3           ', num2str(h3,5),'      ', num2str(n3,4)]);
   disp(['   4           ', num2str(h4,5),'      ', num2str(n4,4)]);
   disp(['   5           ', num2str(h5,5),'      ', num2str(n5,4)]);
   disp(['   6           ', num2str(h6,5),'      ', num2str(n6,4)]);
   disp(['Mass flow : ', num2str(Amass,5)]);
   disp(' ');
   disp(['DR:  ',num2str(ADR,4)]);
   disp(['PR:  ',num2str(APratio,4)]);
   disp('Average Values at sn1')
   disp(['BR:  ',num2str(ABRsn1,4)]);
   disp(['MR:  ',num2str(AMRsn1,4)]);
   disp('Average Values at sn2')
   disp(['BR:  ',num2str(ABRsn2,4)]);
   disp(['MR:  ',num2str(AMRsn2,4)]);
   disp('Average Values at sg')
   disp(['BR:  ',num2str(ABRsg,4)]);
   disp(['MR:  ',num2str(AMRsg,4)]);
```

```
%  ----  Output Graphs  -----

disp(['Outputing Graphs...'])
disp(['File #' num2str(1) ' ' datanames])
disp('1=Blade Temps          2=Time History'   );
disp('3=Slope and Intercept  4=Heat Flux');
disp('5=Span Mach Number');
disp('6=Coolant Temperatures ');
disp('7=Pressure Ratio ');
disp('8=Density Ratio ');
disp('9=Blowing Ratio ');
disp('10=Momentum Ratio ');
disp('99=Temperature History for thesis')
disp('98=Slope Intercept for thesis')
disp('97=Adiabatic Wall Temp for thesis')
disp('96=Heat Transfer Coefficent for thesis')

graphs=input('See what graphs? ','s');
graphs=str2num(graphs);

if isempty(graphs)
   graphs='0';
end

if (sum(graphs==99) )  % ----   Temperature for thesis
   figure
   set(gcf,'Units','Normalized','Position',[.2,.05,1-.2,.8])
   Xone = {t t t t};
   Yone = {Tblade1 Tfree Tr1 coolant};
   Xtwo = {t};
   Ytwo = {q1};
```

```
   [AX,H1,H2,H3,H4]=FANCYPLOT2(...
   Xone,Yone,{200 200 200 200},{'o' 's' 'd' '>'},Xtwo,Ytwo,{200},{'V'});

   set(AX,'FontSize',12)
   set([H1 H2 H3 H4],'color','k')
   axes(AX(1)); ylabel('Temperature, C')
   axes(AX(2)); ylabel('q, W/cm')
   legend2([H3 H4],...
   'Blade Temperature','Freestream Temperature','Recovery Temperature',...
   'Coolant Temeprature','Heat Flux');
   xlabel('Time, s')
   bot=get(gca,'Ylim');
   hold on
   plot([back/100 back/100],[bot(1) bot(2)],'--k')
   plot([front/100 front/100],[bot(1) bot(2)],'--k')
   hold off
end

if (sum(graphs==98) )   % ----   h and eta graph for Thesis
   figure
   set(gcf,'Units','Normalized','Position',[.2,.05,1-.2,.8])
   hold on;
   hand1=plot(deltaT1(front:back),qprime1(front:back),'k.');
   endpts=[ deltaT1(front)+.02 deltaT1(back)-.02 ];
   fit=polyval(p1,endpts);
   plot(endpts,fit,'k-');
   hold off
   set(hand1,'MarkerSize',4)
   set(gca,'FontSize',12)
%   Title(['h and \eta,  ' datanames ' Location #1'],'FontWeight','bold')
   Xlabel('(T_r - T_{blade})/(T_r - T_{coolant})  [ - ]')
   Ylabel('q/(T_r - T_{coolant})  [ W/cm C ]')
```

```
   hand2=gtext(['h= ' num2str(h1,3) ' W/m C    \eta= ' num2str(n1,2) ]);
   set(hand2,'FontSize',12)
   set(gca,'box','on')
end

if (sum(graphs==97) )  % ----   Taw for thesis
   figure
   set(gcf,'Units','Normalized','Position',[.2,.05,1-.2,.8])
   Xone = {t t t};
   Yone = {Tfree Tblade1 Taw1};
   Xtwo = {t};
   Ytwo = {q1};
   [AX,H1,H2,H3,H4]=FANCYPLOT2(...
   Xone,Yone,{200 200 200},{'o' 's' 'd'},Xtwo,Ytwo,{200},{'V'});
   set(AX,'FontSize',12)
   set([H1 H2 H3 H4],'color','k')
   axes(AX(1)); ylabel('Temperature, C')
   axes(AX(2)); ylabel('q, W/cm')
   legend2([H3 H4],...
   'Freestream Temperature','Blade Temperature','Adiabatic Wall Temperature',...
   'Heat Flux');
   xlabel('Time, s')
   hold on
   plot([0 40],[0 0],'-k')
   hold off
end

if (sum(graphs==96) )  % ----   time varying htc for thesis
   figure
   set(gcf,'Units','Normalized','Position',[.2,.05,1-.2,.8])
   Xone = {t(front:back)    [t(front) t(back)]};
   Yone = {htc1(front:back) [h1 h1] };
```

```
   [AX,H1,H2]=FANCYPLOT(Xone,Yone,{100 1},{'o' 's'});
   set(AX,'FontSize',12)
   set([H1 H2],'color','k')
   set([H1(2)],'LineStyle',':')
   set(H2(2),'Marker','none')
   axes(AX(1)); ylabel('Heat Transfer Coefficient, W/m^2 C')
   xlabel('Time, s')
   set(gca,'Ylim',[0 1000])
   legend2([H2(1) H1(2)],...
   'Heat Transfer Coefficient','Average Heat Transfer Coefficient');
   set(gca,'box','on')
end


if (sum(graphs==1))      % ----   Blade Temperatures
   figure
   set(gcf,'Units','Normalized','Position',[.2,.05,1-.2,.8])
   plot(t,Tblade1,t,Tblade2,t,Tblade4,t,Tblade5,t,Tblade6);
   legend('Tblade1','Tblade2','Tblade4','Tblade5','Tblade6')
   title(['Blade Temperatures,  ', datanames],'FontWeight','bold')
   xlabel('Time, s')
   ylabel('Temperature, C')
end

if (sum(graphs==2) )  % ----   Time History
   figure
   set(gcf,'Units','Normalized','Position',[.2,.05,1-.2,.8])
   hold on;
   H1=plot(t,Tplen,'r',t,Tblade1,'m',t,coolant,'k');
   [AX, H2, H3] = PLOTYY(t,Tfree,t,q1);
   bot=get(gca,'Ylim');
   plot([back/100 back/100],[bot(1) bot(2)],'--')
```

```
   plot([front/100 front/100],[bot(1) bot(2)],'--')
   hold off;
   axes(AX(1)); ylabel('Temperature, C')
   axes(AX(2)); ylabel('q, W/cm')
   legend([H1; H2; H3],'Plenum','Blade','Coolant','Freestream','q1')
   Title(['Timehistory,  ' datanames],'FontWeight','bold')
   xlabel('Time, s')
end


if (sum(graphs==4))      % ----   Heat Flux
   figure
   set(gcf,'Units','Normalized','Position',[.2,.05,1-.2,.8])
   plot(t,q6,t,q5,t,q4,t,q3,t,q2,t,q1)
   legend('q6','q5','q4','q3','q2','q1')
   title(['Heat Flux,  ', datanames],'FontWeight','bold')
   xlabel('Time, s')
   ylabel('Flux, W/m^2-C')
end

if (sum(graphs==5))      % ----   Streamwise Mach-Number Profile
   figure
   set(gcf,'Units','Normalized','Position',[.2,.05,1-.2,.8])
   plot(t,M1,t,M2,t,M4,t,M5,t,M6);
   legend('1','2','4','5','6')
   title(['Streamwise Mach-Number Profile,  ', datanames],'FontWeight','bold')
   xlabel('Time, s')
   ylabel('Pressure, psia')

end

if (sum(graphs==6))
```

```
   figure
   set(gcf,'Units','Normalized','Position',[.2,.05,1-.2,.8])
   plot(t,Tplen,t,Tsn1,t,Tsn2,t,Tsg,t,coolant)
   legend('T_{plenum}','T_{sn1}','T_{sn2}','T_{sg}','T_{average}')
   title('Coolant Temperatures')
   xlabel('Time  [ s ]')
   ylabel('Temperature  [ C ]')
end

if (sum(graphs==7) )
   figure
   set(gcf,'Units','Normalized','Position',[.2,.05,1-.2,.8])
   H1=plot(t(front:back),Pratio(front:back));
   title('Time History of Pressure Ratio','FontWeight','bold')
   xlabel('Time  [ s ]')
   ylabel('Pressure Ratio  [ - ]')
end


if (sum(graphs==8) )
   figure
   set(gcf,'Units','Normalized','Position',[.2,.05,1-.2,.8])
   H1=plot(t(front:back),DR(front:back),'-k');
   set(gca,'FontSize',12)
   xlabel('Time  [ s ]')
   ylabel('Density Ratio  [ - ]')
   set(gca,'box','on','ygrid','on')
%   title('Time History of Density Ratio','FontWeight','bold')
end


if (sum(graphs==9) )
```

```
   figure
   set(gcf,'Units','Normalized','Position',[.2,.05,1-.2,.8])
   Xone = {t(front:back) t(front:back) t(front:back)};
   Yone = { BRsn1(front:back) BRsn2(front:back) BRsg(front:back)};
   [AX,H1,H2]=FANCYPLOT(Xone,Yone,{100 100 100},{'o' 's' 'v'});
   set(AX,'FontSize',12)
   set([H1 H2],'color','k')
   legend2([H2],'SN1','SN2','SG');
   set(gca,'box','on','ygrid','on')
%   title('Time History of Blowing Ratio','FontWeight','bold')
   xlabel('Time  [ s ]')
   ylabel('Blowing Ratio  [ - ]')
end

if (sum(graphs==10) )
      figure
   set(gcf,'Units','Normalized','Position',[.2,.05,1-.2,.8])
   Xone = {t(front:back) t(front:back) t(front:back)};
   Yone = { MRsn1(front:back) MRsn2(front:back) MRsg(front:back)};
   [AX,H1,H2]=FANCYPLOT(Xone,Yone,{100 100 100},{'o' 's' 'v'});
   set(AX,'FontSize',12)
   set([H1 H2],'color','k')
   legend2([H2],'SN1','SN2','SG');
   set(gca,'box','on','ygrid','on')
%   title('Time History of Momentum Ratio','FontWeight','bold')
   xlabel('Time  [ s ]')
   ylabel('Momentum Ratio  [ - ]')

end
```

C.3 summary.m

```
% summary.m
% Summary of Blowing Ratio experiments.
% Jim Bubb 3/22/99

clear all
close all

gub=path;
j=gub(1);

% Analysis was done with the code data032299.m
% Sensitivities and Tdrops used were:
% S =     [242 104 146 135 173 151]
% Tdrop = [5.95 5.15 5.78 9.03 10.18 16.33]
%
% Description of data:
% time: run time used for analysis
% mass: mass flow in g/s from Orifice Plate
% PR:   Pressure ratio based on plenum conditions
% DR:   Density ratio based on plenum conditions
% BR:   Blowing Ratio based on [sn1 sn2 sg]
% MR:   Momentum ratio based on [sn1 sn2 sg]
% h:    HTC [g1 g2 g3 g4 g5 g6]
% eta:  film cooling effectivness [g1 g2 g3 g4 g5 g6]
% uh:   Uncertainty in HTC [g1 g2 g3 g4 g5 g6]
% ueta: Uncertainty in eta [g1 g2 g3 g4 g5 g6]

time(1)  = {'7-23'};
mass(1)  = 14.614;
```

```
PR(1)    = 1.014;
DR(1)    = 2.176;
BR(1,:)  = [1.603 1.558 1.532];
MR(1,:)  = [1.182 1.116 1.080];
h(1,:)   = [819.79 786.30 712.06 752.85 744.10 880.68];
eta(1,:) = [0.2809 0.1871 0.3673 0.2254 0.2098 0.3072];
notes1   = {...
      'afosr/data/03_22_99/run1.asc' ...
      'Use Channel_Setup_3_22_99.xls' ...
      'Analyzed with data032299.m (but you must modify the columns)' ...
      'T2 is dead T2=T1' ...
      'T5=T5-5.5   T1=T1-12.5'};

time(2)  = {'7-23'};
mass(2)  = 14.173;
PR(2)    = 1.025;
DR(2)    = 1.906;
BR(2,:)  = [1.584 1.515 1.475];
MR(2,:)  = [1.317 1.205 1.142];
h(2,:)   = [773.91 778.39 653.94 766.90 756.16 893.04];
eta(2,:) = [0.2640 0.1742 0.3494 0.2204 0.2080 0.3324];
notes2   = {...
      'afosr/data/03_22_99/run2.asc' ...
      'Use Channel_Setup_3_22_99.xls' ...
      'Analyzed with data032299.m (but you must modify the columns)' ...
      'A little noise in the temp signals but OK' ...
      'T2 is dead T2=T1' ...
      'T5=T5-5.5   T1=T1-12.5'};

time(3)  = {'8-27'};
mass(3)  = 14.051;
PR(3)    = 1.047;
```

```
DR(3)    = 1.600;
BR(3,:)  = [1.588 1.484 1.418];
MR(3,:)  = [1.580 1.381 1.260];
h(3,:)   = [ 744.71 810.37 622.81 719.15 805.63 920.67];
eta(3,:) = [0.2419 0.18501 0.31052 0.16782 0.20961 0.33356];
uh(3,:)  = [ 43.4895 49.1858 35.0109 42.5161 48.2731 49.387];
ueta(3,:)= [ 0.028327 0.032713 0.023188 0.032383 0.030351 0.020657];

notes3   = {...
      'afosr/data/03_22_99/run3.asc'...
      'Analyzed with data032299.m (but you must modify the columns)' ...
      'Use Channel_Setup_3_22_99.xls'...
      'T5=T6   T1=T2'};

time(4)  = {'8-27'};
mass(4)  = 15.763;
PR(4)    = 1.069;
DR(4)    = 1.396;
BR(4,:)  = [1.596 1.472 1.386];
MR(4,:)  = [1.828 1.554 1.378];
h(4,:)   = [800.32 752.60 610.58 724.48 775.54 827.14];
eta(4,:) = [0.2396 0.1837 0.2761 0.1652 0.2106 0.2997];
uh(4,:)  = [ 34.5119 32.1695 24.7761 30.8922 33.8784 33.5732];
ueta(4,:)= [ 0.026964 0.029173 0.023793 0.029621 0.028293 0.022751];
notes4   = {...
      'afosr/data/03_22_99/run4.asc'...
      'Analyzed with data032299b.m' ...
      'Use Channel_Setup_3_22_99b.xls'};


time(5)  = {'8-26'};
mass(5)  = 16.157;
```

```
PR(5)    = 1.089;
DR(5)    = 1.309;
BR(5,:)  = [1.623 1.491 1.391];
MR(5,:)  = [2.013 1.701 1.479];
h(5,:)   = [826.11 755.24 622.62 756.14 799.41 855.97];
eta(5,:) = [0.2172 0.1928 0.2570 0.1896 0.2336 0.2970];
uh(5,:)  = [48.7047 43.0595 34.6552 43.1662 47.9754 48.9852];
ueta(5,:)= [0.040234 0.040493 0.035751 0.040413 0.039615 0.034144];
notes5   = {...
      'Analyzed with data032299b.m' ...
      'Use Channel_Setup_3_22_99b.xls' ...
      'afosr/data/03_22_99/run5.asc'};

time(6)  = {'8-26'};
mass(6)  = 19.588;
PR(6)    = 1.109;
DR(6)    = 1.882;
BR(6,:)  = [2.062 1.873 1.724];
MR(6,:)  = [2.265 1.870 1.585];
h(6,:)   = [731.39 754.67 575.00 795.10 792.44 846.97];
eta(6,:) = [0.2796 0.2223 0.2698 0.2357 0.2242 0.2710];
uh(6,:)  = [27.0127 27.972 20.4441 27.9846 28.579 28.3697];
ueta(6,:)= [0.014469 0.016334 0.013559 0.014661 0.01531 0.012518];
notes6   = {...
      'Analyzed with data032299b.m' ...
      'Use Channel_Setup_3_22_99b.xls' ...
      'afosr/data/03_22_99/run6.asc'};

time(7)  = {'8-26'};
mass(7)  = 19.115;
PR(7)    = 1.127;
DR(7)    = 1.439;
```

```
BR(7,:)  = [1.872 1.696 1.552];
MR(7,:)  = [2.437 2.002 1.675];
h(7,:)   = [844.46 786.96 642.79 773.81 778.99 817.18];
eta(7,:) = [0.2102 0.2242 0.2449 0.2159 0.1915 0.2428];
uh(7,:)  = [30.484 27.1626 21.847 26.4962 28.0373 28.267];
ueta(7,:)= [0.025258 0.023795 0.022561 0.023772 0.025655 0.022901];
notes7   = {...
      'Analyzed with data032299b.m' ...
      'Use Channel_Setup_3_22_99b.xls' ...
      'afosr/data/03_22_99/run7.asc'};

time(8)  = {'14-25'};
mass(8)  = 21.521;
PR(8)    = 1.148;
DR(8)    = 2.005;
BR(8,:)  = [2.303 2.088 1.886];
MR(8,:)  = [2.654 2.183 1.781];
h(8,:)   = [508.29 617.45 492.52 733.63 707.45 713.00];
eta(8,:) = [0.2830 0.2232 0.2333 0.2389 0.1984 0.2557];
notes8   = {...
      'afosr/data/03_22_99/run8.asc' ...
      'Analyzed with data032299b.m' ...
      'Use Channel_Setup_3_22_99b.xls' ...
      'all the fluxes are screwy - ignore this data'};


time(9)  = {'8-26'};
mass(9)  = 20.009;
PR(9)    = 1.168;
DR(9)    = 1.361;
BR(9,:)  = [1.959 1.774 1.599];
MR(9,:)  = [2.825 2.316 1.882];
```

```
h(9,:)   = [839.93 777.55 662.42 734.07 806.17 815.00];
eta(9,:) = [0.1819 0.2230 0.2295 0.2160 0.1781 0.2755];
notes9   = {...
      'Analyzed with data032299b.m' ...
      'Use Channel_Setup_3_22_99b.xls' ...
      'afosr/data/03_22_99/run9.asc'};


time(10)  = {'8-26'};
mass(10)  = 21.981;
PR(10)    = 1.184;
DR(10)    = 1.484;
BR(10,:)  = [2.125 1.907 1.707];
MR(10,:)  = [3.045 2.453 1.965];
h(10,:)   = [847.40 789.31 644.57 762.65 796.58 787.55];
eta(10,:) = [0.1942 0.2152 0.2217 0.2316 0.16189 0.2553];
notes10   = {...
      'afosr/data/03_22_99/run10.asc' ...
      'Use Channel_Setup_3_22_99b.xls' ...
      'Analyzed with data032299b.m'};

time(11)  = {'9-26'};
mass(11)  = 15.163;
PR(11)    = 1.025;
DR(11)    = 2.138;
BR(11,:)  = [1.666 1.608 1.561];
MR(11,:)  = [1.299 1.210 1.140];
h(11,:)   = [862.92 795.30 667.40 783.25 760.72 889.44];
eta(11,:) = [0.3036 0.1817 0.3620 0.2173 0.2057 0.3110];
notes11   = {...
      'afosr/data/03_22_99/run11.asc' ...
      'Analyzed with data032299b.m' ...
```

```
      'Use Channel_Setup_3_22_99b.xls' ...
      'shock was popped for Oli, data is good'};

time(12)  = {'8-26'};
mass(12)  = 18.970;
PR(12)    = 1.046;
DR(12)    = 2.859;
BR(12,:)  = [2.094 1.984 1.890];
MR(12,:)  = [1.537 1.379 1.252];
h(12,:)   = [775.61 800.27 640.82 779.88 791.61 884.17];
eta(12,:) = [0.3253 0.1934 0.3446 0.2223 0.2046 0.2923];
notes12   = {...
      'afosr/data/03_22_99/run12.asc' ...
      'Analyzed with data032299b.m' ...
      'Use Channel_Setup_3_22_99b.xls' ...
      'shock was popped for Oli, data is good'};

time(13)  = {'10-23'};
mass(13)  = 15.721;
PR(13)    = 1.022;
DR(13)    = 3.342;
BR(13,:)  = [2.044 1.988 1.936];
MR(13,:)  = [1.251 1.183 1.122];
h(13,:)   = [878.14 788.46 655.63 763.74 744.08 840.55];
eta(13,:) = [0.3215 0.1775 0.3604 0.2140 0.2025 0.2914];
notes13   = {...
      'afosr/data/11_24/run11_24_01.asc' ...
      'Use data120298.m to analyze' ...
      'From 11/24 runs'};

time(14)  = {'8-22'};
mass(14)  = 18.601;
```

```
PR(14)    = 1.06;
DR(14)    = 3.217;
BR(14,:)  = [2.320 2.189 2.063];
MR(14,:)  = [1.675 1.492 1.325];
h(14,:)   = [800.99 767.59 591.67 651.25 729.04 844.48];
eta(14,:) = [0.3300 0.1813 0.3326 0.2005 0.1862 0.2984];
notes14   = {...
      'afosr/data/11_24/run11_24_02.asc' ...
      'Use data120298.m to analyze' ...
      'From 11/24 runs'};


time(15)  = {'8-23'};
mass(15)  = 20.256;
PR(15)    = 1.102;
DR(15)    = 2.476;
BR(15,:)  = [2.299 2.127 1.956];
MR(15,:)  = [2.140 1.831 1.549];
h(15,:)   = [736.76 758.61 535.61 777.02 744.47 778.05];
eta(15,:) = [0.2847 0.1979 0.2578 0.2227 0.1835 0.2763];
notes15   = {...
      'afosr/data/11_24/run11_24_03.asc' ...
      'Use data120298.m to analyze' ...
      'From 11/24 runs'};

time(16)  = {'10-22'};
mass(16)  = 22.618;
PR(16)    = 1.145;
DR(16)    = 2.558;
BR(16,:)  = [2.571 2.355 2.127];
MR(16,:)  = [2.591 2.173 1.774];
h(16,:)   = [583.80 691.49 527.83 743.42 732.21 757.22];
```

```
eta(16,:) = [0.2911 0.1948 0.2217 0.2341 0.1785 0.2438];
notes16   = {...
      'afosr/data/11_24/run11_24_04.asc' ...
      'Use data120298.m to analyze' ...
      'Fluxes are a little bit noisy, I somehwat trust them though' ...
      'From 11/24 runs'};

time(17)  = {'8-22'};
mass(17)  = 24.77;
PR(17)    = 1.190;
DR(17)    = 2.684;
BR(17,:)  = [2.864 2.601 2.308];
MR(17,:)  = [3.075 2.537 1.998];
h(17,:)   = [422.58 609.10 541.60 706.15 658.04 711.37];
eta(17,:) = [0.2568 0.1571 0.1927 0.1976 0.1516 0.2218];
notes17   = {...
      'afosr/data/11_24/run11_24_05.asc' ...
      'Use data120298.m to analyze' ...
      'Data is noisy, especially g1, dont use this'  ...
      'From 11/24 runs'};

time(18)  = {'8-25'};
mass(18)  = 0;
PR(18)    = 0;
DR(18)    = 0;
BR(18,:)  = [0];
MR(18,:)  = [0];
h(18,:)   = [674.52 689.82 584.05 695.20 699.88 730.23];
eta(18,:) = [0      0      0      0      0      0     ];
notes18   = {...
      'afosr\data\03_22_99\run13.asc.asc' ...
      'Analyzed with data032299b.m' ...
```

```
      'Uncooled Run' ...
      'Tdrop = [5.87 5.23 6.05 8.92 11.34 16.72]'};

time(19)  = {'8-25'};
mass(19)  = 0;
PR(19)    = 0;
DR(19)    = 0;
BR(19,:)  = [0];
MR(19,:)  = [0];
h(19,:)   = [666.33 690.10 581.96 692.24 694.14 722.37];
eta(19,:) = [0      0      0      0      0      0     ];
notes19   = {...
      'afosr\data\03_22_99\run14.asc' ...
      'Analyzed with data032299b.m' ...
      'Uncooled Run' ...
      'Tdrop = [6.80 6.52 7.27 9.43 11.92 16.87]'};

time(20)  = {'8-25'};
mass(20)  = 17.087;
PR(20)    = 1.039;
DR(20)    = 3.165;
BR(20,:)  = [2.142 2.041 1.960];
MR(20,:)  = [1.449 1.316 1.214];
h(20,:)   = [914.15 829.02 627.78 779.46 782.70 876.90];
eta(20,:) = [0.3079 0.1825 0.3452 0.2255 0.1877 0.2848];
notes20   = {...
      'afosr\data\11_23\Cooling\run11_23_01.asc' ...
      'Analysed with data120298.m'};

time(21)  = {'8-22'};
mass(21)  = 16.353;
PR(21)    = 1.037;
```

```
DR(21)    = 2.513;
BR(21,:)  = [1.895 1.812 1.743];
MR(21,:)  = [1.429 1.308 1.210];
h(21,:)   = [848.88 804.07 625.23 769.37 750.35 886.35];
eta(21,:) = [0.2963 0.1855 0.3274 0.2244 0.1774 0.3021];
notes21   = {...
      'afosr\data\11_23\Cooling\run11_23_02.asc' ...
      'Analysed with data120298.m'};

time(22)  = {'8-22'};
mass(22)  = 16.353;
PR(22)    = 1.037;
DR(22)    = 2.513;
BR(22,:)  = [1.895 1.812 1.743];
MR(22,:)  = [1.429 1.308 1.210];
h(22,:)   = [848.88 804.07 625.23 769.37 750.35 886.35];
eta(22,:) = [0.2963 0.1855 0.3274 0.2244 0.1774 0.3021];
notes22   = {...
      'afosr\data\11_23\Cooling\run11_23_02.asc' ...
      'Analysed with data120298.m'};

time(23)  = {'8-22'};
mass(23)  = 17.864;
PR(23)    = 1.164;
DR(23)    = 1.873;
BR(23,:)  = [2.271 2.076 1.868];
MR(23,:)  = [2.756 2.304 1.866];
h(23,:)   = [783.16 730.50 649.98 785.80 757.00 762.43];
eta(23,:) = [0.1746 0.1545 0.1956 0.2366 0.1594 0.2040];
notes23   = {...
      'afosr\data\11_23\Cooling\run11_23_03.asc' ...
      'Analysed with data120298.m'};
```

```
time(24)  = {'8-22'};
mass(24)  = 22.747;
PR(24)    = 1.16;
DR(24)    = 2.107;
BR(24,:)  = [2.406 2.203 1.978];
MR(24,:)  = [2.750 2.306 1.859];
h(24,:)   = [821.75 748.68 638.40 781.16 782.66 793.37];
eta(24,:) = [0.2309 0.1751 0.1990 0.2379 0.1729 0.2201];
notes24   = {...
      'afosr\data\11_23\Cooling\run11_23_04.asc' ...
      'Analysed with data120298.m'};

time(25)  = {'5-24'};
mass(25)  = 16.381;
PR(25)    = 1.040;
DR(25)    = 2.796;
BR(25,:)  = [2.019 1.932 1.848];
MR(25,:)  = [1.458 1.336 1.221];
h(25,:)   = [843.82 788.76 648.29 733.49 741.98 825.96];
eta(25,:) = [0.3279 0.1844 0.3490 0.2195 0.2037 0.2722];
notes25   = {...
      'afosr\data\11_23\Cooling\run11_23_05.asc' ...
      'Analysed with data120298.m'};

time(26)  = {'7-25'};
mass(26)  = 14.709;
PR(26)    = 1.043;
DR(26)    = 2.170;
BR(26,:)  = [1.795 1.714 1.638];
MR(26,:)  = [1.487 1.356 1.237];
h(26,:)   = [812.08 783.74 616.72 748.30 732.39 808.28];
```

```
eta(26,:) = [0.3085 0.1894 0.3401 0.2208 0.1926 0.2779];
notes26   = {...
      'afosr\data\11_23\Cooling\run11_23_06.asc' ...
      'Analysed with data120298.m'};

time(27)  = {'6-21'};
mass(27)  = 0;
PR(27)    = 0;
DR(27)    = 0;
BR(27,:)  = [0];
MR(27,:)  = [0];
h(27,:)   = [0];
eta(27,:) = [0];
notes27   = {...
      'afosr\data\11_23\Cooling\run11_23_07.asc' ...
      'Analysed with data120298.m' ...
      'Ugly data, dont use, not sure what went wrong with this run'};

time(31)  = {'7-27'};
mass(31)  = 14.302;
PR(31)    = 1.038;
DR(31)    = 1.949;
BR(31,:)  = [1.665 1.599 1.534];
MR(31,:)  = [1.427 1.316 1.211];
h(31,:)   = [790.52 776.83 581.58 744.32 728.25 848.81];
eta(31,:) = [0.2886 0.1636 0.3235 0.2092 0.1779 0.2979];
notes31   = {...
      'afosr\data\11_23\Cooling\run11_23_09.asc' ...
      'Analysed with data120298.m'};

time(32)  = {'6-25'};
mass(32)  = 16.528;
```

```
PR(32)    = 1.036;
DR(32)    = 3.090;
BR(32,:)  = [2.089 2.007 1.925];
MR(32,:)  = [1.416 1.306 1.201];
h(32,:)   = [820.31 775.73 633.50 760.82 740.69 864.26];
eta(32,:) = [0.3278 0.1820 0.3445 0.2254 0.1976 0.2825];
notes32   = {...
      'afosr\data\11_23\Cooling\run11_23_10.asc' ...
      'Analysed with data120298.m'};


time(28)  = {'8-25'};
mass(28)  = 22.616;
PR(28)    = 1.166;
DR(28)    = 2.224;
BR(28,:)  = [2.468 2.272 2.053];
MR(28,:)  = [2.747 2.329 1.902];
h(28,:)   = [621.13 710.93 613.37 916.89 772.83 805.64];
eta(28,:) = [0.2341 0.1736 0.1892 0.2476 0.1757 0.2191];
notes28   = {...
      'afosr\data\11_23\Cooling\run11_23_noshock1.asc' ...
      'Analysed with data120298.m'};

time(29)  = {'8-25'};
mass(29)  = 21.467;
PR(29)    = 1.166;
DR(29)    = 1.877;
BR(29,:)  = [2.273 2.085 1.875];
MR(29,:)  = [2.759 2.321 1.876];
h(29,:)   = [702.66 735.84 611.76 759.60 757.26 756.28];
eta(29,:) = [0.1708 0.1611 0.1908 0.2363 0.1595 0.2103];
notes29   = {...
```

```
      'afosr\data\11_23\Cooling\run11_23_noshock2.asc' ...
      'Analysed with data120298.m'};

time(30)  = {'8-25'};
mass(30)  = 21.456;
PR(30)    = 1.165;
DR(30)    = 1.792;
BR(30,:)  = [2.227 2.038 1.834];
MR(30,:)  = [2.772 2.323 1.880];
h(30,:)   = [776.48 743.02 637.32 763.15 752.34 758.43];
eta(30,:) = [0.1992 0.1734 0.2001 0.2383 0.1591 0.2178];
notes30   = {...
      'afosr\data\11_23\Cooling\run11_23_noshock3.asc' ...
      'Analysed with data120298.m'};


time(33)  = {'7-21'};
mass(33)  = 0;
PR(33)    = 1.311;
DR(33)    = 1.49;
BR(33,:)  = [2.742 2.135 1.765];
MR(33,:)  = [5.052 3.062 2.092];
h(33,:)   = [812.94 704.43 625.11 731.71 789.09 968.4];
eta(33,:) = [0.0765 0.0976 0.1633 0.1892 0.1311 0.3674];
notes33   = {...
      'afosr\data\11_19\pvar_02.asc' ...
      'Analyzed with data61119.m' ...
      'Noisy HFS data, filtered HFS6 ' ...
      'Tblade6=Tblade5 (thermocouple shorted)' ...
      'all of this data is bad because it wasnt documented well' ...
      'Bottom line: dont use it'  };
```

C.4 summaryout.m

```
%Summaryout.m
%output of data summarized in summary.m
%type summary at the command prompt before running this code

close all

gub=path;
j=gub(1);
names    = [ j ':\afosr\bubb\data\bl2d.txt'];
load(names)

%Blade Geometry
% Suction side length (inches)
suction  = 9.760;
% Pressure side length (inches)
pressure = 6.001;
% Arial chord (inches) (stagnation pt to stagnation pt)
archord   = 5.314;
% Axial chord (inches)
axchord    = 4.643;
% Gauge Locations (inches) (front stag pt)
gl = [ 1.515 1.916 2.328 2.730 3.137 3.548];
% Coolant Exit locations (inches) (from stag pt)
cl = [ -0.765 -0.231 0 0.305 0.422 1.130];
% Non-dimensional gauge location (by SS length)
ngl = gl./suction;
% Non-dimension coolant exit (by SS length)
ncl = cl./suction;
% Non-dimensional x for BLD@ HTC values
```

```
ndx = bl2d(:,1)*39.37007/suction;
% BL2D htc values
bl2dh = bl2d(:,2);


%  ----  Output Graphs  -----

disp(['Outputing Graphs...'])
disp('1=Repeatability')
disp('2=Results')
disp('3=Mass Flow')
disp('4=Streamwise eta')
disp('5=Streamwise HTC')
disp('6=BL2D Output')
disp('7=Uncertainty Results')
graphs=input('See what graphs? ','s');
graphs=str2num(graphs);

if isempty(graphs)
   graphs='0';
end
% ----   Rpeatability analysis at PR=1.04
joe1=[3 12 ];
joe2=[20 21 22 25 26 31 32];   % runs that are at 1.04 pratio

m1=mean([h(joe1,:); h(joe2,:)]);
s1=std([h(joe1,:); h(joe2,:)]);

m2=mean([eta(joe1,:); eta(joe2,:)]);
s2=std([eta(joe1,:); eta(joe2,:)]);

%Student t confidence intervals
```

```
t=g01fbf('L',0.95,length([h(joe1,1); h(joe2,1)]));

hmax=m1+t*s1;
hmin=m1-t*s1;
hcb =hmax-m1;
hcbp=hcb./m1;

etamax=m2+t*s2;
etamin=m2-t*s2;
etacb=etamax-m2;
etacbp=etacb./m2;

if (sum(graphs==1) )
   figure(50)
   set(gcf,'Position',[50 50 600 650])
   for i=1:6
      subplot(3,2,i)
      hold on
      plot(PR(joe1),h(joe1,i),'ko')
      plot(PR(joe2),h(joe2,i),'k^')
      hold off
      set(gca,'FontSize',12,'Xlim',[1.02 1.06],'Ylim',[600 1000])
      TH=text(1.025,950,['Gauge ' num2str(i)]);
      set(TH,'FontWeight','bold')
      ylabel('h [ W / m^2 C ]')
      xlabel('Pressure Ratio [ - ]')
   end

   figure(51)
   set(gcf,'Position',[50 50 600 650])
   joe1=[3 12 ];
   joe2=[20 21 22 25 26 31 32];   % runs that are at 1.04 pratio
```

```
   s1=std([h(joe1,:); h(joe2,:)]);
   s2=std([eta(joe1,:); eta(joe2,:)]);
   for i=1:6
      subplot(3,2,i)
      hold on
      plot(PR(joe1),eta(joe1,i),'ko')
      plot(PR(joe2),eta(joe2,i),'k^')
      hold off
      set(gca,'FontSize',12,'Xlim',[1.02 1.06],'Ylim',[.15 .36])
      TH=text(1.021,.34,['Gauge ' num2str(i)]);
      set(TH,'FontWeight','bold')
      ylabel('\eta [ - ]')
      xlabel('Pressure Ratio [ - ]')
   end

   s1;
   s2;
end


% RN = Parses the data for the Runs you want included in the data set
RN1  = [1 2 3 4 5 6 7 9 10 11 12];  %runs from 3/22/99
RN2  = [13 14 15 16];           %runs from 11/22/99
PR1  = PR(RN1);
h1   = h(RN1,:);
eta1 = eta(RN1,:);
PR2  = PR(RN2);
h2   = h(RN2,:);
eta2 = eta(RN2,:);
PR3  = PR([RN1 RN2]);
mass1= mass([RN1 RN2]);
```

```
%sort the runs into ascending pressure ratio
[PR1, I1] = sort(PR1);
h1=h1(I1,:);
eta1=eta1(I1,:);
[PR2, I2] = sort(PR2);
h2=h2(I2,:);
eta2=eta2(I2,:);
[PR3, I3] = sort(PR3);
mass1=mass1(I3);

if (sum(graphs==2) )

   % style : graph style,
   % 0: seperature h and eta graphs, distinguish between days
   % 1: combined h and eta graphs, distinguish between days
   % 2: combined h and eta graph, don't distingish between days
   % 3: combined h and eta graph, error bars

   style=0;

   switch style
   case (0)
      for i=1:6
         figure(2*i-1)
         set(gcf,'Position',[50 50 600 650])
         HAND1=errorbar(PR1,h1(:,i),2*s1(i)*ones(1,length(PR1)),'k-o');
         hold on
         HAND2=errorbar(PR2,h2(:,i),2*s1(i)*ones(1,length(PR2)),'k:^');
         hold off
         set(gca,'Ylim',[0 1000],'FontSize',12)

         ylabel('Heat Transfer Coefficient [ W/m^2 C ]')
```

```
         xlabel('Pressure Ratio [ - ]')
%        Title(['Gauge ' num2str(i)])
         legend([HAND1(2) HAND2(2)],'Runs from 3/22/99','Runs from 11/22/99',4)

         figure(2*i)
         set(gcf,'Position',[50 50 600 650])
         HAND1=errorbar(PR1,eta1(:,i),2*s2(i)*ones(1,length(PR1)),'k-o');
         hold on
         HAND2=errorbar(PR2,eta2(:,i),2*s2(i)*ones(1,length(PR2)),'k:^');
         hold off
         set(gca,'Ylim',[0 .40],'FontSize',12)

         ylabel('Effectiveness [ - ]')
         xlabel('Pressure Ratio [ - ]')
%        Title(['Gauge ' num2str(i)])
         legend([HAND1(2) HAND2(2)],'Runs from 3/22/99','Runs from 11/22/99',4)

         %figure(2*i)
         %Title(['Gauge ' num2str(i)])
         %set(gcf,'Position',[50 50 600 650])
         %plot(PR1,eta1(:,i),'o-',PR2,eta2(:,i),'^-')
         %ylabel('Effectiveness')
         %xlabel('Pressure Ratio')
         %set(gca,'Ylim',[0 0.40])
         %Title(['Gauge ' num2str(i)])
      end
   case(1)
      for i=1:6
         figure(i)
         set(gcf,'Position',[50 50 600 650])
         subplot(2,1,1)
         plot(PR1,h1(:,i),'o-',PR2,h2(:,i),'^-')
```

```
      ylabel ('Heat Transfer Coefficient')
      xlabel('Pressure Ratio')
      set(gca,'Ylim',[0 1000])
      Title(['Gauge ' num2str(i)])
      subplot(2,1,2)
      plot(PR1,eta1(:,i),'o-',PR2,eta2(:,i),'^-')
      ylabel('Effectiveness')
      xlabel('Pressure Ratio')
      set(gca,'Ylim',[0 0.40])
   end
case(2)
   for i=1:6
      figure(i)
      set(gcf,'Position',[50 50 600 650])
      subplot(2,1,1)
      plot(PR1,h1(:,i),'o',PR2,h2(:,i),'o')
      ylabel('Heat Transfer Coefficient')
      xlabel('Pressure Ratio')
      set(gca,'Ylim',[0 1000])
      title(['Gauge ' num2str(i)])
      subplot(2,1,2)
      plot(PR1,eta1(:,i),'o',PR2,eta2(:,i),'o')
      ylabel('Effectiveness')
      xlabel('Pressure Ratio')
      set(gca,'Ylim',[0 0.40])
   end
case(3)
   for i=1:6
      figure(i)
      set(gcf,'Position',[50 50 600 650])
      subplot(2,1,1)
      errorbar(PR1,h1(:,i),s1(i)*ones(1,length(PR1)),'o')
```

```
        hold on
        errorbar(PR2,h2(:,i),s1(i)*ones(1,length(PR2)),'o')
        hold off
        ylabel('Heat Transfer Coefficient')
        xlabel('Pressure Ratio')
        set(gca,'Ylim',[0 1000])
        title(['Gauge ' num2str(i)])
        subplot(2,1,2)
        errorbar(PR1,eta1(:,i),s2(i)*ones(1,length(PR1)),'o')
        hold on
        errorbar(PR2,eta2(:,i),s2(i)*ones(1,length(PR2)),'o')
        hold off
        ylabel('Effectiveness')
        xlabel('Pressure Ratio')
        set(gca,'Ylim',[0 0.40])
      end
   end
end

if (sum(graphs==3) )

   figure
   set(gcf,'Units','Normalized','Position',[.2,.05,1-.2,.8])
   plot(PR3,mass1,'ko')
   set(gca,'FontSize',12)
   set(gca,'box','on')

   title('Massflow')
   ylabel('Mass flow, [ g/s ]')
   xlabel('Pressure Ratio [ - ]')
end
```

```
if (sum(graphs==4) )
   figure
   this = 3; %dataset for 1.04 pressure ratio
   set(gcf,'Position',[50 50 600 650])
   plot(ngl,eta(this,:),'ko-')
   set(gca,'Ylim',[0 .4],'FontSize',12)
   ylabel('Effectiveness [ - ]')
   xlabel('Non-dimensional Suctionside Distance [ - ]')
   hold on
   gauge([]);
   hold off
end

if (sum(graphs==5) )
   figure
   this = 3; %dataset for 1.04 pressure ratio
   set(gcf,'Position',[50 50 600 650])
   plot(ngl,h(this,:),'ko-')
   set(gca,'Ylim',[0 1000],'FontSize',12)
   ylabel('Heat Transfer Coefficient [ W/m^2 C ]')
   xlabel('Non-dimensional Suctionside Distance [ - ]')
   hold on
   gauge([]);
   hold off
end

if (sum(graphs==6) )
   figure
   this = 19; %dataset for Uncooled Run
   set(gcf,'Position',[50 50 600 650])
   plot(ngl,h(this,:),'ko-',ndx,bl2dh,'k-')
   set(gca,'Ylim',[0 1000],'FontSize',12)
```

```
   ylabel('Heat Transfer Coefficient [ W/m^2 C ]')
   xlabel('Non-dimensional Suctionside Distance [ - ]')
   legend('Measured Values','BL2D Output')
   hold on
   gauge([]);
   hold off
end

if (sum(graphs==7) )
   disp('h uncertainty (real values)')
   disp(uh)
   disp('h uncertainty (%)')
   disp(uh./h(1:size(uh,1),:)*100)

   disp('eta uncertainty (real values)')
   disp(ueta)
      disp('eta uncertainty (%)')
   disp(ueta./eta(1:size(ueta,1),:)*100)

end
```

Vita

Jim Bubb was born in Columbus, GA. Being a member of a military family, he lived in locations throughout the United States as well as Europe for most of his childhood. Eventually he graduated from Potomac High School in Woodbridge, VA in 1993. After high school, Jim attended Virginia Polytechnic Institute and State University to study Mechanical Engineering and graduated with a BS in 1998. After his graduation, he enrolled in the graduate program and will receive a Master's of Science August 1999 in Mechanical Engineering.